Mechanical Behavior of Lithium-Ion Batteries and Fatigue Behavior of Ultrasonic Weld-Bonded Lap-Shear Specimens of Dissimilar Magnesium and Steel Sheets

by

Wei-Jen Lai

A dissertation submitted in partial fulfillment
of the requirements for the degree of
Doctor of Philosophy
(Materials Science and Engineering)
in the University of Michigan
2014

Doctoral Committee:

Professor Jwo Pan, Co-Chair
Professor William Hosford, Co-Chair
Assistant Professor Jason McCormick
Professor Richard Robertson

Acknowledgements

I wish to express my sincere appreciation and gratitude to my advisor, Professor Jwo Pan, for his support, advice and guidance throughout my study. I would also like to thank my doctoral committee, Professor William Hosford, Professor Jason McCormick, Professor Richard Robertson for their helpful comments on my thesis.

I would like to thank Dr. Mohamed Yusuf Ali for the helpful discussion in experimental techniques and finite element modeling. The insightful discussions have been invaluable in the completion of this research. The samples prepared by Dr. Tsung-Yu Pan for my research is also appreciated. Besides, I would like to mention my former and current colleges, Dr. Teresa Rinker, Seunghoon Hong, Katherine Avery, Chengming Su, Catherine Amodeo, Shin-Jang Sung for their great help on my research. Special thanks to Marv Cressey and Kent Pruss for their assistance with the machining work. Finally, I would like to express my sincere gratitude to my fiancée, Claire, and my family for their support and encouragement for all the years of my PhD life.

Table of Contents

List of Figures

List of Tables

List of Abbreviations

RVE	representative volume element
ROM	rule of mixture
FSSW	friction stir spot welding
USW	ultrasonic spot welding
HDG	hot dipped galvanized
QS	quasi-static
LC	low-cycle
HC	high-cycle
HC-HL	high-cycle high-load
HC-LL	high-cycle low-load
SEM	scanning electron microscope

List of Symbols

(Chapter 2)

P_m^i buckling load of the i-th component with the two unattached elastic foundation

m number of half waves

E_i compressive elastic modulus of the i-th component

$I_i = bh_i^3/12$ moment of inertia of the i-th component

L length of the cell component

p lateral pressure on the beam

z deflection of the beam

k_1, k_2 spring constants of the harder and softer elastic foundations on the two sides of the beam

$\phi = k_1/k_2$ spring constant ratio

α coefficient depending upon the value of m in Equation (1)

$\overline{m}$ parameter defined in Equation (2)

b width of the cell component

h_i thickness of the i-th component

$E_i^{'}$ effective compressive elastic modulus of the i-th component under plane strain compression conditions

E_i compressive elastic modulus of the i-th component

ν_i Poisson's ratio of the i-th component

k spring constant of the elastic foundation

E out-of-plane compressive elastic modulus of the cell RVE specimen

h thickness of the neighbor cell components

P_c^i critical buckling load of the i-th component

P_n^i buckling load of the i-th component with an unattached elastic foundation on one side and a rigid wall on the other side

n number of waves

$\bar{n}$ parameter defined in Equation (10)

ε_m^i compressive strain of the i-th component with the two unattached elastic foundation

ε_n^i compressive strain of the i-th component with an unattached elastic foundation on one side and a rigid wall on the other side

A_i cross sectional area of the i-th component

P_{cell} buckling load of cell RVE specimen

n_i number of the i-th component in the cell RVE specimen

σ_{cell} buckling stress of the cell RVE specimen

A cross sectional area of the cell RVE specimen

α kink angle

w width of the cell RVE specimen

d kink length

θ shear band angle

θ_i initial shear band angle

θ_f final shear band angle

$\varepsilon_{Y'}$ nominal normal strain in y' direction

$\varepsilon_{Z'}$ nominal normal strain in z' direction

$\gamma_{Y'Z'}$ nominal shear strain in Y'Z' plane

ε_Y^T total nominal strain of one unit cell in cell RVE specimen

h_s shear band height

E'_{cell} effective compressive elastic modulus of the cell RVE specimen

f_i volume fraction of the i-th component

f void volume fraction

(Chapter 3)

$\sigma_{composite}$ nominal stress of the composite

σ_i nominal stress of the i-th component

V_i volume fraction of the i-th component

σ_{cell} nominal stress of the cell

σ_{foam} nominal stress of the foam

σ_{Al} nominal stress of the aluminum heat dissipater sheet

σ_{module} nominal stress of the module

ε_{cell} nominal strain of the cell

ε_{foam} nominal strain of the foam

ε_{Al} nominal strain of the aluminum heat dissipater sheet

ε_{module} nominal strain of the module

V_{cell} volume fraction of the cell

V_{foam} volume fraction of the foam

V_{Al} volume fraction of the aluminum heat dissipater sheet

ν_{Al} Poisson's ratio of the aluminum heat dissipater sheet

E_{Al} elastic modulus of the aluminum heat dissipater sheet

p lateral pressure on the beam

z deflection of the beam

k_1, k_2 spring constants of the harder and softer elastic foundations on the two sides of the beam

P_m^i buckling load of the i-th component with the two unattached elastic foundations

m number of half waves

$E_i^{'}$ effective compressive elastic modulus of the i-th component under plane strain compression conditions

$I_i = bh_i^3/12$ moment of inertia of the i-th component

L length of the module component

$\phi = k_1/k_2$ spring constant ratio

α coefficient depending upon the value of m in Equation (5)

b width of the module component

h_i thickness of the i-th component

$\overline{m}$ parameter defined in Equation (6)

E_i compressive elastic modulus of the i-th component

ν_i Poisson's ratio of the i-th component

P_1^i the lowest or the first mode ($m=1$) buckling load of the i-th component

ε_1^i nominal strain of the i-th component at which the first buckling mode occurs

A_i cross sectional area of the i-th component

ε_1^{Al} the first mode buckling strain of the aluminum heat dissipater sheet

σ_1^{module} the first mode buckling stress of the module RVE specimen

n_i number of the i-th component in the module RVE specimen

A cross sectional area of the module RVE specimen

k spring constant of the elastic foundation

E elastic modulus of the foam and cell as a homogenous material

h thickness of the neighbor components

E_{cell} elastic modulus of the cell

E_{foam} elastic modulus of the foam

(Chapter 5)

b specimen width

L sheet length

t_u thickness of sheet u

t_{l1} thickness of sheet $l1$

t_{l2} thickness of sheet $l2$

V specimen overlap length

w bonded width

E Young's modulus

G shear modulus

ν Poisson's ratio

σ normal stress

J J integral

W strain energy density function

s arc length

Γ path-independent J integration contour

$\mathbf{n}$ unit outward normal

$\mathbf{T}$ traction vector

$\mathbf{u}$ displacement vector

σ_{ij} stress components

ε_{ij} strain components

E' Young's modulus under plane stress or plane strain conditions

σ^* normal structural stress to satisfy the equilibrium and continuity of the strain and strain gradient

δ_u ratio of the sheet u thickness to the total sheet thickness

δ_{l1} ratio of the sheet $l1$ thickness to the total sheet thickness

δ_{l2} ratio of the sheet $l2$ thickness to the total sheet thickness

t total thickness of sheets u, $l1$ and $l2$

η_{u1} modulus ratio of sheet u to sheet $l1$

η_{12} modulus ratio of sheet $l1$ to sheet $l2$

D constant defined in Equation (39)

N_j constants defined in Equations (18) to (38)

C_{ijmnl} constants defined in Equation (40)

θ angle between the loading direction and the x direction

d distance from the load application point to the nearest main crack tip

F applied load

K_e global effective stress intensity factor

$\mathbf{K}(=K_1+iK_2)$ complex stress intensity factor for an interface crack

σ_y normal stress in the y direction

τ_{xy} shear stress

t_c characteristic length

r small distance ahead of an interface crack tip

ε bimaterial constant

κ_u constant defined in Equation (49)

κ_{l1} constant defined in Equation (50)

κ_{l2} constant defined in Equation (52)

E^* constant defined in Equations (54) and (55)

K_I, K_{II} global stress intensity factors for main cracks between similar materials

$\mathbf{K}(= K_1^A + iK_2^A)$ complex stress intensity factor obtained from ABAQUS

F_e dimensionless geometric function for main cracks

a kink length

φ kink angle

k_I, k_{II} local stress intensity factors

k_e local effective stress intensity factor

α, β Dundurs' parameters

c, d complex functions of α, β and φ

f_I, f_{II}, f_e dimensionless geometric functions for kinked cracks

$(k_e)_0$ local effective stress intensity factor at zero kink length

$(k_I)_0$, $(k_{II})_0$ local stress intensity factors at zero kink length

k_{eq} equivalent stress intensity factor

γ material constant

N number of cycles

C material constant for the Paris law

m material constant for the Paris law

Subscripts and Superscripts

u, $l1$, $l2$ upper sheet, lower sheet 1, and lower sheet 2

i, o inner and outer surfaces of the sheets with respect to the main crack

(Chapter 6)

F	applied load
b	specimen width
w	weld width
E	Young's modulus
G	shear modulus
ν	Poisson's ratio
t_u	upper sheet thickness
t_l	lower sheet thickness
$\delta = t_u / t_l$	thickness ratio
$\eta = E'_u / E'_l$	modulus ratio
E'	Young's modulus under plane stress or plane strain conditions
σ_x^u	normal structural stresses in the upper sheet
σ_x^l	normal structural stresses in the lower sheet
σ	normal structural stress
σ^*	normal structural stress to satisfy the equilibrium, and continuity of the strain and strain gradient
$\mathbf{K}$	complex stress intensity factor
$K_1,\ K_2,\ K_3$	stress intensity factors of an interfacial crack between dissimilar materials
σ_y	normal stress near a crack tip in y direction
τ_{xy}	shear stress near a crack tip
r	small distance ahead of an interfacial crack tip

t	characteristic length
ε	bimaterial constant
κ_u	constant defined in Equation (7)
κ_l	constant defined in Equation (8)
ω	angular quantity
J	J integral
E^*	constant defined in Equations (20)
G^*	constant defined in Equations (21)
K_I, K_{II}	stress intensity factors of an interfacial crack between similar materials
k_1, k_2	dimensionless geometric functions of an interfacial crack between dissimilar materials
k_I, k_{II}	dimensionless geometric functions of an interfacial crack between similar materials
K_e	effective stress intensity factor of an interfacial crack between dissimilar materials
k_e, j	dimensionless geometric functions
$\mathbf{K}^A$	complex stress intensity factor obtained from ABAQUS
K_1^A, K_2^A	stress intensity factors obtained from ABAQUS
L	specimen length
V	overlap length
α, β	Dundurs' parameters
δ_T	transition thickness ratio

N	applied load
K_1^E, K_2^E	stress intensity factors developed by Erdogan

Superscripts and Superscripts

u, l	upper and lower sheets of weld
i, o	inner and outer surfaces of the sheets

Chapter 1
Introduction

This thesis is divided into two main topics which are focused on the mechanical behavior of lithium-ion batteries and the fatigue behavior of welds in lap-shear specimens of dissimilar magnesium and steel sheets with adhesive. Lithium-ion batteries have been considered as the solution for electric vehicles for the automotive industry due to their lightweight and high energy density. One of the major design considerations of the lithium-ion batteries is the mechanical performance since it is of great importance for crashworthiness analyses. Therefore, macro homogenized material models of the representative volume elements (RVEs) for both the battery cells and modules have to be developed for crashworthiness analyses with sacrifice of the accuracy at the micro scale. The concept of the macro homogenized material model is to treat the various components in battery cells and modules as a homogeneous material such that a single material model can be used to model the mechanical behaviors of battery cells and modules instead of modeling each component in the cells and modules individually in finite element analyses.

Lightweight materials such as advanced high strength steels, aluminum, and magnesium alloys have been replacing the low-carbon steel in the automotive industry to reduce vehicle weight for better fuel efficiency. Therefore, the failure modes and fatigue properties of the dissimilar joints are of great importance.

In this thesis, the mechanical behavior of representative volume elements of lithium-ion battery cells and modules under various loading conditions and the failure modes and fatigue behavior of lap-shear specimens of dissimilar sheets are investigated. The chapters were prepared as individual papers. Therefore some concepts are repeated as necessary to facilitate comprehension for each chapter separately.

In Chapter 2, the mechanical behavior of lithium-iron phosphate battery cells is investigated by conducting in-plane and out-of-plane compression tests of RVE specimens of dry cells. An innovative test fixture was developed to achieve this goal. The experimental stress-strain curves are correlated to the deformation patterns of battery cells. Buckling analyses were conducted to justify the length selection of cell RVE specimens. The buckling analysis also provides a theoretical basis for future design of cell and module RVE specimens. The buckling of cell components is correlated to the buckling stress of battery cells and the buckling analysis provides an analytical method to estimate the yield stress for cells and modules. Finally, an idealized kinematics model is presented to explain the physical mechanisms of the kink and shear band formation in the cell RVE specimens under in-plane constrained compression.

In Chapter 3, the mechanical behavior of lithium-ion battery modules is investigated by conducting tensile tests of the module components, constrained compression tests of dry module RVE specimens, and a constrained punch indentation test of a small-scale dry module specimen. The results of tensile tests of the module components are used to characterize the tensile behavior of module specimens. The in-plane compressive stress-strain curves are correlated to the deformation patterns of modules. The buckling of the module components is correlated to the buckling stresses of modules. Finally, a small-scale module punch indentation test was also

conducted to benchmark the computational results based on a macroscopic homogenized foam material model.

In Chapter 4, the failure modes and fatigue behaviors of ultrasonic spot welds in lap-shear specimens of magnesium AZ31B and hot-dipped-galvanized mild steel sheets with and without adhesive are investigated. Ultrasonic spot welded, adhesive-bonded, and weld-bonded lap-shear specimens were made. These lap-shear specimens were tested under quasi-static and cyclic loading conditions. Interrupted tests were conducted to investigate the fatigue behavior of adhesive-bonded and weld-bonded lap-shear specimens under cyclic loading conditions. Fracture surfaces of the specimens that failed in the kinked crack failure were also characterized to study the kinked crack growth in the magnesium sheet.

In Chapter 5, stress intensity factor solutions for adhesive-bonded lap-shear specimens of magnesium alloy AZ31B and hot-dip-galvanized mild steel sheets with and without kinked cracks are investigated for fatigue life estimations. The analytical global J integral and effective stress intensity factor solutions for main cracks in lap-shear specimens of three dissimilar sheets under plane strain conditions are developed based on beam bending theory. The global stress intensity factor solutions for the main cracks in the lap-shear specimens from the corresponding finite element analyses are then presented to validate the analytical solutions. Next, the local stress intensity factor solutions for kinked cracks with the experimentally observed kink angle as functions of the kink length from the corresponding finite element analyses are presented and the computational solutions are also compared with the analytical solutions at small kink lengths. The computational local stress intensity factor solutions are then adopted to estimate the fatigue lives of the lap-shear specimens based on a kinked crack growth model and available material constants for the Paris law.

In Chapter 6, the analytical stress intensity factor and J integral solutions for welds in lap-shear specimens for two dissimilar sheets based on the beam bending theory are first reviewed. The solutions are then presented in the normalized forms. Next, two-dimensional finite element analyses were selectively conducted to validate the analytical solutions based on the beam bending theory. The interfacial crack parameters, the stress intensity factor solutions, and the J integral solutions for welds in lap-shear specimens of different combinations of steel, aluminum, and magnesium and the combination of aluminum and copper sheets of different thickness ratios are then presented for convenient fracture and fatigue analyses. The transition thickness ratios for critical crack locations for different combinations of dissimilar materials are then determined from the analytical solutions. The transition weld widths for applicable ranges of the weld widths for the analytical solutions based on the beam bending theory are also presented. Finally, fracture and fatigue behaviors of dissimilar ultrasonic magnesium/steel, dissimilar laser aluminum/copper, and similar laser steel welds in lap-shear specimens are examined and demonstrate the usefulness of the graphical stress intensity factor solutions.

Chapter 2
Mechanical Behavior of Representative Volume Elements of Lithium-Ion Battery Cells under Compressive Loading Conditions

2.1. Introduction

Lithium-ion batteries have been considered as the solution for electric vehicles for the automotive industry due to their lightweight and high energy density. The major design considerations for lithium-ion batteries involve electrochemistry, thermal management and mechanical performance. The electrochemistry has been widely studied since it directly determines the battery performance and its life cycle. Different active materials on electrodes form different types of lithium-ion batteries. However, the basic chemical reactions of battery cells are similar. For automotive applications, the mechanical performance is of great importance for crashworthiness analyses. Mechanical tests such as shock, drop, penetration, roll-over, and crush tests for abuse conditions of battery cells, modules and packs were documented in SAE J2462 [1]. Research was conducted on the safety performance of the battery cells under mechanical tests such as nail penetration tests, round bar crush tests, and pinch tests, for example, see [2-4]. However, the research on the mechanical behavior of the representative volume elements (RVEs) of lithium-ion batteries are quite limited.

Sahraei et al. [5] conducted a series of mechanical tests and computational works on commercial $LiCoO_2$/graphite cells used for cell phones. The results indicate that the compressive mechanical behavior is characterized by the buckling and densification of the cell components. Other testing and modeling data available were also conducted on commercial

$LiCoO_2$ cylindrical or prismatic battery cells [6,7]. However, this information is of limited use for researchers to model the mechanical performance of automotive high-voltage $LiFePO_4$ battery cells and modules for crashworthiness analyses. Sahraei et al. [5] indicated that computational effort is quite significant to model local buckling phenomenon of battery cells under in-plane compression. Therefore, macro homogenized material models of the representative volume elements (RVEs) for both the battery cells and modules have to be developed for crashworthiness analyses with sacrifice of the accuracy at the micro scale.

One of the primary objectives of this investigation is to develop testing methods to determine the detailed mechanical properties of lithium-ion battery cells and modules [8] in a systematic fashion. Another is to provide the necessary experimental data for the development of macro homogenized material models, see [9,10]. At this point, there is no test standard for characterizing the mechanical properties of the representative volume elements (RVEs) of lithium-ion batteries under large deformation because it is difficult to test a live battery due to the safety concern. Even in the discharged state, the volatile and toxic electrolyte still poses a severe safety concern. Further, standard compression tests in an in-plane direction of cell specimens do not provide useful information since there are almost no bonding forces between the anode, cathode, separator and cover sheets. The cell specimens fall apart when no out-of-plane constraints are applied. Therefore, a constrained compression test procedure needs to be developed and provide other researchers a way to conduct tests and compare the test results. The results presented in this study can also help to understand the deformation process and mechanical behavior of battery cells such that homogenized material models can be developed for battery cells.

One ultimate goal of this investigation is to provide test data for development of computational models for multi-scale multi-physics analyses of battery packs in vehicles under crash loading conditions. Battery pack designs are different for different electric vehicles. Battery packs can have various shapes of plastic or metal shells that enclose a cooling system, electronics, and battery modules, that contain battery cells with electronics cover plates, control electronics, pressure plates, laser welded bus bars, heat sink plates, interconnected covers and compression bands. Battery pack designs are usually quite complex. Different types of finite elements such as shell elements, solid elements, rigid elements, and weld elements are typically used in computational models to reduce the sizes of the models. However, the sizes of the computational models for battery packs can still be quite large for crashworthiness analyses since the sizes of finite elements have to be small with consideration of small thicknesses of pack components and deformation patterns of interest. It is not possible to model the details of all battery pack components for computational efficiency in full vehicle crashworthiness analyses.

Finite element models for small cell specimens under compression in Sahraei et al. [5] showed the complexity of the finite element analyses at the length scale of cell components. Finite element models for cell RVE specimens under in-plane constrained compression in Ali et al. [9] also showed the complexity of the finite element analyses at the length scale of cell components. Sahraei et al. [7] conducted finite element analyses of an idealized battery pack with an outer steel shell and a homogenized crushable foam core to simulate a drop test of the battery pack on a rigid cylinder. The results showed that with the homogenized foam model, it was computationally efficient to model the drop test of the battery pack for optimum design. Ali et al. [10] conducted finite element analyses of a small-scale module specimen under in-plane punch indentation [8] based on several homogenized material models. The computational results

indicated that it was computationally efficient to simulate the module specimen under punch indentation with the homogenized material models. Therefore, homogenized material models for cells and modules can be quite useful for simulation and control of the crush responses of battery packs for optimum design under crash loading conditions with computational efficiency. Based on homogenized material models, computational results for deformed battery cells from full vehicle crashworthiness analyses can then be used for further combined structural, electrical and thermal analyses of battery cells at the smaller length scales.

In this investigation, cell RVE specimens were first made from the individual cell components and in-plane constrained compression tests were then conducted. Out-of-plane compression tests of cell RVE specimens were also conducted to understand the different behaviors in the in-plane and out-of-plane directions. Based on the experimental observations of the cell RVE specimens under in-plane constrained compression and the results of the corresponding finite element analyses, the buckling mode of the cell RVE specimens under in-plane constrained compression is examined by elastic buckling analyses of a beam with lateral constraints. The buckling loads for the cell RVE specimens are then obtained based on the elastic buckling solutions and the composite rule of mixture (ROM). In addition, an idealized kinematics model is developed to explain the physical mechanisms of the kink and shear band formation in the cell RVE specimens under in-plane constrained compression. Finally, some conclusions are made.

2.2. Specimens

The structure of a typical battery module based on prismatic pouch cells is shown in Figure 2.1. As shown in the figure, the module is composed of many compartments separated by

aluminum heat dissipater sheets. Inside each compartment (in the middle portion of the module where the side aluminum heat dissipater sheet is removed), there are two cells (shown in grey) with one layer of foam (shown in black) between the two cells. The battery module is usually held together by two stainless steel bands (not shown) with a specified tension and adhesive (between the cell and the foam layer, and between the cell and the aluminum heat dissipater sheet).

Each cell consists of five major components: cover sheet, anode, cathode, separator and electrolyte. Since the electrolyte is difficult to handle during assembly due to its toxicity, all the cell RVE specimens tested in this study were made without electrolyte. Table 2.1 lists all the detailed material and thickness information of the cell and module components. The cover sheet is composed of aluminum foil with polyamide and polypropylene layers on both sides bonded together by adhesive. The thicknesses of the individual layers of the cover sheet are shown in Table 2.1 and the total thickness of the cover sheet is 0.111 mm. The anode and cathode selected for this study are graphite coated on copper foil and $LiFePO_4$ coated on aluminum foil, respectively. The copper foil has a thickness of 9 μm and the total thickness of the anode sheet is 0.2 mm. The aluminum foil has a thickness of 15 μm and the total thickness of the cathode sheet is 0.2 mm. Both the anode and cathode sheets are double-side coated. The SEM images of the graphite and $LiFePO_4$ on the anode and cathode sheets are shown in Figures 2.2(a) and 2.2(b), respectively. It is noted that both active materials on the electrodes are in a powder form held together by binders and therefore possess a high degree of porosity. It is not the intent of this investigation to characterize the morphology of the active materials. The separator is made of polyethylene with the porosity ranging from 36 to 44% and a thickness from 16 to 25 μm. All the cell components are purchased commercially.

Figure 2.3(a) shows a schematic of a pouch cell and a cell RVE specimen with the z-y-z coordinate system. Here, x and y are referred to as the in-plane directions and z is referred to as the out-of-plane plane direction. A small cell RVE specimen with the dimensions is shown in Figure 2.3(b). Figure 2.3(c) shows a side view of a portion of a cell RVE specimen with the individual cell components. The large arrows shown in the figures indicate the in-plane compressive direction. As shown in Figure 2.3(c), the anodes and cathodes form alternating layers with two cover sheets. The separators are located between electrode and cover sheets. The cell RVE specimen is composed of 10 anode, 10 cathode, 21 separator and 2 cover sheets. The cell components were manually cut and assembled. The assembly of the cell components in the generic cell RVE specimen as schematically shown in Figure 2.3(c) may be slightly different from those in usual lithium-ion cells for convenience of assembly of the purchased cell components. However, generic cell RVE specimens with slightly different assemblies should have the similar buckling, kink and shear band mechanisms under constrained compression as discussed later due to their layered structures. The specimen has the size of 25 mm × 25 mm × 4.6 mm. No electrolyte was added for the dry cells. Due to the large specimen width in the x direction compared to the specimen thickness, the specimen width does not change before and after in-plane compression tests. Therefore, the specimens are subject to the plane strain conditions in the x direction under in-plane compression tests.

2.3. Quasi-static compression tests of cell RVE specimens

2.3.1. In-plane (y direction) constrained compression tests of cell RVE specimens

Battery modules are usually held together by adhesive between the cells and the neighbor foam layers and aluminum heat dissipater sheets as well as two wrapping bands with tension as

shown in Figure 2.1. In the middle portion of a module, the cells are constrained by the neighbor foam layer and aluminum heat dissipater sheet. In an individual cell, the cell components can buckle individually with constraints from the neighbor cell components since there are no bonding forces between the cell components. Hence, a fully constrained die set was designed for constrained compression tests of cell RVE specimens. The punch and die setup for in-plane constrained compression tests of cell RVE specimens is shown in Figure 2.4. The setup is composed of a male rectangular punch and a female die such that the specimen slot can be adjusted for different specimen geometries. A PMMA side window was made for recording the deformation process during the compression. The specimen slot in the die has an opening of 5 mm × 25 mm which leaves a gap of about 0.4 mm between the specimen and the side walls. The compression tests were conducted with the displacement rate of 0.5 mm/min (nominal strain rate of 0.0003 s^{-1}). The punch displacement was taken from the cross-head displacement recorded during the experiments.

Figure 2.5 shows the nominal compressive stress-strain curves of three cell RVE specimens tested at a displacement rate of 0.5 mm/min. The specimens showed a nearly linear behavior in the beginning with the effective compressive elastic modulus of 188 MPa. The term "effective compressive elastic modulus" is used since the specimens are subjected to the plane strain conditions in the x direction. This value of 188 MPa is in good agreement with the effective compressive elastic modulus of 190 MPa which is estimated from the effective compressive elastic moduli of the nominal stress-strain curves of the cell component specimens under in-plane constrained compression tests based on the composite rule of mixture (ROM) presented in Appendix A. As shown in Figure 2.5, a noticeable change of slope takes place when the strain increases to about 2%. As the strain continues to increase, the slope appears to

remain constant until the strain reaches about 20%. Then the slope starts to increase gradually as the strain increases to about 34%. Some minor stress drops were observed after the initial linear stage due to the development of kinks and shear bands. The trends of all three curves are quite consistent. The nominal compressive stress-strain curve of the RVE specimen from the finite element analysis of Ali et al. [9] is also shown in Figure 2.5 for comparison.

Figures 2.6(a) to 2.6(d) show the deformation patterns of a cell RVE specimen at the nominal strain of 1% in the initial linear stage, at the nominal strain of 2% where the slope changes, and at the nominal strains of 10% and 15%. A careful examination of the deformation pattern shown in Figure 2.6(a) indicates the initial linear stage corresponds to the development of a smooth buckling mode of the cell components. A detailed analysis of the elastic buckling of the cell components will be presented in the next section. As the displacement increases toward the nominal strain of 2% where the slope starts to level off, the cell RVE specimen shows the development of kinks or plastic hinges of the cell components as indicated in Figure 2.6(b). The presence of the kinks promotes the shear band formation as indicated in Figure 2.6(b). The shear band formation accommodates for the in-plane compression and hence induces the slope change of the nominal stress-strain curve. As the strain continues to increase, more kinks and shear bands form across the cell RVE specimen, as shown in Figures 2.6(c) and 2.6(d). Figures 2.6(e) and 2.6(f) show the front and back views of the tested cell RVE specimen at the nominal strain of about 34%. As shown in the figures, the kinks are fully developed to the folds and many shear band regions can be identified. After the efficient compaction mechanism of shear bands is completed, further compression can be accommodated by the micro buckling of the cell components outside the shear band regions, as marked in Figures 2.6(e) and 2.6(f), and the compression in the shear band regions.

It should be noted that although the cell RVE specimen was almost fully constrained during the test, the clearance in the die between the specimen and the die walls in the out-of-plane direction still provided some space for the cell RVE specimen to buckle. Also, the large porosities of the graphite, $LiFePO_4$ and separator layers provided extra space for the components of the cell RVE specimen to buckle. In addition, the microscopic gaps between the cell components provided more space for the cell components to compact. As the displacement further increases in the last stage of compression, the cell RVE specimen reaches the nearly fully dense stage. At this stage, nearly 7 half waves of the macro buckling can be seen in Figures 2.6(d) to 2.6(f). Based on the original specimen length, each half wavelength is about 3.6 mm, which is close to the specimen thickness (4.6 mm). The experimental results can also be compared with the results of the finite element analysis reported in Ali et al. [9]. As shown in Figure 2.5, the nominal stress-strain curve from the finite element analysis based on the Gurson's yield function for the porous components of the cell specimen is in good agreement with the test results by selecting a proper void volume fraction for the porous components of the cell RVE specimen. Images of the deformed cell at the strain of 34% from the experiment and the corresponding finite element analysis [9] are shown as two inserts in Figure 2.5 for comparison. As shown in the figures, 7 half waves were observed in the experiment whereas 10 half waves were obtained from the finite element analysis.

As indicated in Sahraei et al. [5], cutting specimens from commercial full sized battery cells poses a formidable task. Testing high voltage automotive battery cells and modules is expensive and needs special safety attention since electrolyte is toxic and difficult to handle. The results of a companion research program on testing full sized commercial battery cells under in-plane constrained compression showed similar stress-strain curves as those presented in this

study. However, with the potential severe heating and fire hazard for the full sized commercial battery cells under compression, it was difficult to observe and understand the fundamental deformation mechanisms of the battery cells under compression. The compressive stress-strain curves of small lithium cobalt dioxide cells for cell phones presented in Sahraei et al. [5] are also similar to those presented in this study. It should be noted that one focus of this study is on characterizing and understanding the compressive behavior of cells rather than characterizing specific battery cells, with or without electrolyte, which may vary from one manufacturer to another.

2.3.2. Out-of-plane (z direction) compression tests of cell RVE specimens

Figure 2.7(a) shows a schematic of a pouch cell and a cell RVE specimen with the x-y-z coordinate system. A small out-of-plane compression cell RVE specimen is shown in Figure 2.7(b) with the dimensions. Figure 2.7(c) shows a side view of a small portion of the cell RVE specimen with the individual cell components. The large arrows shown in the figure indicate the out-of-plane compressive direction. The out-of-plane compression cell RVE specimen was smaller than the in-plane compression cell RVE specimen in order to avoid exceeding the load limit of the load cell. The size of the out-of-plane compression cell RVE specimen is reduced to 10 mm × 10 mm × 4.6 mm as shown in Figure 2.7(b). The layered structure of the cell RVE specimen is the same as that of the cell RVE specimens for in-plane constrained compression tests. The test was conducted with a displacement rate of 0.25 mm/min (nominal strain rate of 0.0009 s^{-1}). No constraint was applied to the lateral sides of the specimen in the x and y directions.

Three nominal compressive stress-strain curves of the cell RVE specimens under out-of-plane compression are shown in Figure 2.8(a). The three in-plane nominal compressive stress-strain curves in Figure 2.5 are also shown for comparison. As shown in the figure, the low stress response in the early stage of the out-of-plane compression tests can be attributed to the consumption of the porosity in the cell components and the microscopic gaps between the cell components. With the increasing strain, densification of the cell components started to contribute to the sharp increase of the stress. The nominal stress-strain curves appear to be linear elastic again at the strain of about 40% as the strain increases. This suggests that the total volume fraction of the porosity in the components and the microscopic gaps between the components is about 40% when the cell RVE specimens are nearly fully condensed and become linear elastic as the strain increases. The tested specimens retained the final thicknesses and appeared to be permanently deformed. However, no dimension change was observed in the two lateral directions perpendicular to the loading direction, which corresponds to zero Poisson's ratio. Figure 2.8(b) shows pictures of cell RVE specimens before (left) and after (right) the compression.

2.4. Buckling analyses of cell RVE specimens under in-plane (y direction) constrained compression

Based on the experimental observations of the cell RVE specimens under in-plane constrained compression, the physical mechanism to accommodate the compression starts with the elastic buckling of the cell components. When a cell RVE specimen was made, the component sheets were first assembled and packed together. The specimen was then put in the slot of the female die. When a cell RVE specimen is under in-plane compression, the component

sheets buckle independently with the lateral constraints from the neighbor component sheets. Since the component sheets were only packed together, each component sheet can be treated as an individual thin plate or beam under in-plane compression with the lateral constraints which can be treated as unattached elastic foundations.

Figure 2.9 shows a uniform straight beam under end loads and supported by two unattached elastic foundations. Both ends are hinged and the beam is supported by the elastic foundations through the lateral pressure p proportional to the deflection z in the Z direction. Here, k_1 and k_2 represent the spring constants of the harder and softer elastic foundations on the two sides of the beam, respectively. The buckling load solution of the beam can be found in [11]. Based on the solution listed in [11], the buckling load of the i-th component with the two unattached elastic foundations can be expressed as

$$P_m^i = \frac{m^2\pi^2 E_i' I_i}{L^2} + \frac{k_2 L^2}{m^2\pi^2}\phi^\alpha \tag{1}$$

where m represents the number of half waves in which the component buckles and is equal to the lowest integer greater than $\overline{m}$. Here, $\overline{m}$ is defined as

$$\overline{m} = \frac{1}{2}\left(\sqrt{1+\frac{4L^2}{\pi^2}\sqrt{\frac{k_2}{E_i' I_i}}} - 1\right) \tag{2}$$

In Equation (1), $\phi = k_1/k_2$ and α depends upon the value of m. In Equations (1) and (2), I_i ($= bh_i^3/12$) is the moment of inertia for the i-th component. E_i' is the effective elastic modulus for a thin plate under plane strain compression conditions and is equal to $E_i/(1-\nu_i^2)$, where E_i and ν_i are the compressive elastic modulus and Poisson's ratio of the i-th component. The effective compressive elastic moduli for the cell component specimens are listed in Table 2.2. Here, L, b and h_i are the length, width, and thickness of the i-th component.

After the buckling of the cell components, kinks and shear bands are formed according to the buckling mode of the cell components. Based on the experimental observations, the cell RVE specimens appear to buckle in an asymmetric fashion where no symmetry with respect to the central anode sheet was observed. However, the results of the finite element analysis [9] indicated that in the very early stage the component sheets buckle in the symmetric mode. For anode, cathode, and separator sheets in the cell RVE specimen, the sheets can be thought as a beam with two unattached elastic foundations on both sides. For the anode, cathode and separator sheets in the middle portion of the cell RVE specimens, the buckling mode will be dominated by the constraints on both sides of the sheets. It is assumed that the spring constants for the elastic unattached foundations are the same and denoted by k. Here, k represents the lateral force per unit plate length per unit deflection of the neighbor components in the out-of-plane direction. The spring constant k can be expressed in terms of the out-of-plane compressive elastic modulus E of the cell RVE specimens as

$$k = \frac{Eb}{h} \tag{3}$$

where h represents the thickness of the neighbor cell components. With the elastic spring constant k on both sides of the beam is equal to each other, Equation (1) becomes

$$P_m^i = \frac{m^2\pi^2 E_i' I_i}{L^2} + \frac{kL^2}{m^2\pi^2} \tag{4}$$

where m again represents the number of half waves in which the component buckles and is equal to the lowest integer greater than $\overline{m}$ as before. Here, $\overline{m}$ is defined as

$$\overline{m} = \frac{1}{2}\left(\sqrt{1+\frac{4L^2}{\pi^2}\sqrt{\frac{k}{E_i' I_i}}} - 1\right) \tag{5}$$

Equations (4) and (5) represent the buckling solution in Timoshenko [12] for a beam with an attached elastic foundation. Considering m as a real number as in Ali et al. [9], $\partial P_m^i / \partial m = 0$ gives

$$m = \left(\frac{k}{E_i' I_i} \right)^{\frac{1}{4}} \frac{L}{\pi} \tag{6}$$

The critical buckling load P_c^i can be determined as

$$P_c^i = 2(kEI)^{\frac{1}{2}} \tag{7}$$

Equation (6) can be rewritten for the half wavelength L/m as

$$\frac{L}{m} = \left(\frac{E_i' I_i}{k} \right)^{\frac{1}{4}} \pi \tag{8}$$

As indicated in Equations (7) and (8), the critical buckling load P_c^i and the half wavelength L/m are independent of the specimen length.

The cover sheets have only one unattached elastic foundation and are free to buckle to the unconstrained side due to the small clearances in the die for the cell RVE specimen. However, the small clearances will limit the cover sheets to fully develop a lower order buckling mode. For the anode, cathode and separator sheets near the cover sheets, they can start to buckle in a lower order mode but will also be constrained by the rigid walls through the cover sheets. The results of the finite element analysis [9] indicate that the cover sheets are constrained by the rigid walls and buckle in a high order mode. For a beam with one unattached elastic foundation on one side and a small clearance to a rigid wall on the other side, the elastic buckling solution is approximated by the elastic buckling solution for a beam with an unattached elastic foundation on one side and a rigid wall on the other side as discussed in Ali et al. [9]. For the cover sheets

and the neighbor sheets, the buckling load of the i-th component can approximately be expressed as

$$P_n^i = \frac{4n^2\pi^2 E_i' I_i}{L^2} + \frac{3kL^2}{4n^2\pi^2} \tag{9}$$

where n represents the number of waves in which the component buckles and is equal to the lowest integer greater than $\bar{n}$. Here, $\bar{n}$ is defined as

$$\bar{n} = \frac{1}{2}\left(\sqrt{1+\frac{4L^2}{\pi^2}\sqrt{\frac{3k}{16E_i' I_i}}} - 1\right) \tag{10}$$

Considering n as a real number as in Ali et al. [9], $\partial P_n^i / \partial n = 0$ gives

$$n = \left(\frac{3k}{16E_i' I_i}\right)^{\frac{1}{4}} \frac{L}{\pi} \tag{11}$$

The critical buckling load P_c^i can be determined as

$$P_c^i = 2\sqrt{3}(kE_i' I_i)^{\frac{1}{2}} \tag{12}$$

Equation (11) can be rewritten for the wavelength L/n as

$$\frac{L}{n} = \left(\frac{16E_i' I_i}{3k}\right)^{\frac{1}{4}} \pi \tag{13}$$

As indicated in Equations (12) and (13), the critical buckling load P_c^i and the wavelength L/n are independent of the specimen length.

Based on the nominal out-of-plane compressive stress-strain curves shown in Figure 2.8(a), the elastic compressive modulus E of the cell RVE specimens can be approximated by taking the initial slope of the curve. The estimated compressive modulus E of the cell RVE specimens is 8.5 MPa. The spring constant k can be estimated as 4.6×10^7 N/m^2 for the cover

sheets and neighbor sheets near the die walls, and 9.2×10^7 N/m^2 for the component sheets in the middle portion of the cell specimen. For the sheets in the middle portion of the cell specimen, the original solution given by Timoshenko [12] in Equations (4) and (5) can be used to estimate the buckling modes and loads of the component sheets in the middle portion of the specimen as listed in Table 2.3. The results for the cover sheets are not applicable (NA) but are listed in Table 2.3 for reference only. As listed in Tables 1.3, the values for $\overline{m}$ are 21.3, 22.2, 16.3 and 124.6 based on Equation (5) which give the buckling modes of 22, 23, 17 and 125 that give the lowest buckling loads with the constraints for the cover sheet, anode, cathode and separator sheets in the middle portion of the cell specimen, respectively.

For the cover sheets and the neighbor sheets near the die walls, the buckling modes and loads can be estimated based on Equations (9) and (10) for a beam with an unattached elastic foundation on one side and a rigid boundary on the other side as listed in Table 2.4. Note that one wave of the cover sheets and neighbor sheets corresponds to two half waves of the component sheets in the middle portion of the cell RVE specimen. Therefore, the values for $2\overline{n}$ are listed in Table 2.4 for comparison. As listed in Table 2.4, the values for $2\overline{n}$ are 23.1, 24.1, 17.6 and 137.4, which give the buckling mode number $2n$ of 24, 26, 18 and 138 that give the lowest buckling loads with the constraints for the cover sheet, anode, cathode and separator sheets near the sides of the cell RVE specimen, respectively. The corresponding buckling loads for the component sheets are listed in Tables 2.3 and 2.4.

The corresponding compressive strains at these buckling loads can be calculated by

$$\varepsilon_m^i = \frac{P_m^i}{E_i' A_i} \qquad \text{or} \qquad \varepsilon_n^i = \frac{P_n^i}{E_i' A_i} \tag{14}$$

for the component sheets in the middle portion or near the sides of the cell specimen. Here, A_i is the cross sectional area of the i-th component. Equation (14) gives the strains at these buckling loads for the i-th components. The values are also listed in Tables 2.3 and 2.4. As listed in the tables, the strains for all the cell components calculated in both buckling analyses are comparable to those obtained from the experiments and from the results of the finite element analysis [9].

The buckling loads of the cell RVE specimen when the cell components buckle can be obtained by summing over the loads of the cell components at the strains when the cell components buckle as

$$P_{cell} = \varepsilon_m^i \sum n_i E_i' A_i \qquad \text{or} \qquad P_{cell} = \varepsilon_n^i \sum n_i E_i' A_i \tag{15}$$

where n_i is the number of the i-th component in the cell RVE specimen according to the composite rule of mixture. The nominal buckling stress of the cell RVE specimen can be obtained by dividing the load by the cross sectional area of the cell RVE specimen as

$$\sigma_{cell} = \frac{P_{cell}}{A} \tag{16}$$

The buckling stresses for the cell RVE specimen based on the buckling loads of the cover sheets, anode, cathode and separator sheets near the sides of the cell RVE specimen are 3.33, 11.7, 6.47, and 3.56 MPa as listed in Table 2.4. It should be noted that the results of the finite element analysis in [9] suggest that the cover sheets actually buckle first. The buckling stress of 3.33 MPa based on the buckling load of the cover sheets near the sides of the cell RVE specimen in Table 2.4 in general agrees with the critical stress of 4.0 MPa obtained from the experiments. The buckling stresses for the cell RVE specimen based on the buckling loads of the anode, cathode and separator sheets in the middle portion of the cell RVE specimen are 9.90, 5.47, and

2.91 MPa as listed in Table 2.3. The buckling stresses listed in Tables 2.3 and 2.4 in general agree with the critical stress of 4.0 MPa obtained from the experiments.

It should be noted again that the results of the finite element analysis in [9] suggest that the cover sheets actually buckle first. Based on Equation (10), $\bar{n} = 11.62$ and $n = 12$ for the cover sheets. This corresponds to 24 half waves for the cell RVE specimen. Note that 7 half waves were observed in the experiment whereas 10 half waves are obtained from the corresponding finite element analysis [9]. However, the in-plane constrained compression test conducted in this investigation has a total clearance of 0.358 mm between the cell RVE specimen and the die walls. This can reduce the spring constants for the unattached elastic foundations. The computational results indicate that when the clearance is reduced to 0, 15 half waves appear which is reasonably in agreement with about 20 half waves obtained by both elastic buckling analyses. It should be noted that the analytical results based on Equations (5) and (10) are approximate in nature and the analytical results are in reasonable agreement with the experimental and computational results.

As indicated in Equations (8) and (13), the half wavelength L/m for the component sheets in the middle portion of the cell RVE specimens and the wavelength L/n for the component sheets near the sides of the cell RVE specimens are independent of the specimen length. As indicated in Equations (7) and (12), the buckling loads are functions of the elastic bending rigidity and the out-of-plane elastic modulus of the cell RVE specimens, and they are independent of the specimen length. The results suggest that the length of the cell RVE specimens is appropriately selected since the cell RVE specimens buckle with multiple half waves under in-plane constrained compression. Therefore, the constrained compressive behavior of the cell RVE specimens obtained in this investigation can in general represent that of battery

cells with a full length. After the buckling mode is settled, plastic hinges or kinks will develop and the shear band mechanism will start to efficiently compact the cell RVE specimens as the compression continues.

2.5. Kink and shear band formation under in-plane (y direction) constrained compression

Based on the experimental observations of the cell RVE specimens under in-plane constrained compression, the physical mechanism to accommodate the compression can be summarized in the following. First, the elastic buckling of the cell RVE components takes place. Next, kinks of the components are initiated and consequently shear band regions across the specimen are formed. As the compression continues, the shear band regions are compressed, sheared and rotated. Also, the regions outside the shear bands are under compression. Once the shear band regions reach their shear and rotational limits, compaction takes place in both regions inside and outside of the shear bands.

Figures 2.10(a) to 2.10(f) show an idealized deformation process in a cell RVE specimen under in-plane constrained compression without any clearance between the specimen and the die walls to explain the kink and shear band formation mechanism in the specimen and estimate the strains inside and outside of the shear band region in terms of the kink length, kink angle and shear band angle. Figures 2.10(a) to 2.10(c) show schematics of a cell RVE specimen before, during, and after the formation of shear band regions under in-plane constrained compression, respectively. Figures 2.10(d) to 2.10(f) show the detailed schematics of one unit cell of the specimen corresponding to Figures 2.10(a) to 2.10(c), respectively. Figures 2.10(a) and 2.10(d) show the original configuration of the specimen before the kinks and shear band regions are formed. In Figure 2.10(a), region I between two parallel dashed lines as marked represents the

shear band region. Since no shear bands are formed, the initial kinked angle α (as marked in Figure 2.10(e)) is 90^{o}. Figures 2.10(b) and 2.10(e) show the configuration where the kinks are formed and the shear band regions are compressed, sheared and rotated. During the deformation process, the kinked angle α decreases from the original kink angle of $\alpha = 90^{o}$ to the final kink angle of $\alpha = 0^{o}$. Figures 2.10(c) and 2.10(f) show the configuration when the shear band region has reached its shear and rotational limit.

Figures 2.10(d) to 2.10(f) show the deformation history of one unit cell of the specimen. In Figure 2.10(d), the global y and z coordinates are shown. In Figures 2.10(d) to 2.10(f), the local material y' and z' coordinates represent the coordinates that rotate or move with the material during the deformation. In Figures 2.10(d) to 2.10(f), w represents the cell thickness, d represents the kink length (which is assumed to be constant in this idealized model), θ represents the shear band angle, and θ_i and θ_f represent the initial and final shear band angles, respectively. As shown in Figure 2.10(d), shear bands (between two parallel dashed lines) are to be formed across the cell RVE specimen (shown in gray) to accommodate the compression. During the deformation, the kink angle α deceases from 90^{o} toward 0^{o} while the shear band angle θ changes due to the rotation of the shear band region and the deformation in the regions inside and outside the shear band. As shown in Figures 2.10(d) to 2.10(f), the shear band region I can be represented by the parallelogram ABCD which is deformed into A'B'C'D' and then A"B"C"D". Therefore, in region I inside the shear band, the material has the compressive strains in the y' and z' directions and the shear strain in the Y'-Z' plane. As shown in Figures 2.10(d) to 2.10(f), region II outside the shear band can be represented by the triangle CDE which is deformed into C'D'E' and then C"D"E". Therefore, in region II outside the shear band, the material is under biaxial compressive strains in the y' and z' directions. After α reaches 0^{o}, θ

decreases as the compression continues. It should be noted that Figures 2.10(a) to 2.10(f) are idealized. In reality, the shear bands do not form at the same time and the shear band angles are different for different parts of the specimens.

Based on the idealized shear band deformation process, the local material strains inside and outside the shear band regions can be estimated in terms of the compressive strain of the cell RVE specimen. The shear band mechanism appears to optimize the total compressive strain in the y direction. It should be mentioned that the cell can be thought of a unidirectional composite where the load carrying capacity is high in the y or y' direction and low in the z or z' direction under compression. Therefore, the strain in the y' direction is assumed to be zero in the shear band region for this idealized model. The nominal strains in region I inside the shear band with respect to the local material coordinate system are

$$\varepsilon_{Y'} = 0 \tag{17}$$

$$\varepsilon_{Z'} = \frac{\left(\frac{w - d\cos\alpha}{\cos\theta}\right)\sin(\alpha+\theta) - w}{w} \tag{18}$$

$$\gamma_{Y'Z'} = \frac{\pi}{2} - \alpha - \theta + \tan^{-1}\left(\frac{(w - d\cos\alpha)\tan\theta}{w}\right) \tag{19}$$

Here, the engineering shear strain $\gamma_{YZ'}$ is defined according to the definition of the engineering shear strain of the small strain theory. The nominal strains in region II outside the shear band with respect to the local coordinate system can be expressed as

$$\varepsilon_{Y'} = \frac{(w - d\cos\alpha)\tan\theta - w\tan\theta_i}{w\tan\theta_i} \tag{20}$$

$$\varepsilon_{Z'} = \frac{(w - d\cos\alpha) - w}{w} = \frac{-d\cos\alpha}{w} \tag{21}$$

The total nominal strain ε_Y^T for one unit cell of the specimen can be written as

$$\varepsilon_Y^T = \frac{\Delta h_s}{h_s} = \frac{\left[(w - d\cos\alpha)\tan\theta + d\sin\alpha\right] - (w\tan\theta_i + d)}{w\tan\theta_i + d} \tag{22}$$

where h_s is the shear band height. The nominal strains inside and outside the shear band can be estimated for a given set of w, d, θ_i, and θ.

When the compressive strain in the Y' direction in region II increases uniformly, the shear band angle remain unchanged. Since the change of the shear band angle θ was found to be small as α decreases, the shear band angle is assumed to be constant. With this assumption, the equations for the nominal strains in both regions can be simplified. For region I inside the shear band region, Equation (18) can be simplified to

$$\varepsilon_{Z'} = \frac{\left(\frac{w - d\cos\alpha}{\cos\theta_i}\right)\sin(\alpha + \theta_i) - w}{w} \tag{23}$$

In region II outside of the shear band region, Equation (20) can be simplified to

$$\varepsilon_{Y'} = \frac{-d\cos\alpha}{w} \tag{24}$$

Equations (21) and (24) indicate that region II is now subjected to equal biaxial compression. The total nominal strain for one unit cell of the specimen in Equation (22) can be simplified to

$$\varepsilon_Y^T = \frac{-d\cos\alpha\tan\theta_i + d\sin\alpha - d}{w\tan\theta_i + d} \tag{25}$$

The nominal strains inside and outside the shear band region can be estimated for $\alpha = 0$ when the shear band reaches its shear and rotational limit. The total nominal strain in Equation (25) becomes

$$\varepsilon_Y^T = \frac{-d\tan\theta_i - d}{w\tan\theta_i + d} = \frac{-\frac{d}{w}(\tan\theta_i + 1)}{\tan\theta_i + \frac{d}{w}} \tag{26}$$

As indicated in Equation (26), the shear band compaction mechanism is quite efficient to produce compaction with the extra contribution due to the kink length d. After α reaches the limit of 0, the shear band angle θ decreases as the compression increases in both regions I and II.

Another idealization can also be made with the assumption that the cell components are rigid in the y or Y' direction but plastic hinges or kinks can be formed whereas the components are compliant in the z or z' direction. In this case, the nominal strain in the y or Y' direction in region II becomes

$$\varepsilon_{Y'} = 0 \tag{27}$$

The additional term due to the compressive strain in the y or Y' direction in region II in Equation (26) disappears and the total strain of one unit cell of the specimen becomes

$$\varepsilon_Y^T = \frac{-d}{w\tan\theta_i + d} = \frac{-\frac{d}{w}}{\tan\theta_i + \frac{d}{w}} \tag{28}$$

As indicated in Equation (28), the total compressive strain of the specimen can be estimated easily from the normalized kinked length d/w. Finally, it should be mentioned that the deformation mechanism as discussed here is purely kinematic and it gives some physical insight on the deformation mechanism of the cell RVE specimens under in-plane constrained compression as observed in experiments and as obtained from the results of the finite element analysis [9].

It should be mentioned that the physical mechanism of the kink and shear band formation appears in different types of battery cells such as the lithium iron phosphate battery RVE specimens under in-plane constrained compression as investigated in this study and the lithium cobalt dioxide battery cells under in-plane constrained compression as reported in [5]. The physical mechanism also appears in cover sheet, anode, cathode and separator specimens as

shown in Figures A1 to A4. Note that the anode, cathode and separator are compressible porous sheets while the cover sheet is made of nearly incompressible polyamide, polypropylene and adhesives. It seems that the physical mechanism of the kink and shear band formation is a general deformation mechanism that can appear in unattached sheets under in-plane constrained compression.

2.6. Conclusions

In this study, the mechanical behavior of cell RVE specimens was investigated under both in-plane constrained and out-of-plane compressive loading conditions. The designs of the cell RVE specimens and the in-plane constrained compression test setup are for cells in the middle portion of a module with the lateral constraints in the out-of-plane direction. For this investigation, conclusions can be made in the following.

1. The deformation process is correlated to the nominal stress-strain curve by carefully examining the recorded deformation patterns and the stress-strain curves concurrently. The results indicate the load carrying behavior of cell RVE specimens is characterized by the buckling of cells with a wavelength approximately in the order of the thickness of the cells, kink and shear band formation, and the final densification of the cell components.
2. The nominal compressive stress-strain curves of cell RVE specimens under in-plane constrained and out-of-plane compression are different. The different nominal compressive stress-strain curves in the in-plane and out-of-plane directions suggest that the cells can be modeled as anisotropic foams or cellular materials. The in-plane and out-of-plane nominal compressive stress-strain curves presented in this study can be used to develop macro homogenized anisotropic material models for crashworthiness analyses.

3. The initial elastic buckling mode of the cell RVE specimen under in-plane constrained compression can be correlated to the elastic buckling solution of a beam with lateral constraints. The development of the higher order buckling modes of the component sheets and the critical stresses observed in experiments are in agreement with the results of the analytical buckling solutions and the corresponding finite element analyses. The elastic buckling analyses also justify the length selection of the cell RVE specimens.
4. An idealized kinematics model is developed to explain the kink and shear band formation in the cell RVE specimens under in-plane constrained compression. The nominal strains in the regions inside and outside of the shear band can be estimated by the idealized model and the results give some insight on the physical deformation process observed in experiments. The kinematics model appears to be valid in general for unattached sheets under in-plane constrained compression.

Appendix A: Effective compressive elastic moduli of cell components under in-plane (y direction) constrained compression

In-plane constrained compression tests were conducted for the component sheets to examine the deformation patterns and to estimate the effective compressive elastic moduli of the component sheets. These effective compressive elastic moduli are then used to estimate the effective compressive elastic modulus of the cell RVE specimens based on the composite ROM and compared to the value obtained from the test results of the cell RVE specimens under in-plane constrained compression tests. The specimens of cell components were made by stacking different numbers of sheets of cell components to a total thickness of 5 mm. The specimens have the in-plane dimensions of 25 mm × 25 mm. The numbers of sheets for the cover sheet, anode, cathode, and separator specimens are 45, 25, 25, and 250, respectively, to make the total specimen thickness of 5 mm. The test procedure is the same as stated in section 3.3.1.

Figure A1(a) shows the nominal stress-strain curves of cover sheet specimens. The effective compressive elastic modulus is estimated by taking a linear fitting curve for the beginning part of the curve. The fitting curve is indicated by a dashed line shown in the figure. The estimated effective compressive elastic modulus is about 575 MPa. Estimations of the effective compressive elastic moduli for all component specimens follow the same procedure. Figures A1(b) to A1(d) show the deformation patterns of a cover sheet specimen at different nominal strains. The deformation patterns are similar to those of the cell RVE specimens.

Figure A2(a) shows the nominal stress-strain curves of anode specimens. The estimated value of the effective compressive elastic modulus is about 90 MPa. Figures A2(b) to A2(d) show the deformation patterns of an anode specimen at different nominal strains. It is noted that the deformation patterns are similar to those of the cell RVE specimens.

Figure A3(a) shows the nominal stress-strain curve of a cathode specimen. The estimated effective compressive elastic modulus is about 275 MPa. Figures A3(b) to A3(d) show the deformation patterns of the cathode specimen at different nominal strains. The deformation patterns are similar to those of the cell RVE specimens in the beginning of the test. As the strain increases, the deformation pattern deviates from those of the cell RVE specimens.

Figure A4(a) shows the nominal stress-strain curves of separator specimens. The estimated effective compressive elastic modulus is about 83 MPa. Figures A4(b) to A4(d) show the deformation patterns of a separator specimen at different nominal strains. The deformation patterns show a much shorter wavelength compared to those of the cell RVE specimens. The effective compressive elastic moduli for the cell component specimens are listed in Table 2.2.

The composite ROM is used to estimate the effective compressive elastic modulus of the cell RVE specimen based on the effective compressive elastic moduli of the component sheet specimens. The effective compressive elastic modulus of the cell RVE specimen, E'_{cell}, can be estimated as

$$E'_{cell} = \sum f_i E'_i \tag{A1}$$

where f_i and E'_i are the volume fraction and the effective compressive elastic modulus of the i-th cell component. The estimated E'_{cell} is 190 MPa, which is close to the effective compressive elastic modulus of 188 MPa obtained from the test results of the cell RVE specimens under in-plane constrained compression tests. The effective compressive elastic moduli of the cell component specimens are then used for the input for the elastic buckling analysis of the cell components in this investigation, the simulations of the deformation process of the cell RVE specimens [9], and the elastic buckling analysis of the module RVE specimens [8].

Table 2.1. Specifications of cell and module components.

	Material	**Thickness**		**Notes**
Cover sheet	Polyamide (JIS Z1714)	0.025 mm	0.111 mm	
	Adhesive (Polyester-polyurethane)	4-5 g/m^2		
	Aluminum foil (JIS A8079, A8021)	0.040 mm		
	Adhesive (Urethane-free Adhesive)	2-3 g/m^2		
	Polypropylene	0.040 mm		
Anode	Copper foil	9 μm	0.2 mm	Double side coated
	Graphite			Graphite density: 140-160 g/m^2 Active material proportion in powder: 95.7% Binder: Styrene-butadiene rubber (SBR)+carboxymethyl cellulose (CMC)
Cathode	Aluminum foil	15 μm	0.2 mm	Double side coated
	$LiFePO_4$			$LiFePO_4$ density: 326-346 g/m^2 Active material proportion in powder: 91.0%
Separator	Polyethylene (PE)	16-25 μm		Porosity: 36%-44% Pore size: 0.01-0.1 μm
Aluminum heat dissipater sheet	Aluminum	0.4 mm	0.6 mm	Double side painted
	Paint	0.1 mm		
Foam between cells	Typical foam material	1.5 mm		

Table 2.2. Effective compressive elastic moduli of cell components.

	Effective compressive elastic modulus E_i' (MPa)
Cover sheet	575
Anode	83
Cathode	275
Separator	90

Table 2.3. Buckling modes, loads, and strains for the component sheets in the middle portion of the cell RVE specimen with $k = 9.2 \times 10^7$ N/m^2 and buckling loads and stresses for the cell RVE specimen.

	Cover sheet	Anode	Cathode	Separator
$\overline{m}$	21.3 (NA)	22.2	16.3	124.6
P_m^i (N)	25.3 (NA)	23.3	42.7	0.744
ε_m^i	0.0159 (NA)	0.0562	0.0310	0.0165
Cell buckling load P_{cell} (N) at the component buckling strain ε_m^i	350 (NA)	1240	684	364
Cell buckling stress σ_{cell} (MPa) at the component buckling strain ε_m^i	2.80 (NA)	9.90	5.47	2.91

Table 2.4. Buckling modes, loads, and strains for the component sheets near the sides of the cell RVE specimen with $k = 4.6\times10^{7}\,\mathrm{N/m^2}$ and buckling loads and stresses for the cell RVE specimen.

	Cover sheet	Anode	Cathode	Separator
$2\bar{n}$ (for comparison with those in Table 2.3)	23.1	24.1	17.6	137.4
P_n^i (N)	30.1	27.7	50.5	0.908
ε_n^i	0.0189	0.0666	0.0367	0.0202
Cell buckling load P_{cell} (N) at the component buckling strain ε_n^i	416	1470	809	445
Cell buckling stress σ_{cell} (MPa) at the component buckling strain ε_n^i	3.33	11.7	6.47	3.56

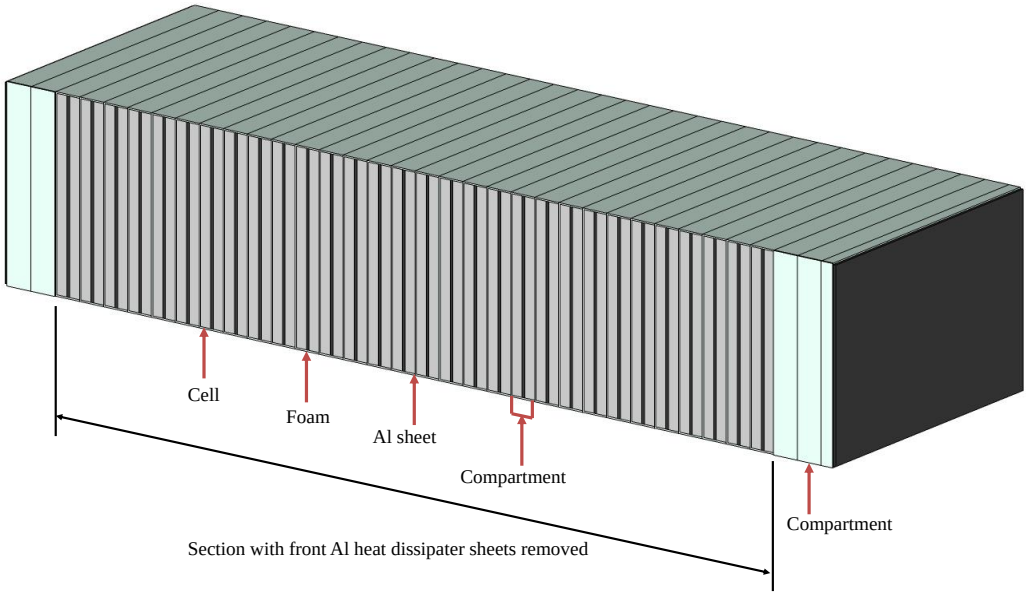

Figure 2.1. A typical battery module.

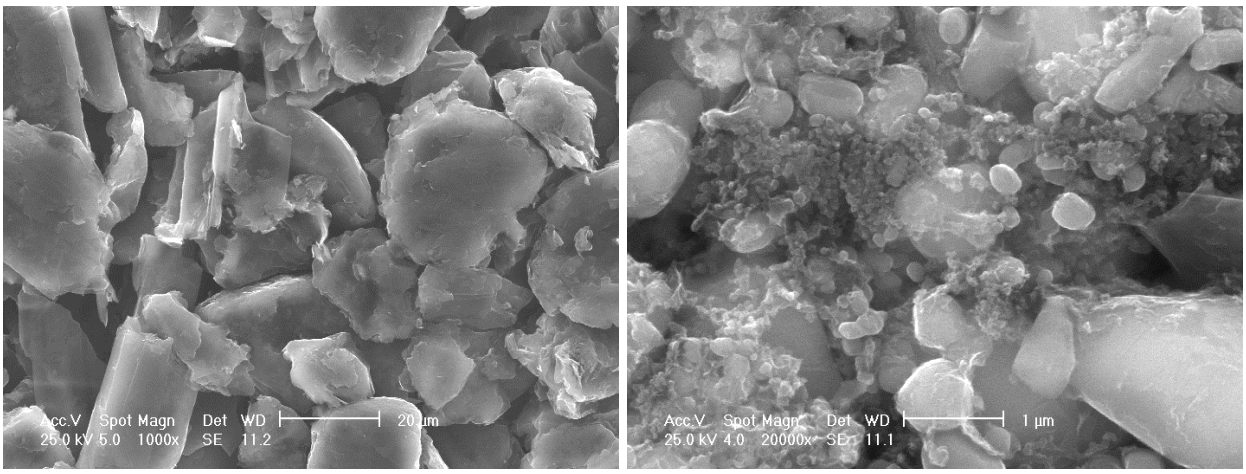

(a) (b)

Figure 2.2. SEM images of (a) graphite and (b) LiFePO4 on the anode and cathode sheets, respectively.

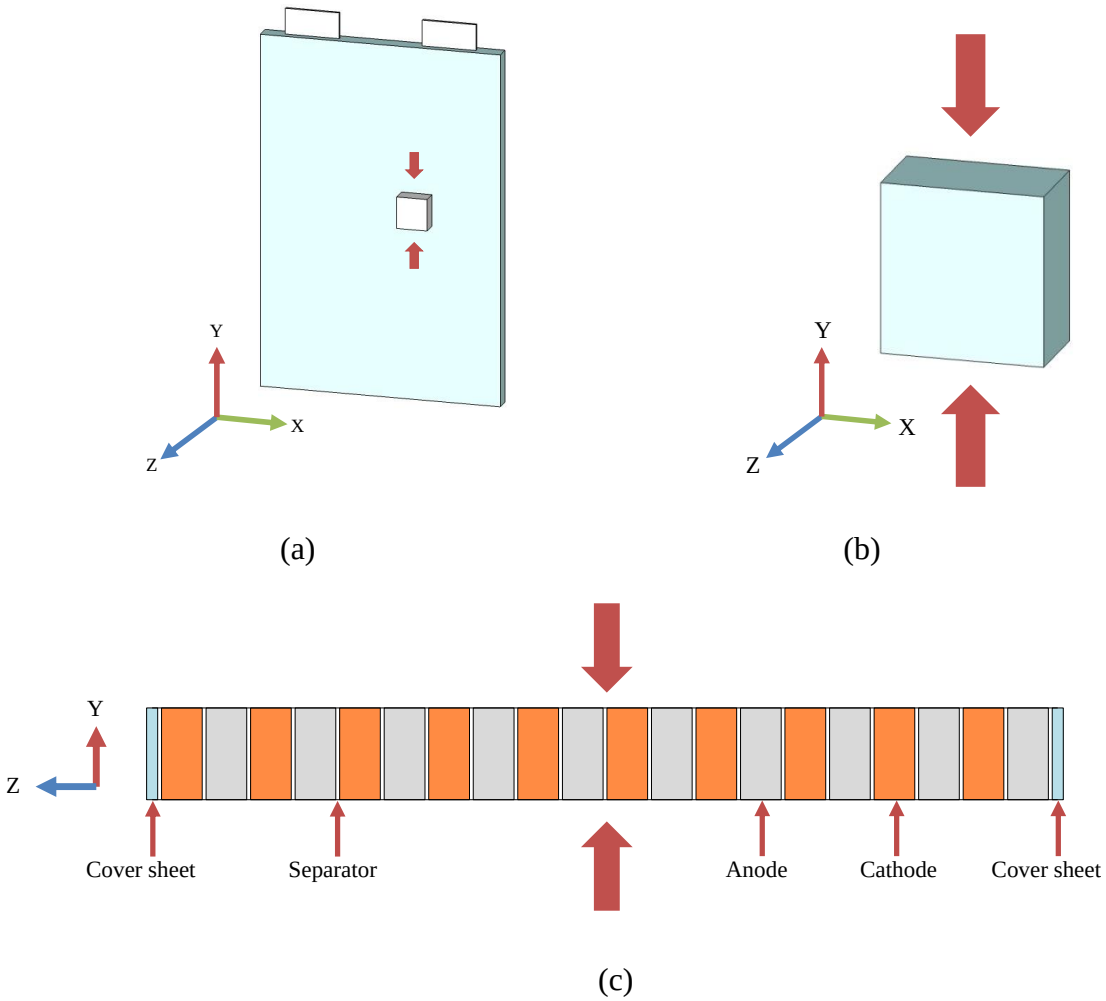

Figure 2.3. A schematic of (a) a pouch cell and a cell RVE specimen for the in-plane constrained compression test, (b) a cell RVE specimen with the dimensions, and (c) a side view of a small portion of the cell RVE specimen showing the individual cell components. The large arrows indicate the compressive direction.

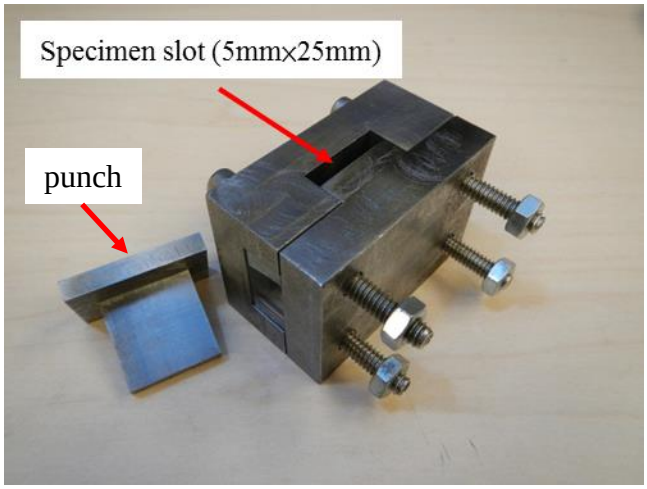

Figure 2.4. A punch and die setup for in-plane compression tests of cell RVE specimens.

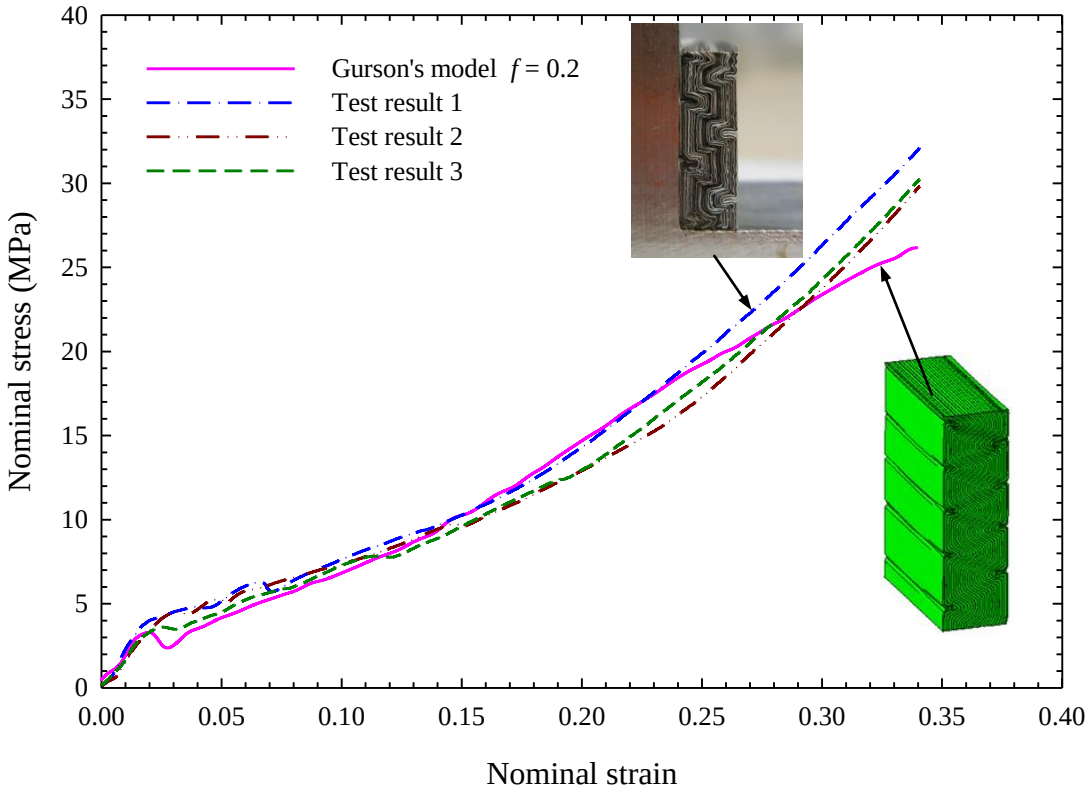

Figure 2.5. The in-plane nominal compressive stress-strain curves of three cell RVE specimens tested at a displacement rate of 0.5 mm/min (nominal strain rate of 0.0003 s^{-1}). The in-plane nominal compressive stress-strain curve of the cell RVE specimen from the finite element analysis using the Gurson's material model with a void volume fraction f set to 0.2 for the electrode and separator sheets is also shown for comparison. The images on the top and lower right show a real tested specimen and a simulated tested specimen using finite element analyses.

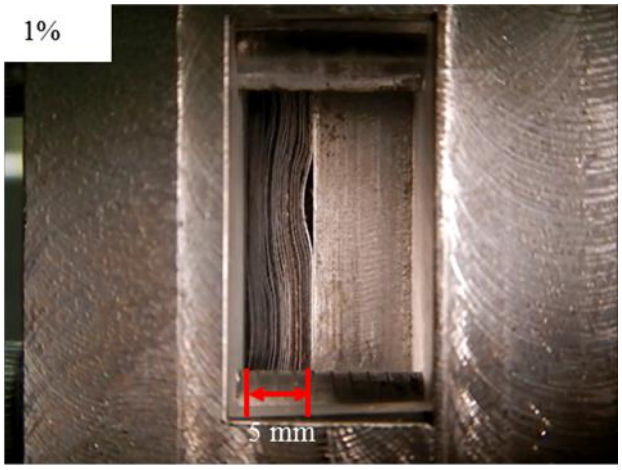
1%
5 mm

(a)

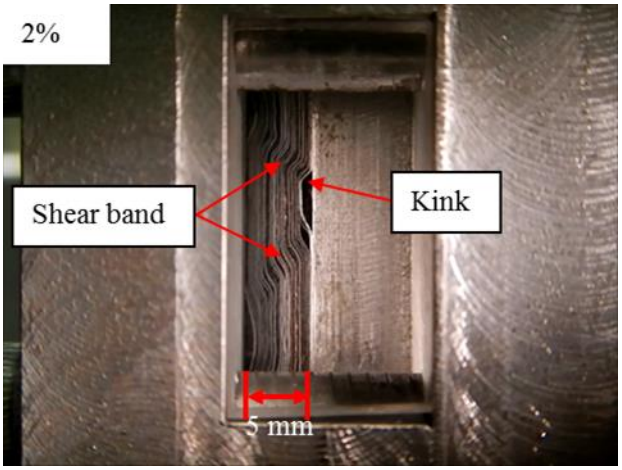
2%
Shear band
Kink
5 mm

(b)

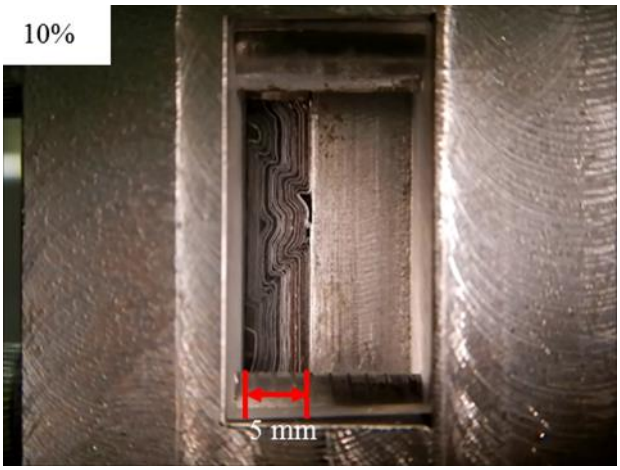
10%
5 mm

(c)

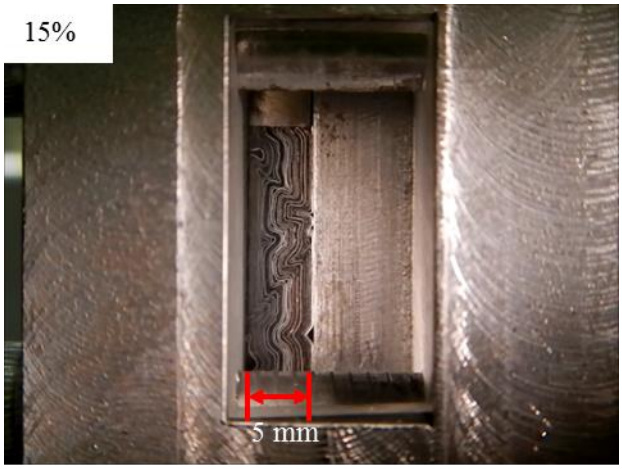
15%
5 mm

(d)

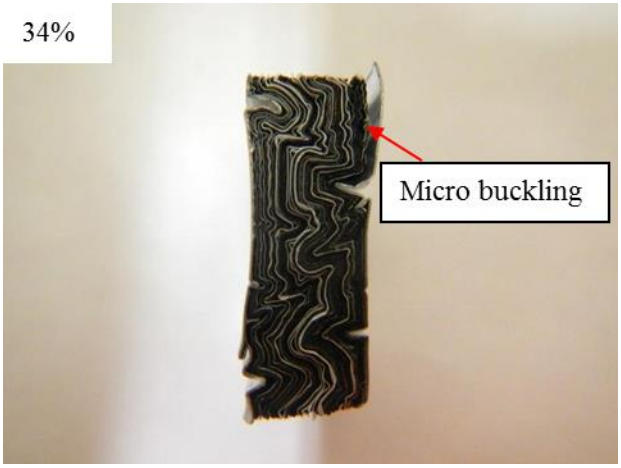
34%
Micro buckling

(e)

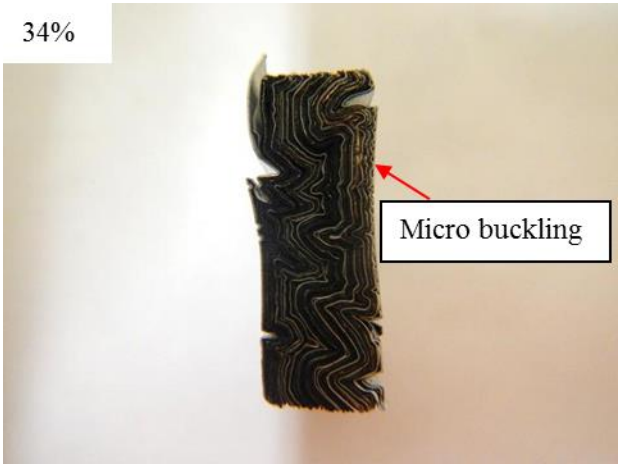
34%
Micro buckling

(f)

Figure 2.6. Deformation patterns of a cell RVE specimen during the in-plane constrained compression test at the displacement rate of 0.5 mm/min: (a) at the nominal strain of 1% in the initial linear stage, (b) at the nominal strain of 2% where the slope change occurs, (c) at the nominal strain of 10%, (d) at the nominal strain of 15%, (e) at the nominal strain of 34% after the test (front view), and (f) at the nominal strain of 34% after the test (back view).

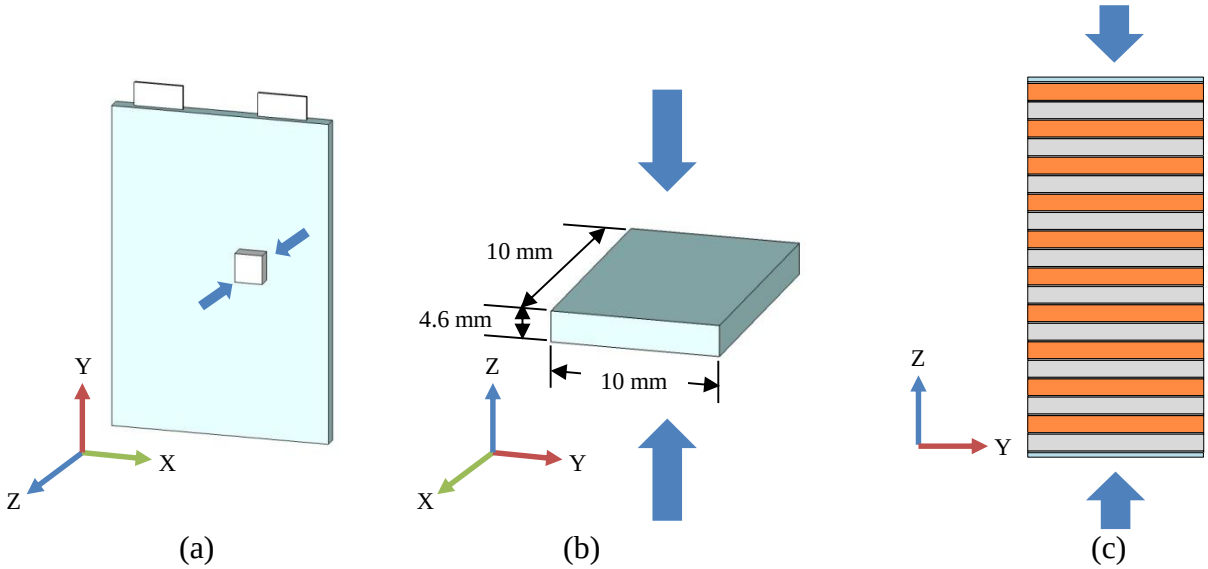

Figure 2.7. A schematic of (a) a pouch cell and a cell RVE specimen for the out-of-plane compression test, (b) a cell RVE specimen with the dimensions, and (c) a side view of a small portion of the cell RVE specimen showing the individual cell components. The large arrows indicate the compressive direction.

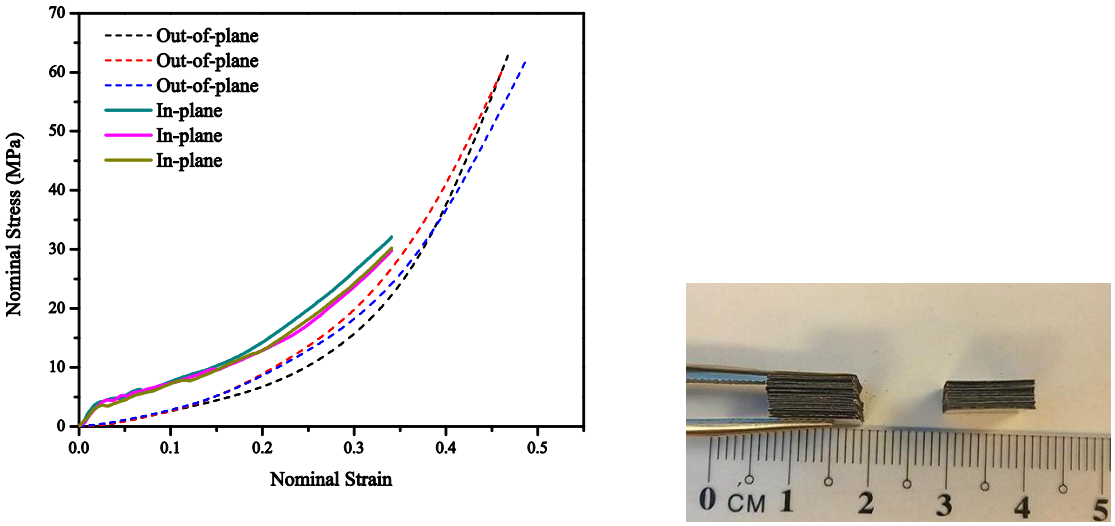

(a) (b)

Figure 2.8. (a) The out-of-plane nominal compressive stress-strain curves of cell RVE specimens tested at a displacement rate of 0.25 mm/min (nominal strain rate of 0.0009 s^{-1}) and (b) pictures of two specimens before (left) and after (right) compression. The three in-plane nominal compressive stress-strain curves as shown in Figure 2.5 are also shown in (a) for comparison.

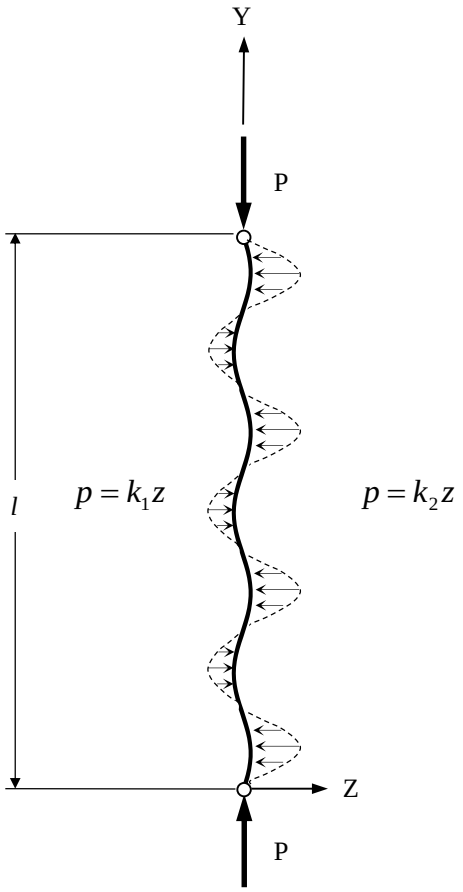

Figure 2.9. A schematic of a uniform straight beam under end loads and supported by unattached elastic foundations. Both ends are hinged and the beam is supported by the elastic foundations through the lateral pressure p proportional to the deflection z in the z direction. The elastic foundations on two sides of the beam have the spring constants k_1 and k_2.

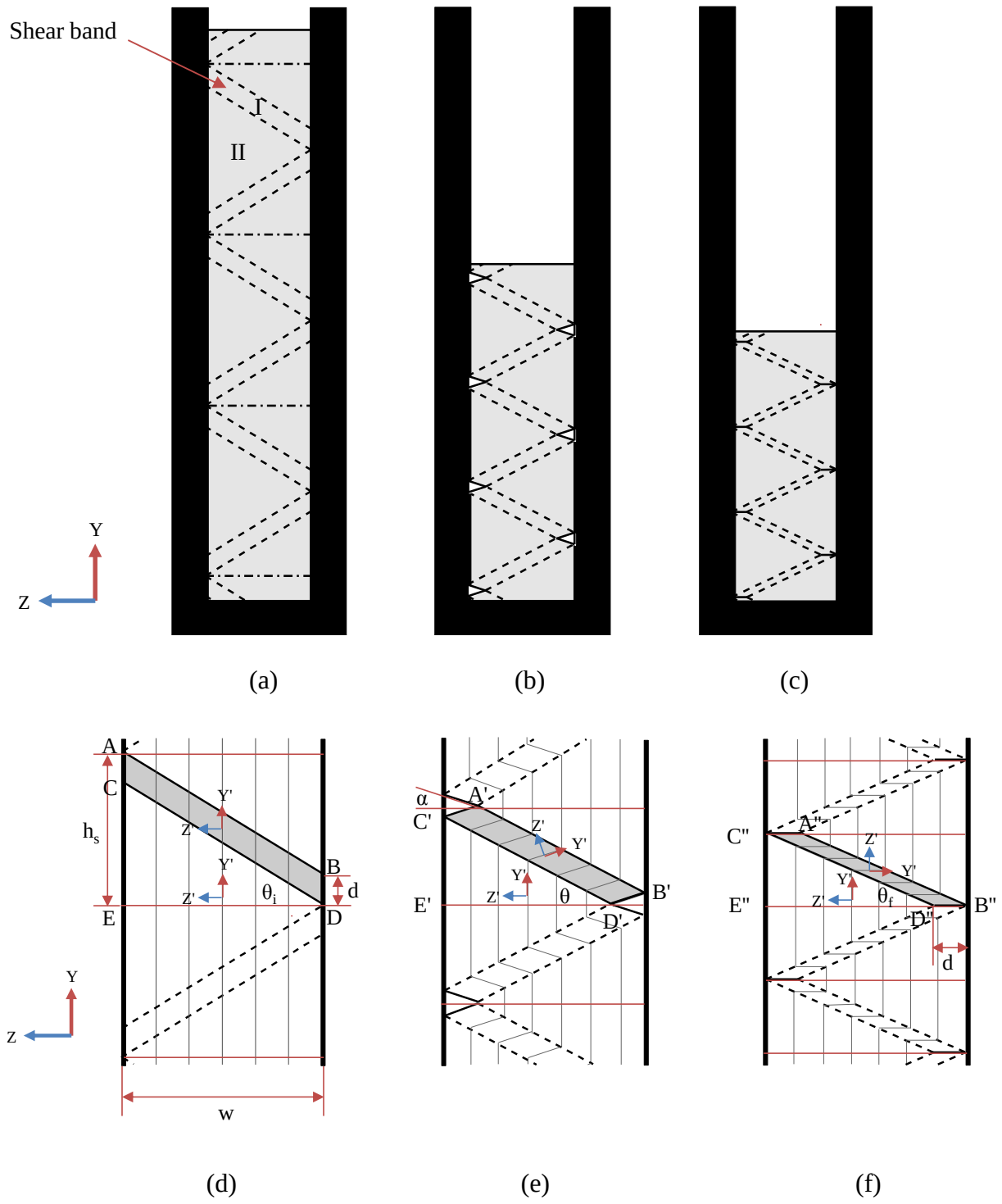

Figure 2.10. Schematics of a cell RVE specimen (a) before, (b) during, and (c) after the shear band formation. (d) to (f) are detailed schematics corresponding to (a) to (c), respectively. The y and z coordinates are the global coordinates and the Y' and z' coordinates are the local material coordinates in (d) to (f).

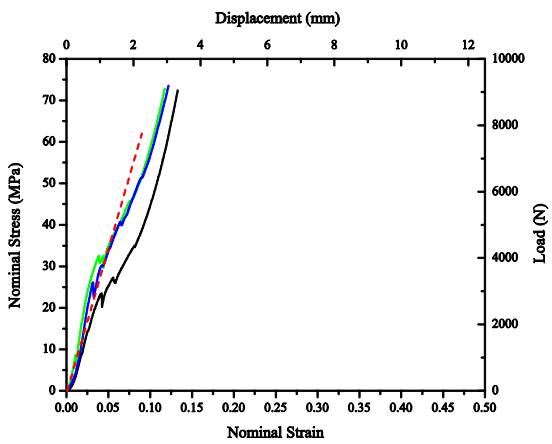

(a)

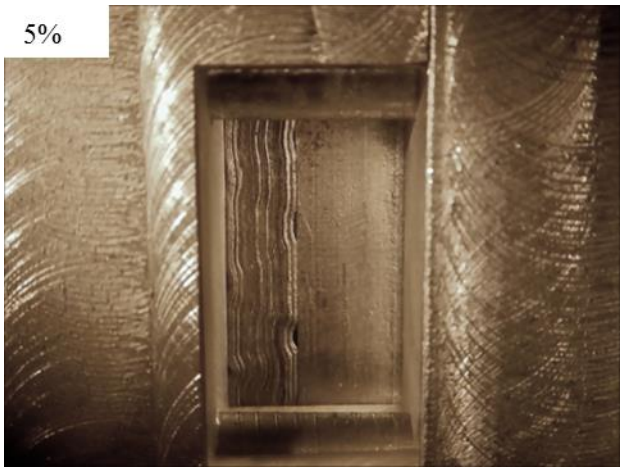

(b)

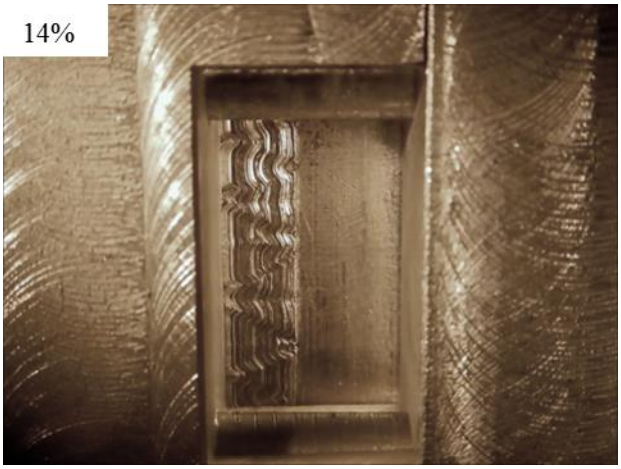

(c)

(d)

Figure A1.1. (a) The in-plane nominal compressive stress-strain curves of cover sheet specimens tested at a displacement rate of 0.5 mm/min (nominal strain rate of 0.0003 s^{-1}). (b-d) show the deformation patterns of a cover sheet specimen at the nominal strains of 5%, 14% and 14% (after test), respectively.

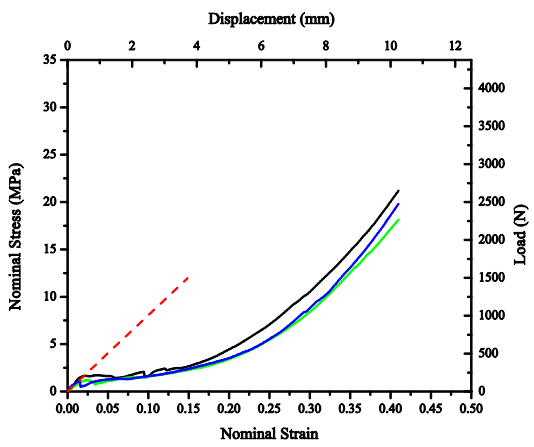

(a)

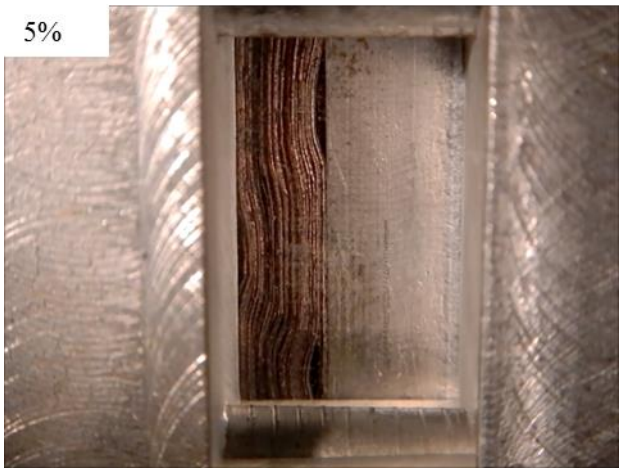

(b)

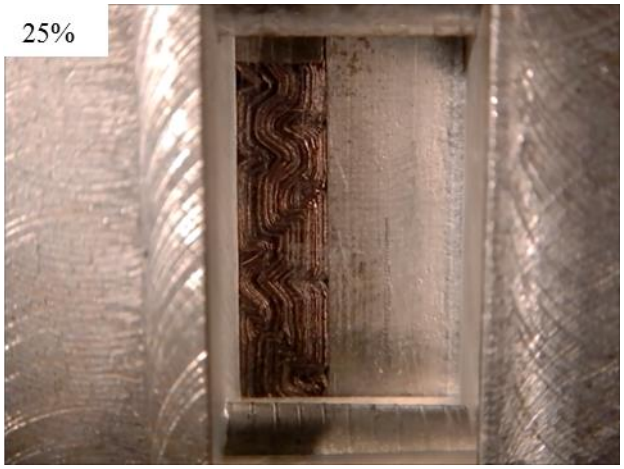

(c)

(d)

Figure A1.2. (a) The in-plane nominal compressive stress-strain curves of anode specimens tested at a displacement rate of 0.5 mm/min (nominal strain rate of 0.0003 s^{-1}). (b-d) show the deformation patterns of an anode specimen at the nominal strains of 5%, 25%, and 40% (after test), respectively.

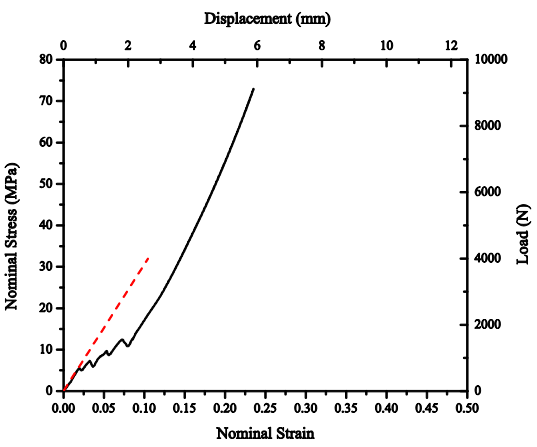

(a)

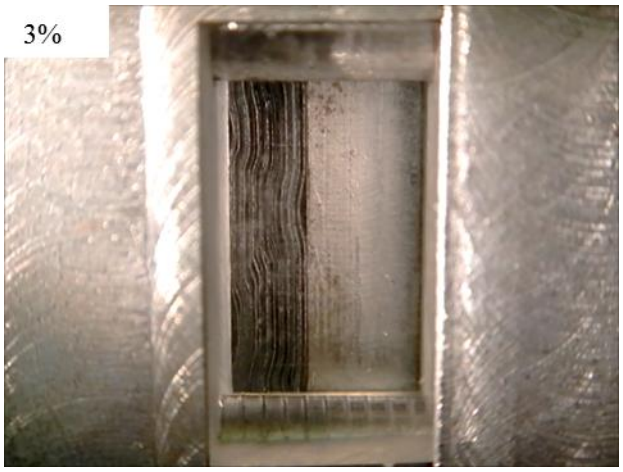

(b)

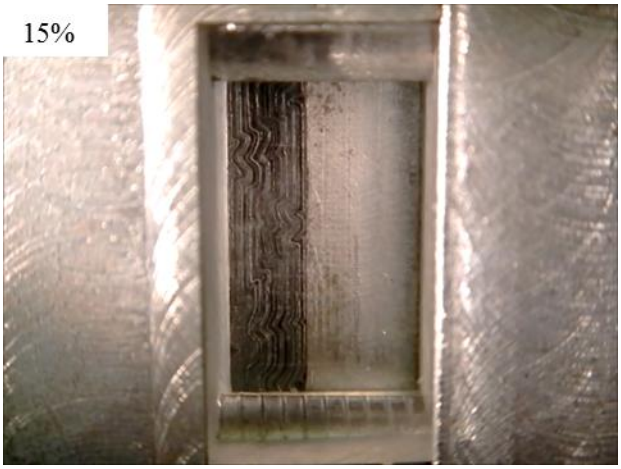

(c)

(d)

Figure A1.3. (a) The in-plane nominal compressive stress-strain curve of a cathode specimen tested at a displacement rate of 0.5 mm/min (nominal strain rate of 0.0003 s^{-1}). (b-d) show the deformation patterns of the cathode specimen at the nominal strains of 3%, 15%, and 24% (after test), respectively.

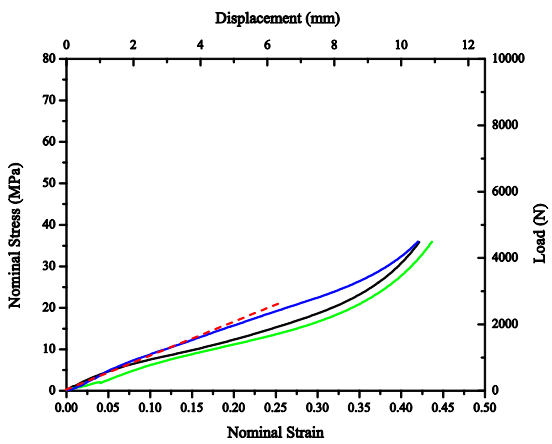

(a)

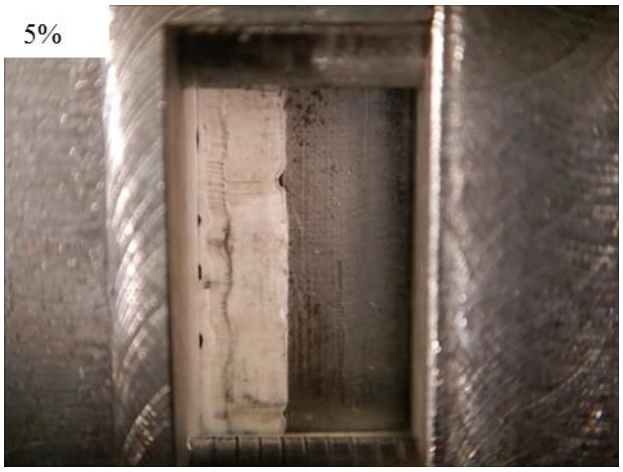

(b)

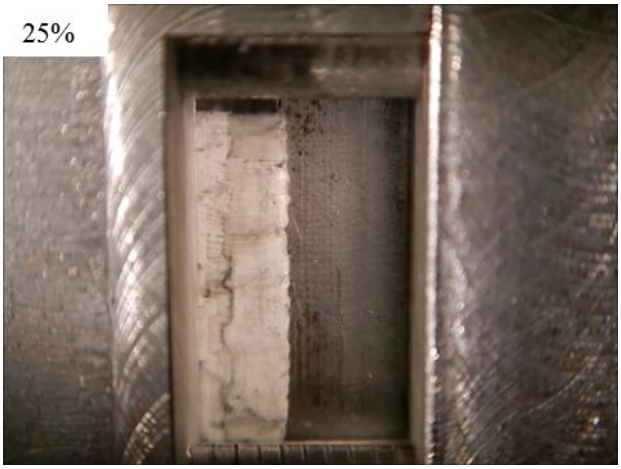

(c)

(d)

Figure A1.4. (a) The in-plane nominal compressive stress-strain curves of separator specimens tested at a displacement rate of 0.5 mm/min (nominal strain rate of 0.0003 s^{-1}). (b-d) show the deformation patterns of a separator specimen at the nominal strains of 5%, 25% and 42% (after test), respectively.

Acknowledgement

The support of this work by the Crash Safety Working Group (CSWG) of the United States Council on Automotive Research (USCAR) and Ford Motor Company is appreciated. Helpful discussions with Yibing Shi, Guy Nusholtz, and Ronald Elder of Chrysler, Saeed Barbat, Bill Stanko, and Mark Mehall of Ford, Jenne-Tai Wang, Ravi Nayak, Kris Yalamanchili and Stephen Harris of GM, Christopher Orendorff of Sandia National Laboratory, Seung-Hoon Hong of University of Michigan, and Natalie Olds of USCAR are greatly appreciated.

References

[1] SAE J2464 NOV2009, Electric and Hybrid Electric Vehicle Rechargeable Energy Storage System (RESS) Safety and Abuse Testing, Society of Automotive Engineers, Warrendale, PA, 2009.

[2] J. Nguyen, C. Taylor, Safety Performance for Phosphate Based Large Format Lithium-Ion Battery, Telecommunications Energy Conference, INTELEC 2004. 26th Annual International (2004) 146-148.

[3] M. Otsuki, T. Ogino, K. Amine, Investigation of Flame-Retardant Additives for Safety Usage of Lithium-Ion Batteries, ECS Transactions 1 (2006) 13-19.

[4] W. Cai, H. Wang, H. Maleki, J. Howard, E. Lara-Curzio, Experimental Simulation of Internal Short Circuit in Li-Ion and Li-Ion-Polymer Cells, Journal of Power Sources 196 (2011) 7779-7783.

[5] E. Sahraei, R. Hill, T. Wierzbicki, Calibration and Finite Element Simulation of Pouch Lithium-Ion Batteries for Mechanical Integrity, Journal of Power Sources 201 (2012) 307-321.

[6] R. Hill, Development for a Representative Volume Element of Lithium-Ion Batteries for Thermo-Mechanical Integrity, Department of Mechanical Engineering, Massachusetts Institute of Technology, 2011.

[7] E. Sahraei, T. Wierzbicki, R. Hill, M. Luo, Crash Safety of Lithium-Ion Batteries Towards Development of a Computational Model, SAE Technical Paper 2010-01-1078, Society of Automotive Engineers, Warrendale, PA, 2010.

[8] W. Lai, M.Y. Ali, J. Pan, Mechanical Behavior of Representative Volume Elements of Lithium-Ion Battery Modules under Various Loading Conditions, companion paper to be submitted publication (2013).

[9] M.Y. Ali, W. Lai, J. Pan, Computational Models for Simulations of Lithium-Ion Battery Cells under Constrained Compression Tests, Journal of Power Sources 242 (2013) 325-340.

[10] M. Y. Ali, W. Lai, J. Pan, Computational Models for Simulation of a Lithium-Ion Battery Module Specimen under Punch Indentation, companion paper to be submitted publication (2013).

[11] W.C. Young, R.G. Budaynas, Roark's Formulas for Stress and Strain, 7th ed., McGraw-Hill, 2001.

[12] S. Timoshenko, Theory of Elastic Stability, McGraw-Hill, 1936.

Chapter 3
Mechanical Behavior of Representative Volume Elements of Lithium-Ion Battery Modules under Various Loading Conditions

3.1. Introduction

In the previous chapter, the mechanical behavior of Li-ion battery cells is investigated by conducting various constrained compression tests. In this chapter, the mechanical behavior of Li-ion battery modules is investigated. First, tensile specimens were made from the individual components of modules: anode, cathode, separator, cover sheet, and aluminum heat dissipater sheet. Tensile tests were performed to obtain the nominal stress-strain curves for these individual components for development of the nominal tensile stress-strain curves of cells and modules based on the composite rule of mixture. Next, module RVE specimens were tested under in-plane constrained compression. In-plane constrained compression tests of the module RVE specimens with different heights and with adhesive were also conducted to understand the effects of the specimen height and adhesive. Compression tests of foam layers were also conducted to examine the different mechanical behaviors of the module RVE specimens in the in-plane and out-of-plane directions. The buckling stress of the module RVE specimens was then investigated. The buckling stresses for the cell components and the aluminum heat dissipater sheet based on the analytical buckling solution for a thin plate with unattached elastic foundations were obtained and compared with the experimental results of the module RVE specimens under in-plane constrained compression. Finally, a constrained punch indentation test on a small-scale module specimen with the same layered structure as that of the module RVE

specimens was conducted to understand the mechanical behavior of battery modules under non-uniform in-plane deformation and to provide the necessary experimental data for benchmark and validation of the macro homogenized material model development based on the results of in-plane constrained compression tests and out-of-plane compression tests. Finally, conclusions will be made from the experimental results.

3.2. Specimens

The ultimate goal of this investigation is to model the mechanical behavior of battery modules. Hence the mechanical behaviors of the individual components of the battery modules should be first examined. The structure of a typical battery module based on prismatic pouch cells is shown in Figure 2.1.

Each cell consists of five major components: cover sheet, anode, cathode, separator and electrolyte. Since the electrolyte is difficult to handle during assembly due to its toxicity, all the module RVE specimens tested in this study were made without electrolyte. Table 2.1 lists all the detailed material and thickness information of the module components. The anode, cathode, separate and cover sheets are the same as those in Chapter 2. The aluminum heat dissipater sheet and the foam sheet were acquired from a battery module. The aluminum heat dissipater is painted on both sides with a total thickness of 0.6 mm. The thickness of the foam sheet is 1.5 mm. They were later machined into different specimens according to the test need.

3.3. Quasi-static tensile tests of module components

3.3.1. Test procedure and results

Tensile tests were conducted. An extensometer was used for all specimens with a gauge length of 2 inches. The ASTM E8/E8M-11 tensile specimen standard for thin sheet materials was adopted. Figure 3.1(a) shows a schematic of a tensile specimen with the dimensions. Figure 3.1(b) shows the tensile specimens of the cover sheet, cathode, anode, separator, and aluminum heat dissipater sheets from the top to bottom, respectively. The displacement rate was set at 5.08 mm/min (nominal strain rate of 0.0017 s^{-1}) for all tensile specimens except for that of the aluminum heat dissipater sheet (tested at a lower displacement rate of 2.54 mm/min or a nominal strain rate of 0.00085 s^{-1}) to better observe the deformation patterns near the yield stress.

Five nominal stress-strain curves of the cover sheets (with aluminum foils) are shown in Figure 3.2(a). The nominal stress-strain curves of the cover sheets do not show a distinct linear portion since the cover sheet is a composite made of layers of polymers and an aluminum foil. The nominal stress is about 60 to 65 MPa at failure at this nominal strain rate of 0.0017 s^{-1}. The total elongation is about 52 to 57%. The typical canoeing effect for thin composite tensile specimens was observed during the test. Figure 3.2(a) also shows a picture of the failed region of a specimen where the canoeing effect of the specimen can be seen. The failure appears to be initiated by the failure of the middle aluminum foil with the polymer layers remained connected. The fracture region showed little signs of necking in the width direction. The fracture surface of the composite sheet is perpendicular to the tensile (vertical) loading direction.

Four nominal stress-strain curves of the anode sheets (with copper foils) are shown in Figure 3.2(b). The tensile stress is about 11 MPa at failure. The total elongation is quite small at about 1.7 to 3.1% for the four specimens. The curves show slight load drops after reaching the

maximum tensile stresses. Figure 3.2(b) also shows a picture of the failed region of a specimen. The fracture surface of the composite specimen is perpendicular to the tensile (vertical) loading direction. As shown in the picture, no necking in the width direction was observed. A simple calculation was conducted to estimate the contribution of the graphite layers to the load carrying capacity and it indicates that the elastic modulus is about 105 GPa by dividing the load by the cross sectional area of the copper foil (12.7 mm × 0.009 mm) and the corresponding strain. This elastic modulus of 105 GPa is about the same as that of copper sheets. This indicates that the graphite layers barely have any load carrying capacity when compared to that of the copper foil. The elastic modulus of the anode sheets as composites is 4.7 GPa.

Four nominal stress-strain curves of the cathode sheets (with aluminum foils) are shown in Figure 3.2(c). The nominal stress is about 12 MPa at failure. The total elongation is quite small at about 0.9 to 1.5% for the four specimens. Figure 3.2(c) also shows a picture of the failed region of a specimen. The fracture surface of the composite specimen is perpendicular to the tensile (vertical) loading direction. As shown in the picture, no necking in the width direction was observed. A simple calculation was conducted to estimate the contribution of the $LiFePO_4$ layers to the load carrying capacity. It indicates that the elastic modulus is about 68 GPa by dividing the load by the cross sectional area of the aluminum foil (12.7 mm × 0.015 mm) and the corresponding strain. This elastic modulus of 68 GPa is close to the usual elastic modulus of 70 GPa of aluminum sheets. This indicates that the $LiFePO_4$ layers barely have any load carrying capacity when compared to that of the aluminum foil. The elastic modulus of the cathode sheets as composites is 5.1 GPa.

Five nominal stress-strain curves of the separator sheets are shown in Figure 3.2(d). The tensile yield stress is about 11 MPa at this displacement rate of 5.08 mm/min (nominal strain rate

of 0.0017 s^{-1}). The total elongation varies from 50 to 80% for the five specimens. The curves show approximate linear strain hardening after the apparent elastic response. Figure 3.2(d) also shows a picture of the failed region of a specimen. Necking in the width direction was observed before fracture. The fracture surface of the separator specimen is perpendicular to the tensile (vertical) loading direction. The elastic modulus for the initial part of the stress-strain curve is estimated as 0.5 GPa.

Three nominal stress-strain curves of the aluminum heat dissipater sheets are shown in Figure 3.3. The modulus was estimated to be about 53 GPa from the initial linear portion of the curves. Since the modulus of aluminum sheets is about 70 GPa, we can estimate the paint thickness with the assumption that the load is carried only by the aluminum portion of the sheet. The estimated paint thickness is 0.75 mm, which is close to the direct measurement of 0.1 mm. It is noted that the material shows low strain hardening after yielding. The total elongation ranges from 1.6 to 2.3% for the three specimens. Figure 3.3 also shows a picture of the failed region of a specimen. The failure surface of the specimen is inclined to the tensile (vertical) direction and this failure mode is typical for tensile specimens of ductile sheet metals under uniaxial loading conditions. Table 3.1 lists the elastic moduli of all module components and the estimated elastic moduli for the metal portions of the anode, cathode and aluminum heat dissipater sheets for comparison.

3.3.2. Tensile behavior estimation based on composite rule of mixture (ROM)

Conducting tensile tests for individual module components are easier to handle. Conducting tensile tests for multi-layered cell specimens can also be done. However, a battery cell and module may contain different numbers of unit of cathode, anode and separator sheets.

Therefore, a simple way to estimate the tensile behavior of cells and modules based on the composite rule of mixture (ROM) should be useful to understand the tensile behavior of cells and modules. A simple composite ROM estimation scheme may also be useful in the future for the development of a user material subroutine for a homogenized material model to represent the battery cells and modules.

The composite ROM is a method to estimate the properties of composite materials. According to the composite ROM, properties of composite materials such as the density, coefficient of thermal expansion, modulus of elasticity, shear modulus, and Poisson's ratio can be estimated as the volume weighed averages of those of individual phases (matrix and fibers). For a given strain, the composite stress $\sigma_{composite}$ can be estimated from the stress σ_i of the i-th component with the volume fraction V_i as

$$\sigma_{composite} = \sum_{i=1}^{n} \sigma_i V_i \tag{1}$$

First, a battery cell with a single unit of anode, cathode and separator, and two cover sheets with two additional separator sheets is considered. Another battery cell with ten units of anode, cathode and separator, and two cover sheets with additional separator sheets is also considered. Figure 3.4 shows a side view of a portion of the cell RVE with a single unit of anode, cathode and separator, and two cover sheets with additional two separator sheets. Figure 2.3(c) shows a side view of a portion of a cell RVE with 10 units of anode, cathode and separator, and two cover sheets with additional separator sheets. The assemblies of the cell components in the generic cell RVE specimens as schematically shown in Figures 3.4(c) and 3.4(d) may be slightly different from those of the usual lithium-ion cells for the convenience of using the tensile stress-

strain curves of the available anode, cathode and separator sheets to demonstrate the usefulness of the composite ROM.

Figure 3.5 shows a comparison of the engineering stress-strain curves obtained from the composite ROM for the two battery cells with a single unit and ten units of anode, cathode and separator, and two cover sheets with two additional separator sheets. The cathode failed at about the strain of 1% and the anode failed at about the strain of 2.4%. After the failures of the anode and cathode, the loads are carried by the cover sheets and separator sheets. At about the strain of 53%, the cover sheets failed. As shown in the figure, the tensile stress-strain curve is lower for the ten unit specimen.

Next, we consider a module of two battery cells (each cell consists of 7 units of anode, cathode and separator, and two cover sheets with additional separator sheets), and one aluminum heat dissipater sheet. Figure 3.6(a) shows a schematic of a module and a module RVE for the in-plane test with the x-y-z coordinate system. Figure 3.6(b) shows a module RVE. Figure 3.6(c) shows a side view of the module RVE with two cells and one aluminum heat dissipater sheet. Each cell has 7 units of anode, cathode and separator, and two cover sheets with two additional separator sheets. Note that the foam was not considered for the module RVE since the tensile load carrying capacity of a typical foam is very low. Figure 3.7 shows the nominal stress-strain curve obtained from the composite ROM for the module RVE. Note that the aluminum heat dissipater sheet failed at about the strain of 2.3% that is about the same at which the anode sheets fail. As shown in Figure 3.7, the peak stress of the tensile stress-strain curve for the module depends on those of the components of the module RVE.

3.4. Quasi-static compression of module RVE specimens

3.4.1. In-plane (y direction) constrained compression tests of module RVE specimens

Module RVE specimens were made to represent the middle portion of a typical battery module shown in Figure 2.1. The module RVE specimens were designed to be small for test convenience. Figure 3.8(a) shows a schematic of a battery module and a module RVE specimen with the x-y-z coordinate system. A small module RVE specimen is shown in Figure 3.8(b) with the dimensions. Figure 3.8(c) shows a side view of the module RVE specimen with the individual components. The large arrows shown in the figure indicate the in-plane compressive direction. The module RVE specimen is composed of two cells with an aluminum heat dissipater sheet between the two cells. Two foam layers are on the two sides of the module RVE specimen, as shown in Figure 3.8(c). It should be noted that the dimension of the module RVE specimen in the out-of-plane (Z) direction is 10.2 mm. This was designed to account for the pre-compression condition where a pre-compressive load is applied to the battery module by two stainless steel bands. This dimension was chosen to give the pre-compression in the out-of-plane (Z) direction in a typical battery module. The specimen was then pre-compressed to a 10 mm cube such that the foam layer thickness was compressed to the thickness as observed in a real module before testing in the die for in-plane constrained compression testing. The thickness in the z direction of the cell RVE specimen in this case was designed to reduce to 3.3 mm, which is composed of 7 anode, 7 cathode, 15 separator and 2 cover sheets. It should be noted again that the assembly of the cell components in the generic cell RVE specimen as schematically shown in Figure 3.8(c) may be slightly different from those of the usual lithium-ion cells for convenience of using the available anode, cathode and separator sheets.

A set of module RVE specimens with its height doubled in the y direction was also made and tested to study the size effect. Another set of module RVE specimens with adhesive was also made and tested to study the effect of the adhesive. In a typical battery module, the adhesive is applied between the cell cover sheet and the foam, and between the cell cover sheet and the aluminum heat dissipater sheet. Instant Krazy® glue was applied in the positions indicated by the small arrows in Figure 3.8(c) for the specimens with different heights (10 mm and 20 mm). The glue was applied as uniform and as thin as possible to maintain consistency and reduce imperfections.

The setup for module RVE compression tests is shown in Figure 3.9. The setup is composed of a male square punch and a female die. A square punch is in the die cavity is shown in the figure. A side window was made of PMMA for recording the deformation process during the compression. The module RVE specimen is placed in the die cavity and the punch compresses downward with a displacement rate is 0.3 mm/min (nominal strain rate of 0.0005 s^{-1}).

Figures 3.10(a) and 3.10(b) show the nominal compressive stress-strain curves of 10 mm × 10 mm × 10 mm module RVE specimens tested at a displacement rate of 0.3 mm/min (nominal strain rate of 0.0005 s^{-1}) without and with adhesive, respectively. Figures 3.10(c) and 3.10(d) show the nominal compressive stress-strain curves of 10 mm × 10 mm × 20 mm module RVE specimens at a displacement rate of 0.6 mm/min (nominal strain rate of 0.0005 s^{-1}) without and with adhesive, respectively. The deformation patterns for three selected specimens with the nominal stress-strain curves shown in Figure 3.10 are shown in Figures 3.11(a-c), (d-f), and (g-i), respectively.

As shown in Figure 3.10(a) for the cubic specimens, the nominal stress-strain curves show two very distinct stress drops at the nominal strains of about 2% and 5%. After a carefully

examination of the deformation patterns, the first stress drop is believed to be caused by a full development of the first buckling mode at a nominal strain of 2% as shown in Figure 3.11(a). A detailed analysis of the buckling stress of the module RVE specimens is presented in the next section. The calculated buckling stress is 4.44 MPa, which is very close to the test result of about 5 MPa at the nominal strain of 2%. The second stress drop was identified to be caused by the onset of the top sliding against the punch. The top sliding can be seen in Figure 3.11(b) at the nominal strain of 5%. After the onset of the top sliding, the specimen managed to fill up the vacant space provided by the porosity of the components and the microscopic gaps between the components, corresponding to the stage with a relatively low stress increase. After consuming most of the vacant space provided by the porosity of the components and the microscopic gaps between the components, the densification started and led to the large stress increase toward the end of the test. The final crushed specimen at a nominal strain of 50% is shown in Figure 3.11(c).

As shown in Figure 3.10(c) for the double height specimens, the nominal stress-strain curves show slightly different behaviors from those of the cubic specimens. A few stress drops were observed but they are not too consistent. A carefully examination of the deformation patterns indicates that the first buckling load drop is hard to see due to the specimen height increase because it decreases the first buckling stress to about one quarter of the one for the 10 mm cubic specimen according to the analytical buckling load solution as discussed later. Depending on the development of the higher-order buckling modes, the nominal stress-strain behavior could be slightly different. For example, the dotted curve shows the buckling mode evolution from the first to the second buckling mode. The first small load drop corresponds to the first buckling mode at a nominal strain of 1% as shown in Figure 3.11(d) and the second load

drop corresponds to the second buckling mode at a nominal strain of 2% as shown in Figure 3.11(e). The final crushed specimen at a nominal strain of 50% is shown in Figure 3.11(f).

The dashed curve as shown in Figure 3.10(c), however, buckled in a different way. The specimen shows the first buckling mode and continues to build up stress on one side of the wall as shown in Figure 3.11(g). Until the point where the stress was too high against the wall, the middle portion suddenly buckled to the right and switched to the third buckling mode as shown in Figure 3.11(h). This corresponds to the load drop at about the nominal strain of 20%. The final crushed specimen is then in the third buckling mode, as shown in Figure 3.11(i). The development of different buckling modes is random and most likely related to the geometric and materials imperfections of the specimens as well as the local geometric and load variation of the test setup. However, the general shapes of the curves are quite the same.

The in-plane constrained compression test results shown in Figures 3.10(a) and 3.10(c) for the specimens with different heights (10 mm and 20 mm) can be compared to study the size effect. It is noted that although the nominal stress of the double height specimens is indeed higher when the nominal strain approaches 50%, the nominal stress magnitude and the general shape of the curves are almost the same when the nominal strain is below 30%. The effects of the adhesive in the module RVE specimens are also shown in Figures 3.10(b) and 3.10(d). A comparison of Figures 3.10(a) to 3.10(d) shows that the nominal stress-strain curves are higher when the adhesive was applied, which is possibly due to the volume increase from the adhesive. However, the general trends of the nominal stress-strain curves are the same as those without the adhesive.

An important observation on the shape of the in-plane nominal compressive stress-strain curves is that the deformation is highly dominated by the buckling mode initially and the curves

resemble the typical behavior of cellular materials, which possess an initial linear region, a nearly plateau region, and a final densification region. This is reasonable since the module specimens are comprised of mostly powder-like active materials and the foam layers with a void volume fraction of about 30%. Therefore, the general module compressive behavior could be modeled by utilizing proper foam material models such as in [1, 2].

3.4.2. Out-of-plane (z direction) compression of module RVE specimens

3.4.2.1. Foam

Typical foam layers that are used in battery modules were obtained. The measured thickness of these foam layers is 1.5 mm. A specimen was made by stacking four pieces of 20 mm × 20 mm × 1.5 mm foam layers to get more accurate test results. The total thickness of the specimen is 6 mm. The test was conducted with the displacement rate of 1 mm/min (nominal strain rate of 0.003 s^{-1}). The nominal compressive stress-strain curve of the foam is shown in Figure 3.12. The final exponential increase of the stress is due to densification. It is also noted that the foam showed extremely low stress below the strain of about 60%.

3.4.2.2. Out-of-plane (z direction) compression of module RVE specimens

For module RVE specimens, the nominal stress-strain curve can be obtained by the nominal stress-strain curves of the cell, foam and aluminum heat dissipater sheet since the Poisson's ratios of the cell RVE specimens as tested in Lai et al. [3] and the foam specimen as tested in this investigation are nearly zero under out-of-plane compression. Based on the composite ROM, the nominal stresses of the cell, foam, aluminum heat dissipater sheet, and module, denoted as σ_{cell}, σ_{foam}, σ_{Al} and σ_{module}, respectively, are equal.

$$\sigma_{cell} = \sigma_{foam} = \sigma_{Al} = \sigma_{module} \tag{2}$$

For a given σ_{module}, the nominal strain of the module specimen can be obtained from the component strains weighted by the volume fractions as

$$\varepsilon_{module} = \varepsilon_{cell} V_{cell} + \varepsilon_{foam} V_{foam} + \varepsilon_{Al} V_{Al} \tag{3}$$

where ε_{module}, ε_{cell}, ε_{foam} and ε_{Al} represent the nominal strains of the module, cell, foam, and aluminum heat dissipater sheet, respectively. Here, V_{cell}, V_{foam} and V_{Al} represent the volume fractions of the cell, foam and aluminum heat dissipater sheet, respectively, for the module RVE specimen. For the nominal stress range considered, the contribution of the aluminum heat dissipater sheets to the strain of the module is quite small and the aluminum heat dissipater sheet is in the linear elastic range. The nominal stress-strain relation for the aluminum heat dissipater sheet with zero in-plane strains under out-of-plane loading conditions is

$$\varepsilon_{Al} = \frac{1-\nu_{Al}-2\nu_{Al}^2}{1-\nu_{Al}} \cdot \frac{\sigma_{Al}}{E_{Al}} \tag{4}$$

where E_{Al} and ν_{Al} are the Young's modulus and Poisson's ratio of the aluminum sheet.

Figure 3.13 shows the nominal out-of-plane compressive stress-strain curve of the module specimen obtained from Equation (3) based on the data shown in Figure 3.12 for the foam specimen, Equation (4) with the value of E_{Al} from Table 3.1 for the aluminum dissipater sheet, and the out-of-plane compression data of the cell RVE specimens reported in [3]. It should be noted that the cell RVE specimen in [3] has 10 units of anode, cathode and separator sheets whereas the cell RVE specimen in this investigation has 7 units of anode, cathode and separator sheets. However, the nominal stress-strain curves for the two cell RVE specimens under out-of-plane compression should be quite similar due to the large numbers of units of

anode, cathode and separator sheets. Figure 3.13 also shows the nominal stress-strain curves of the module RVE specimens for the in-plane constrained compression tests. The results indicate that the module RVE specimens show a similar compressive stress-strain behavior in both in-plane and out-of-plane directions and these curves resemble those for typical foam materials. The curves for in-plane compression is higher than the one for out-of-plane compression as expected due to the stiffening effects of the aluminum heat dissipater sheet, aluminum and copper foils, separator and cover sheets in the module RVE specimens under in-plane compression. It is also noted that both curves from the in-plane and out-of-plane compression tests appear to be parallel to each other with a gap around 5 to 8 MPa. The results indicate that the module RVE specimens can be modeled as anisotropic foam materials (for example, see Wang and Pan [2]).

3.5. Buckling analysis of module RVE specimens under in-plane (y direction) constrained compression

When a module RVE specimen was made, the component sheets were first assembled and packed together. The specimen was then put in the slot of the female die and pre-compressed to the thickness of 10 mm. When a module RVE specimen is under in-plane compression, the component sheets buckle independently with the lateral constraints from the neighbor component sheets. As indicated in the experimental results, the general behaviors for the module RVE specimens without and with adhesive under in-plane constrained compression are quite similar. Therefore, the buckling behavior of the module RVE specimens under in-plane constrained compression without adhesive is first investigated here. Since the component sheets were only packed together, each component sheet can be treated as an individual sheet or thin

plate under in-plane compression with the lateral constraints which can be treated as unattached elastic foundations.

Figure 2.9 shows a uniform straight beam under end loads and supported by two unattached elastic foundations. Both ends are hinged and the beam is elastically supported by the lateral pressure p proportional to the deflection z in the z direction. Here, k_1 and k_2 represent the spring constants of the softer and harder elastic foundations on the two sides of the beam, respectively. The buckling load solution of the beam can be found in [4]. Based on the solution listed in [4], the buckling load P_m^i of the i-th component with the two unattached elastic foundations can be expressed as

$$P_m^i = \frac{m^2\pi^2 E_i' I_i}{L^2} + \frac{k_2 L^2}{m^2\pi^2}\phi^\alpha = \frac{m^2\pi^2 E_i' b h_i^3}{12L^2} + \frac{k_2 L^2}{m^2\pi^2}\phi^\alpha \tag{5}$$

where m represents the number of half waves in which the component buckles and is equal to the lowest integer greater than the $\overline{m}$. Here, $\overline{m}$ is defined as

$$\overline{m} = \frac{1}{2}\left(\sqrt{1+\frac{4L^2}{\pi^2}\sqrt{\frac{k_2}{E_i' I_i}}} - 1\right) \tag{6}$$

In Equation (5), $\phi = k_1/k_2$ and α depends upon the value of m. Here, I_i is the moment of inertia for the i-th component. E_i' is the effective elastic modulus for a thin plate under plane strain uniaxial compression conditions and is equal to $E_i/(1-\nu_i^2)$, where E_i and ν_i are the elastic modulus and Possion's ratio of the i-th component. L, b and h_i are the height, width, and the thickness of the i-th component. The first term on the right hand side of Equation (5) represents the buckling load without the lateral constraints or the unattached elastic foundations. The second term on the right hand side of Equation (5) is the additional buckling load due to the lateral constraints or the unattached elastic foundations.

For the 10 mm × 10 mm × 10 mm module RVE specimen, the lowest or the first mode ($m=1$) buckling load P_1^i of the i-th component without the lateral constraints can be expressed as

$$P_1^i = \frac{\pi^2 b E_i' h_i^3}{12 L^2} \tag{7}$$

Since the aluminum heat dissipater sheet is painted on both sides and the elastic modulus of the paint is much smaller than the elastic modulus of the aluminum sheet, only the aluminum portion is used for the calculation of the buckling load. For the aluminum heat dissipater sheet, the effective compressive modulus E_i' is based on the tensile elastic modulus of 70 GPa and the Poisson's ratio of 0.33. For the other module components, the effective compressive moduli E_i' obtained from the corresponding constrained compression tests as reported in [3] are used. The effective compressive moduli E_i' for the cover sheet, anode, cathode and separator sheets are listed in Table 3.2. With the elastic moduli and the values of the thicknesses listed in Table 2.1, the first mode buckling loads for the component sheets can be calculated from Equation (7) and summarized in Table 3.3. The corresponding compressive strains at the buckling loads of the components can be calculated by

$$\varepsilon_1^i = \frac{P_1^i}{E_i' A_i} \tag{8}$$

where A_i is the cross sectional area of the i-th component. The results are summarized in Table 3.3. The result shows that the buckling load is the highest for the aluminum heat dissipater sheet. The other components buckle at very low strains based on the effective compressive and estimated Poisson's ratios. Note that the metal portions of the cover sheet, anode and cathode

sheets cannot fully contribute to the effective compressive elastic moduli as for the tensile elastic moduli.

The nominal strain at which the first buckling mode of the module RVE specimen starts is based on the nominal strain ε_1^{Al} at which the first buckling mode of the aluminum heat dissipater sheet occurs. The nominal stress of the module RVE specimen at this nominal strain $\varepsilon_1^{Al} = 1.48 \times 10^{-3}$ can be obtained by summing over the loads of all components (listed in Table 3.3) divided by the cross sectional area of the module RVE specimen. This value represents the first buckling stress of the module RVE specimen. In this case, the load carried by the foam layers is ignored since the elastic modulus of the foam is much smaller than those of the other components. The first mode buckling stress of the module RVE specimen without considering the lateral constraints is calculated as

$$\sigma_1^{module} = \frac{\varepsilon_{Al} \sum n_i E_i' A_i}{A} = 4.32 \text{ MPa} \tag{9}$$

where n_i is the number of the i-th component in the module RVE specimen. This value is close to that of test results (about 5 MPa at the nominal strain of 0.02), as shown in Figure 3.10(a). It is noted that the aluminum heat dissipater sheet contributes to more than 90% of the buckling stress. However, the above calculation does not account for the effect of the small pre-compression, the friction between the components, and the lateral constraints experienced by the aluminum heat dissipater sheet.

In order to understand the effect of the lateral constraints, the second term on the right hand side of Equation (5) is evaluated to account for the additional load due to the lateral constraints considered as two unattached elastic foundations [4]. In this case, the aluminum heat dissipater sheet is considered as the beam and the neighbor cells and foams are considered as the

unattached elastic foundations. For the aluminum heat dissipater sheet, k_1 and k_2 are the same and can be expressed as k. Here, k represents the lateral force per unit plate length per unit deflection of the neighbor cell and foam in the out-of-plane direction. The spring constant k can be expressed in terms of the elastic modulus E of the neighbor cell and foam as a composite material as

$$k = \frac{Eb}{h} \tag{10}$$

where b represents the width of the specimen, and h represents the thickness of the neighbor components. Note that the Possion's ratios for both the cell and the foam are 0 under out-of-plane compression. The elastic modulus E of the foam and cell as a homogenous material can be estimated from the elastic moduli E_{cell} and E_{foam} of the cell and foam, respectively, using the composite ROM as

$$E = \frac{E_{cell}E_{foam}}{E_{cell}V_{foam} + E_{foam}V_{cell}} \tag{11}$$

where V_{cell} and V_{foam} represent the volume fractions of the cell and foam, respectively. The elastic moduli of the foam and cell obtained from the out-of-plane compression data of the foam specimen and the cell RVE specimen reported in [3] are 0.175 and 8.5 MPa, respectively. The elastic modulus E of the foam and cell is estimated as 0.538 MPa. The spring constant k becomes 1.12×10^6 N/m^2. Based on Equation (6), $\overline{m} = 0.15$ and therefore $m = 1$. The corresponding value of α is 1. Therefore, the additional buckling contribution due to the lateral constraints calculated from Equation (5) is 12 N. This load is quite small compared to the first mode buckling load of 432 N for the module RVE specimen without consideration of the lateral

constraints. With consideration of the lateral constraints, the first buckling stress is slightly increased to 4.44 MPa.

For the double height module specimens (10 mm × 10 mm × 20 mm), $\overline{m} = 0.45$ and therefore $m = 1$. The corresponding value of α is 1. According to the first term on the right hand side of Equation (5), for the double height module RVE specimen, the first mode buckling stress is 1.08 MPa which is a quarter of that for the original 10 mm height specimen. The additional buckling contribution due to the lateral constraints calculated from Equation (5) is 48 N. With consideration of the lateral constraints, the first buckling stress is 1.56 MPa. Based on the first term on the right hand side of Equation (5), the second mode buckling stress of the double height RVE specimen is 4.32 MPa, which is the same as the first mode buckling stress for the original 10 mm height specimen. The additional buckling contribution due to the lateral constraints calculated from Equation (5) is 12 N. With consideration of the lateral constraints, the first buckling stress is 4.44 MPa. The second mode bucking stress obtained from the test data shown in Figure 3.10(c) at the nominal strain of about 2% compares fairly well to the calculated value. However, the first mode buckling occurs too early and is difficult to observe with the current experimental setup.

The effects of the adhesive can also be examined using Equation (5). When the cover sheets are bonded to the aluminum heat dissipater sheet, the flexural rigidity or bending stiffness of the aluminum heat dissipater sheet with the bonded cover sheets increases. Consequently, the buckling load of the aluminum heat dissipater sheet increases and in turns the buckling stress of the module RVE specimen increases. This is in agreement with the experimental results shown in Figure 3.10. Finally, if we consider m as a real number as in Ali et al. [5] and Lai et al. [3], the values of m can be calculated as 0.407 and 0.813 for the specimens with the length of 10

mm and 20 mm, respectively. The half wavelength for the elastic buckling of the aluminum dissipater sheet can be calculated as 24.6 mm. The half wavelength can be used as a guideline to select the length of module RVE specimens. It appears that module specimens with the length of 20 mm nearly satisfy the length requirement of module RVE specimens according to the elastic buckling analysis. In this investigation, experiments were conducted for the module specimens with the length of 10 mm and 20 mm. The test results show that the nominal stress-strain curves and the general buckling behavior for the module specimens with different lengths are quite similar. Therefore, the test results presented in this study can be used to represent the nominal stress-strain curves of module RVE specimens for development of macroscopic homogenized material models for simulations of battery modules under compressive loading conditions [6].

3.6. Quasi-static punch indentation test

The in-plane and out-of-plane compression test results can be used to develop macro homogenized material models for cell and module RVEs. However, the macro homogenized material models need validations. A limited validation will be achieved by conducting a punch indentation test of a small-scale module specimen and comparing the computational results based on the macro homogenized material models with the experimental results. The layered structure of the small-scale module specimen for the punch indentation test is the same as that of the module RVE specimens except for the size and shape. Figure 3.14(a) shows the small-scale module specimen and its dimensions. Figure 3.8(c) shows a side view of the small-scale module specimen with the individual components. The large arrows indicate the compressive direction. The specimen length is designed to be 8 times longer than the specimen thickness to create a non-uniform stress distribution under the punch. The punch indentation test setup is shown in

Figure 3.15(a). The setup consists of a male punch of a circular shape and a female die with a slot of the same size to fit the specimen (10 mm × 80 mm) such that the specimen is fully constrained on its lateral sides with a pre-compression in the out-of-plane direction. The dimensions of the punch are shown in Figure 3.15(b). The test procedure is the same as that for the in-plane constrained compression tests of the module RVE specimens with a displacement rate of 0.6 mm/min (nominal strain rate of 0.0005 s^{-1}).

The load-displacement curve of the punch indentation test is shown in Figure 3.16. The curve shows a relative linear stage in the beginning, followed by a load drop and a slow load increase region and a final rapid load increase region due to densification. The results are similar to those of the in-plane constrained compression tests of the module RVE specimens. Similar load drops were observed due to the buckling after the initial linear stage for the module RVE specimens. From the deformation pattern of the small-scale module specimen after the punch indentation test as shown in Figure 3.17, the load drop appears to come from the buckling of the small-scale module specimen directly under the punch. The load-displacement curves from the corresponding finite element analyses reported in Ali et al. [6] are also plotted in Figure 3.16. The finite element analyses are based on a crushable foam material model and the nominal compressive stress-strain curve of a module RVE specimen with the dimension of 10 mm × 10 mm × 20 mm with and without adjustment for softening. As shown in Figure 3.16, the general trends of the results of the finite element analyses agree reasonably well with the test results.

The tested specimen shows the similar buckling mode as that of the module RVE specimens under in-plane constrained compression tests. A schematic of the specimen after the punch indentation test is shown in Figure 3.17(a). A top view and a side view of the tested specimen are shown in Figures 3.17(b) and 3.17(c), respectively. At least three half waves of

buckling were developed near the central portion of the specimen, as indicated in Figure 3.17(c) by the two concave regions and a convex region on the aluminum heat dissipater sheet. This is in general consistent with the observation for the module RVE specimens under in-plane constrained compression tests, as shown in Figure 3.11(i).

A schematic of the dimensional changes of the specimen is shown in Figure 3.18. The dashed line represents the final position of the punch. After removing the punch, the specimen shows a 2.2 mm springback near the center. Small lift-ups of the bottom corners were observed. This was expected since the center was compressed and forced the sides to bend toward the center. The load-displacement behavior and the dimensional changes will be used to benchmark and validate the macro homogenized material models for the module RVE specimens reported in Ali et al. [6].

3.7. Conclusions

1. The active materials on the cathode and anode sheets were found to have nearly no load carrying capacity in the tensile tests. The nominal tensile stress-strain curves of cells and modules are developed based on the composite ROM.
2. The nominal stress-strain curves of the module RVE specimens showed stress drops due to buckling and then final densification. The stress drops of the curves were correlated to the deformation patterns. The details of the stress drops depend on the imperfections of the specimens and the conditions of the test fixture setup.
3. No significant size effect was observed for the module RVE specimens of different heights under in-plane constrained compression tests when the strain is below 30%.

Above the strain of 30%, the nominal stress of the double-height specimens increases faster as the strain increases.

4. The nominal stress-strain curves of the module RVE specimens with adhesive under in-plane constrained compression are higher than those without adhesive.
5. The nominal out-of-plane compressive behaviors of the module RVE specimens and the foam between cells in a module are similar. The different nominal compressive stress-strain curves of module RVE specimens under in-plane and out-of-plane compression suggest that the lithium-ion battery modules can be modeled as anisotropic foams or cellular materials. This is important information for development of macro homogenized anisotropic material models for crashworthiness analyses.
6. A buckling analysis for the module RVE specimens under in-plane constrained compression was conducted based on the analytical solution for a beam with unattached elastic foundations, the effective compressive moduli of the cell components, and the tensile modulus of the aluminum heat dissipater sheet. The calculated buckling stress agrees well with the experimental results. The analytical buckling analysis presented in this study can be used to determine the yield stresses, corresponding to the buckling stresses, in macro homogenized material models based on crushable foam models.
7. In the constrained punch indentation test on a small-scale module specimen, the tested specimen shows the similar buckling mode as observed for the module RVE specimens under in-plane constrained compression tests. The load-displacement curve and the dimensional change of the punch indentation test were recorded and used to benchmark and validate the macro homogenized material models developed from the nominal stress-strain curves of the module RVE specimens under in-plane compression. The

experimental results for the small-scale module specimen can be used to benchmark and validate new macro homogenized material models.

Table 3.1. Tensile elastic moduli of module components.

	Elastic modulus (GPa) (divided by the total cross sectional area)	Elastic modulus (GPa) (divided by the cross sectional area of the metal portion)
Cover sheet	5.6	NA
Anode	4.7	105
Cathode	5.1	68
Separator	0.5	NA
Aluminum heat dissipater sheet	53	70

Table 3.2. Effective compressive elastic moduli of module components as reported in [3].

	Effective compressive elastic modulus E_i' (MPa)
Cover sheet	575
Anode	83
Cathode	275
Separator	90

Table 3.3. The first mode buckling loads, the strains of module components at the first mode buckling loads, and the loads at the nominal strain of $\varepsilon_1^{Al} = 1.48 \times 10^{-3}$.

	Cover sheet	Anode	Cathode	Separator	Aluminum heat dissipater sheet
P_1^i (N)	0.078	0.056	0.186	6.3×10^{-5}	413
ε_1^i	1.22×10^{-4}	3.38×10^{-4}	3.38×10^{-4}	3.5×10^{-6}	1.48×10^{-3}
P_1^i (N) at $\varepsilon_1^{Al} = 1.48 \times 10^{-3}$	0.94	0.25	0.81	0.027	413

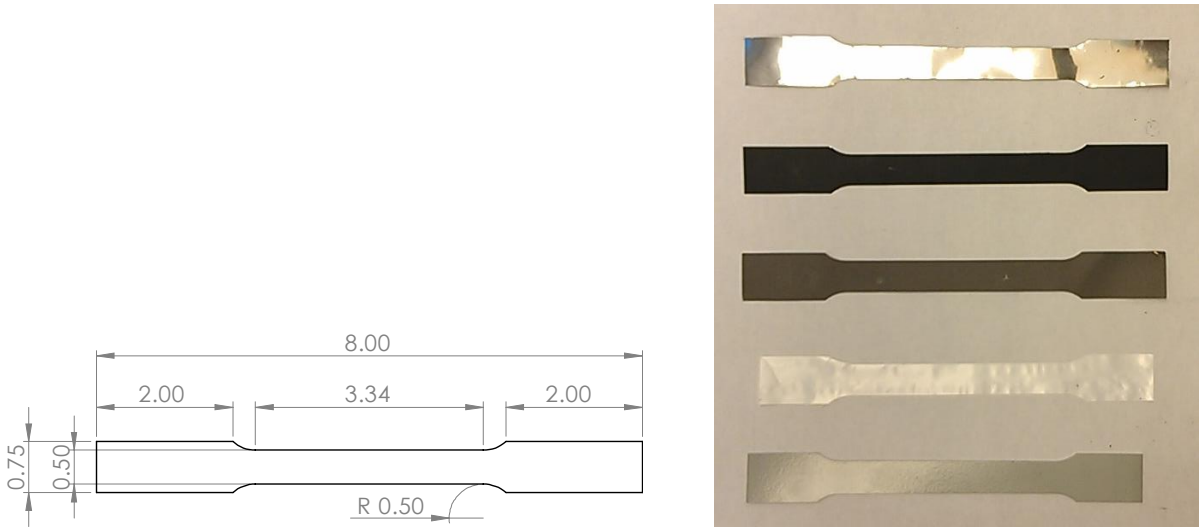

Figure 3.1. (a) A schematic of a tensile specimen with the dimensions (ASTM E8/E8M-11). (b) A picture of the tensile specimens of the cover sheet, cathode, anode, separator and aluminum heat dissipater sheets (from the top to bottom).

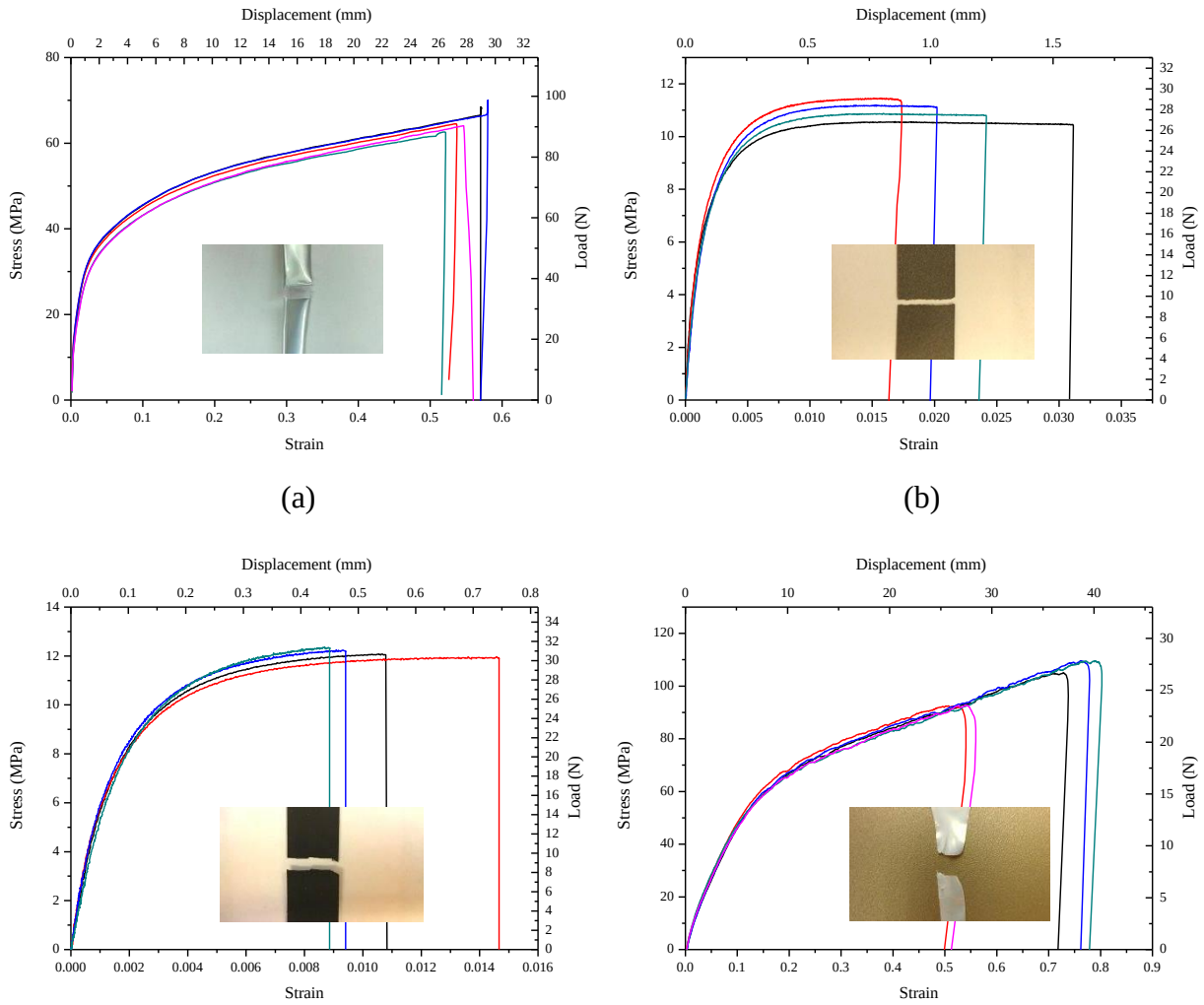

Figure 3.2. Nominal tensile stress-strain curves of the (a) cover sheet, (b) anode, (c) cathode, and (d) separator sheets tested at a displacement rate of 5.08 mm/min (nominal strain rate of 0.0017 s^{-1}).

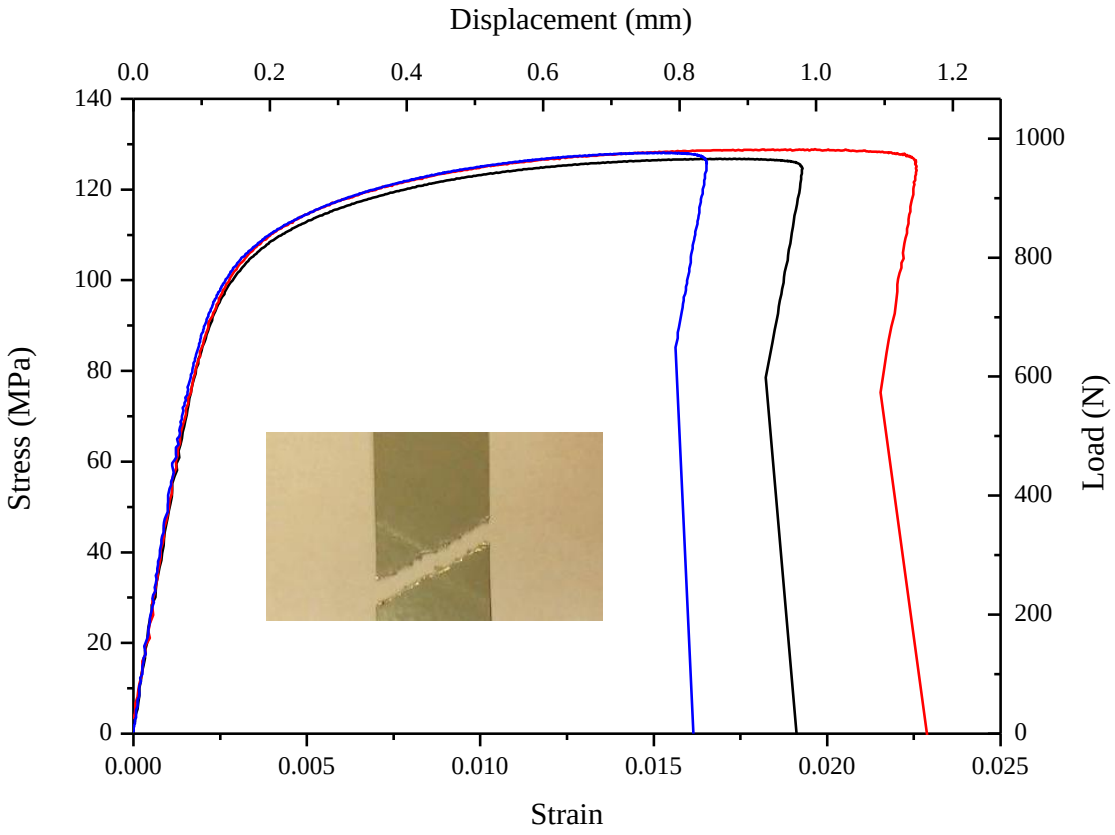

Figure 3.3. Nominal tensile stress-strain curves of the aluminum heat dissipater sheets tested at a displacement rate of 2.54 mm/min (nominal strain rate of 0.00085 s^{-1}).

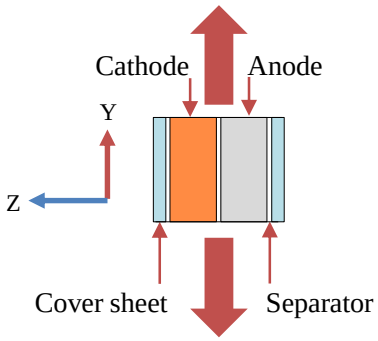

Figure 3.4. A side view of a small portion of cell RVEs with a single unit of anode, cathode and separator, and two cover sheets with two additional separator sheets. The large arrows indicate the tensile direction.

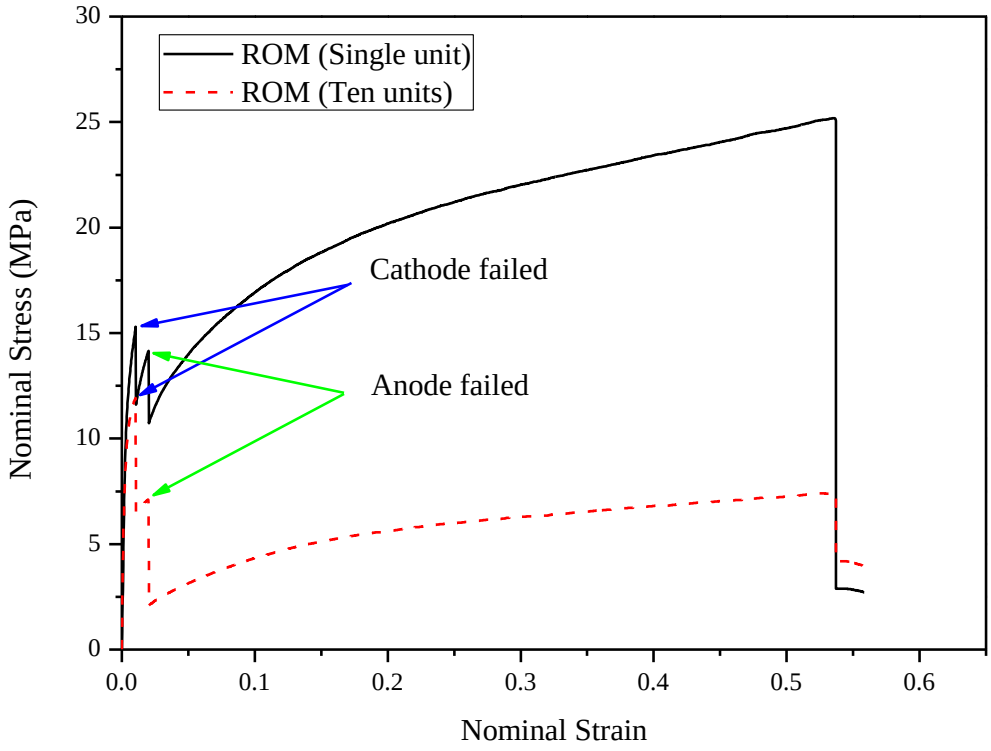

Figure 3.5. A comparison of the nominal stress-strain curves obtained from the composite ROM for the battery cells with single unit and ten units of anode, cathode and separator.

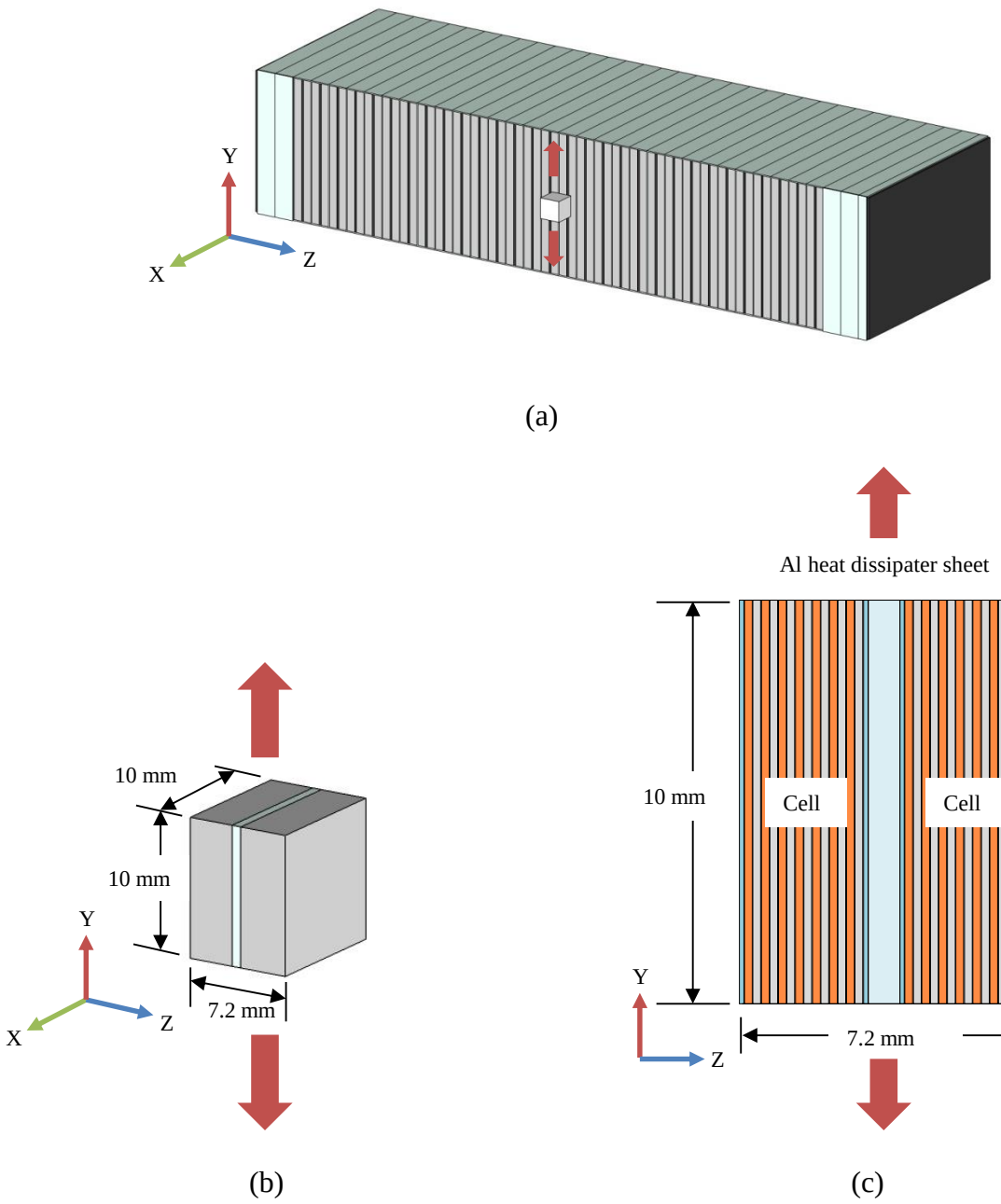

Figure 3.6. A schematic of (a) a battery module and a module RVE under in-plane tensile loading, (b) a module RVE specimen, and (c) a side view of the module RVE specimen showing two cells and one aluminum heat dissipater sheet. The large arrows indicate the tensile direction.

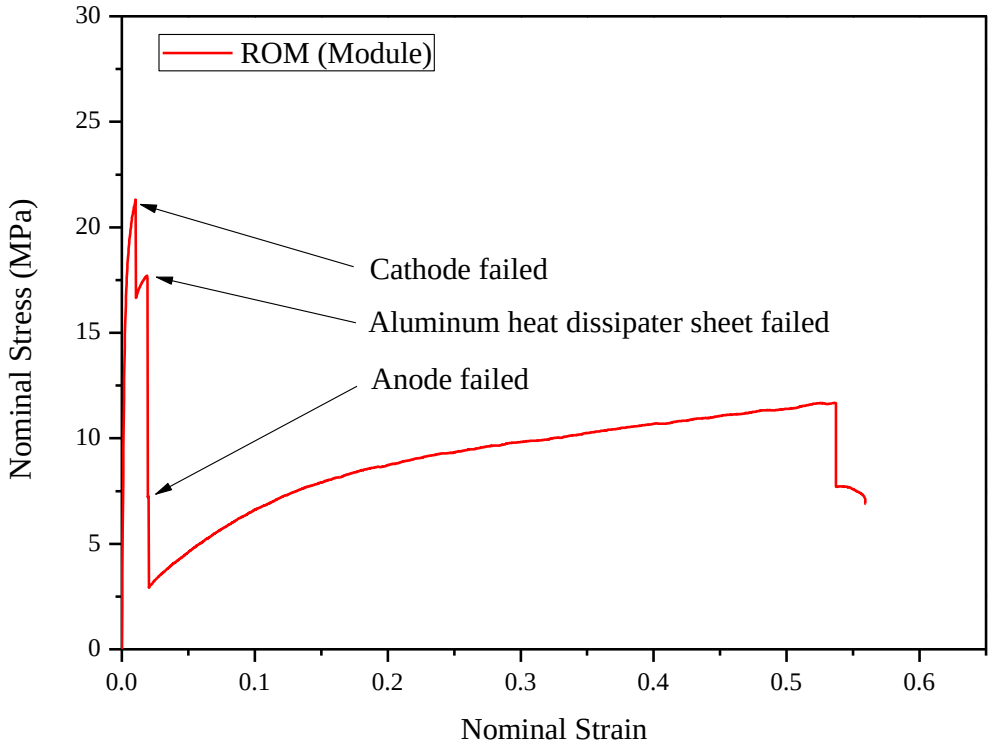

Figure 3.7. The nominal stress-strain curve obtained from the composite ROM for a battery module RVE shown in Figure 3.6(c).

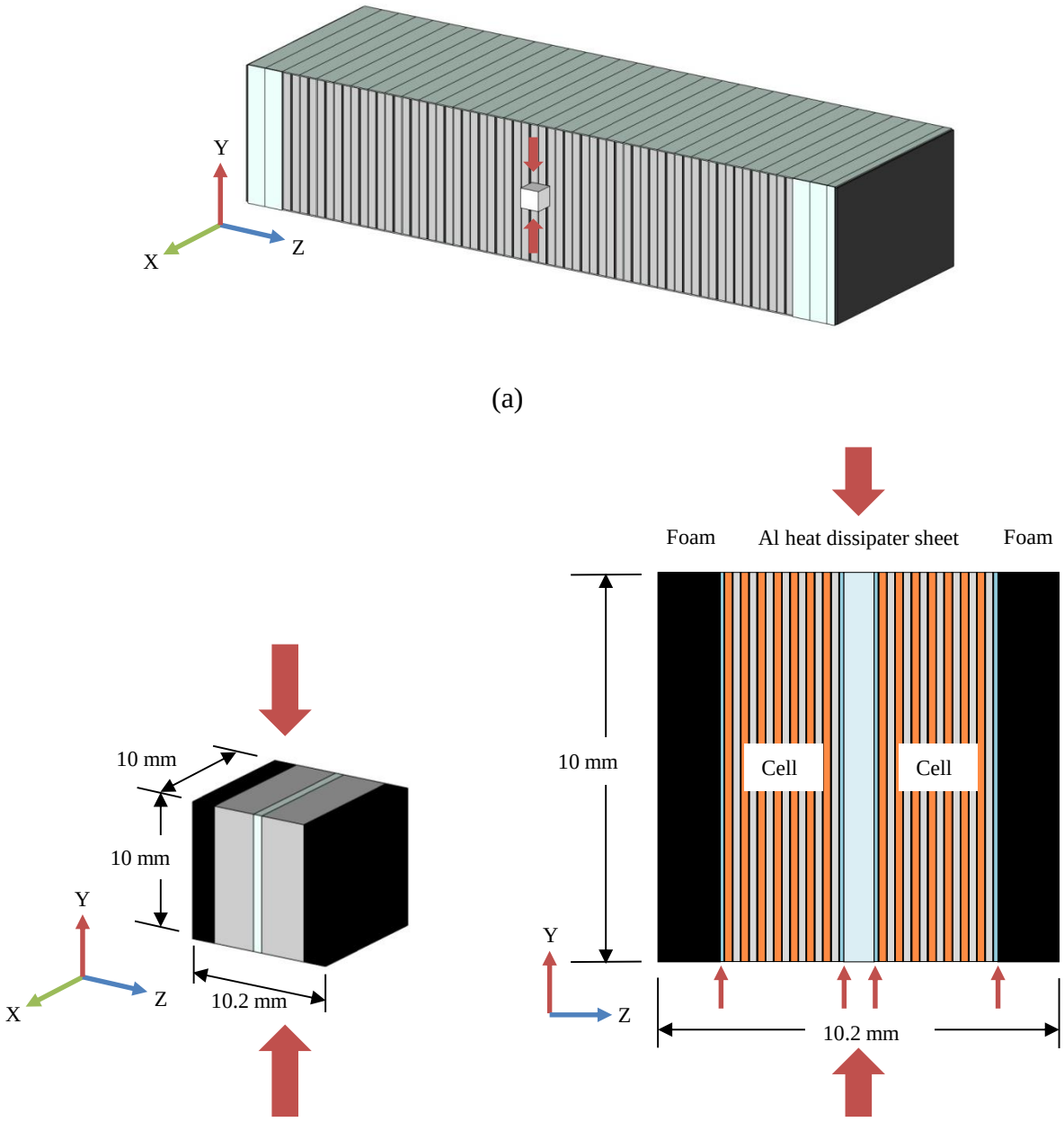

Figure 3.8. A schematic of (a) a battery module and a module RVE specimen for the in-plane constrained compression test, (b) a module RVE specimen with the dimensions, and (c) a side view of the module RVE specimen showing the individual components. The large arrows indicate the compressive direction.

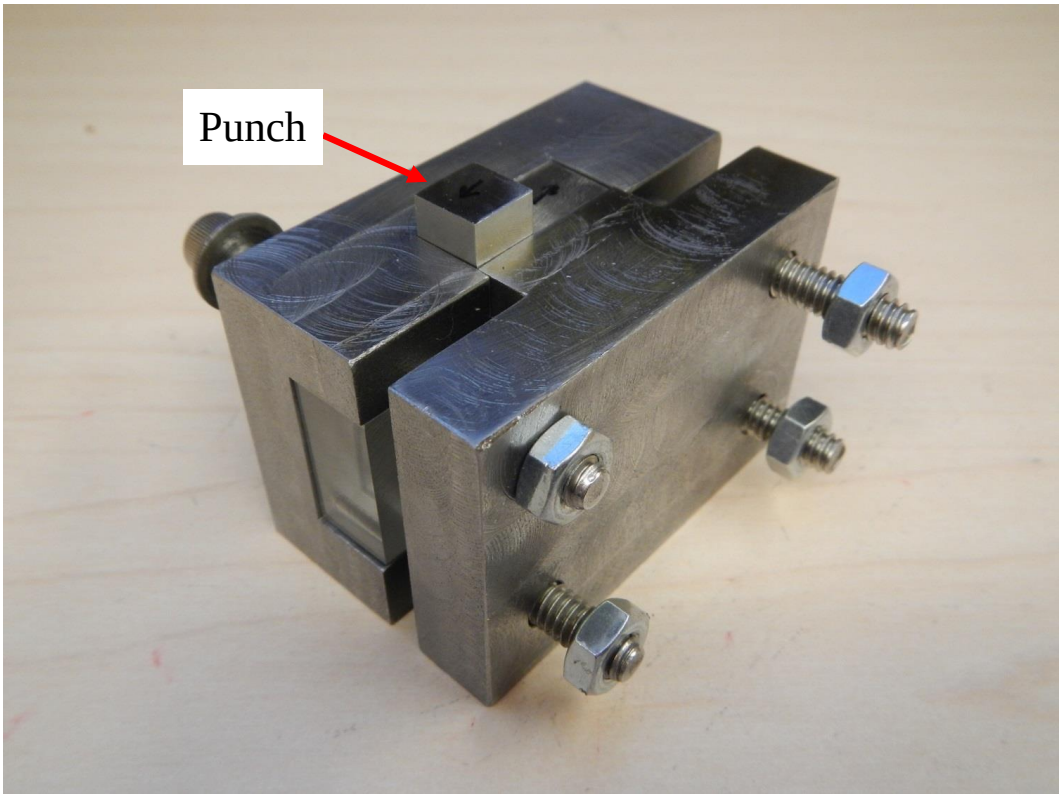

Figure 3.9. A punch and die setup for in-plane compression tests of module RVE specimens.

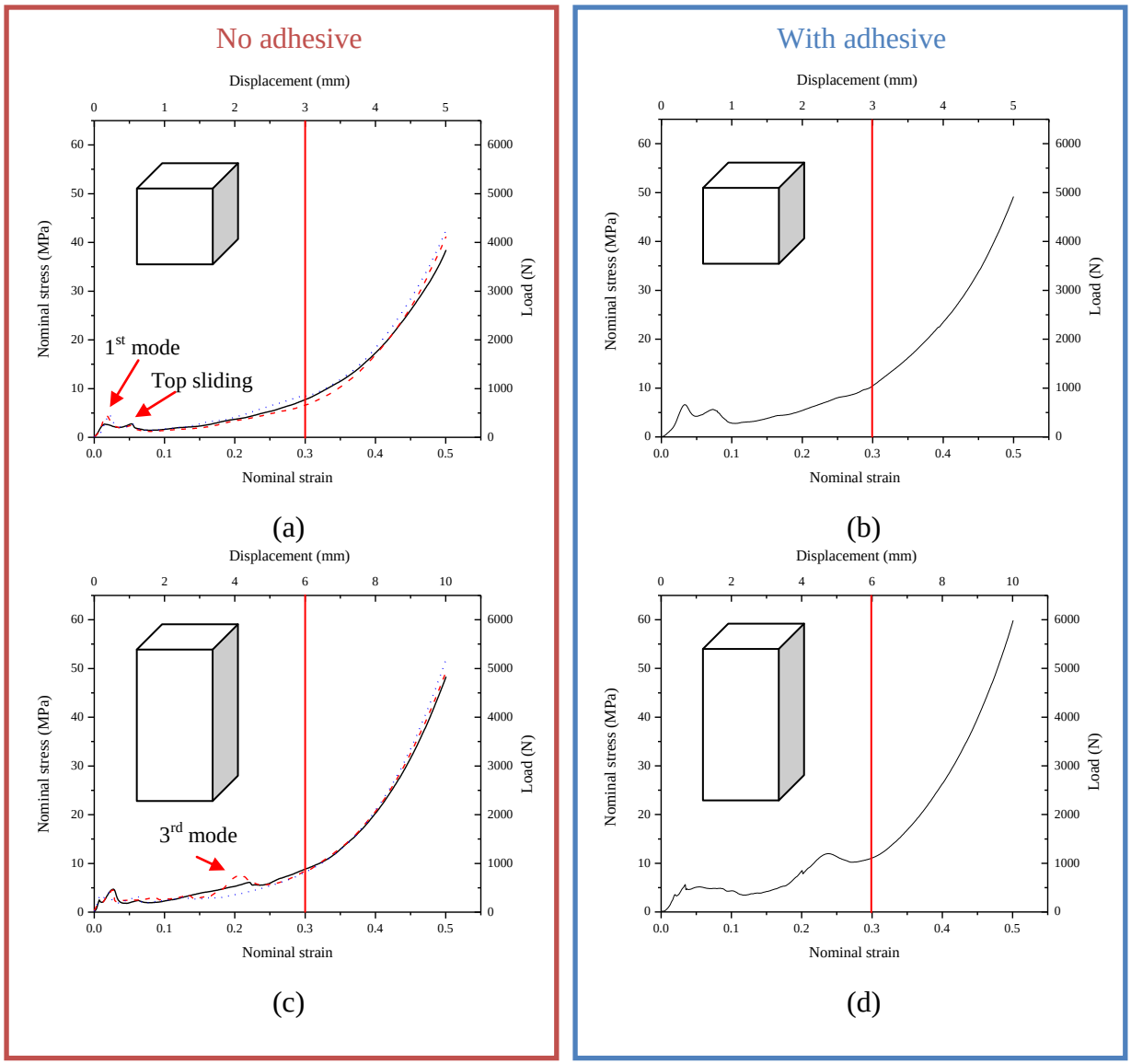

Figure 3.10. Nominal in-plane constrained compressive stress-strain curves of the module RVE specimens of the size of 10 mm × 10 mm × 10 mm at a displacement rate of 0.3 mm/min (nominal strain rate of 0.0005 s^{-1}) (a) without and (b) with adhesive, and of the module RVE specimens of the size of 10 mm × 10 mm × 20 mm at a displacement rate of 0.6 mm/min (nominal strain rate of 0.0005 s^{-1}) (c) without and (d) with adhesive.

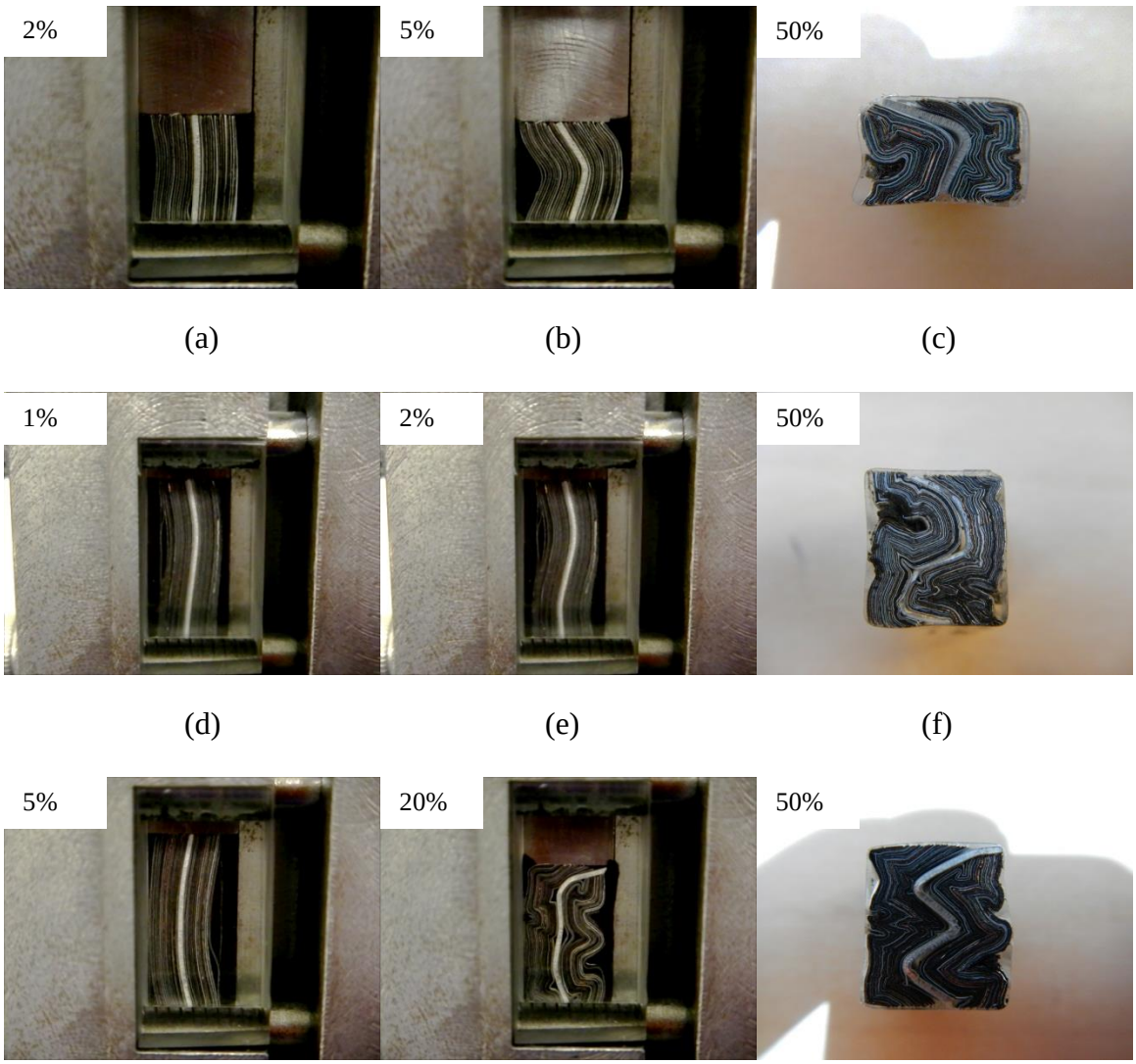

Figure 3.11. (a-c) show the deformation patterns for a 10 mm cubic module RVE specimen. (d-f) show the deformation patterns of the dotted curve in Figure 12(b). (g-i) show the deformation patterns of the dashed curve in Figure 12(c). The nominal strain corresponding to the deformation pattern is marked in each figure.

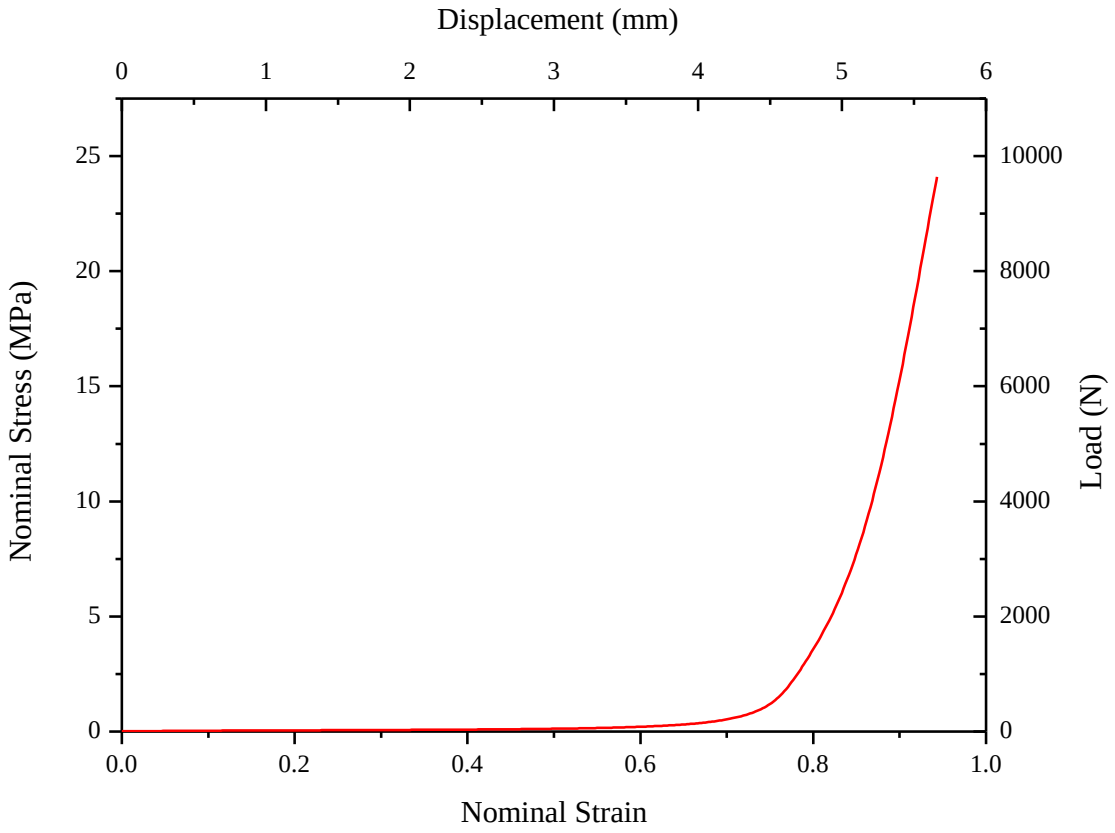

Figure 3.12. A nominal compressive stress-strain curve of the foam used in a battery module. The displacement rate is 1 mm/min (nominal strain rate of 0.003 s^{-1}).

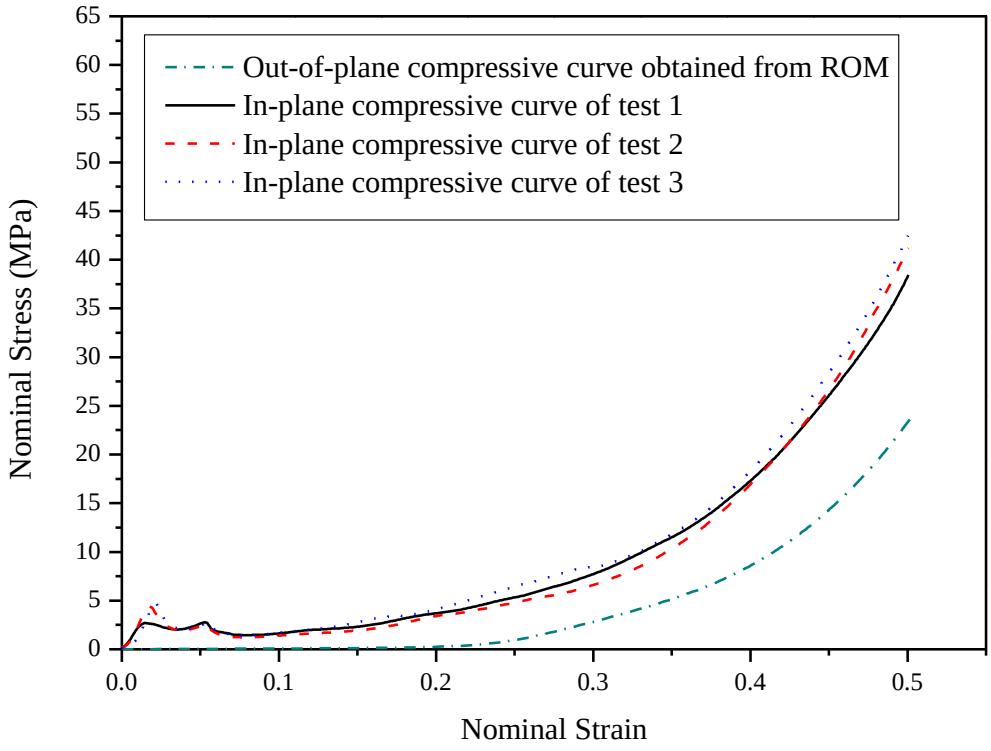

Figure 3.13. A nominal out-of-plane compressive stress-strain curve of a module RVE specimen obtained from Equation (3) based on the composite ROM. The nominal in-plane compressive stress-strain curves of module RVE specimens in Figure 12(a) are also shown for comparison.

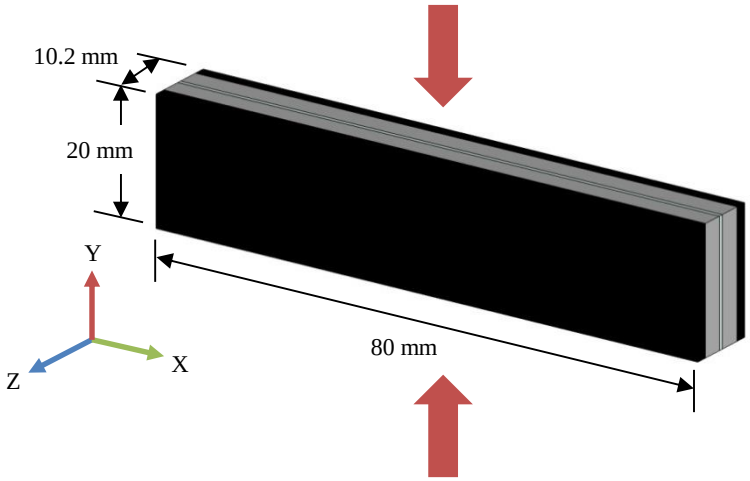

Figure 3.14. A schematic for a small-scale module specimen with the dimensions for a punch indentation test. The large arrows indicate the compressive direction.

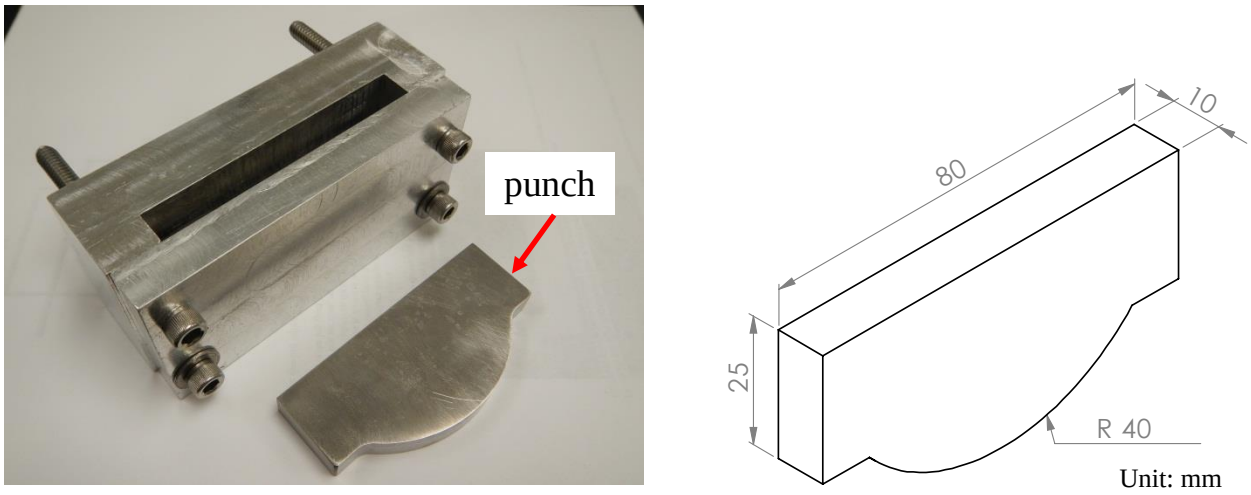

(a) (b)

Figure 3.15. (a) A punch indentation test setup and (b) the punch dimensions (in mm).

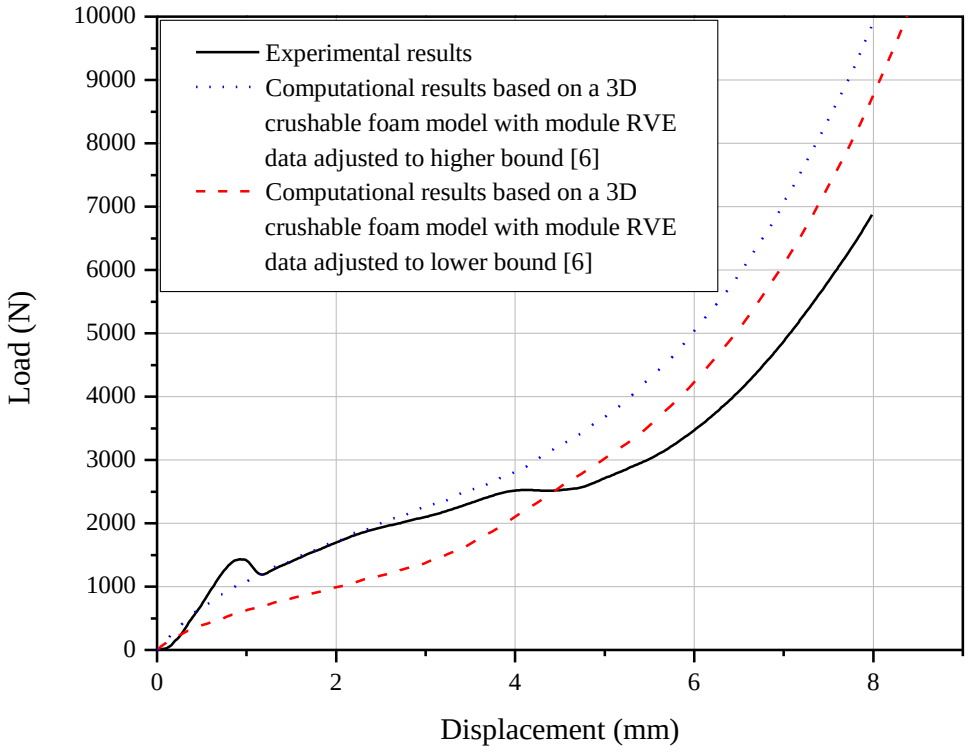

Figure 3.16. The load-displacement curve of the punch indentation test at a displacement rate of 0.6 mm/min. The results of the finite element analyses based on a crushable foam material model as reported in [6] are also shown.

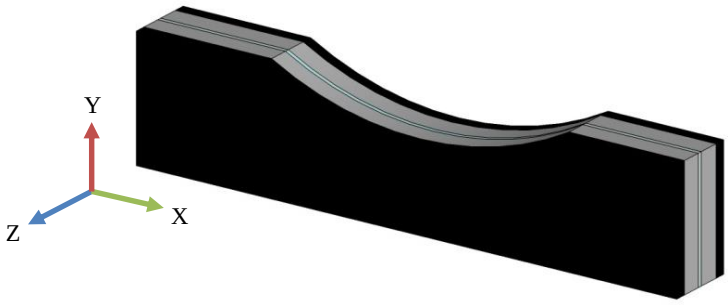

(a)

(b)

(c)

Figure 3.17. (a) A schematic of the specimen after the punch indentation test. (b) A top view and (c) a side view of the tested specimen. The foam layers on both sides of the specimen were removed for (b) for clarity.

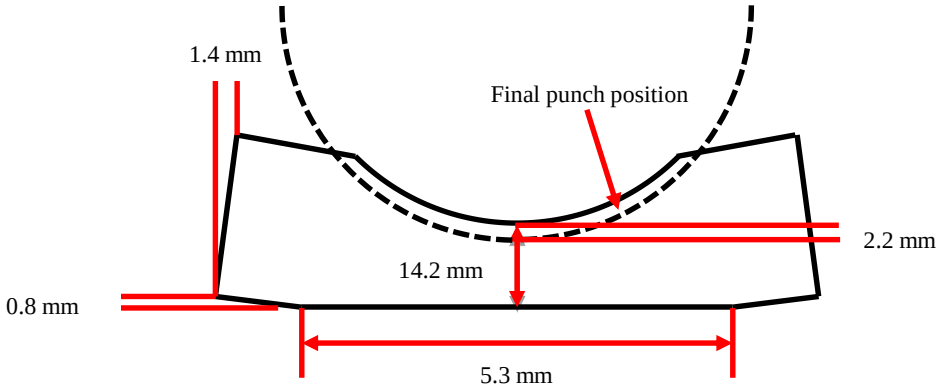

Figure 3.18. A schematic of the dimensional changes of the specimen after the punch indentation test. The dashed line represents the final position of the punch during the punch indentation test.

Acknowledgement

The support of this work by the Crash Safety Working Group (CSWG) of the United States Council on Automotive Research (USCAR) and Ford Motor Company is appreciated. Helpful discussions with Yibing Shi, Guy Nusholtz, and Ronald Elder of Chrysler, Saeed Barbat, Bill Stanko, and Mark Mehall of Ford, Jenne-Tai Wang, Ravi Nayak, Kris Yalamanchili and Stephen Harris of GM, Christopher Orendorff of Sandia National Laboratory, Seung-Hoon Hong of the University of Michigan, and Natalie Olds of USCAR are greatly appreciated.

References

[1] V.S. Deshpande, N.A. Fleck, Multi-Axial Yield Behaviour of Polymer Foams, Acta Materialia, 49 (2001) 1859-1866.

[2] D.A. Wang, J. Pan, A Non-Quadratic Yield Function for Polymeric Foams, International Journal of Plasticity, 22 (2006) 434-458.

[3] W. Lai, M.Y. Ali, J. Pan, Mechanical Behavior of Representative Volume Elements of Lithium-Ion Battery Cells under Various Loading Conditions, Journal of Power Sources 245 (2014) 609-623.

[4] W.C. Young, R.G. Budaynas, Roark's Formulas for Stress and Strain, 7th ed., McGraw-Hill, 2001.

[5] M.Y. Ali, W. Lai, J. Pan, Computational Models for Simulations of Lithium-Ion Battery Cells under Constrained Compression Tests, Journal of Power Sources 242 (2013) 325-340.

[6] M.Y. Ali, W. Lai, J. Pan, Computational Models for Simulation of a Lithium-Ion Battery Module Specimen under Punch Indentation, companion paper to be submitted publication (2013).

Chapter 4
Failure Mode and Fatigue Behavior of Weld-Bonded Lap-Shear Specimens of Magnesium and Steel Sheets

4.1. Introduction

Lightweight materials such as advanced high strength steels, aluminum, and magnesium alloys have been replacing the low-carbon mild steel in the automotive industry to reduce the vehicle weight for better fuel efficiency. Since magnesium alloys are much lighter than the steels commonly used in vehicles, using magnesium alloys could result in a substantial weight reduction. One of the major issues for introducing magnesium alloys into vehicle structures is joining magnesium components to the existing steel structures. Joining magnesium alloys to steels is especially difficult due to the extreme difference in their melting temperatures and immiscibility of magnesium and iron [1]. If magnesium and steel are melted together, vaporization of magnesium would create unacceptable porosity in the weld nugget. Both friction stir spot welding (FSSW) and ultrasonic spot welding (USW) are capable of joining similar and dissimilar materials. A comprehensive review of FSSW on joining similar materials can be found in Pan [2]. The research on joining dissimilar materials by FSSW was carried out mostly on joining aluminum and steel sheets, for example, see Gendo et al. [3]. Liyanage et al. [4] conducted research on joining magnesium to steel sheets by FSSW with tool penetration into the lower steel sheets by using a tungsten-based W-25Re tool. However, it would be difficult to implement the technology in the mass production due to tool wear.

Hetrick et al. [5], Jahn et al. [6] and Wright et al. [7] have conducted research on processing conditions of joining similar aluminum sheets using USW for automotive applications. For joining dissimilar sheets by USW, research has been done by Watanabe et al. [8] on joining aluminum and steel sheets. Santella et al. [1] successfully joined magnesium to zinc-coated steel sheets by USW. Shakil et al. [9] studied the microstructure and mechanical properties of welds of aluminum and stainless steel sheets produced by USW. Matsuoka and Imai [10] conducted research on joining aluminum and copper sheets by USW. The fatigue behavior of dissimilar ultrasonic spot welds in lap-shear specimens of magnesium AZ31B-H24 and hot-dipped-galvanized mild steel sheets was investigated by Franklin et al. [11]. For joining similar materials using ultrasonic weld bonding (USW+adhesive), Carboni and Moroni [12] conducted research on joining aluminum and magnesium sheets by ultrasonic weld bonding and found better fatigue performance than the ones made by USW alone. Lai et al. [13] explored the failure mode and fatigue behavior of ultrasonic weld-bonded specimens. However, no work has yet been reported on joining magnesium and steel sheets in details by ultrasonic weld bonding.

In this chapter, the failure modes and fatigue behaviors of ultrasonic spot welded, adhesive-bonded, and weld-bonded lap-shear specimens of dissimilar magnesium AZ31B-H24 sheets and galvanized mild steel sheets were examined. Ultrasonic spot welded, adhesive-bonded, and weld-bonded lap-shear specimens were first made from dissimilar magnesium AZ31B-H24 sheets and galvanized mild steel sheets. These lap-shear specimens were tested under quasi-static and cyclic loading conditions. Quasi-static and fatigue strengths of the three types of joints in lap-shear specimens were then obtained. Optical micrographs and SEM images of the failed joints after testing are also examined to identify the failure modes of the joints. Finally, conclusions are made based on the experimental results.

4.2. Experiment

Magnesium AZ31B-H24 and hot-dip-galvanized (HDG) mild steel sheets with the thicknesses of 1.6 mm and 0.8 mm, respectively, were used in this investigation. First, tensile tests were conducted. An extensometer was used for all specimens with a gauge length of 2 inches. The ASTM E8/E8M-11 tensile specimen standard for sheet materials was adopted. Figure 4.1(a) shows a schematic of a tensile specimen with the dimensions. Figure 4.1(b) shows the tensile specimens of the magnesium and steel sheets from the top to the bottom, respectively. The displacement rate was set at 2.54 mm/min (nominal strain rate of 0.00085 s^{-1}) for all tensile specimens. Three specimens were tested for each material. The stress-strain curves of the magnesium and steel sheets are shown in Figure 4.2. It is noted that the magnesium shows low strain hardening after yielding. The total elongation ranges from 11 to 21% for the three specimens. The steel sheet shows higher strain hardening after yielding. However, due to the strain limit of the extensometer, the tests were conducted up to the nominal strain of 40% for the steel sheets. Table 4.1 lists the elastic moduli, yield strengths, and tensile strengths of the magnesium and steel sheets.

Ultrasonic spot welded (USW), adhesive-bonded, and ultrasonic spot welded and adhesive-bonded (weld-bonded) lap-shear specimens were prepared for this study. Each lap-shear specimen was made by a 30 mm $\times$ 100 mm magnesium sheet and a 30 mm $\times$ 100 mm HDG steel sheet with a 30 mm $\times$ 40 mm overlap area. Figure 4.3(a) shows the top views of the USW, adhesive-bonded, and weld-bonded lap-shear specimens from the top to the bottom. Figures 4.3(b) to 4.3(d) show schematics of the top and the side views of USW, adhesive-bonded, and weld-bonded lap-shear specimens with doublers. The loading direction is shown by the

arrows. The adhesive is shown as the red lines in Figures 4.3(c) and 4.3(d) for the adhesive-bonded and weld-bonded lap-shear specimens.

For the USW lap-shear specimens, a Sonobond CLF 2500 single-transducer, wedge-reed ultrasonic welder was used for the ultrasonic spot welding. The sonotrode tip has a square face of 7 mm $\times$ 7 mm and the face has a grooved pattern. The ultrasonic spot welding was done with a power of 1500 W, an impedance setting of 6, and a welding time of 2.1 s. The spot welding was centered in the overlap area. Figure 4.3(a) shows the indentation of the sonotrode tip on the upper magnesium of the USW specimen. The microstructures of the sheets, the specimen preparation procedure, and the processing conditions for the USW lap-shear specimens were detailed in Santella et al. [1].

For the adhesive-bonded lap-shear specimens, the magnesium and steel sheets were bonded by BETAMATE™ 73305, a one-part heat-curing epoxy adhesive. Prior to applying the adhesive, two tapes were placed on the magnesium and steel sheets to form two pre-cracks between the sheets and the adhesive, as shown in Figure 4.3(a). The locations of the tape tips are indicated in Figure 4.3(c). The tape tips extend 5 mm from the edges of the overlap region. The adhesive thickness is controlled by placing a few 0.3-mm zirconia balls on the bonded surfaces. The specimen was heated to cure the epoxy. The area joined by the adhesive is 30 mm $\times$ 30 mm which is smaller than the overlap area of the two sheets.

For the weld-bonded lap-shear specimens, the adhesive was first applied and then the sheets were ultrasonic spot welded. The ultrasonic spot welding procedure is the same as that for the USW lap-shear specimens. Figure 4.3(a) also shows the indentation of the sonotrode tip on the upper magnesium sheet of the weld-bonded specimen. Two tapes were also placed on the magnesium and steel sheets to form two pre-cracks between the sheets and the adhesive, as those

for the adhesive-bonded specimen. Each welded specimen was then heated to the curing temperature to further join the rest of the overlap region.

Prior to testing, all three types of lap-shear specimens were sectioned through the center line parallel to the loading direction to observe the cross sections of the bonded regions. The lap-shear specimens were first tested with doublers under quasi-static loading conditions at a displacement rate of 5 mm/min. The average failure loads, defined as the averages of the maximum loads of the load-displacement curves obtained from the three types of lap-shear specimens, are listed in Table 4.2. The failure loads were used as the reference loads to determine the applied loads for the fatigue tests. The lap-shear specimens were then tested with doublers under cyclic loading conditions using an Instron servo-hydraulic fatigue testing machine with the load ratio of 0.1. The test frequency was 10 Hz. The tests were terminated when specimens were separated or transverse cracks from the welds became clearly visible. Figure 4.4 shows the load range as a function of the fatigue life for the three types of lap-shear specimens under cyclic loading conditions.

4.3. Quasi-static and fatigue test results

The results of the quasi-static tests indicate that the failure load per bonded area for USW lap-shear specimens is higher than that for adhesive-bonded lap-shear specimens. However, the adhesive-bonded and weld-bonded lap-shear specimens have almost the same failure load. This means the ultrasonic spot welds do not provide significant extra strength to the weld-bonded joints. This is possibly due to the poor weld quality since the thickness of the adhesive layer was controlled and limited by the zirconia balls between the magnesium and steel sheets such that the sheets cannot have good surface contact during the welding process. Under cyclic loading

conditions, the adhesive-bonded and weld-bonded specimens have longer fatigue lives than those of the USW specimens for given load ranges. Also, adhesive-bonded and weld-bonded lap-shear specimens have the same load range-life curves. This confirms that the ultrasonic spot weld in the weld-bonded lap-shear specimen does not contribute to additional fatigue lives for given load ranges.

4.4. Failure mode

4.4.1. USW lap-shear specimen

An overview of the failure modes of ultrasonic spot welds in the lap-shear specimen is schematically shown in Figure 4.5. Figure 4.5(a) shows the cross section near the ultrasonic spot weld. The thin solid lines represent the fracture surface or fatigue crack. Figure 4.5(b) is a table that summarizes the failure modes under quasi-static, low-cycle and high-cycle loading conditions. As schematically shown in the figure, the weld fails in a partial nugget pullout failure mode with the fracture surfaces A and B1 through the magnesium sheet under quasi-static loading conditions. Under low-cycle loading conditions, the weld fails in a kinked crack failure with a crack C growing through the magnesium sheet and partial nugget pullout with the fracture surface B2. Under high-cycle high-load loading conditions, the weld fails from a kinked crack C growing through the magnesium sheet and finally fails along the interface D. Under high-cycle low-load loading conditions, the weld fails in a kinked crack failure with a crack E and finally fails in a transverse crack growing through the specimen width.

Figure 4.6(a) shows the cross section of an untested specimen. As shown in the figure, the weld is asymmetric since the specimen was no constrained during the welding (Santella et al. [1]). Under quasi-static loading conditions, the ultrasonic spot welds failed in a partial nugget

pullout failure. Figure 4.6(b) shows the top view of the upper magnesium sheet and the top view of the lower steel sheet near a failed weld under quasi-static loading conditions from the top to the bottom. These failed welds have a partial nugget of the upper magnesium remaining on the lower steel sheets. Figure 4.6(c) shows the cross section of the failed weld in Figure 4.6(b) with a nearly full nugget remaining on the lower steel sheet. It is noted that the fracture took the shortest path from the interfacial crack tip to the corner of the indentation.

Under low-cycle loading conditions for the fatigue lives from 3×10^2 to 3×10^3 cycles, the specimens mainly failed in a kinked crack failure with the kink angle close to 90^o. These failed welds also have partial nuggets of the upper magnesium remaining on the lower steel sheets. Figure 4.6(d) shows the top view of the upper magnesium sheet and the top view of the lower steel sheet near a failed weld under low-cycle loading conditions at the fatigue life of 1.2×10^3 cycles under the load range of 2,844 N from the top to the bottom. Figure 4.6(e) shows the cross section of the failed weld in Figure 4.6(d) with a partial nugget remaining on the lower steel sheet. It is noted that the 90^o kinked crack did not grow all the way up through the magnesium sheet. It turned to the corner of the indentation in the half way due to the final fracture.

Under both low-cycle and high-cycle loading conditions, the dominant failure mode of the lap-shear specimens is the kinked fatigue cracks growing through the upper right magnesium sheets. Note that the low-cycle and high-cycle loading conditions in this study are defined based on the failure modes. Under high-cycle high-load loading conditions, the failure occurred from a kinked crack growing through the upper magnesium sheet but later failed along the interface without nugget pullout. Figure 4.6(f) shows the top view of the upper magnesium sheet and the top view of the lower steel sheet near a failed weld under high-cycle high-load loading conditions at the fatigue life of 8.0×10^3 cycles under the load range of 2,152 N from the top to

the bottom. Figure 4.6(g) shows the cross section of the failed weld in Figure 4.6(f). The kinked crack grew through the magnesium sheet but finally failed along the weld interface.

Under high-cycle low-load loading conditions for the fatigue lives from 5×10^4 to 10^5 cycles, the specimens mainly failed in a kinked crack failure. The kinked crack first grew through the magnesium sheet and then grew as two transverse cracks to the sides of the magnesium sheet. The welds finally failed with a transverse crack. Figure 4.6(h) shows the bottom view of the upper magnesium sheet and the top view of the lower steel sheet near a failed weld under high-cycle low-load loading conditions at the fatigue life of 5.6×10^4 cycles under the load range of 1,450 N from the top to the bottom. Figure 4.6(i) shows the cross section of the failed weld in Figure 4.6(h). As indicated from the experimental results, a kinked crack grew through the upper magnesium sheet and then the specimens failed in the transverse crack growth mode.

4.4.2. Adhesive-bonded lap-shear specimen

An overview of the failure modes of adhesive-bonded lap-shear specimens is schematically shown in Figure 4.7. Figures 4.7(a) and 4.7(b) show the cohesive failure near the interface between the steel and adhesive and the interfacial failure of the ultrasonic spot weld under quasi-static and low-cycle loading conditions, respectively. Cohesive failure means the adhesive-bonded specimen fails in the adhesive. Figure 4.7(c) shows the kinked crack failure in the magnesium sheet under high-cycle loading conditions.

Figure 4.8(a) shows the cross section of an untested specimen. Under quasi-static loading conditions, the adhesive-bonded joint failed in a cohesive failure near the interface between the steel and adhesive and the interfacial failure of the ultrasonic spot weld. Figure

4.8(b) shows the bottom view of the upper magnesium sheet and the top view of the lower steel sheet for a failed joint under quasi-static loading conditions from the top to the bottom. Figure 4.8(c) shows the cross section of the failed joint in Figure 4.8(b). A test on an adhesive-bonded lap-shear specimen under quasi-static loading conditions was interrupted at the load of 5,500 N (85% of the failure load). Figures 4.9(a) and 4.9(b) show the cross sections near the left and right tape tips, respectively, of the partially failed specimen. In Figure 4.9(a), the crack grew from the left tape tip due to the extensive plastic deformation of the steel sheet. As indicated in Figure 4.9(b), no crack growth is observed near the right tape tip. Figure 4.7(a) shows a schematic of the near interface cohesive failure of the specimen under quasi-static loading conditions. The crack appears to grow in the adhesive but close to the interface between the steel and adhesive.

Under low-cycle loading conditions for the fatigue lives from 3×10^3 to 10^4 cycles, the joints also failed in a near interface cohesive failure. Figure 4.8(d) shows the bottom view of the upper magnesium sheet and the top view of the lower steel sheet for a failed joint under low-cycle loading conditions at the fatigue life of 6.3×10^3 cycles under the load range of 5,200 N from the top to the bottom. In Figure 4.8(d), the crack on the left side grew initially about 10 mm in the partial cohesive failure due to the high maximum load of the first cycle. The failure mode due to the first cycle shows the partial cohesive failure (partial interfacial and partial cohesive failure) possibly due to the strain rate effect because the feature of the fracture surface is different from that of the near interface cohesive failure observed in the specimen under quasi-static loading conditions. During the following fatigue cycles, the crack grew from the new crack front which corresponds to the starter crack tip as marked in Figure 4.7(b). Figure 4.8(e) shows the cross section of the failed joint in Figure 4.8(d). An interrupted test of an adhesive-

bonded lap-shear specimen was conducted under low-cycle loading conditions at the fatigue life of 1,500 cycles under the load range of 5,200 N. Figures 4.9(c) and 4.9(d) show the cross sections near the left and right tape tips, respectively, of the partially failed specimen. In Figure 4.9(c), the crack grew from the left tape tip. As indicated in Figure 4.9(d), no crack growth is observed near the right tape tip. Figure 4.7(b) shows a schematic of the near interface cohesive failure of the specimen under low-cycle loading conditions. Note the failure mode changes from partial cohesive failure to near interface cohesive failure near the beginning of the cyclic crack growth.

Under high-cycle loading conditions for the fatigue lives from 10^4 to 10^5 cycles, the specimens failed in a kinked crack failure. Figure 4.8(f) shows the bottom view of the upper magnesium sheet and the top view of the lower steel sheet for a failed joint under high-cycle loading conditions at the fatigue life of 3.6×10^4 cycles under the load range of 4,222 N from the top to the bottom. Figure 4.8(g) shows the cross section of the failed joint in Figure 4.8(f). A kinked crack was initiated from the tape tip and grew up at an angle of about 30°. Once it reached a critical kink length, the kinked crack turned to 90° and grew into the upper magnesium sheet. The 30° kinked crack was observed in all the specimens failed in the magnesium sheet.

Figures 4.10(a) to 4.10(d) show the fracture surfaces of the upper right magnesium sheets of four failed specimens under different load ranges. Note that significant variation in the geometries of the kinked cracks was observed from these fracture surfaces. However, there is a general trend of increasing kink length with decreasing load range, as indicated by the red arrows in the figure. Also, the 90° crack after the 30° kinked crack was observed for all the specimens, as indicated by the white arrows in the figure. Note that the geometries of the 90° cracks also vary significantly across the fracture surfaces. Finally, when the average stress in the remaining

magnesium cross section reached about the tensile strength of the magnesium, the magnesium sheets appeared to fail in shear with various angles inclined to the surface of the specimen sheets as observed in those of the failed magnesium sheet specimen under uniaxial tensile loading conditions.

Figures 4.11(a) and 4.11(b) show SEM images of the 30^{o} kinked crack surface of the upper right magnesium sheet of a failed specimen at low and high magnifications, respectively, under cyclic loading conditions at the fatigue life of 2.5×10^{4} cycles under the load range of 4,080 N. The fatigue striations can be clearly seen in Figure 4.11(b) and are in general perpendicular to the crack growth direction. Figures 4.11(c) and 4.11(d) show SEM images of the 90^{o} crack surface of the upper right magnesium sheet of a failed specimen at low and high magnifications, respectively, under cyclic loading conditions at the fatigue life of 2.5×10^{4} cycles under the load range of 4,080 N. It is noted that no dimple was observed on the fracture surface. The formation of the 90^{o} crack is possibly due to reaching the fracture resistance of the magnesium [14]. Figure 4.11(e) shows an SEM image of the final fracture surface of the upper right magnesium sheet of a failed specimen under cyclic loading conditions at the fatigue life of 2.5×10^{4} cycles under the load range of 4,080 N. Figure 4.11(e) shows dimpled ductile fracture surface.

Note that Figure 4.7(c) shows a schematic of the kinked crack failure under high-cycle loading conditions. It was observed that the left crack on the steel side also grew a bit but did not cause the final failure for the load ranges that are close to those under low-cycle loading conditions. Note that the low-cycle and high-cycle loading conditions in this study are defined based on the failure modes.

Under both quasi-static and cyclic loading conditions, large plastic deformation in the steel sheet due to bending near the crack tip was observed. As the crack grew, the deformed

region moved along with the crack front under both quasi-static and cyclic loading conditions. Figures 4.12(a) and 4.12(b) show the bottom views of the lower steel sheets under quasi-static and low-cycle loading conditions, respectively. Figure 4.12(a) shows the plastic deformation patterns of the steel sheets along the crack fronts in the failed and partially failed specimens under quasi-static loading conditions. The partially failed specimen was under the load at 85% of the failure load. Figure 4.12(b) shows the plastic deformation patterns of the steel sheets along the crack fronts in the failed specimen under low-cycle loading conditions at the fatigue life of 3,462 cycles under the load range of 5,560 N and a partially failed specimens under low-cycle loading conditions at the fatigue life of 1,500 cycles under the load range of 5,200 N. As shown in both figures, the plastic deformation along the crack fronts of the failed specimens is closer to the right compared to that for the partially failed specimen. Note that the crack grew from the left tape tip to the right tape tip for both cases. Finally, it is noted that a small amount of necking was also observed in the steel sheets of the failed specimens in the width direction.

4.4.3. USW + adhesive (weld-bonded) lap-shear specimen

An overview of the failure modes of weld-bonded lap-shear specimens is schematically shown in Figure 4.13. Figures 4.13(a) and 4.13(b) show the cohesive failure near the interface between the steel and adhesive under quasi-static and low-cycle loading conditions, respectively. Figure 4.13(c) shows the kinked crack failure in the magnesium sheet under high-cycle loading conditions.

Figure 4.14(a) shows the cross section of the joint of an untested specimen. Under quasi-static loading conditions, the weld-bonded joint failed in a cohesive failure near the interface between the steel and adhesive. Figure 4.14(b) shows the bottom view of the upper magnesium

sheet and the top view of the lower steel sheet for a failed joint under quasi-static loading conditions from the top to the bottom. The failure mode is similar to that for the adhesive-bonded lap-shear specimen in Figure 4.8(b). Figure 4.14(b) shows the residual adhesive on the interface of the ultrasonic spot weld. The residual adhesive suggests that the weld quality was not good and did not provide good bonding. Figure 4.14(c) shows the cross section of the failed joint in Figure 4.14(b). A test on a weld-bonded lap-shear specimen under quasi-static loading conditions was interrupted at the load of 5,500 N (85% of the failure load). Figures 4.15(a) and 4.15(b) show the cross sections near the left and right tape tips, respectively, of the partially failed specimen. In Figure 4.15(a), the crack grew from the left tape tip toward the right due to the extensive plastic deformation of the steel sheet. As indicated in Figure 4.15(b), no crack growth is observed near the right tape tip. Figure 4.13(a) shows a schematic of the near interface cohesive failure of the specimen under quasi-static loading conditions. The crack grows in the adhesive but close to the interface between the steel and adhesive. Figure 4.13(a) also shows an interfacial failure for the ultrasonic spot weld.

Under low-cycle loading conditions for the fatigue lives from 3×10^3 to 3×10^4 cycles, the adhesive failed in a near interface cohesive failure and the ultrasonic spot weld failed in an interfacial failure. Figure 4.14(d) shows the bottom view of the upper magnesium sheet and the top view of the lower steel sheet for a failed joint under low-cycle loading conditions at the fatigue life of 1.4×10^4 cycles under the load range of 5,138 N from the top to the bottom. Figure 4.14(d) shows that the crack on the left side grew initially about 10 to 20 mm in the partial cohesive failure due to the high maximum load of the first cycle. The failure mode due to the first cycle shows the partial cohesive failure (partial interfacial and partial cohesive failure) possibly due to the strain rate effect because the feature of the fracture surface is different from

that of the near interface cohesive failure observed in the specimen under quasi-static loading conditions as discussed earlier. During the following fatigue cycles, the crack grew from the new crack front which corresponds to the starter crack tip as marked in Figure 4.14(b). Figure 4.14(e) shows the cross section of the failed joint in Figure 4.14(d). Note that some residual adhesive on the interface of the ultrasonic spot weld can be seen. An interrupted test of a weld-bonded lap-shear specimen was conducted under low-cycle loading conditions at the fatigue life of 2,000 cycles under the load range of 5,240 N. Figures 4.15(c) and 4.15(d) show the cross sections near the left and right tape tips, respectively, of the partially failed specimen. In Figure 4.15(c), the crack grew from the left tape tip. As indicated in Figure 4.15(d), no crack growth is observed on the right tape tip. Figure 4.13(b) shows a schematic of the near interface cohesive failure and the interfacial failure of the ultrasonic spot weld of the specimen under low-cycle loading conditions. Note the failure mode changes from the partial cohesive failure to the near interface cohesive failure near the beginning of the cyclic crack growth.

Under high-cycle loading conditions for the fatigue lives from 10^4 to 10^5 cycles, the specimens failed in a kinked crack failure. Figure 4.14(f) shows the bottom view of the upper magnesium sheet and the top view of the lower steel sheet for a failed joint under high-cycle loading conditions at the fatigue life of 7.1×10^5 cycles under the load range of 3,202 N from the top to the bottom. Figure 4.14(g) shows the cross section of the failed joint in Figure 4.14(f). A kinked crack was initiated from the tape tip and grew up into the magnesium sheet. A kinked crack initiated from the tape tip and grew up at an angle of about 30^o. Once it reached a critical kink length, the kinked crack turned to 90^o and grew into the upper magnesium sheet. Note that Figure 4.13(c) shows a schematic of the kinked crack failure under high-cycle loading conditions. It is observed that the left crack on the steel side also grew a bit but did not cause the final failure

for the load ranges close to those under low-cycle loading conditions. Note that the low-cycle and high-cycle loading conditions in this study are defined based on the failure modes.

Under both quasi-static and cyclic loading conditions, large plastic deformation in the steel sheet due to bending near the crack tip was observed. As the crack grew, the deformed region moved along with the crack front under both quasi-static and cyclic loading conditions. Figures 4.16(a) and 4.16(b) show the bottom views of the lower steel sheets under quasi-static and low-cycle loading conditions, respectively. Figure 4.16(a) shows the plastic deformation patterns of the steel sheets along the crack fronts in the failed and partially failed specimens under quasi-static loading conditions. The partially failed specimen was under the load at 85% of the failure load. Figure 4.16(b) shows the plastic deformation patterns of the steel sheets along the crack fronts in the failed specimen under low-cycle loading conditions at the fatigue life of 4,628 cycles under the load range of 5,140 N and a partially failed specimens under low-cycle loading conditions at the fatigue life of 2,000 cycles under the load range of 5,240 N. As shown in both figures, the plastic deformation along the crack fronts of the failed specimens is closer to the right compared to that for the partially failed specimen. Note that the crack grew from the left tape tip to the right tape tip for both cases. Finally, it is noted that a small amount of necking was also observed in the steel sheets of the failed specimens in the width direction.

4.5. Conclusion

The ultrasonic spot weld appeared not to provide extra strength to the weld-bonded lap-shear specimen under quasi-static and cyclic loading conditions. The quasi-static and fatigue strengths of adhesive-bonded and weld-bonded lap-shear specimens appeared to be the same. For the ultrasonic spot welded lap-shear specimens, the optical micrographs indicated that failure

mode changes from the partial nugget pullout mode under quasi-static and low-cycle loading conditions to the kinked crack failure under high-cycle loading conditions. For the adhesive-bonded lap-shear specimens, the optical micrographs indicated that failure mode changes from the near interface cohesive failure under quasi-static and low-cycle loading conditions to the kinked crack growth mode under high-cycle loading conditions. For the weld-bonded lap-shear specimens, the optical micrographs indicated that failure mode changes from the near interface cohesive failure through the adhesive and interfacial failure through the spot weld under quasi-static and low-cycle loading conditions to the kinked crack failure under high-cycle loading conditions.

Table 4.1. Elastic moduli, yield strengths, and tensile strengths of the magnesium and steel sheets tested under quasi-static loading conditions at a displacement rate of 5 mm/min.

	Elastic modulus (GPa)	Yield strength (MPa)	Tensile strength (MPa)
AZ31	45	260	318
HDG mild steel	210	145	293

Table 4.2. Failure loads of the lap-shear specimens tested under quasi-static loading conditions at a displacement rate of 5 mm/min.

	Failure load (N)
USW	4,040 ± 13
Adhesive-bonded	6,524 ± 65
Weld-bonded	6,403 ± 61

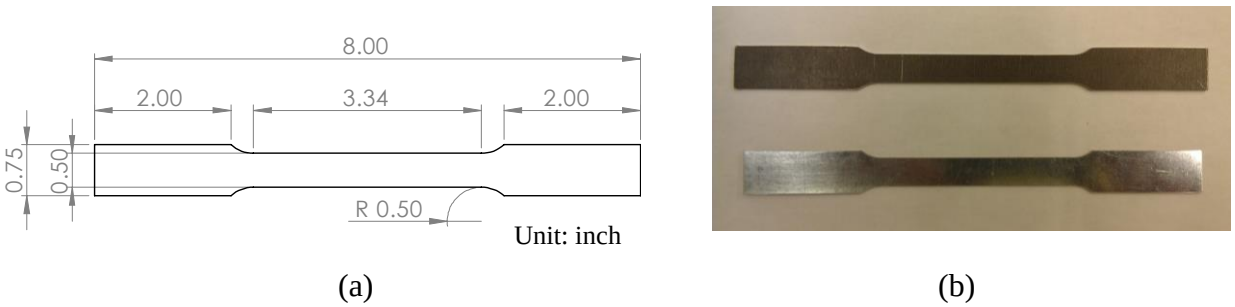

(a) (b)

Figure 4.1. (a) A schematic of a tensile specimen with the dimensions (ASTM E8/E8M-11) and (b) a picture of the tensile specimens of the magnesium and steel sheets from the top to the bottom.

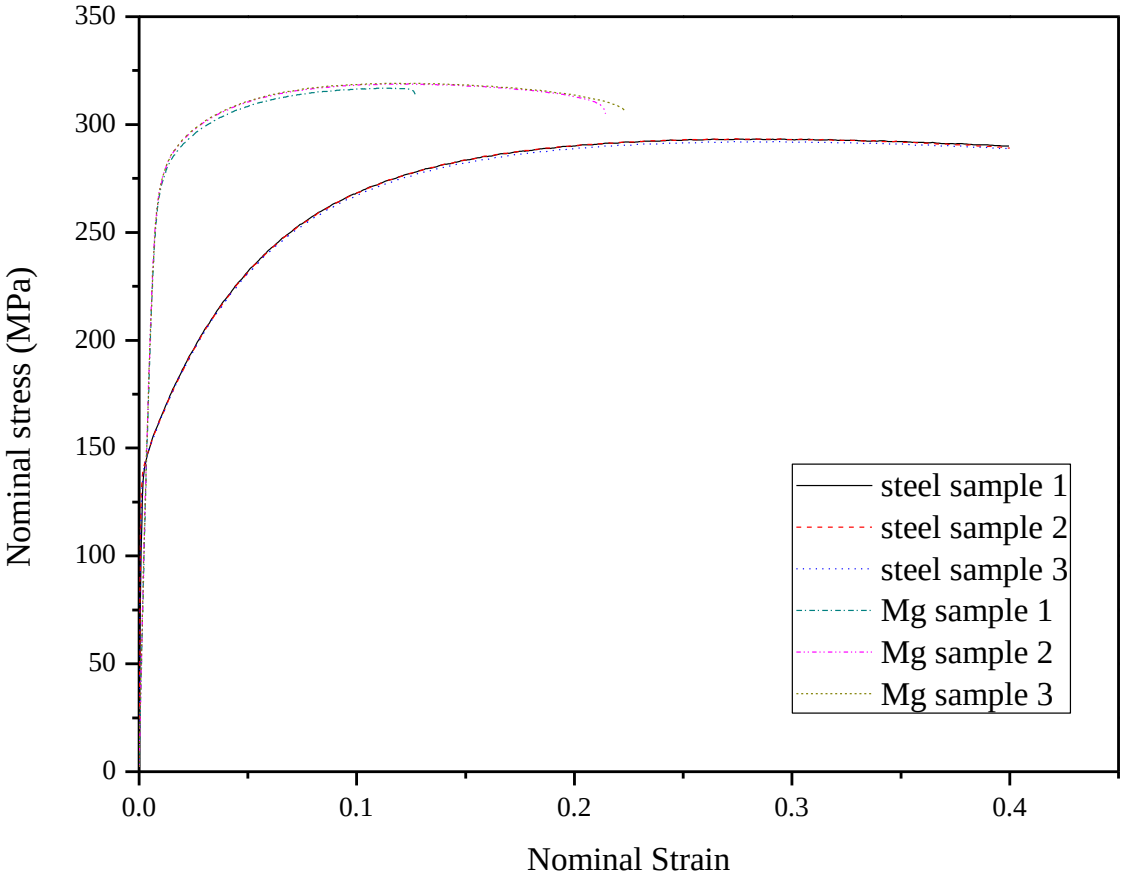

Figure 4.2. Nominal tensile stress-strain curves of the magnesium and steel sheets tested at a displacement rate of 2.54 mm/min (nominal strain rate of 0.00085 s^{-1}).

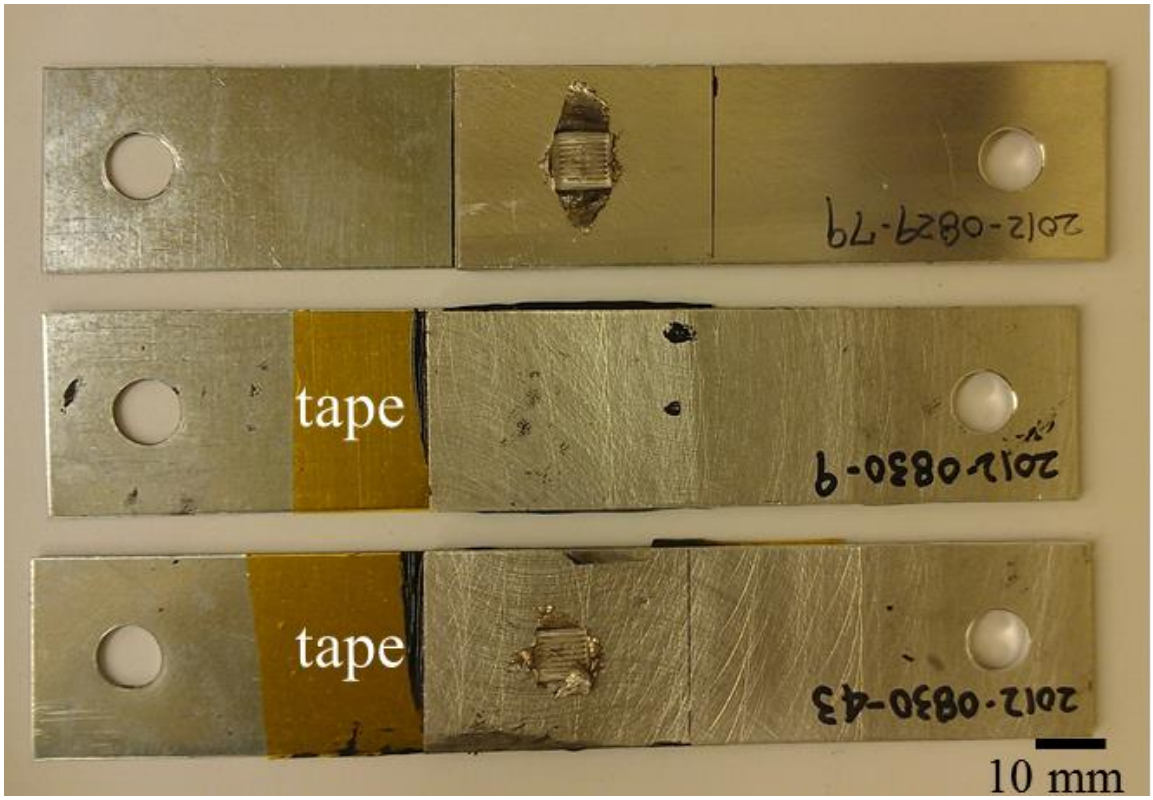

4.3(a)

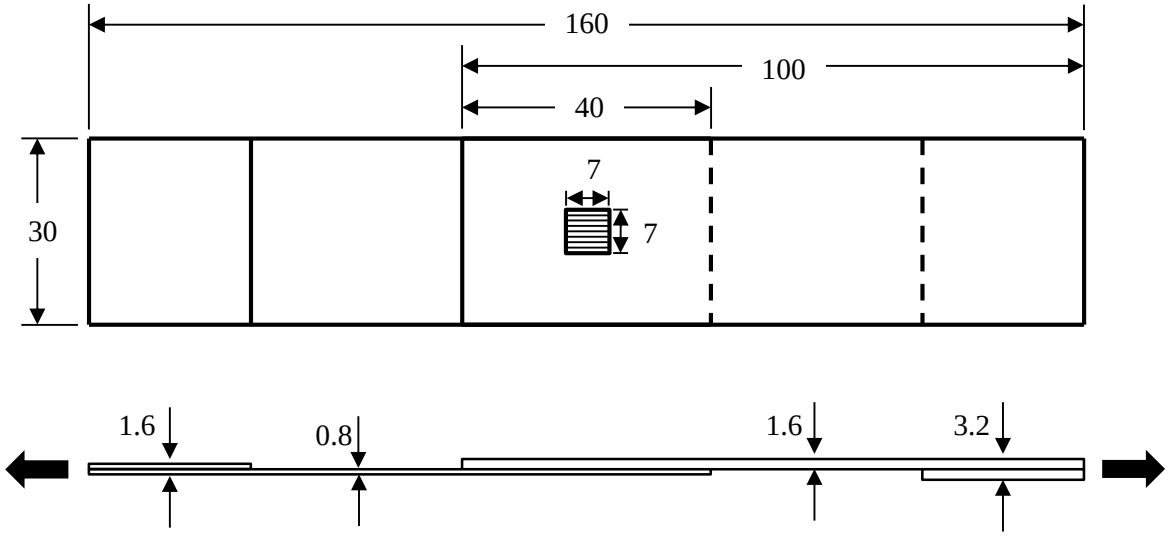

Unit: mm

4.3(b)

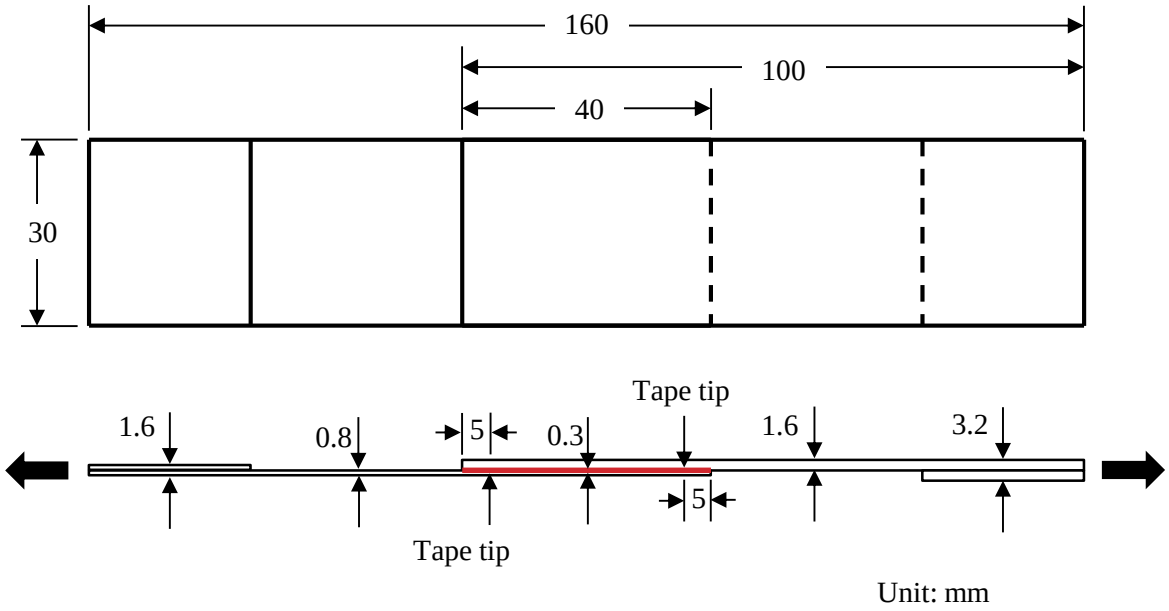

4.3(c)

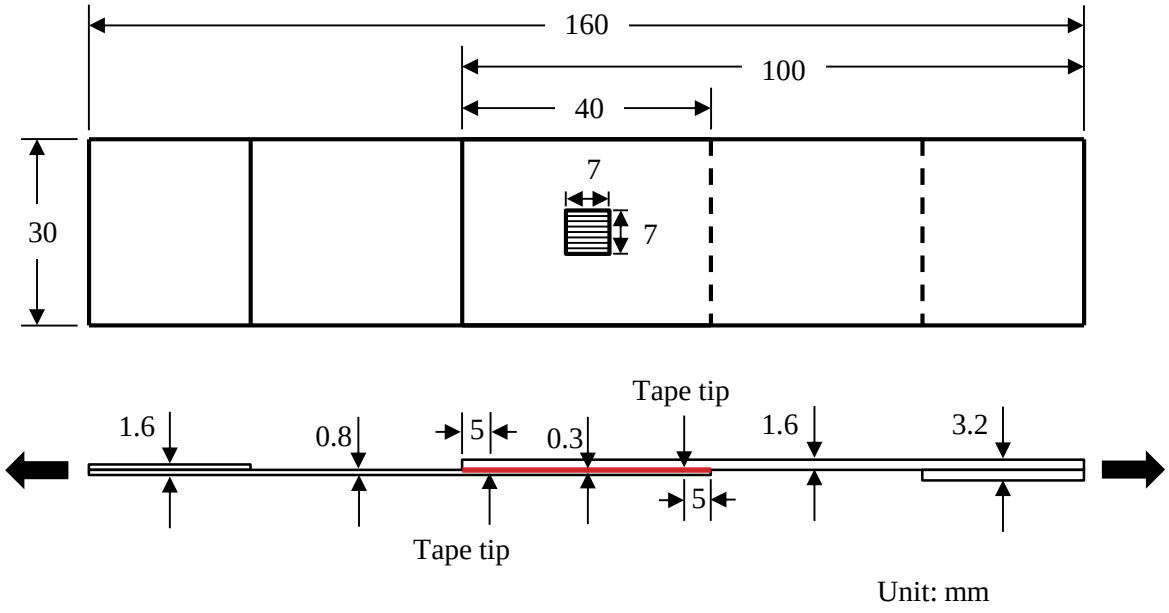

4.3(d)

Figure 4.3. (a) A top view of USW, adhesive-bonded, and weld-bonded lap-shear specimens, from the top to the bottom. (b)-(d) Schematics of the top and the side views of the USW, adhesive-bonded, and weld-bonded specimens with the loading directions shown by the arrows. The red lines represent the adhesive.

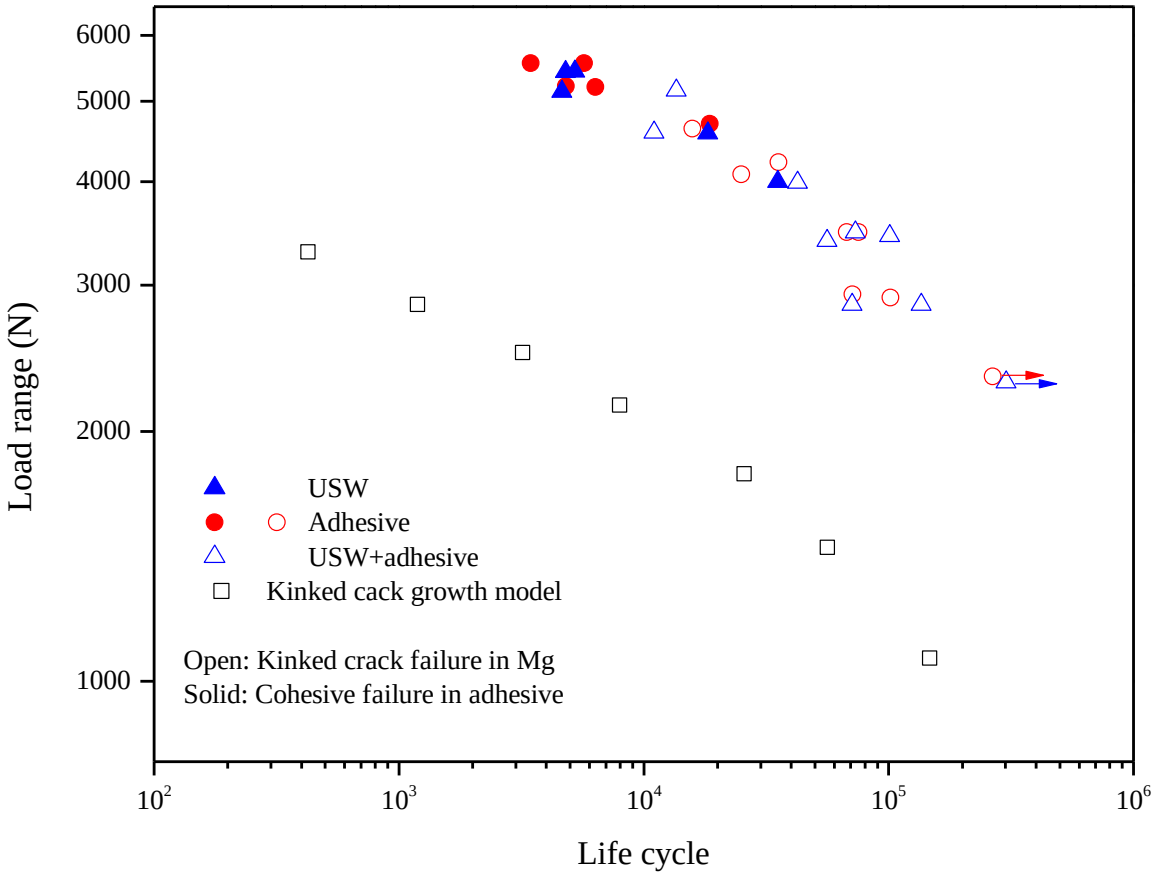

Figure 4.4. The experimental results of the fatigue tests for the three types of lap-shear specimens and the fatigue life estimations based on a kinked fatigue crack growth model for the adhesive-bonded and weld-bonded lap-shear specimens.

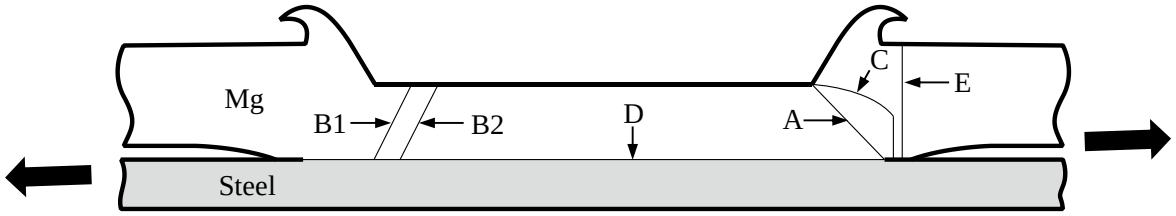

(a)

	Failure mode
Quasi-static (QS)	A→B1, partial nugget pullout
Low-cycle (LC)	C→B2, kinked crack and partial nugget pullout
High-cycle high-load (HC-HL)	E→D, kinked crack and interfacial failure
High-cycle low-load (HC-LL)	E, kinked crack and transverse crack

(b)

Figure 4.5. (a) A schematic of the cross section near the ultrasonic spot weld and (b) the failure modes of ultrasonic spot welds under quasi-static, low-cycle, high-cycle high-load, and high-cycle low-load loading conditions.

4.6(a)

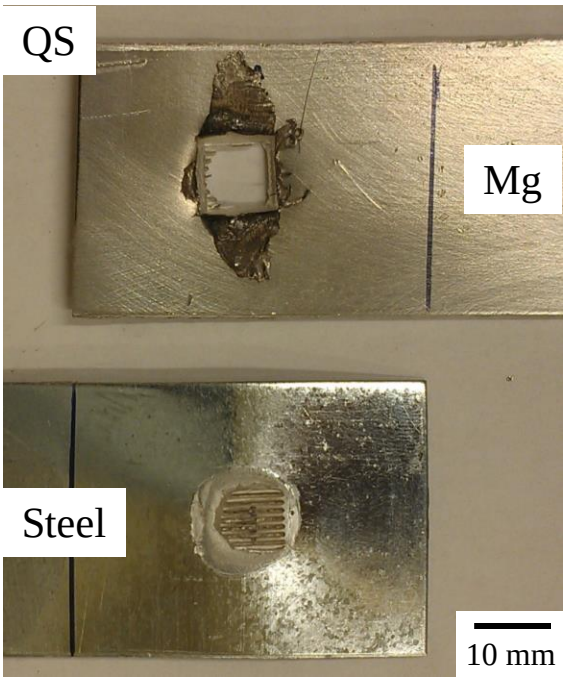

4.6(b)

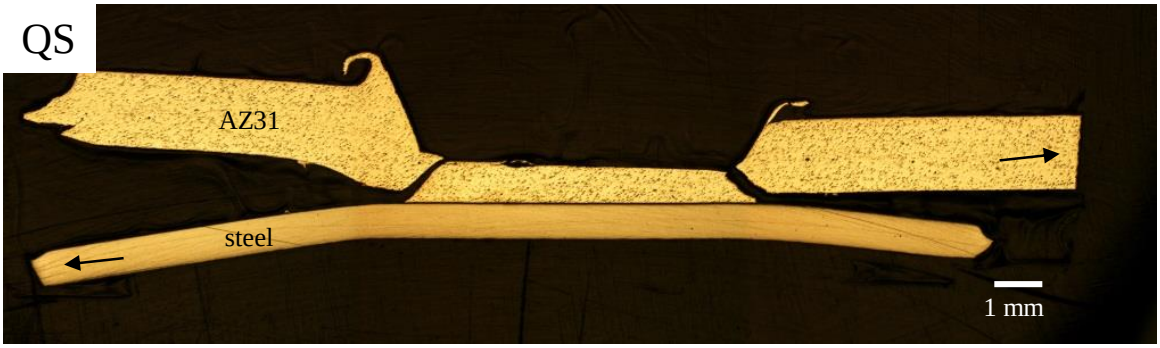

4.6(c)

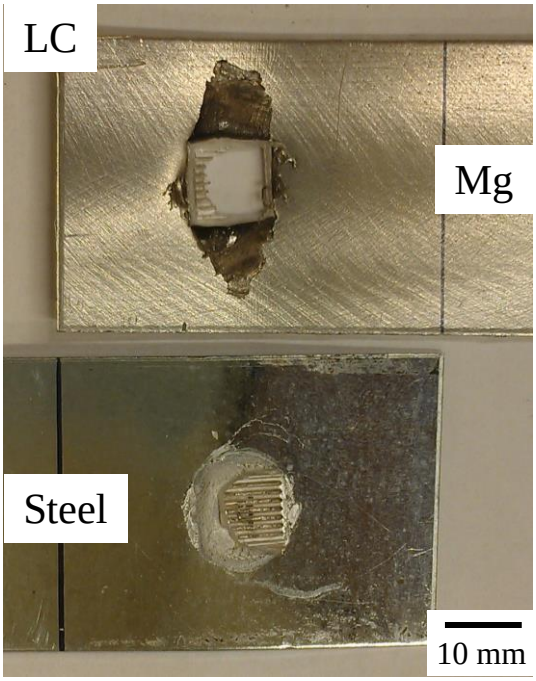

4.6(d)

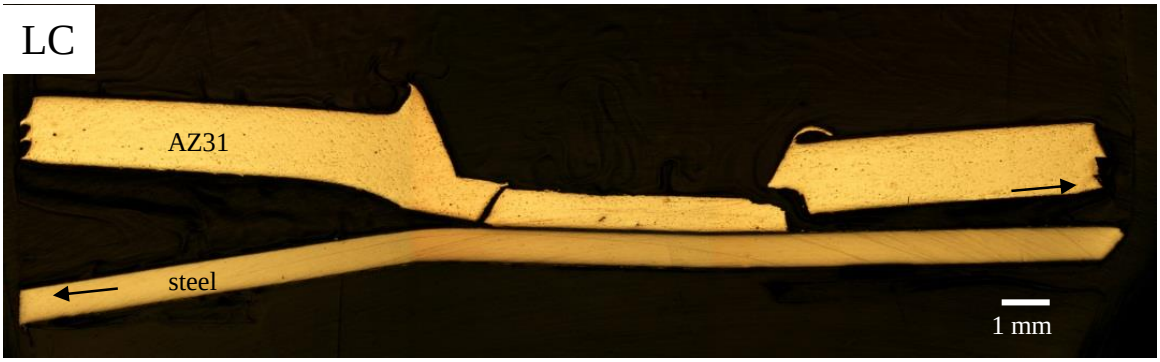

4.6(e)

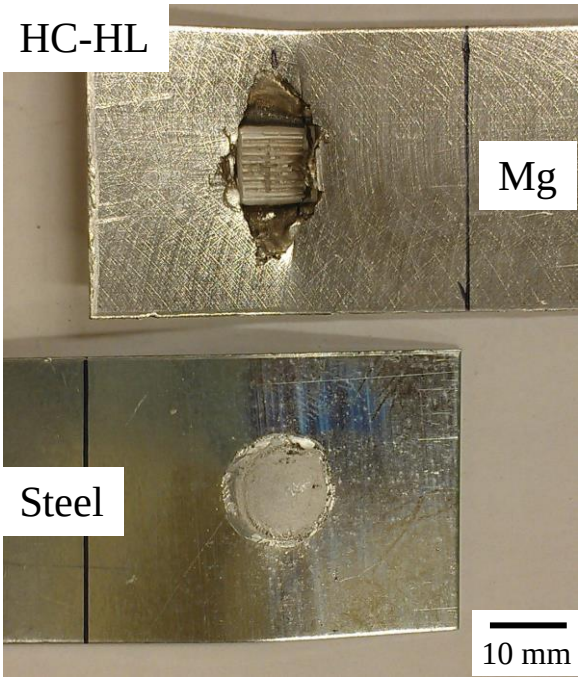

4.6(f)

4.6(g)

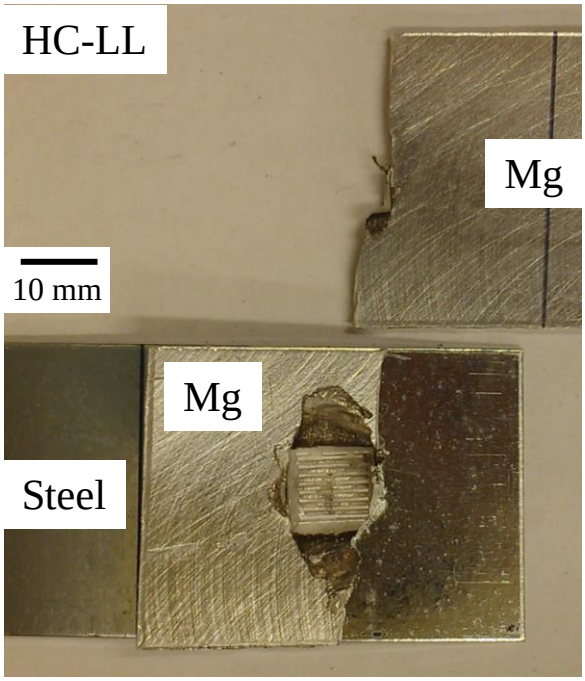

4.6(h)

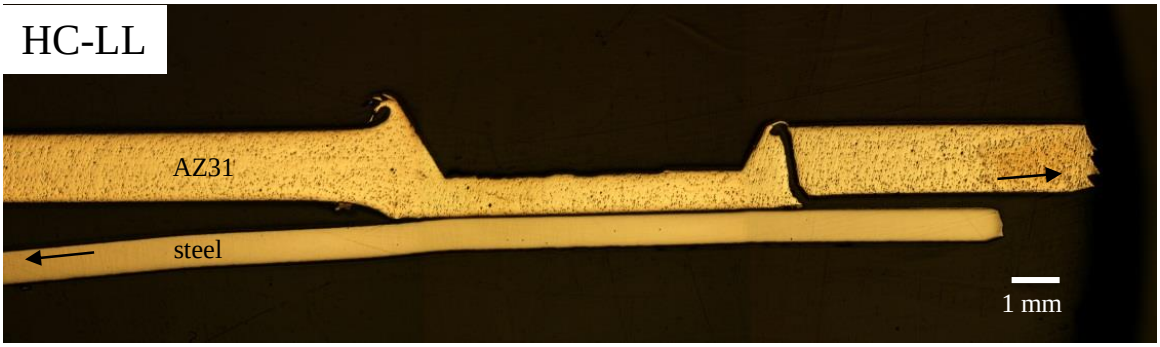

4.6(i)

Figure 4.6. (a) An optical micrograph of the symmetry cross section near an ultrasonic weld in an untested USW lap-shear specimen. Images near the failed welds and the corresponding optical micrographs of the symmetry cross sections of the welds in the USW lap-shear specimens (b, c) under quasi-static loading condition, (d, e) under low-cycle loading conditions at the fatigue life of 1.2×10^3 cycles under the load range of 2,844 N, (f, g) under high-cycle high-load loading conditions at the fatigue life of 8.0×10^3 cycles under the load range of 2,152 N, and (h, i) under high-cycle low-load loading conditions at the fatigue life of 5.6×10^4 cycles under the load range of 1,450 N. The arrows indicate the loading directions.

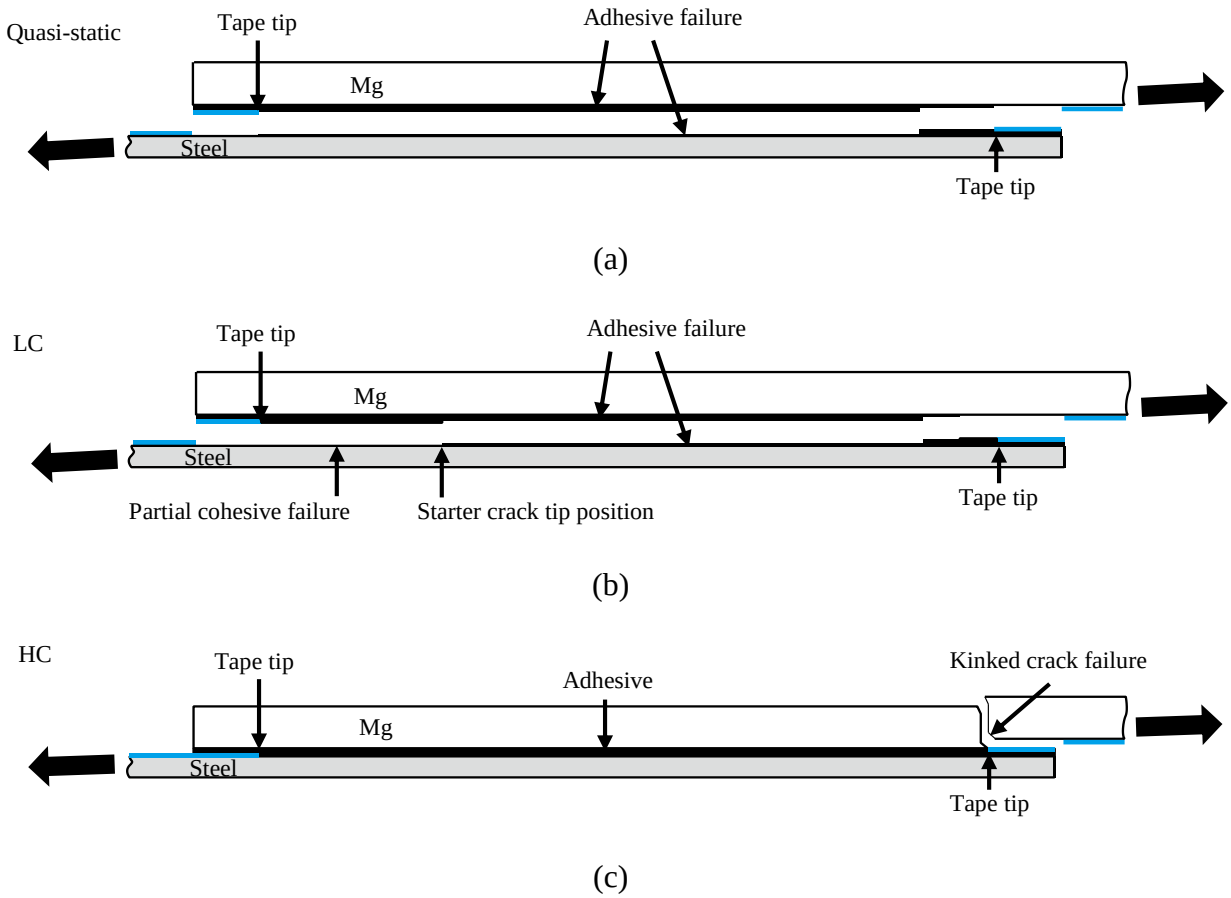

Figure 4.7. Schematics of the cohesive failure mode between the steel and the adhesive (a) under quasi static loading conditions and (b) under low-cycle loading conditions and (c) the kinked crack failure mode in the magnesium sheet under high-cycle loading conditions for adhesive-bonded lap-shear specimens. The blue lines indicate the tapes.

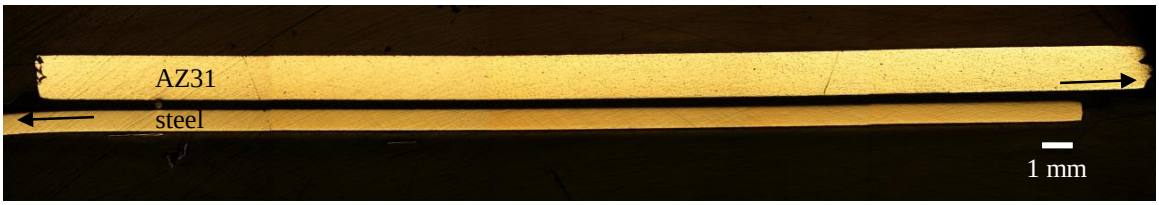

4.8(a)

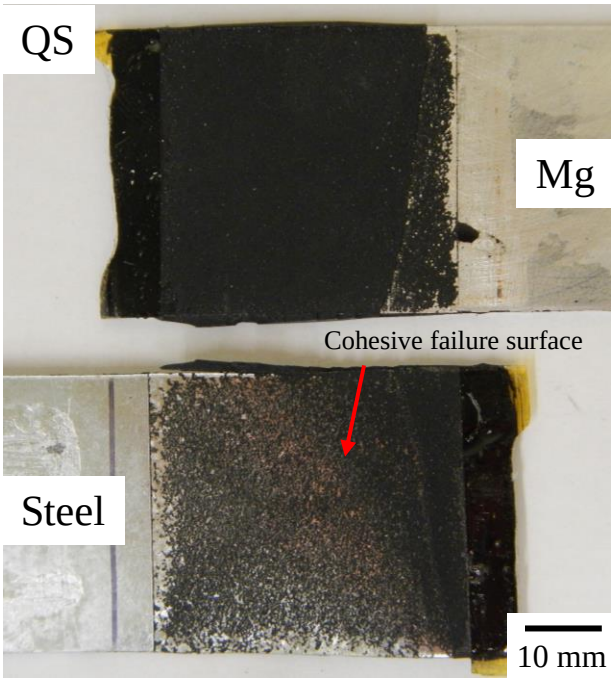

4.8(b)

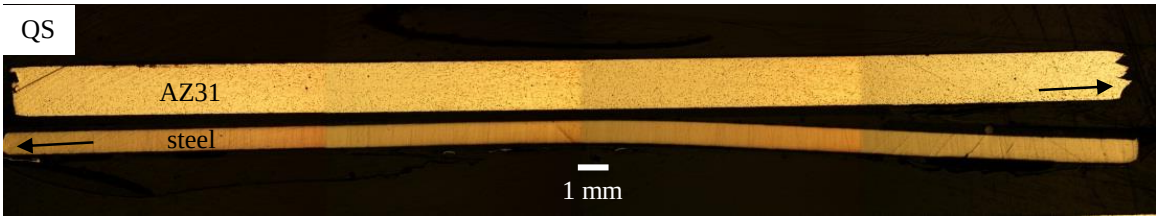

4.8(c)

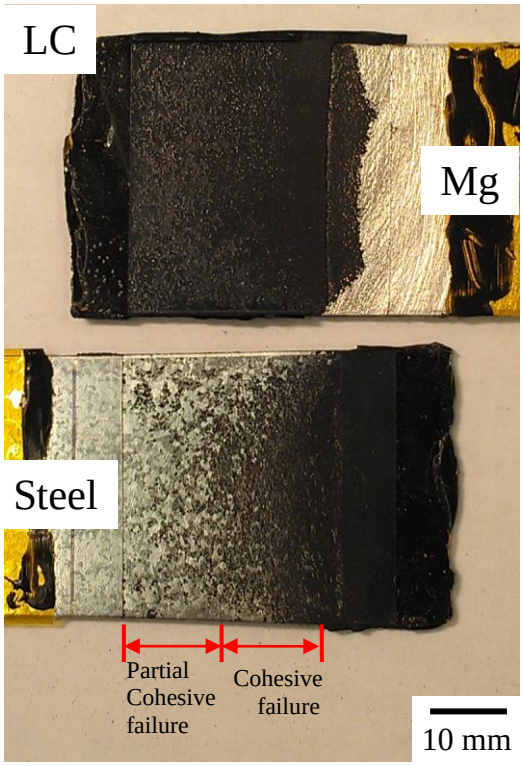
LC
Mg
Steel
Partial
Cohesive
failure
Cohesive
failure
10 mm

4.8(d)

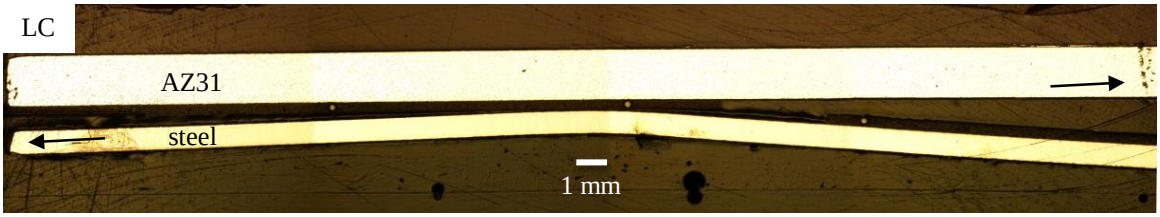
LC
AZ31
steel
1 mm

4.8(e)

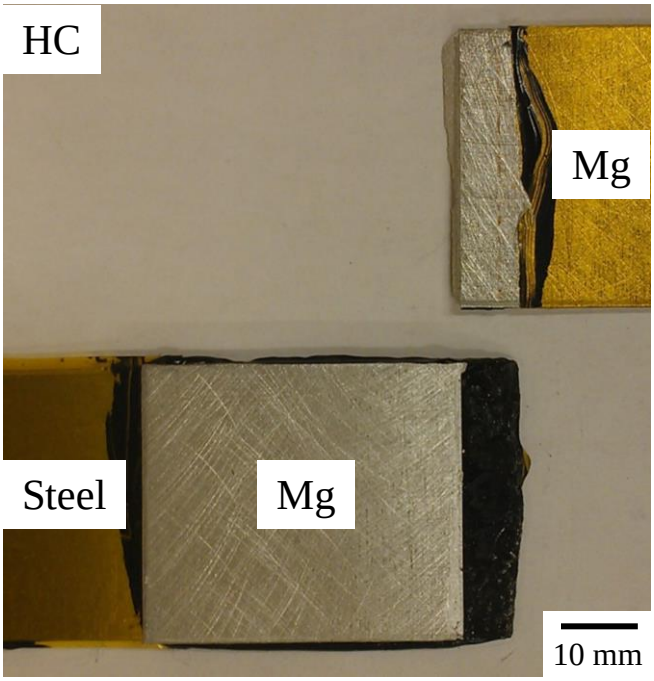

4.8(f)

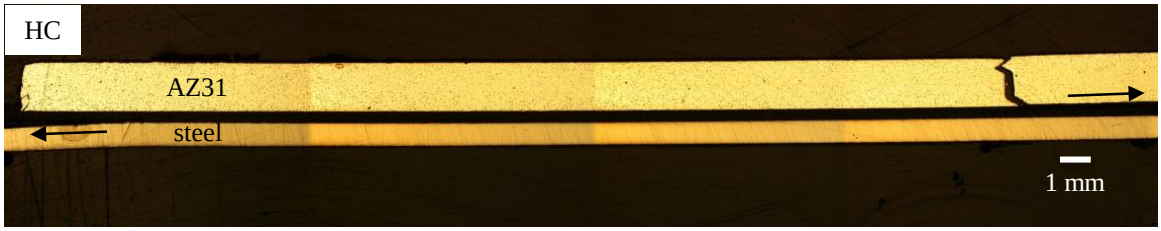

4.8(g)

Figure 4.8. (a) An optical micrograph of the symmetry cross section near the joint in an untested adhesive-bonded lap-shear specimen. Images near the failed joints and the corresponding optical micrographs of the symmetry cross sections of the joints in the adhesive-bonded lap-shear specimens (b, c) under quasi-static loading condition, (d, e) under low-cycle loading conditions at the fatigue life of 6.3×10^{3} cycles under the load range of 5,200 N, and (f, g) under high-cycle loading conditions at the fatigue life of 3.6×10^{4} cycles under the load range of 4,222 N. The arrows indicate the loading directions.

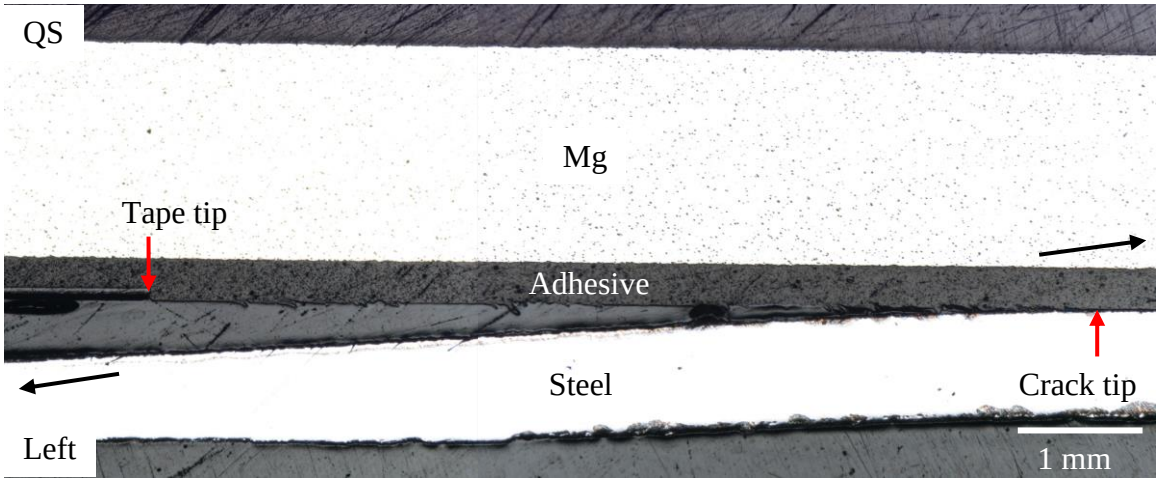
QS
Mg
Tape tip
Adhesive
Steel
Crack tip
Left
1 mm

4.9(a)

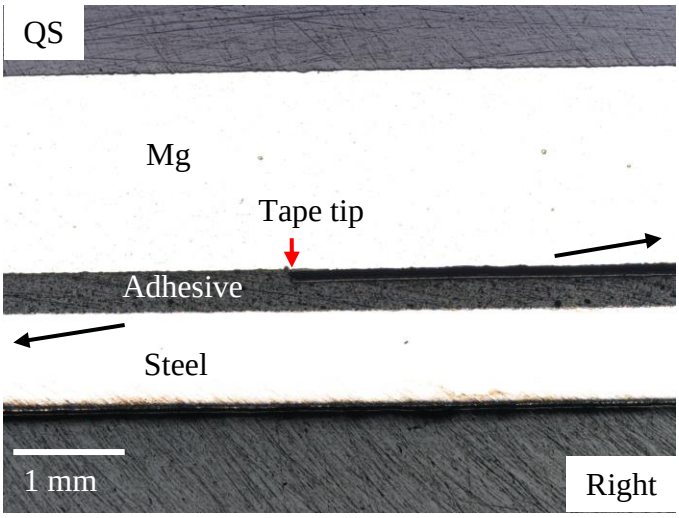
QS
Mg
Tape tip
Adhesive
Steel
1 mm
Right

4.9(b)

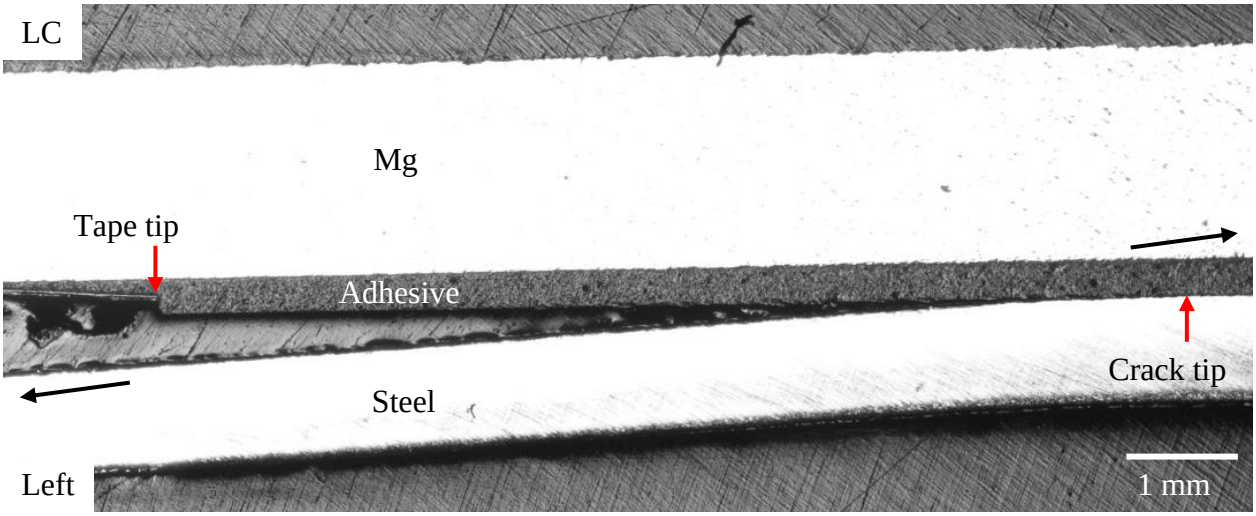

4.9(c)

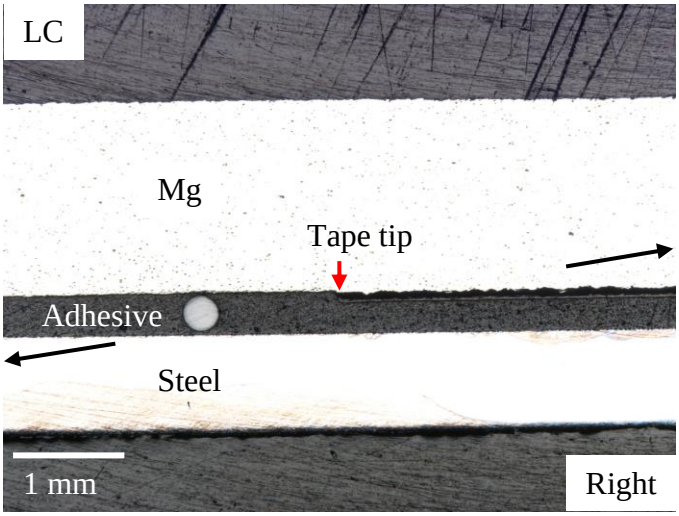

4.9(d)

Figure 4.9. The cross sections near the (a) left and (b) right tape tips of a partially failed adhesive-bonded lap-shear specimen under quasi-static loading conditions at the load of 5,500 N (85% of the failure load) and the cross sections near the (c) left and (d) right tape tips of a partially failed adhesive-bonded lap-shear specimen under cyclic loading conditions at the fatigue life of 1,500 cycles under the load range of 5,200 N. The black arrows indicate the loading directions.

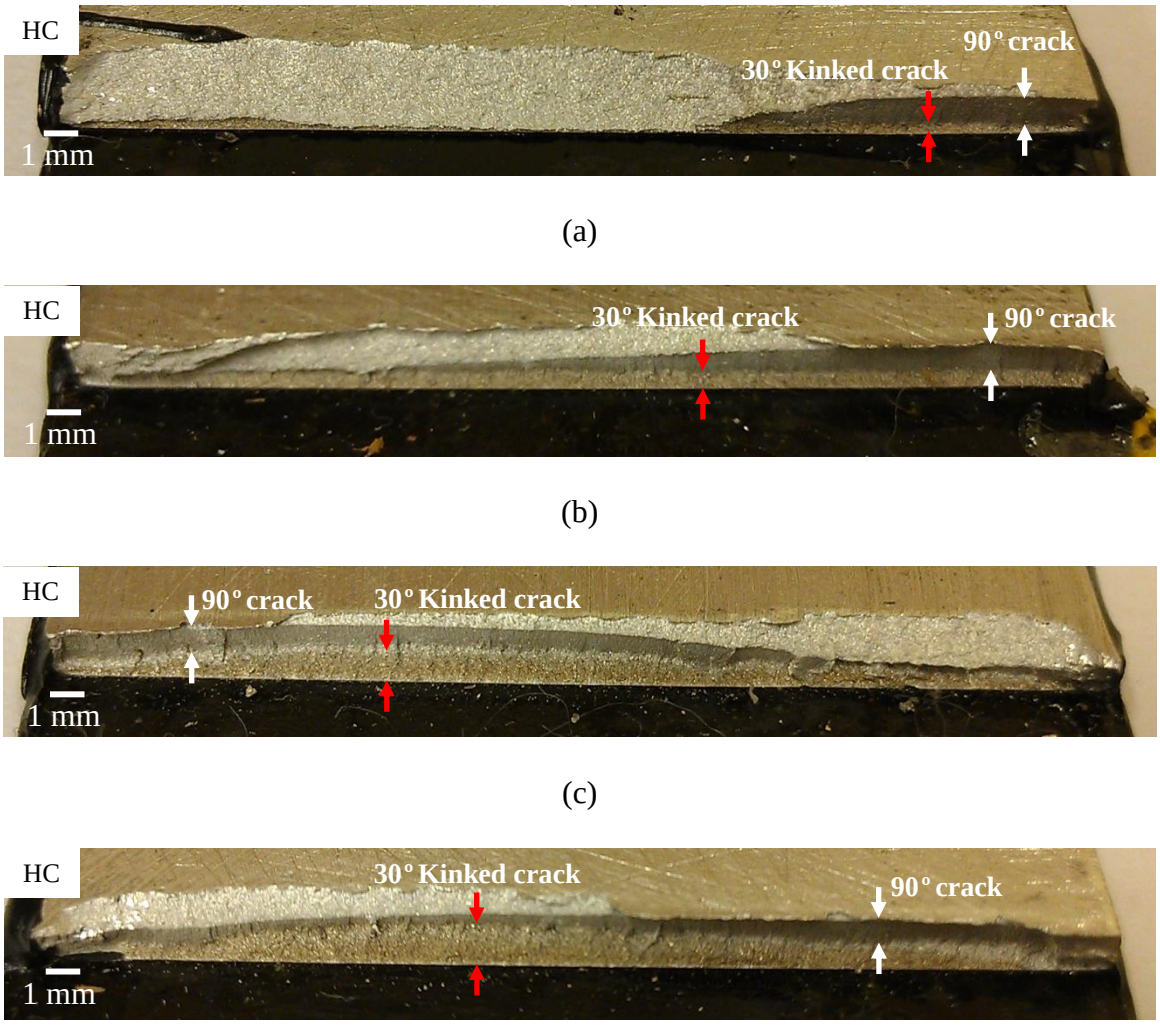

Figure 4.10. Fracture surfaces of the upper right magnesium sheets of failed adhesive-bonded lap-shear specimens under load ranges of (a) 4,630 N, (b) 4,080 N, (c) 3,480 N, and (d) 2,900 N. The red arrows indicate the 30° kinked cracks and the white arrows indicate the 90° cracks.

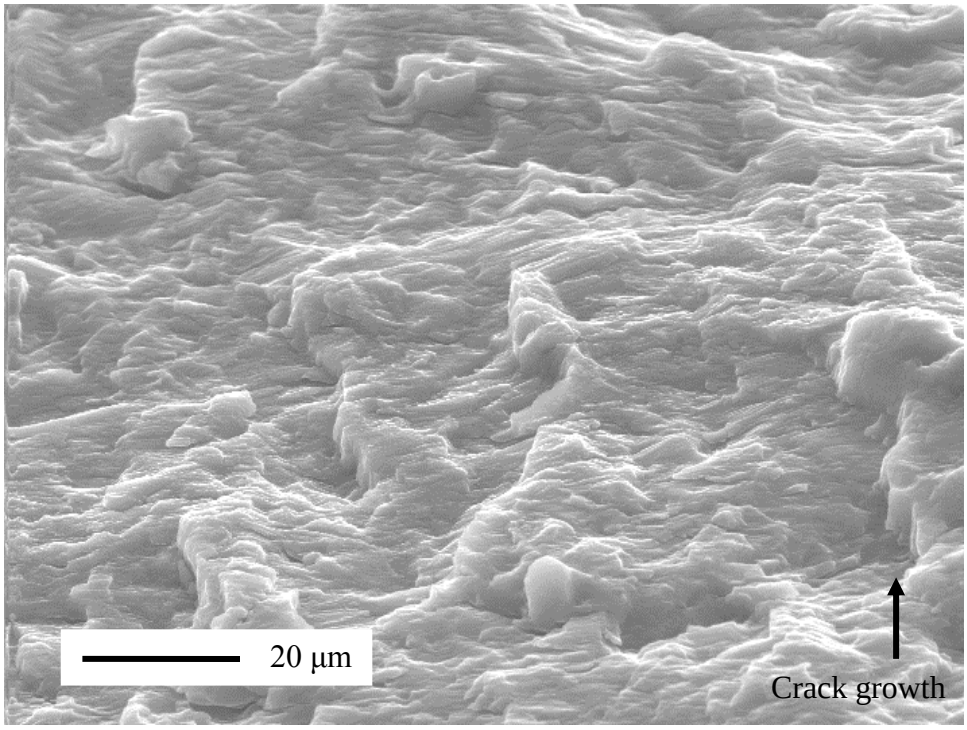

4.11(a)

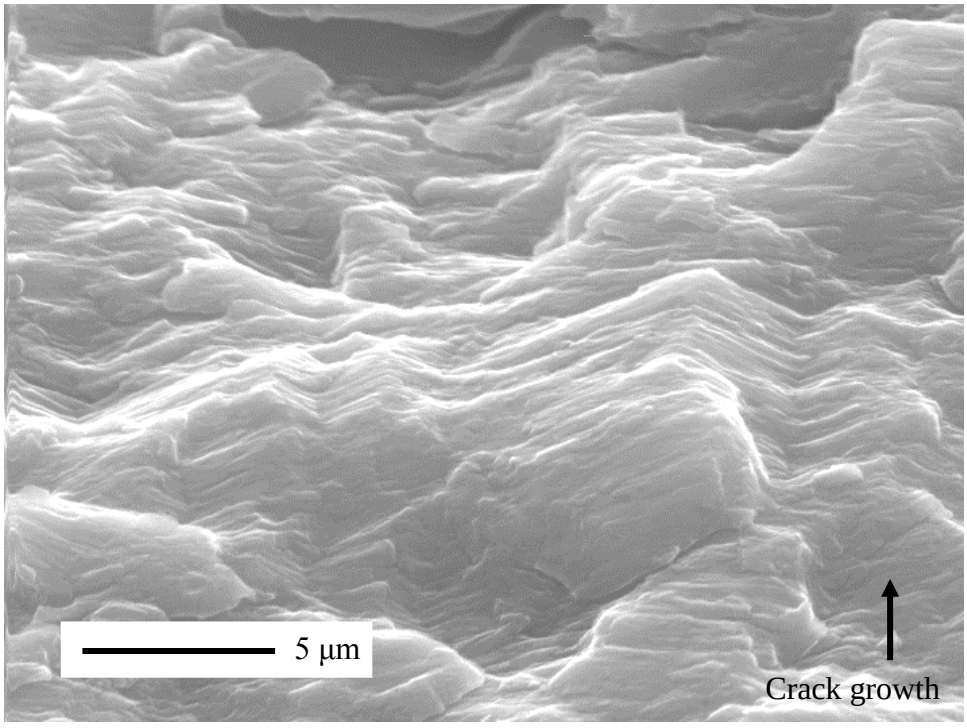

4.11(b)

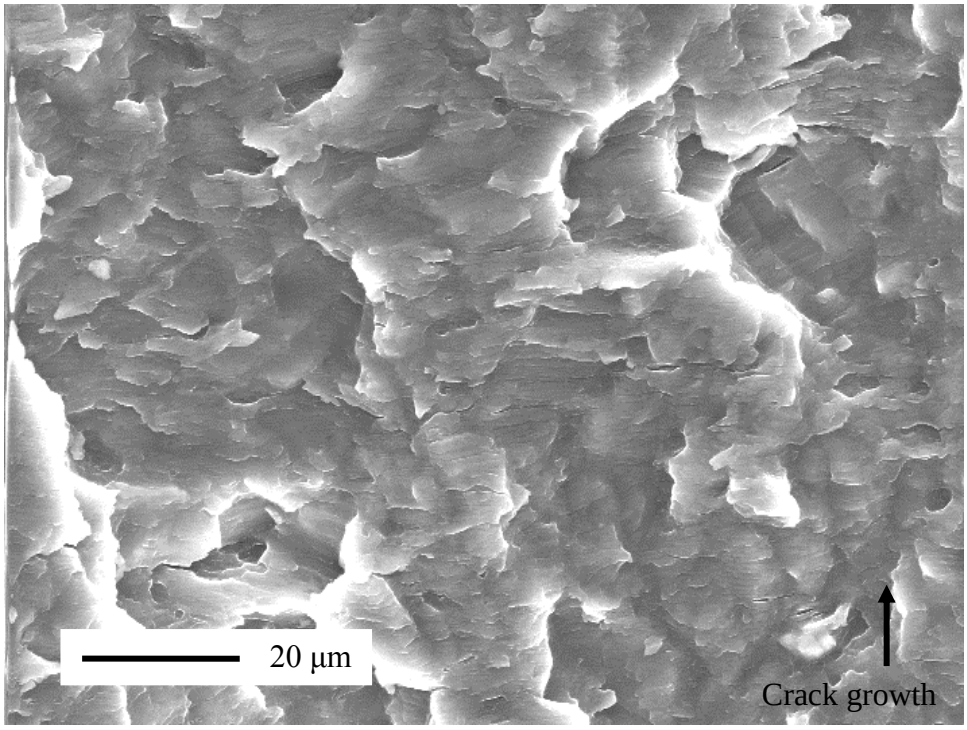

4.11(c)

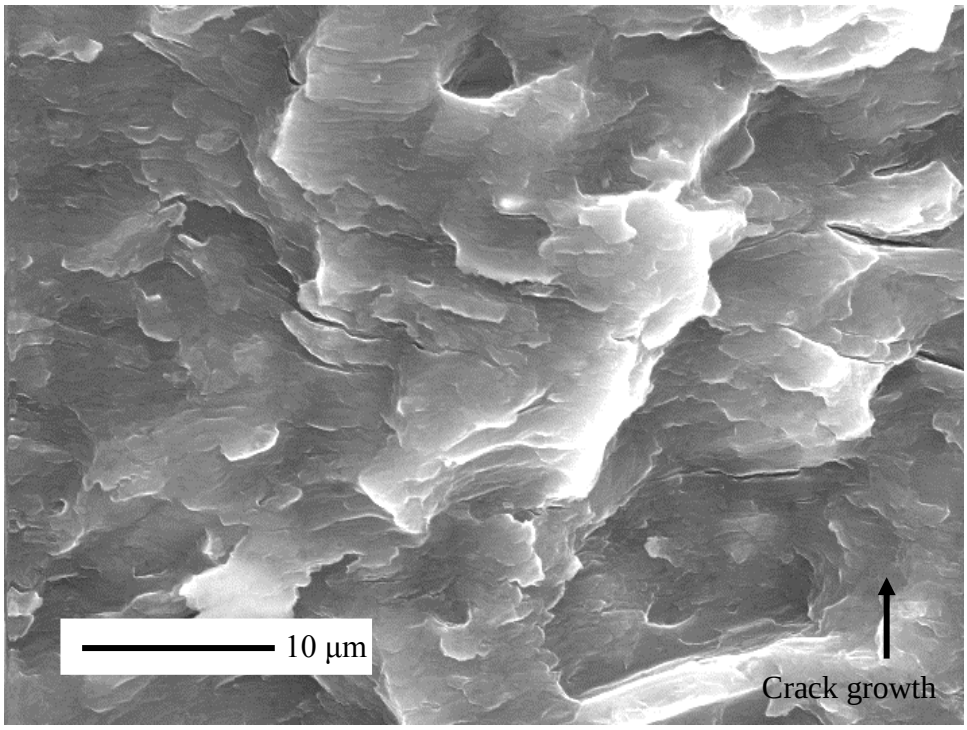

4.11(d)

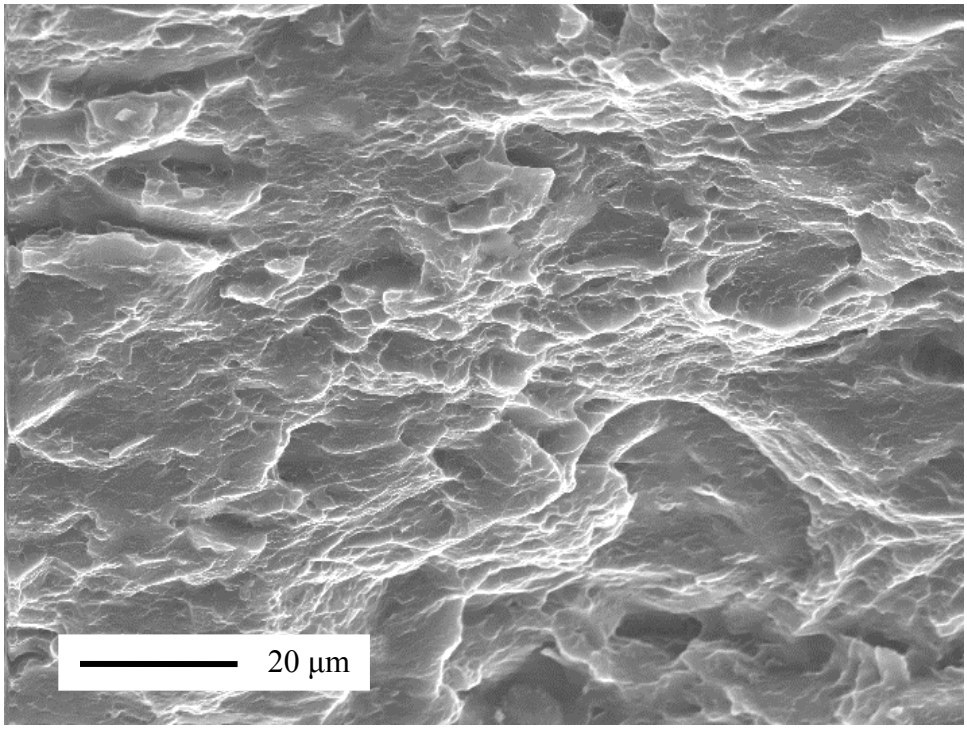

4.11(e)

Figure 4.11. SEM images of (a, b) the 30° kinked crack surface, (c, d) the 90° crack surface, and (e) the final fracture surface of a failed specimen under cyclic loading conditions at the fatigue life of 2.5×10^4 under the load range of 4,080 N.

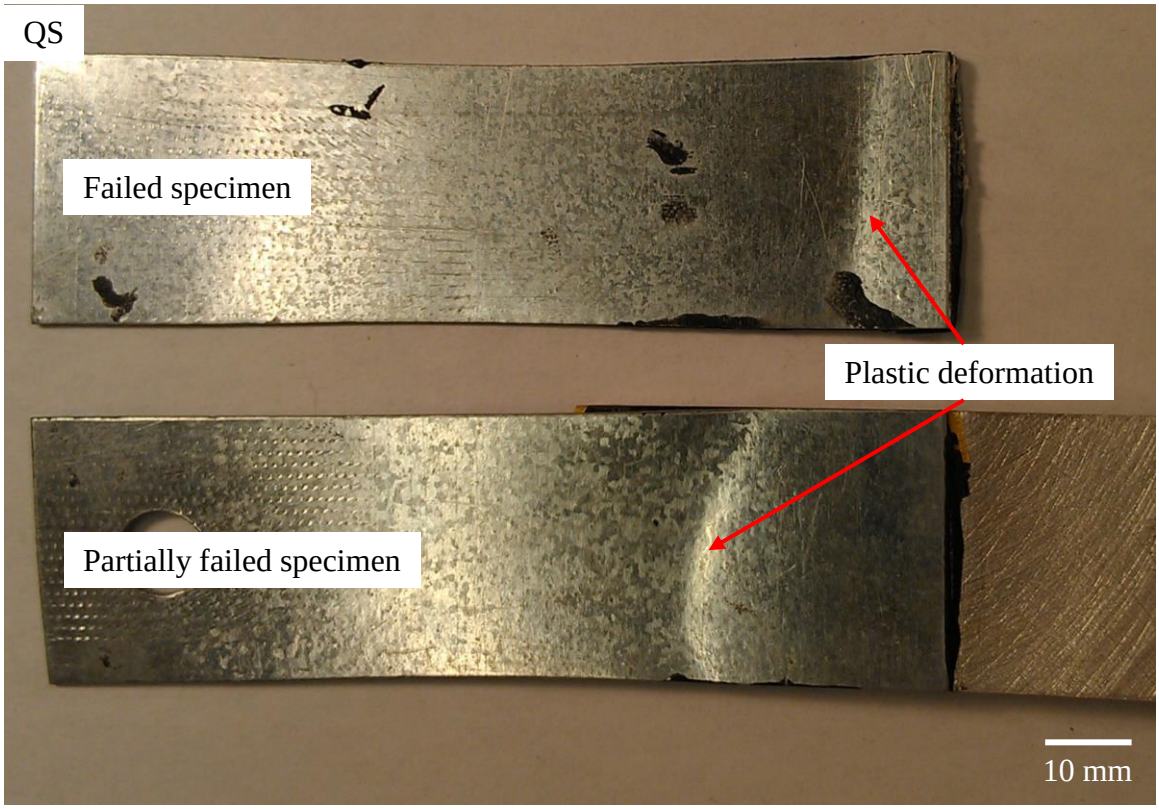
QS
Failed specimen
Plastic deformation
Partially failed specimen
10 mm

4.12(a)

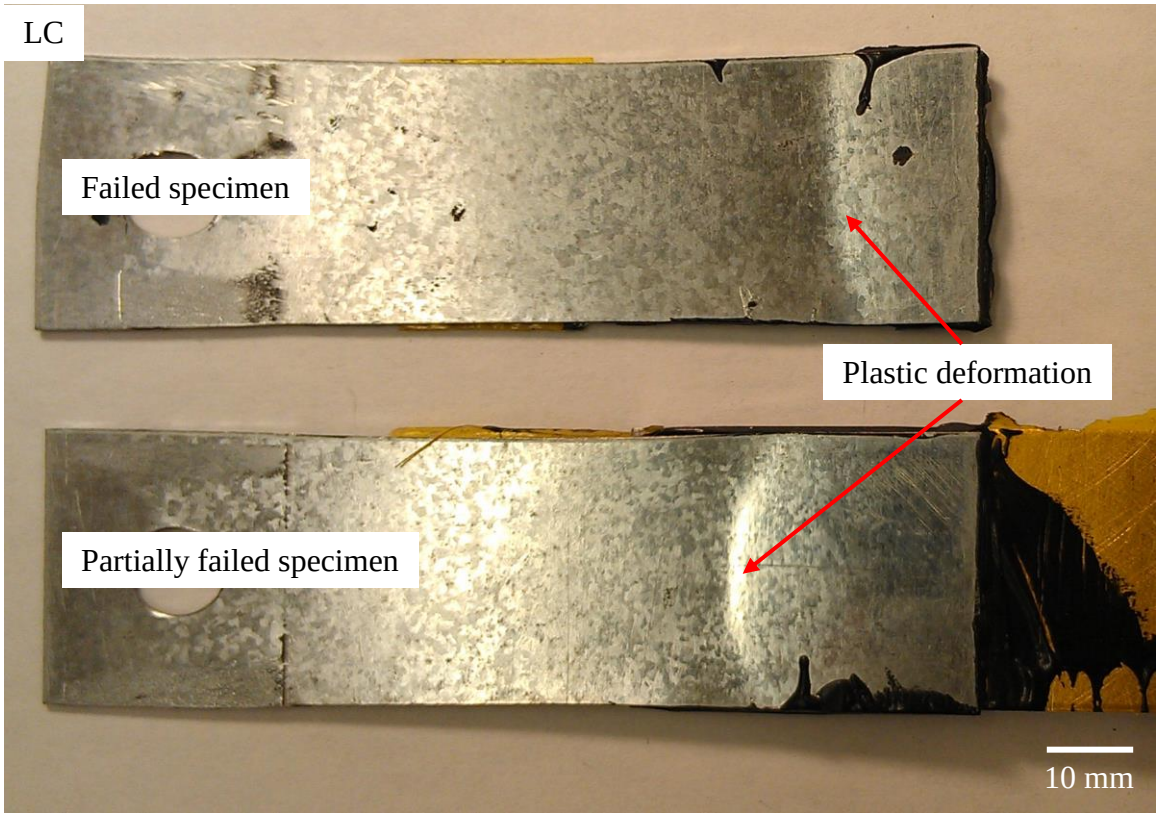

4.12(b)

Figure 4.12. (a) Bottom views of the plastic deformation patterns of the steel sheets along the crack fronts in the failed and partially failed specimens under quasi-static loading conditions. (b) Bottom views of the plastic deformation patterns of the steel sheets along the crack fronts in the failed specimen under low-cycle loading conditions at the fatigue life of 3,462 cycles under the load range of 5,560 N and a partially failed specimen at the fatigue life of 1,500 cycles under the load range of 5,200 N under low-cycle loading conditions.

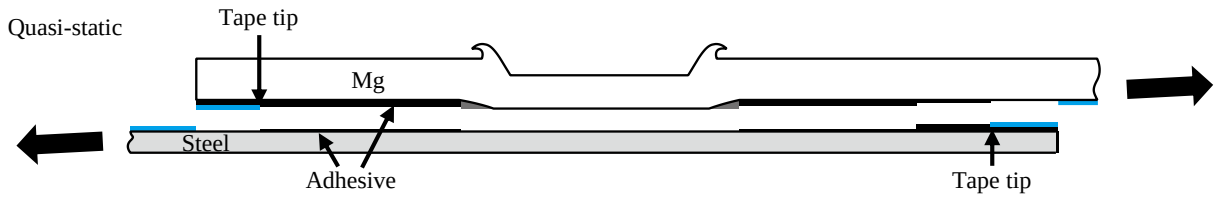

(a)

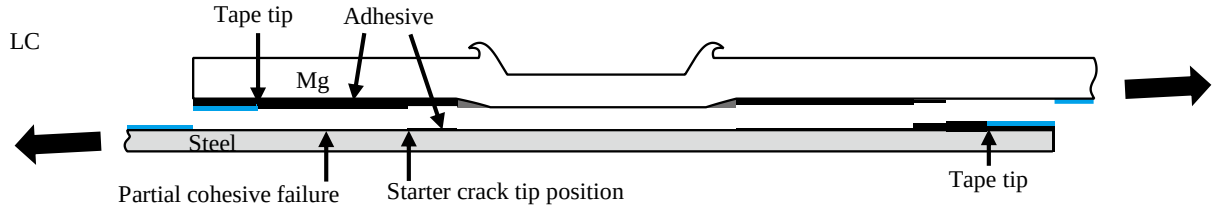

(b)

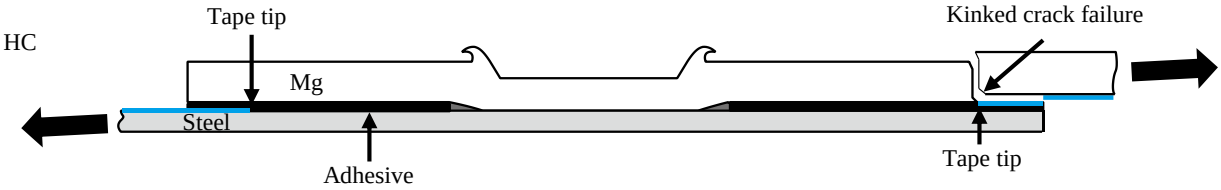

(c)

Figure 4.13. Schematics of the cohesive failure mode between the steel and the adhesive and the interfacial failure mode of the ultrasonic spot weld (a) under quasi-static loading conditions and (b) under low-cycle loading conditions and (c) the kinked crack failure mode in the magnesium sheet under high-cycle loading conditions for the weld-bonded lap-shear specimens. The blue lines indicate the tapes.

4.14(a)

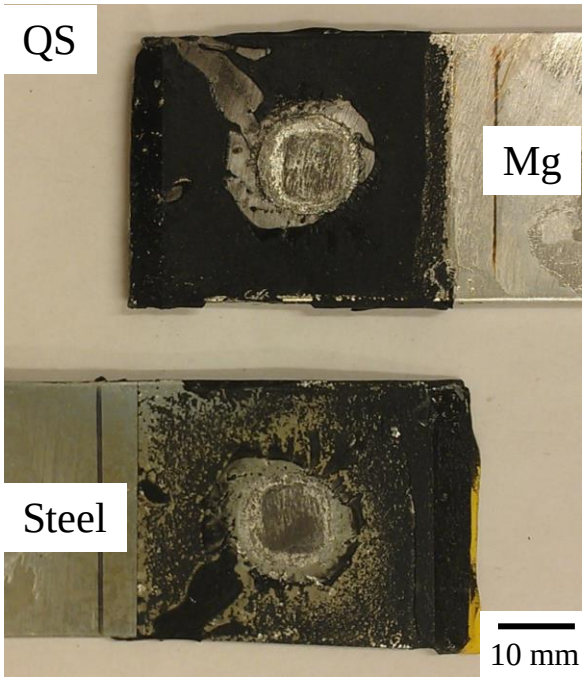

4.14(b)

4.14(c)

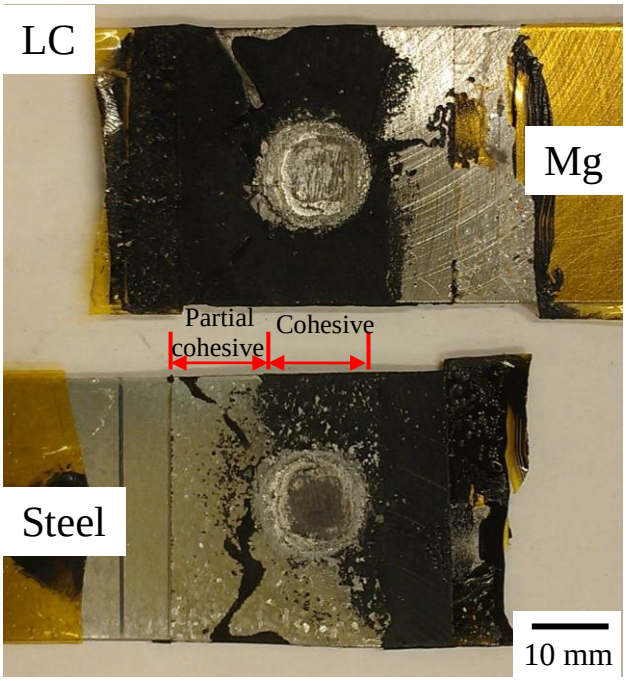
LC
Mg
Partial cohesive
Cohesive
Steel
10 mm

4.14(d)

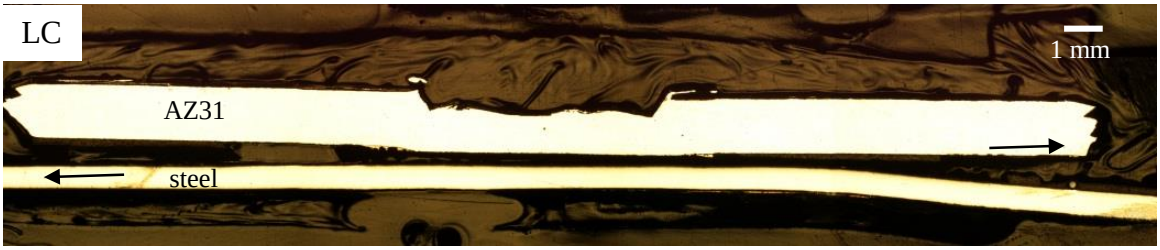
LC
1 mm
AZ31
steel

4.14(e)

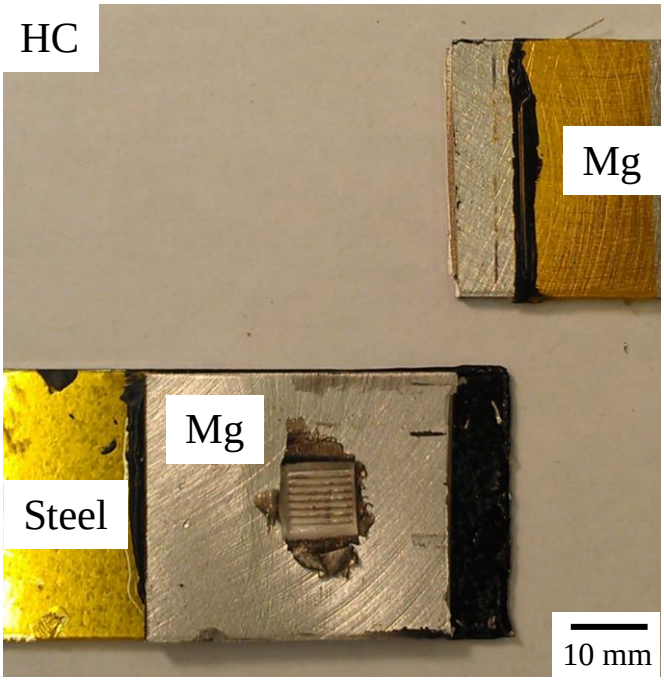

4.14(f)

4.14(g)

Figure 4.14. (a) An optical micrograph of the symmetry cross section near the joint in an untested weld-bonded lap-shear specimen. Images near the failed joints and the corresponding optical micrographs of the symmetry cross sections of the joint in the weld-bonded lap-shear specimens (b, c) under quasi-static loading conditions, (d, e) under low-cycle loading conditions at the fatigue life of 1.4×10^4 cycles under the load range of 5,138 N, and (f, g) under high-cycle loading conditions at the fatigue life of 7.1×10^5 cycles under the load range of 3,202 N. The arrows indicate the loading directions.

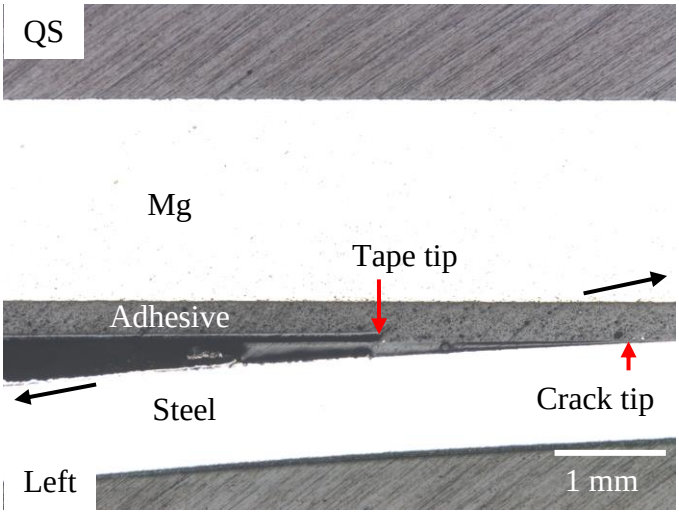
QS
Mg
Tape tip
Adhesive
Steel
Crack tip
Left
1 mm

4.15(a)

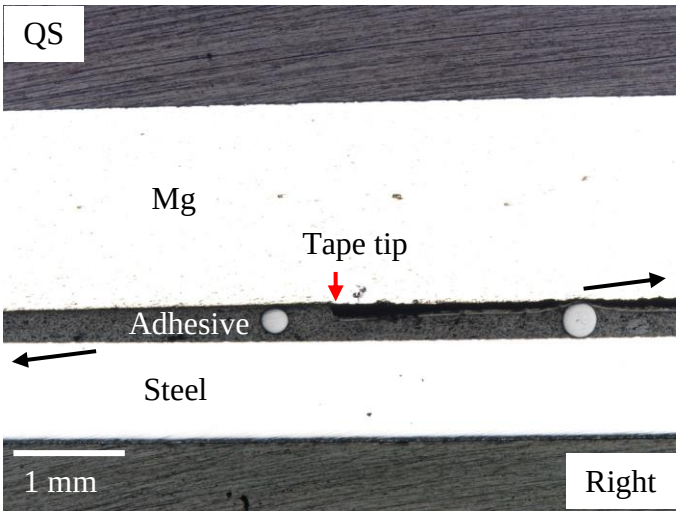
QS
Mg
Tape tip
Adhesive
Steel
1 mm
Right

4.15(b)

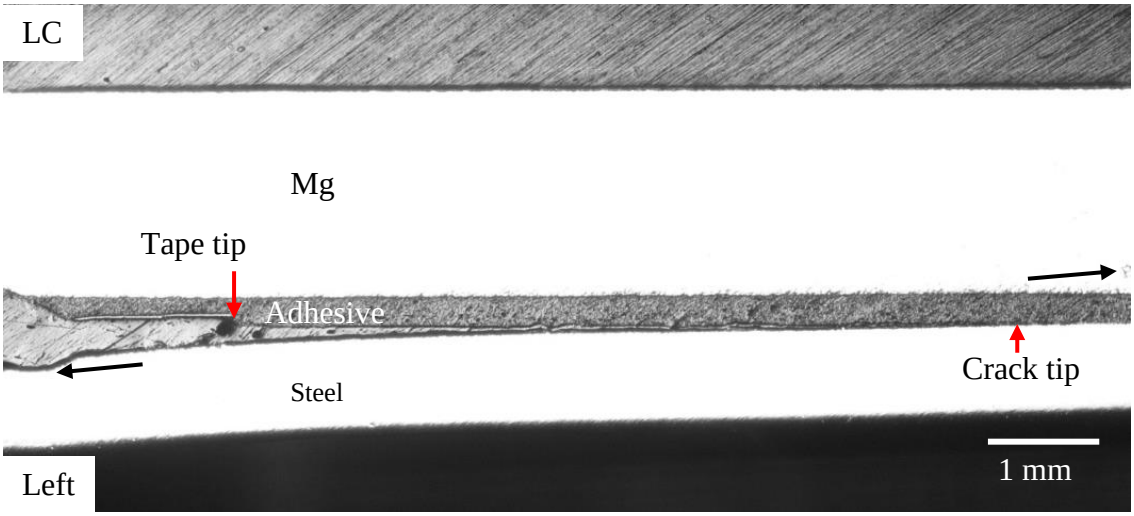

4.15(c)

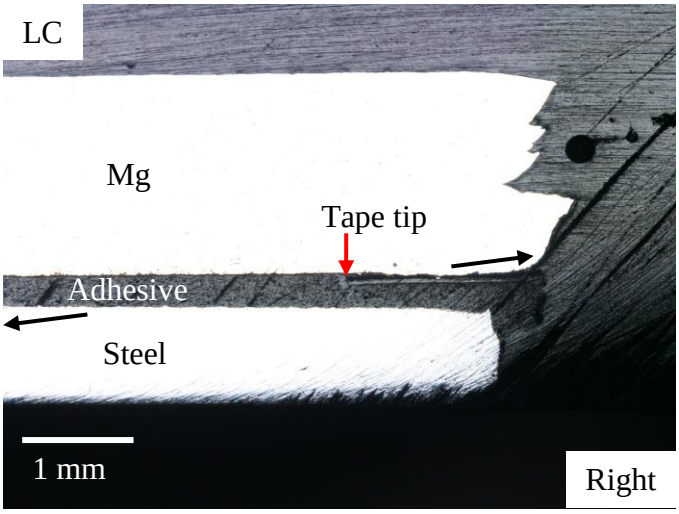

4.15(d)

Figure 4.15. The cross sections near (a) the left and (b) right tape tips of a partially failed weld-bonded lap-shear specimen under quasi-static loading conditions at the load of 5,500 N (85% of the failure load) and the cross sections near the (c) left and (d) right tape tips of a partially failed weld-bonded lap-shear specimen under cyclic loading conditions at the fatigue life of 2,000 cycles under the load range of 5,240 N. The black arrows indicate the loading directions.

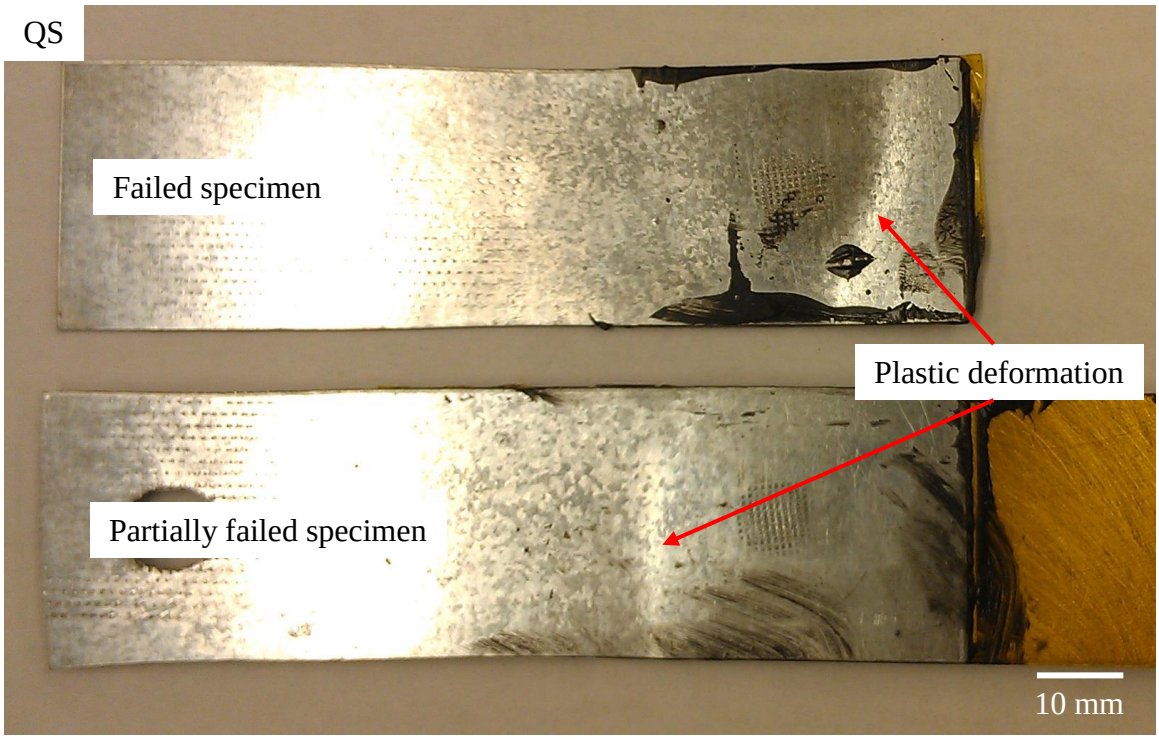
QS
Failed specimen
Plastic deformation
Partially failed specimen
10 mm

4.16(a)

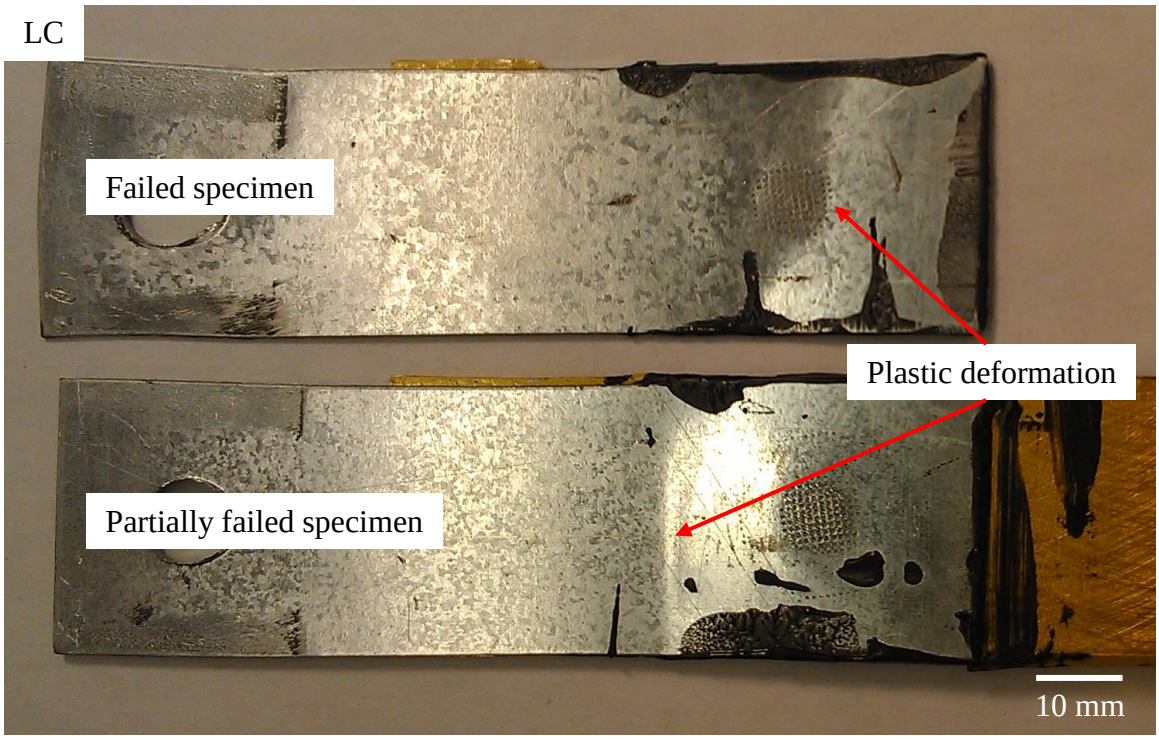

4.16(b)

Figure 4.16. (a) Bottom views of the plastic deformation patterns of the steel sheets along the crack fronts in the failed and partially failed specimens under quasi-static loading conditions. (b) Bottom views of the plastic deformation patterns of the steel sheets along the crack fronts in the failed specimen under low-cycle loading conditions at the fatigue life of 4,628 cycles under the load range of 5,140 N and a partially failed specimen at the fatigue life of 2,000 cycles under the load range of 5,240 N under low-cycle loading conditions.

Acknowledgments

This research was sponsored by the U.S. Department of Energy, Assistant Secretary for Energy Efficiency and Renewable Energy, Office of Vehicle Technologies, as part of the Lightweight Materials Program. Helpful discussions with Drs. Tsung-Yu Pan, Michael Santella, and Zhili Feng of Oakridge National Laboratory and Dr. Teresa Franklin of General Motors are greatly appreciated.

References

[1] M. Santella, T. Franklin, J. Pan, T.-Y. Pan, and E. Brown, "Ultrasonic Spot Welding of AZ31B to Galvanized Mild Steel," SAE International Journal of Materials and Manufacturing, vol. 3, pp. 652-657, 2010.

[2] T. Pan, "Friction Stir Spot Welding (FSSW) - a Literature Review," SAE Technical Paper No. 2007-01-1702, Society of Automotive Engineers, Warrendale, PA, 2007.

[3] T. Gendo, K. Nishiguchi, M. Asakawa, and S. Tanioka, "Spot Friction Welding of Aluminum to Steel," SAE Technical Paper No. 2007-01-1703, Society of Automotive Engineers, Warrendale, PA, 2007.

[4] T. Liyanage, J. Kilbourne, A. P. Gerlich, and T. H. North, "Joint Formation in Dissimilar Al Alloy/Steel and Mg Alloy/Steel Friction Stir Spot Welds," Science and Technology of Welding and Joining, vol. 14, pp. 500-508, 2009.

[5] E. Hetrick, R. Jahn, and L. Reatherford, "Ultrasonic Spot Welding: A New Tool for Aluminum Joining," Welding Journal, vol. 84, pp. 26-30, 2005.

[6] R. Jahn, R. Cooper, and D. Wilkosz, "The Effect of Anvil Geometry and Welding Energy on Microstructures in Ultrasonic Spot Welds of AA6111-T4," Metallurgical and Materials Transactions A: Physical Metallurgy and Materials Science, vol. 38, pp. 570-583, 2007.

[7] N. W. Wright, J. D. Robson, and P. B. Prangnell, "Effects of Thickness Combinations on Joint Properties and Process Windows in Ultrasonic Metal Welding," SAE Technical Paper No. 2009-01-0027, Society of Automotive Engineers, Warrendale, PA, 2009.

[8] A. Watanabe, T. Watanabe, T. Sasaki, and N. University, "Ultrasonic Welding Mild Steel Sheet to Al-Mg Alloy Sheet," Advanced Materials Research, vol. 89-91, pp. 627-632, 2010.

[9] M. Shakil, N. H. Tariq, M. Ahmad, M. A. Choudhary, J. I. Akhter, and S. S. Babu, "Effect of Ultrasonic Welding Parameters on Microstructure and Mechanical Properties of Dissimilar Joints," Materials & Design, vol. 55, pp. 263-273, 2014.

[10] S. Matsuoka and H. Imai, "Direct Welding of Different Metals Used Ultrasonic Vibration," Journal of Materials Processing Technology, vol. 209, pp. 954-960, 2009.

[11] T. Franklin, J. Pan, M. Santella, and T.-Y. Pan, "Fatigue Behavior of Dissimilar Ultrasonic Spot Welds in Lap-Shear Specimens of Magnesium and Steel Sheets," SAE International Journal of Materials and Manufacturing, vol. 4, pp. 581-588, 2011.

[12] M. Carboni and F. Moroni, "Tensile-Shear Fatigue Behavior of Aluminum and Magnesium Lap-Joints Obtained by Ultrasonic Welding and Adhesive Bonding," Procedia Engineering, vol. 10, pp. 3561-3566, 2011.

[13] W.-J. Lai, J. Pan, Z. Feng, M. Santella, and T. Y. Pan, "Failure Mode and Fatigue Behavior of Ultrasonic Spot Welds with Adhesive in Lap-Shear Specimens of Magnesium and Steel Sheets," SAE International Journal of Materials and Manufacturing, vol. 6, pp. 279-285, 2013.

[14] W.-J. Lai and J. Pan, "Stress Intensity Factor Solutions for Adhesive-Bonded Lap-Shear Specimens of Dissimilar Sheets with and without Kinked Crack for Fatigue Life Estimations," companion paper to be submitted for publication, 2014.

Chapter 5
Stress Intensity Factor Solutions for Adhesive-Bonded Lap-Shear Specimens of Magnesium and Steel Sheets with and without Kinked Cracks for Fatigue Life Estimations

5.1. Introduction

The results in the previous chapter indicate that the adhesive-bonded and weld-bonded specimens of magnesium and steel sheets failed from the kinked fatigue crack growth through the magnesium sheet under high-cycle loading conditions. Also, the ultrasonic spot welds in lap-shear specimens of magnesium and steel sheets also failed from the kinked fatigue crack growth through the magnesium sheets. Franklin [1] machined the lap-shear specimens of ultrasonic spot welds of the magnesium and steel sheets into a dog-bone shaped profile. The ultrasonic spot welds in these dog-boned lap-shear specimens of magnesium and steel sheets also failed from the kinked fatigue crack growth through the magnesium sheets. For fatigue life estimations of these ultrasonic spot welded and adhesive bonded specimens based on the kinked fatigue crack growth model using the Paris law, one needs to obtain the stress intensity factor solutions for kinked cracks at various kink lengths including zero kink length. For a kink crack growing out from a main crack between similar materials, the analytical solutions of Cotterell and Rice [2] can be used to calculate the stress intensity factors at zero kink length. However, analytical solutions for interfacial cracks between dissimilar sheets of He and Hutchinson [3] are functions of the kink length, and the stress intensity factor solutions for kinked cracks growing out from a main crack between dissimilar sheets at "zero" kink length cannot be determined.

In order to determine the fatigue life of the adhesive-bonded lap-shear specimen of dissimilar sheets based on a kinked fatigue crack growth model for kinked cracks growing out from an interface between dissimilar sheets, stress intensity factor solutions for kinked cracks with zero (or small) and various kink lengths are needed. In this chapter, the analytical global J integral and effective stress intensity factor solutions for main cracks in lap-shear specimens of three dissimilar sheets under plane strain conditions were developed based on the beam bending theory. The global stress intensity factor solutions for the main cracks in the lap-shear specimens from the corresponding finite element analyses were then presented and compared with the analytical solutions. Next, the local stress intensity factor solutions for kinked cracks with the experimentally observed kink angle as functions of the kink length from the corresponding finite element analyses were presented. The computational results were also compared with the analytical solutions at small kink lengths. The experimentally observed kink angle was then compared with the analytical solution. Based on the computational results, the local stress intensity factor solutions at a small kink length of microstructural significance, used as the initial stress intensity factor solutions at zero kink length, and the computational local stress intensity factor solutions at various kink lengths were adopted to estimate the fatigue lives of the lap-shear specimens based on a kinked crack growth model. The fatigue life estimations were then compared with the experimental results. Finally, some conclusions were made.

5.2. Analytical global *J* integral solutions for main cracks

Figure 5.1 shows a schematic of the adhesive-bonded lap-shear specimen with the applied loads shown as the bold arrows. The specimen has a width b and an overall length L for the magnesium and steel sheets. The specimen has the thickness t_u for the upper magnesium

sheet, thickness t_{l1} for the adhesive layer, and thickness t_{l2} for the steel sheet. The specimen has an overlap length V. The bonded width w is defined as the distance between two crack tips.

The analytical J integral solutions for main cracks between two dissimilar sheets was derived by Zhang [4] using the beam bending theory. However, one of the two preformed main cracks in the adhesive-bonded specimens is between the upper magnesium sheet and the middle adhesive layer. The other preformed main crack is between the lower steel sheet and the middle adhesive layer. Therefore, the analytical J integral solutions for main cracks between two dissimilar sheets of Zhang [4] are not applicable. In this investigation, the J integral solutions for a main crack in three dissimilar sheets are developed. Figure 5.2(a) shows a main crack between sheets u and $l1$ in three dissimilar sheets of u, $l1$ and $l2$. The three sheets are well bonded with each other and are assumed to be isotropic and linear elastic with Young's modulus E_u, shear modulus G_u and Poisson's ratio ν_u for the upper sheet u with the thickness t_u, E_{l1}, G_{l1} and ν_{l1} for the lower sheet $l1$ with the thickness t_{l1}, and E_{l2}, G_{l2} and ν_{l2} for the lower sheet $l2$ with the thickness t_{l2}. For the normal stresses σ_{ui}, σ_{uo}, σ_{l1i}, σ_{l1o}, σ_{l2i} and σ_{l2o} as shown in Figure 5.2(a), the subscripts u, $l1$ and $l2$ indicate the upper sheet, the lower sheet 1 and the lower sheet 2, respectively, and the subscripts *i* and *o* indicate the inner and outer surfaces of the sheets, respectively, with respect to the main crack. The coordinate system is also shown in the figure. The bonded width *w* is assumed to be much larger than the thicknesses of the sheets so that the beam bending theory is applicable.

According to Rice [5], the J integral solutions can be expressed as

$$J = \int_{\Gamma} (W n_x - T_i \frac{\partial u_i}{\partial x}) \, \mathrm{d}s, \; i = x, y \tag{1}$$

where Γ represents a contour counterclockwise from the lower crack face to the upper crack face, $\mathrm{d}s$ represents the differential arc length of the contour Γ, n_x represents the x component of the unit outward normal $\mathbf{n}$ to the differential arc length $\mathrm{d}s$, T_i $(=\sigma_{ij}n_j)$ represents the components of the traction vector $\mathbf{T}$ on the differential arc length $\mathrm{d}s$, and u_i represents the components of the displacement vector $\mathbf{u}$. In Equation (1), the strain energy density W is defined as

$$W=\int_0^{\varepsilon_{ij}}\sigma_{ij}\,\mathrm{d}\varepsilon_{ij}\quad(i,j=x,y) \tag{2}$$

where σ_{ij} are the stress components and ε_{ij} are the strain components. Consider a main crack on the right side as shown in Figure 5.2(a), the path-independent integration contour Γ is selected as ABCDEFGHI in this case. The J integral is 0 on the segments BC and FG because $n_x=0$ and $T_i=0$. Recently, the three-dimensional finite element computational results of Wang et al. [6, 7] and Lin and Pan [8] for various types of spot weld specimens indicate that the structural stresses from the bending moments and the membrane forces provide the dominant contributions to the stress intensity factors along the nugget circumference whereas the structural stresses from the transverse shear forces may not have significant contributions. The J integral on the segments AB, CD, DE, EF, GH and HI can therefore be written as

$$J=-\left(\int_{AB}W\,\mathrm{d}y+\int_{CD}W\,\mathrm{d}y+\int_{DE}W\,\mathrm{d}y+\int_{EF}W\,\mathrm{d}y+\int_{GH}W\,\mathrm{d}y+\int_{HI}W\,\mathrm{d}y\right) \tag{3}$$

with

$$W=\frac{1}{2E'_j}\sigma_x^2\quad(j=u,\,l1,\,l2) \tag{4}$$

where $E'_j=E_j$ under plane stress conditions and $E'_j=E_j/\left(1-\nu_j^2\right)$ under plane strain conditions. The stresses σ_x on segments AB, GH and HI can be determined directly from the applied load

using the beam bending theory. The stresses σ_x on the segments CD, DE and EF are determined by the six stresses σ^*_{ui}, σ^*_{uo}, σ^*_{l1i}, σ^*_{l1o}, σ^*_{l2i} and σ^*_{l2o} which can be determined from the linear strain distribution in the three dissimilar sheets according to the beam bending theory. To solve for the six stresses, six equations are derived based on the beam bending theory with the thickness ratios defined as

$$\delta_u = t_u / t \tag{5}$$

$$\delta_{l1} = t_{l1} / t \tag{6}$$

$$\delta_{l2} = t_{l2} / t \tag{7}$$

where

$$t = t_u + t_{l1} + t_{l2} \tag{8}$$

The Young's modulus ratios are defined as

$$\eta_{u1} = E'_u / E'_{l1} \tag{9}$$

$$\eta_{12} = E'_{l1} / E'_{l2} \tag{10}$$

The six equations based on the beam bending theory are

$$\begin{aligned}&\delta_{l2}\left(\sigma^*_{l2o} + \sigma^*_{l2i}\right) + \delta_{l1}\left(\sigma^*_{l1o} + \sigma^*_{l1i}\right) + \delta_u\left(\sigma^*_{ui} + \sigma^*_{uo}\right)\\ &= \delta_{l2}\left(\sigma_{l2o} + \sigma_{l2i}\right) + \delta_{l1}\left(\sigma_{l1o} + \sigma_{l1i}\right) + \delta_u\left(\sigma_{ui} + \sigma_{uo}\right)\end{aligned} \tag{11}$$

$$\begin{aligned}&\frac{1}{6}\delta_{l2}\left[3\delta_{l1}\left(\sigma^*_{l2o} + \sigma^*_{l2i}\right) + \delta_{l2}\left(2\sigma^*_{l2o} + \sigma^*_{l2i}\right)\right] + \frac{1}{6}\delta^2_{l1}\sigma^*_{l1i} + \frac{1}{3}\delta^2_{l1}\sigma^*_{l1o} - \left(\frac{1}{3}\delta^2_u\sigma^*_{uo} + \frac{1}{6}\delta^2_u\sigma^*_{ui}\right)\\ &= \frac{1}{6}\delta_{l2}\left[3\delta_{l1}\left(\sigma_{l2o} + \sigma_{l2i}\right) + \delta_{l2}\left(2\sigma_{l2o} + \sigma_{l2i}\right)\right] + \frac{1}{6}\delta^2_{l1}\sigma_{l1i} + \frac{1}{3}\delta^2_{l1}\sigma_{l1o} - \left(\frac{1}{3}\delta^2_u\sigma_{uo} + \frac{1}{6}\delta^2_u\sigma_{ui}\right)\end{aligned} \tag{12}$$

$$\frac{\sigma^*_{ui} - \sigma^*_{uo}}{\delta_u} = \eta_{u1}\frac{\sigma^*_{l1i} - \sigma^*_{l1o}}{\delta_{l1}} \tag{13}$$

$$\frac{\sigma_{l1i}^{*}-\sigma_{l1o}^{*}}{\delta_{l1}}=\eta_{12}\frac{\sigma_{l2i}^{*}-\sigma_{l2o}^{*}}{\delta_{l2}} \tag{14}$$

$$\sigma_{ui}^{*}=\eta_{u1}\sigma_{l1i}^{*} \tag{15}$$

$$\sigma_{l1o}^{*}=\eta_{12}\sigma_{l2i}^{*} \tag{16}$$

Equations (11) and (12) are from the force and moment equilibrium conditions, respectively. Equations (13) and (14) are from the linear strain distribution in the three dissimilar sheets. Equations (15) and (16) are from the strain continuity conditions along the two surfaces. Solving Equations (11) to (16) gives the six normal structural stresses σ_{ui}^{*}, σ_{uo}^{*}, σ_{l1i}^{*}, σ_{l1o}^{*}, σ_{l2i}^{*} and σ_{l2o}^{*}. Substituting the six normal structural stresses σ_{ui}^{*}, σ_{uo}^{*}, σ_{l1i}^{*}, σ_{l1o}^{*}, σ_{l2i}^{*} and σ_{l2o}^{*} into Equation (4) and integrating over the contour Γ, the J integral solutions for the main crack in three dissimilar sheets can be expressed as

$$J=\frac{t}{6E'_{u}D}\begin{pmatrix} N_1\sigma_{ui}^{2}+N_2\sigma_{uo}^{2}+N_3\sigma_{l1i}^{2}+N_4\sigma_{l1o}^{2}+N_5\sigma_{l2i}^{2}+N_6\sigma_{l2o}^{2} \\ +N_7\sigma_{ui}\sigma_{uo}+N_8\sigma_{ui}\sigma_{l1i}+N_9\sigma_{ui}\sigma_{l1o}+N_{10}\sigma_{ui}\sigma_{l2i}+N_{11}\sigma_{ui}\sigma_{l2o} \\ +N_{12}\sigma_{uo}\sigma_{l1i}+N_{13}\sigma_{uo}\sigma_{l1o}+N_{14}\sigma_{uo}\sigma_{l2i}+N_{15}\sigma_{uo}\sigma_{l2o} \\ +N_{16}\sigma_{l1i}\sigma_{l1o}+N_{17}\sigma_{l1i}\sigma_{l2i}+N_{18}\sigma_{l1i}\sigma_{l2o} \\ +N_{19}\sigma_{l1o}\sigma_{l2i}+N_{20}\sigma_{l1o}\sigma_{l2o} \\ +N_{21}\sigma_{l2i}\sigma_{l2o} \end{pmatrix} \tag{17}$$

where

$$\begin{aligned} N_1 &= C_{04100}+4C_{31110}+6C_{22110}+4C_{13110}+C_{40120}+3C_{21211}+3C_{12211}+C_{03211}+6C_{11311} \\ &+3C_{02311}+3C_{01411}+C_{30221}+3C_{20321}+3C_{10421} \end{aligned} \tag{18}$$

$$N_2 = C_{04100}+4C_{31110}+6C_{22110}+4C_{13110}+C_{40120}+3C_{21211}+3C_{12211}+C_{03211}+C_{30221} \tag{19}$$

$$\begin{aligned} N_3 &= C_{14012}+C_{23011}+12C_{31112}+12C_{22112}+4C_{13112}+12C_{21212}+6C_{12212}+4C_{11312}+3C_{40122} \\ &+3C_{30222}+C_{20322}+C_{10423} \end{aligned} \tag{20}$$

$$\begin{aligned} N_4 &= C_{14001}+3C_{41011}+3C_{32011}+C_{23011}+12C_{31112}+12C_{22112}+4C_{13112}+12C_{21212}+6C_{12212} \\ &+4C_{11312}+C_{20322}+C_{10423} \end{aligned} \tag{21}$$

$$N_5 = C_{32021} + 3C_{23021} + 3C_{14021} + C_{41031} + 3C_{22122} + 6C_{13122} + 3C_{04122} + 3C_{12222} + 3C_{03222} + C_{02322} + 4C_{31132} + 6C_{21232} + 4C_{11332} + C_{01433} \quad (22)$$

$$N_6 = C_{32021} + C_{41031} + 3C_{22122} + 3C_{12222} + C_{02322} + 4C_{31132} + 6C_{21232} + 4C_{11332} + C_{01433} \quad (23)$$

$$N_7 = C_{04100} + 4C_{31110} + 6C_{22110} + 4C_{13110} + C_{40120} - 6C_{21211} - 6C_{12211} - 2C_{03211} - 6C_{11311} - 3C_{02311} - 2C_{30221} - 3C_{20321} \quad (24)$$

$$N_8 = -12C_{31111} - 15C_{22111} - 6C_{13111} - 4C_{21211} - 3C_{12211} - 3C_{40121} - C_{30221} - C_{20322} - 3C_{10422} \quad (25)$$

$$N_9 = -6C_{31111} - 12C_{22111} - 6C_{13111} - 2C_{21211} - 3C_{12211} + C_{30221} - 2C_{20322} - 3C_{10422} \quad (26)$$

$$N_{10} = -3C_{13111} - 3C_{04111} - C_{03211} + 3C_{31121} + 3C_{22121} + 3C_{21221} + 2C_{12221} - 3C_{11322} - C_{02322} - 3C_{01422} \quad (27)$$

$$N_{11} = 3C_{13111} + C_{03211} + 3C_{31121} + 6C_{22121} + 3C_{21221} + 4C_{12221} - 3C_{11322} - 2C_{02322} + 3C_{01422} \quad (28)$$

$$N_{12} = -12C_{31111} - 15C_{22111} - 6C_{13111} - 8C_{21211} - 6C_{12211} - 3C_{40121} - 2C_{30221} + C_{20322} \quad (29)$$

$$N_{13} = -6C_{31111} - 12C_{22111} - 6C_{13111} - 4C_{21211} - 6C_{12211} + 2C_{30221} + 2C_{20322} \quad (30)$$

$$N_{14} = -3C_{13111} - 3C_{04111} - 2C_{03211} + 3C_{31121} + 3C_{22121} + 6C_{21221} + 4C_{12221} + 3C_{11322} + C_{02322} \quad (31)$$

$$N_{15} = 3C_{13111} + 2C_{03211} + 3C_{31121} + 6C_{22121} + 6C_{21221} + 8C_{12221} + 3C_{11322} + 2C_{02322} \quad (32)$$

$$N_{16} = C_{14001} - 3C_{32011} - 2C_{23011} + 12C_{31112} + 12C_{22112} + 4C_{13112} + 12C_{21212} + 6C_{12212} + 4C_{11312} - 3C_{30222} - 2C_{20322} + C_{10423} \quad (33)$$

$$N_{17} = -2C_{23011} - 3C_{14011} + C_{32021} - 6C_{31122} - 2C_{22122} - 12C_{21222} - 3C_{12222} - 6C_{11322} \quad (34)$$

$$N_{18} = 2C_{23011} + 2C_{32021} - 6C_{31122} - 4C_{22122} - 12C_{21222} - 6C_{12222} - 6C_{11322} \quad (35)$$

$$N_{19} = -C_{23011} - 3C_{14011} - 3C_{41021} - C_{32021} - 12C_{31122} - 4C_{22122} - 15C_{21222} - 3C_{12222} - 6C_{11322} \quad (36)$$

$$N_{20} = C_{23011} - 3C_{41021} - 2C_{32021} - 12C_{31122} - 8C_{22122} - 15C_{21222} - 6C_{12222} - 6C_{11322} \quad (37)$$

$$N_{21} = -2C_{32021} - 3C_{23021} + C_{41031} - 6C_{22122} - 6C_{13122} - 6C_{12222} - 3C_{03222} - 2C_{02322} + 4C_{31132} + 6C_{21232} + 4C_{11332} + C_{01433} \quad (38)$$

$$D = C_{04000} + 4C_{31010} + 6C_{22010} + 4C_{13010} + C_{40020} + 12C_{21111} + 12C_{12111} + 4C_{03111} + 12C_{11211} + 6C_{02211} + 4C_{01311} + 4C_{30121} + 6C_{20221} + 4C_{10321} + C_{00422} \quad (39)$$

where

$$C_{ijklm} = \delta_{l1}^{i}\delta_{l2}^{j}\delta_{u}^{k}\eta_{12}^{l}\eta_{u1}^{m} \quad (40)$$

Figure 5.2(b) shows a schematic of the lap-shear specimen near the crack tips. Figure 5.3(a) shows a schematic of the lap-shear specimen with the applied load F/b. The positions of the two main crack tips are also shown in Figures 5.2(b) and 5.3(a). For the loading conditions shown in Figures 5.2(b) and 5.3(a), the normal structural stresses σ_{ui}, σ_{uo}, σ_{l1i}, σ_{l1o}, σ_{l2i} and σ_{l2o} for the right crack tip are

$$\sigma_{ui,right} = \frac{4F\cos\theta}{bt_u} + \frac{6Fd\sin\theta}{bt_u^2} \quad (41)$$

$$\sigma_{uo,right} = -\frac{2F\cos\theta}{bt_u} - \frac{6Fd\sin\theta}{bt_u^2} \quad (42)$$

$$\sigma_{l1i,right} = 0 \quad (43)$$

$$\sigma_{l1o,right} = 0 \quad (44)$$

$$\sigma_{l2i,right} = 0 \quad (45)$$

$$\sigma_{l2o,right} = 0 \quad (46)$$

where θ is the angle between the loading direction and the *x* direction, d is the distance from the load application point to the nearest main crack tip, and F/b is the applied load per unit width as shown in Figure 5.3(a). The first and second terms in Equations (41) and (42) are due to the decomposed forces, $F\cos\theta$ and $F\sin\theta$, in the horizontal and vertical directions, respectively. Substituting Equations (41) to (46) into Equation (17) gives the value of the J integral for the right crack tip.

The asymptotic in-plane stress field around a main crack tip is an oscillatory field that can be characterized by a complex stress intensity factor **K** ($= K_1 + iK_2$, $i = \sqrt{-1}$) (Rice and Sih [9]). The stresses σ_y and τ_{xy} at a small distance r ahead of a main crack tip are characterized by **K** as

$$\sigma_y + i\tau_{xy} = \frac{K_1 + iK_2}{\sqrt{2\pi r}} \left(\frac{r}{t_c} \right)^{i\varepsilon} \tag{47}$$

For the right crack as shown in Figure 5.2(b), the bimaterial constant ε is defined as

$$\varepsilon = \frac{1}{2\pi} \ln \frac{\kappa_u / G_u + 1/G_{l1}}{\kappa_{l1} / G_{l1} + 1/G_u} \tag{48}$$

where

$$\kappa_u = 3 - 4\nu_u \tag{49}$$

and

$$\kappa_{l1} = 3 - 4\nu_{l1} \tag{50}$$

under plane strain conditions. For the left crack as shown in Figure 5.2(b), the bimaterial constant ε is defined as

$$\varepsilon = \frac{1}{2\pi} \ln \frac{\kappa_{l2} / G_{l2} + 1/G_{l1}}{\kappa_{l1} / G_{l1} + 1/G_{l2}} \tag{51}$$

where

$$\kappa_{l2} = 3 - 4\nu_{l2} \tag{52}$$

under plane strain conditions. In Equation (47), t_c represents a characteristic length [4, 10]. It should be noted that when the two materials are identical, $\varepsilon = 0$. In this case, K_1 and K_2 in Equation (47) for the main crack become the conventional stress intensity factors K_I and K_{II}, respectively.

The J integral solutions is directly related to the effective stress intensity factor K_e for both the right and left cracks as

$$K_e = \sqrt{K_1^2 + K_2^2} = \sqrt{J \cosh^2(\pi\varepsilon) E^*} \tag{53}$$

where

$$\frac{1}{E^*} = \frac{1}{2}\left(\frac{1}{E'_u} + \frac{1}{E'_{l1}} \right) \tag{54}$$

for the right crack and

$$\frac{1}{E^*} = \frac{1}{2}\left(\frac{1}{E'_{l1}} + \frac{1}{E'_{l2}} \right) \tag{55}$$

for the left crack.

5.3. Computational global stress intensity factor solutions for main cracks

Figure 5.3(a) shows a schematic of a two-dimensional finite element model of a lap-shear specimen and the boundary conditions. The specimen has the upper sheet thickness t_u, the lower sheet 1 thickness t_{l1}, and the lower sheet 2 thickness t_{l2}, the length L, the overlap length V, and the bonded width w. The $x-y$ coordinate system is shown in the figure. The left edge is fixed at the middle surface while the right edge has a concentrated force per unit width, F/b, applied at the middle surface.

The two-dimensional plane strain finite elemental model has $t_u = 1.6$ mm, $t_{l1} = 0.3$ mm, $t_{l2} = 0.8$ mm, $L = 100$ mm and $V = 40$ mm. The width b of the specimen is 30 mm, the angle θ between the loading direction and the *x* direction is 0.107°, and the distance d from the load application point to the crack tip is 65 mm based on the specimen geometry and the test setup in

Chapter 4. Note that the ratio of the bonded width w to the upper sheet thickness t_u is 37.5 for the specimens used in the experiments. The two-dimensional plane strain finite element model is used to obtain the global stress intensity factor solutions for calculating the local stress intensity factor solutions for kinked cracks. Figures 5.3(b) and 5.3(c) show the closed-up views of the mesh near the right and left main crack tips, respectively. All the materials are assumed to be isotropic and linear elastic. The top AZ31-H24 sheet is modeled with the Young's modulus $E_u = 45$ GPa and the Poisson's ratio $\nu_u = 0.35$. The middle adhesive layer is modeled with the Young's modulus $E_{l1} = 4.1$ GPa and the Poisson's ratio $\nu_{l1} = 0.36$. The bottom steel sheet is modeled with the Young's modulus $E_{l2} = 207$ GPa and the Poisson's ratio $\nu_{l2} = 0.3$. Second-order, isoparametric, quadrilateral, reduced integration, plane strain elements (CPE8R) were used in the model. The crack-tip elements were modified with collapsed nodes at the crack tip and the midside nodes on the sides were moved to the quarter points from the crack tip to model the $1/\sqrt{r}$ singularity near the crack tip. The commercial finite element program ABAQUS [11] was employed to perform the computation.

It should be noted that the K_1^A and K_2^A of the complex stress intensity factor $\mathbf{K}^A$ $(= K_1^A + iK_2^A)$ obtained directly from ABAQUS [11] are defined such that the stresses σ_y and τ_{xy} at a small distance r ahead of a main crack tip are characterized by $\mathbf{K}^A$ $(= K_1^A + iK_2^A)$ as

$$\sigma_y + i\,\tau_{xy} = \frac{K_1^A + iK_2^A}{\sqrt{2\pi r}} r^{i\varepsilon} \tag{56}$$

By comparing Equations (47) and (56), the K_1 and K_2 solutions can be related to the K_1^A and K_2^A solutions as

$$K_1 = K_1^A \cos(\varepsilon \ln t_c) - K_2^A \sin(\varepsilon \ln t_c) \tag{57}$$

$$K_2 = K_1^A \sin(\varepsilon \ln t_c) + K_2^A \cos(\varepsilon \ln t_c) \tag{58}$$

It is noted that the global effective stress intensity factor K_e ($= \sqrt{K_1^2 + K_2^2} = \sqrt{\left(K_1^A\right)^2 + \left(K_2^A\right)^2}$) is independent of the selection of a characteristic length t_c. In this investigation, the computational K_1 and K_2 solutions for the interfacial cracks are obtained from Equations (57) and (58) with the K_1^A and K_2^A solutions obtained from ABAQUS [11].

The computational results are compared with the analytical results derived from the beam bending theory in Equation (17) in a normalized form as

$$K_e = F_e\left(\delta_u, \delta_{l1}, \delta_{l2}, \eta_{u1}, \eta_{12}\right) \cdot \frac{F}{b\sqrt{t_u}} \tag{59}$$

where F_e is a dimensionless geometric function which depends on the thickness ratios and modulus ratios of the three sheets. The normalized stress intensity factor F_e solutions obtained from the finite element analyses and the analytical solutions in Equations (17) and (53) are 0.830 and 0.828, respectively, for the right main crack (as shown in Figure 5.2(b)). The normalized stress intensity factor F_e solutions obtained from the finite element analyses and the analytical solutions in Equations (17) and (53) are 0.625 and 0.622, respectively, for the left main crack (as shown in Figure 5.2(b)). The results show that the analytical solution agrees very well with the computational results with less than a small difference of 0.5%.

5.4. Analytical local stress intensity factor solutions for kinked cracks

Figure 5.4 shows a schematic of a main crack and a kinked crack with the kink length a and the kink angle φ. The schematic of the kinked crack is consistent with the kinked crack shown in Figure 4.8(g) by rotating 180° either clockwise or counterclockwise. Here, k_I and k_{II}

represent the local stress intensity factor solutions for the kinked crack. The arrows shown in the figure represent the positive values of the local stress intensity factors k_I and k_{II}. The selection of the *x*-*y* coordinate system with respect to the main crack tip is consistent with that in He and Hutchinson [3].

For kinked cracks that kink out from a main interfacial crack between dissimilar sheets, the k_I and k_{II} solutions can be expressed as functions of the kink angle φ, the Dundurs' parameters α and β, and the global K_1^A and K_2^A solutions for the main crack when the kink length approaches to 0. The local stress intensity factors k_I and k_{II} are expressed in the complex form (He and Hutchinson [3]) as

$$k_I + ik_{II} = (c_R + ic_I)(K_1^A + iK_2^A)a^{i\varepsilon} + (d_R - id_I)(K_1^A - iK_2^A)a^{-i\varepsilon} \tag{60}$$

where c_R, c_I, d_R and d_I are the real and imaginary parts of the complex function c and d. Both c and d are complex functions of α, β and φ. The Dundur's parameters α and β are defined as

$$\alpha = \frac{(\kappa_l + 1)G_u - (\kappa_u + 1)G_l}{(\kappa_l + 1)G_u + (\kappa_u + 1)G_l} \tag{61}$$

$$\beta = \frac{(\kappa_l - 1)G_u - (\kappa_u - 1)G_l}{(\kappa_l + 1)G_u + (\kappa_u + 1)G_l} \tag{62}$$

where the subscripts u and l represent the upper and lower sheets, respectively, following the notation shown in Figure 5.4. Equation (60) indicates that k_{I} and k_{II} depend on the kink length a and the bimaterial constant ε. Note that Equation (60) is only applicable when the kink length approaches to 0. Based on Equation (60), k_{I} and k_{II} can be expressed as

$$\begin{aligned} k_I = {} & [-c_I \sin(\varepsilon \ln a) + c_R \cos(\varepsilon \ln a) - d_I \sin(\varepsilon \ln a) + d_R \cos(\varepsilon \ln a)]K_1^A \\ & + [-c_I \cos(\varepsilon \ln a) - c_R \sin(\varepsilon \ln a) - d_I \cos(\varepsilon \ln a) - d_R \sin(\varepsilon \ln a)]K_2^A \end{aligned} \tag{63}$$

$$k_{II} = [c_I \cos(\varepsilon \ln a) + c_R \sin(\varepsilon \ln a) - d_I \cos(\varepsilon \ln a) - d_R \sin(\varepsilon \ln a)]K_1^A$$

$$+ [-c_I \sin(\varepsilon \ln a) + c_R \cos(\varepsilon \ln a) + d_I \sin(\varepsilon \ln a) - d_R \cos(\varepsilon \ln a)]K_2^A \quad (64)$$

The global stress intensity factors K_1^A and K_2^A are obtained computationally as mentioned in the previous section. The functions c_R, c_I, d_R and d_I are tabulated in He and Hutchinson [12]. The values for c and d are extrapolated from that report. Based on the material properties used in the finite element analyses in section 4, $c_R = 1.026$, $c_I = -1.016$, $d_R = 0.467$ and $d_I = -0.352$ for $\alpha = -0.832$, $\beta = -0.181$ and $\varepsilon = 0.058$ for the right crack. As indicated in Equations (63) and (64), the values for the local stress intensity factor solutions depend on the kink length a when the kink length approaches to 0 for $\varepsilon \neq 0$. The dependence of the solutions on the kink length a presents a challenge to evaluate the local stress intensity factors k_{I} and k_{II} at zero kink length for estimation of fatigue lives based on a fatigue crack growth model, even though the oscillation is well within the kink length that is too small to be of concern. This challenge prevents the evaluation of k_{I} and k_{II} at zero kink length ($a = 0$) in Equations (63) and (64).

For cracks between similar materials, Equations (63) and (64) can be reduced to those of Cotterell and Rice [2] as

$$k_I = (c_R + d_R)K_I^A - (c_I + d_I)K_{II}^A \quad (65)$$

$$k_{II} = (c_I - d_I)K_I^A + (c_R - d_R)K_{II}^A \quad (66)$$

It should be noted that the stresses at the crack tip recover the traditional $1/\sqrt{r}$ singularity in this case.

The local stress intensity factor solutions k_{I} and k_{II} for kinked cracks with finite kink lengths in lap-shear specimens can be expressed in the normalized forms based on the beam bending theory as

$$k_I\left(\frac{a}{t_u}\right) = f_I\left(\frac{a}{t_u}\right)\cdot\frac{F}{b\sqrt{t_u}} \tag{67}$$

$$k_{II}\left(\frac{a}{t_u}\right) = f_{II}\left(\frac{a}{t_u}\right)\cdot\frac{F}{b\sqrt{t_u}} \tag{68}$$

and the local effective stress intensity factor solution k_e can be expressed as

$$k_e\left(\frac{a}{t_u}\right) = \sqrt{k_I^2\left(\frac{a}{t_u}\right) + k_{II}^2\left(\frac{a}{t_u}\right)} = f_e\left(\frac{a}{t_u}\right)\cdot\frac{F}{b\sqrt{t_u}} \tag{69}$$

where f_I, f_{II} and f_e are dimensionless geometric functions which depend on the normalized kink length a/t_u for this particular set of the geometry and material combination in the lap-shear specimen. The analytical local stress intensity factor k_I and k_{II} solutions for the kinked cracks in the lap-shear specimens can be obtained using Equations (63) and (64) with the values of K_1 and K_2 obtained from the finite element analyses. The results will be presented in the normalized form in the following section.

5.5. Computational local stress intensity factor solutions for kinked cracks

In this investigation, two-dimensional plane strain finite element analyses were conducted for the adhesive-bonded lap-shear specimen to investigate the local stress intensity factor solutions for kinked cracks with different kink lengths. It should be mentioned that the analytical local stress intensity factor solutions based on the global stress intensity factor solutions in Equations (63) and (64) are only valid when the kink length a is small. Figure

5.5(a) shows a schematic of a two-dimensional finite element model of an adhesive-bonded lap-shear specimen and the boundary conditions. The geometry, the loading and the boundary conditions of the specimen are the same as those shown in Figure 5.3(a). In Figure 5.5(a), a kinked crack is shown to grow from the right main crack tip into the upper magnesium sheet. Based on the micrograph in Figure 4.8(g), the kink angle is selected to be $30°$. Figure 5.5(b) shows a close-up view of the finite element mesh near the kinked crack for $a/t_u = 0.1$. The procedure of the finite element analyses is the same as that stated in section 4. Thirteen normalized kink lengths, $a/t_u = 1.25\times10^{-5}$, 3.125×10^{-3}, 6.25×10^{-3}, 0.0125, 0.025, 0.05, 0.1, 0.2, 0.3, 0.4, 0.5, 0.6 and 0.7 are used in this study since the maximum normalized kink length as observed in the experiment in Chapter 4 is about 0.7. First, the local stress intensity factor solutions are obtained computationally for the adhesive-bonded lap-shear specimen with the material properties as specified in section 5.3. These computational results are then compared with the analytical solutions in Equations (63) and (64) with the values of K_1^A and K_2^A obtained from the finite element analyses.

Figures 5.6(a) and 5.6(b) show the computational results and the analytical solutions for the dimensionless geometric function f_I (normalized k_I) as a function of the normalized kink length a/t_u in the linear and semi-log scales, respectively. As shown in Figure 5.6(b), the computational results approach to the analytical solution as the normalized kink length decreases to a very small value. Also, the computational local stress intensity factor k_I increases significantly as the kink length increases while the analytical local stress intensity factor stays almost the same at large kink lengths.

Figures 5.6(c) and 5.6(d) show the computational results and the analytical solutions for the dimensionless geometric function f_{II} (normalized k_{II}) as a function of the normalized kink length a/t_u in the linear and semi-log scales, respectively. It is noted that the magnitude of the local stress intensity factor k_{II} is small compared to that of the local stress intensity factor k_I. As shown in Figure 5.6(d), the computational results approach to the analytical solution as the normalized kink length decreases to a very small value. Also, the computational local stress intensity factor k_{II} increases significantly as the kink length increases while the analytical local stress intensity factor just increases slightly at large kink lengths.

Figures 5.6(e) and 5.6(f) show the computational results and the analytical solutions for the dimensionless geometric function f_e (normalized k_e) as a function of the normalized kink length a/t_u in the linear and log-log scales, respectively. As shown in Figure 5.6(f), the computational results approach to the analytical solution as the kink length decreases. Also, the computational local stress intensity factor k_e increases as the kink length increases while the analytical local stress intensity factor stays almost the same at large kink lengths. It is noted that both the computational results and the analytical solutions for k_e are similar to those for k_I because the magnitudes of the k_{II} solutions are small compared to those of the k_I solutions. The results in Figure 5.6 indicate that the analytical solution may be used to estimate the effective local stress intensity factors when the kink length is very small.

For fatigue life estimation, the local effective stress intensity factor at zero kink length is needed for a kinked fatigue crack growth model. Based on the results presented earlier, a simple way to estimate the local stress intensity factor solution at zero kink length in lap-shear specimen of dissimilar sheet materials under plane strain conditions is to choose a kink length that is

reasonably small from Equations (63) and (64). A suggested kink length is the average grain size. Using a kink length smaller than the average grain size for Equations (63) and (64) may not be practical since the material can no longer be treated as homogeneous linear elastic. The magnesium sheet used in this study contains highly deformed grain structure due to the rolling process. The microstructure consists of small broken grains and twins in larger grains. The grain size of the magnesium sheet ranges from 2 to 15 μm with an average grain size of 5 μm in Santella et al. [13]. As shown in Figure 5.6(f), the effective stress intensity factor solution obtained from the analytical solution is 20% smaller than that obtained from the finite element analysis for the kink length equal to the average grain size. This value may be considered for the solution for zero kink length. The method provides an easy and yet reasonable approach for evaluating the stress intensity factor solutions for zero or near zero kink length and is useful for fatigue life estimations since the fatigue crack growth model needs the local stress intensity factors at zero kink length.

The increasing stress intensity factor solutions with the increasing kink length as shown from the results of the finite element analyses also explain the increasing kink length with the decreasing load range observed in the failed specimens under cyclic loading conditions. Since the stress intensity factors at the kinked crack tip increase as the kinked crack grows, it can eventually reach the critical fracture resistance of the magnesium sheet and causes the kinked crack to grow through the magnesium sheet. The maximum kink length calculated using the stress intensity factor solutions obtained from the finite element analyses and the fracture toughness of the magnesium (K_{Ic} = 17.6 $\mathrm{MPa}\sqrt{\mathrm{m}}$ in Somekawa and Mukai [14]) are 0.91 and 1.37 mm at the load ranges of 4,630 and 2,900 N, respectively, for the kinked crack failure observed in the experiment. The critical maximum kink lengths observed in the magnesium

sheets are 0.3 and 0.9 mm at the upper and lower bounds of load ranges of 4,630 and 2,900 N, respectively. The general trends of the predicted and observed maximum kink lengths are in agreement. When the fracture toughness of K_{Ic} = 10.8 $\mathrm{MPa}\sqrt{\mathrm{m}}$ is selected, the predicted maximum kink lengths at these two load ranges exactly match the experimental results. This suggests that the sharp turning of the kinked crack from 30° to 90° is due to reaching the critical fracture resistance of the magnesium sheet.

5.6. Fatigue life estimation

The fatigue life estimations for the lap-shear specimens are based on the Paris law for crack growth and the stress intensity factor solutions obtained from the finite element analyses. For the kinked crack failures in the lap-shear specimens, the fatigue crack growth is under local combined mode I and mode II loading conditions. An equivalent stress intensity factor k_{eq} is defined in Broek [15] as

$$k_{eq}(a) = \sqrt{k_I(a)^2 + \gamma\, k_{II}(a)^2} \tag{70}$$

where γ is an empirical constant to account for the sensitivity of materials to the mode II loading conditions. For lack of any further information, γ is assumed 1 in this study. Now the Paris law is used to describe the fatigue crack growth for the kinked crack as

$$\frac{\mathrm{d}a}{\mathrm{d}N} = C\left(\Delta k_{eq}(a)\right)^m \tag{71}$$

where N is the life or number of cycles, C and m are material constants, and Δk_{eq} is the range of the equivalent stress intensity factor as a function of the kink length a.

Since the local stress intensity factors are functions of the kink length a, the fatigue life of the lap-shear specimens can be obtained by integrating Equation (71) as

$$N = \frac{1}{C}\left\{\int_0^{a_1}\left[\Delta k_{eq}(a)\right]^{-m}\mathrm{d}a + \int_{a_1}^{a_2}\left[\Delta k_{eq}(a)\right]^{-m}\mathrm{d}a + \cdots + \int_{a_{i-1}}^{a_i}\left[\Delta k_{eq}(a)\right]^{-m}\mathrm{d}a\right\} \quad (72)$$

where a_1, a_2,…, a_{i-1} and a_i represent the values of different kink lengths. Here, a_i represents the crack length when the maximum equivalent or effective stress intensity factor reaches the fracture toughness value of 17.6 $\mathrm{MPa}\sqrt{\mathrm{m}}$ (which represents the fracture toughness of the 90° specimens in Somekawa and Mukai [14]). The stress intensity factor solutions for different kink lengths obtained from finite element analyses were used to estimate the fatigue lives. Since the material constants for the Paris law for the rolled AZ31B-H24 used in this study are not available, the material constants were chosen from the AZ31B with a similar grain size and load ratio. The values of C and m used to estimate the fatigue life are 4×10^{-7} $\mathrm{mm/cycle}/\left(\mathrm{MPa}\sqrt{\mathrm{m}}\right)^m$ and 2.7, respectively, as presented in Ishihara et al. [16]. It should be noted that the fatigue crack growth rate varies with the grain size, load ratio, texture and test condition for AZ31B. Uematsu et al. [17] studied the fatigue crack growth rate for extruded AZ31B and found the fatigue crack growth rate decreases with the decreasing grain size. Zheng et al. [18] conducted tests to obtain the fatigue crack growth rates under different load ratios for extruded AZ31B and found the fatigue crack growth rate increases with the increasing load ratio. Ishihara et al. [19] studied the fatigue crack growth rates for extruded and rolled AZ31 and found a significant texture effect on the fatigue crack growth rate for both extruded and rolled AZ31. Tokaji et al. [20] conducted the fatigue tests under dry and humid air conditions for rolled AZ31 and found an order of magnitude difference in fatigue crack growth rate.

Figure 5.7 shows the experimental results and fatigue life estimations for adhesive-bonded lap-shear specimens of magnesium and steel sheets. Under low-cycle loading conditions, the crack grew in an interfacial failure between the epoxy layer and the steel sheet during the initial load. As cyclic loads continued, the interfacial failure gradually changed to near interface

cohesive failure in the epoxy layer. Under high-cycle loading conditions, the specimens failed in the kinked crack failure. The estimated fatigue lives for the kinked crack failure for the adhesive-bonded lap-shear specimens are shown as the dash line in Figure 5.7. It appears that the fatigue life estimations are lower than the experimental results. However, the trend of the fatigue life estimations in general agrees well with that of the experimental results. It is noted that the values of C and m used to estimate the fatigue lives in this study are from an extruded AZ31. The distinct texture feature in the rolled AZ31 compared to that of the extruded AZ31 can change the values of C and m and, in turn, change the corresponding fatigue lives. It should be mentioned that the computational results of the local stress intensity factor solutions at the kinked crack length of 5 μm was used for the fatigue life estimation from the crack length of 0 μm to 5 μm. When the computational stress intensity factor solutions are not available, the analytical solution at the kinked crack length of 5 μm may be used for fatigue life estimation in this crack length range.

Based on the linear elastic fracture mechanics, the plastic zone size of the kinked crack in the magnesium sheet under cyclic loading conditions at the time when the effective local stress intensity factor reaches the fracture toughness of 17.6 $\mathrm{MPa}\sqrt{\mathrm{m}}$ or 10.8 $\mathrm{MPa}\sqrt{\mathrm{m}}$ are small compared to the crack lengths of interest. Therefore, the use of linear elastic fracture mechanics and the kinked crack growth model for the fatigue life estimations is reasonable in this study. Based on the beam bending theory, the magnesium sheet is yielded substantially at the maximum load of 5,144 N of the load range of 4,630 N due to the combined tension and bending. However, the magnesium sheet near the right main crack tip was under elastic loading and unloading condition after the initial loading sine the stress range for elastic loading and unloading is quite large. The plastic flow near the crack tip is due to the singular behavior near the crack tip.

Therefore, the fatigue life estimations based on the kinked crack growth model is reasonable with the stress intensity factor solutions.

5.7. Conclusions

In this chapter, stress intensity factor solutions for adhesive-bonded lap-shear specimens of magnesium alloy AZ31 and hot-dip-galvanized (HDG) mild steel sheets with and without kinked cracks are investigated for fatigue life estimations. First, the analytical global J integral and effective stress intensity factor solutions for main cracks in lap-shear specimens of three dissimilar sheets under plane strain conditions are developed based on the beam bending theory. The global stress intensity factor solutions for the main cracks in the lap-shear specimens from the corresponding finite element analyses are then presented to validate the analytical solutions.

Next, the local stress intensity factor solutions for kinked cracks with the experimentally observed kink angle as functions of the kink length from the corresponding finite element analyses are presented and the computational solutions are also compared with the analytical solutions at small kink lengths. The results indicate that the computational local stress intensity factor solutions for kinked cracks appear to approach to the analytical solutions as the kink length decreases to a very small kink length and the kinked crack is under dominant mode I loading conditions. The experimentally observed kink angle in general agrees with the analytical solution. The computational results also indicate that the local stress intensity factor solutions at a small kink length of microstructural significance may be used as the initial stress intensity factor solutions for zero kink length for fatigue life estimations when the computational results are not available.

Finally, the computational local stress intensity factor solutions are adopted to estimate the fatigue lives of the lap-shear specimens based on a kinked crack growth model and available material constants for the Paris law. The general trend of fatigue life estimations agrees with that of the experimental results but the fatigue life estimations are lower than the experimental results.

Table 5.1. The normalized local stress intensity factor solutions obtained from ABAQUS for different kink lengths at a kink angle of $\varphi = 30°$.

a/t_u	1.25×10^{-5}	3.125×10^{-3}	6.25×10^{-3}	0.0125	0.025	0.05
f_I	1.346	1.486	1.529	1.590	1.680	1.808
f_{II}	-0.241	0.073	0.146	0.243	0.372	0.545
f_e	1.368	1.488	1.536	1.609	1.720	1.888

Table 5.1. continued

a/t_u	0.1	0.2	0.3	0.4	0.5	0.6	0.7
f_I	1.999	2.312	2.618	2.956	3.346	3.810	4.368
f_{II}	0.767	1.066	1.300	1.520	1.750	2.004	2.299
f_e	2.141	2.546	2.923	3.324	3.776	4.305	4.936

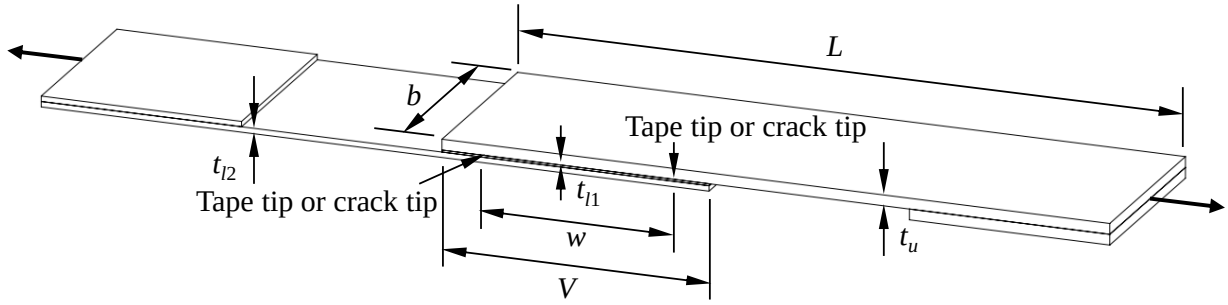

Figure 5.1. A schematic of an adhesive-bonded lap-shear specimen. The applied force F is shown as the bold arrows.

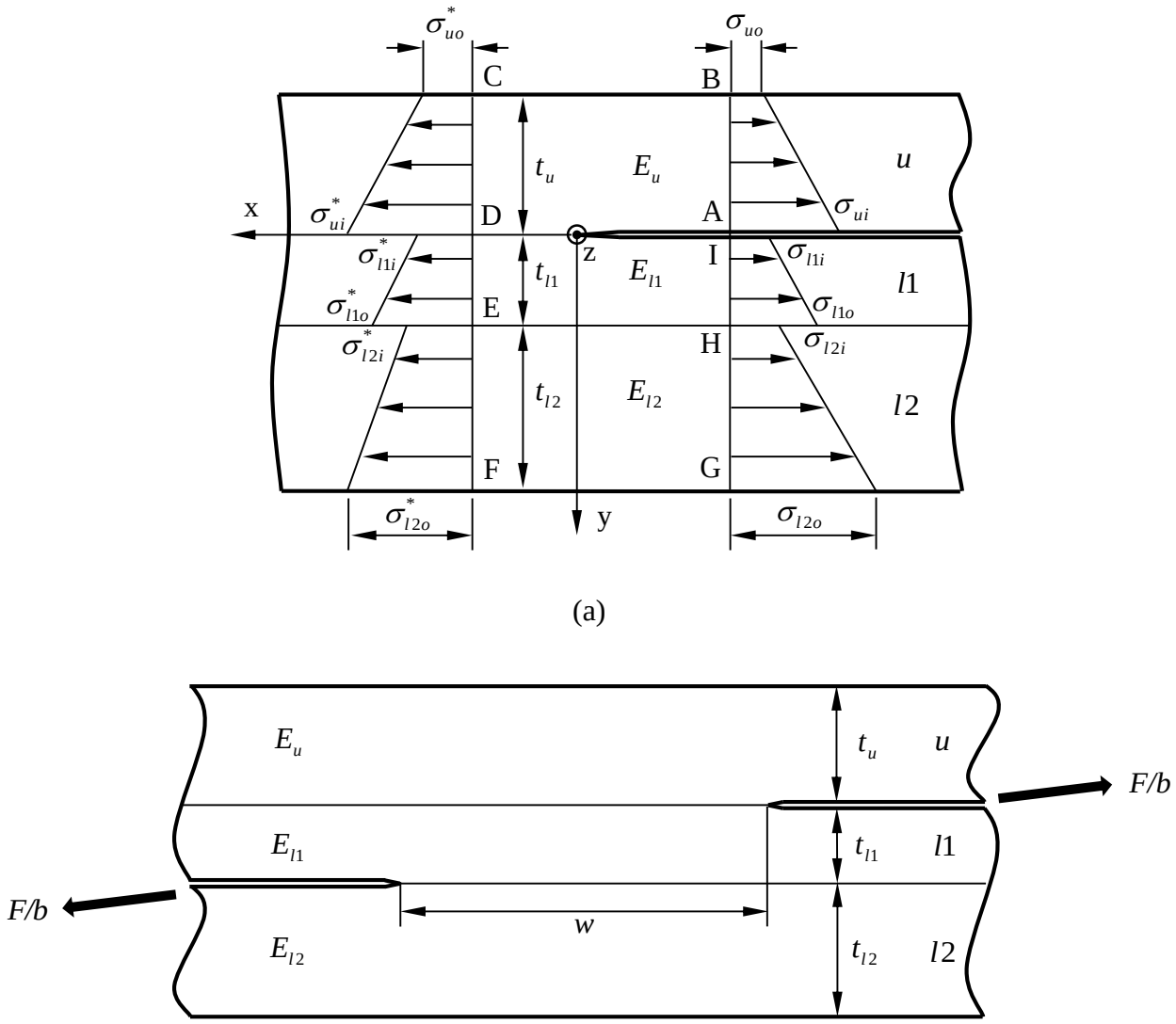

Figure 5.2. (a) A schematic of the right crack tip in an adhesive-bonded lap-shear specimen showing the normal stresses σ_{ui}, σ_{uo}, σ_{l1i}, σ_{l1o}, σ_{l2i} and σ_{l2o} at the inner (i) and outer (o) surfaces of the upper sheet (u), lower sheet 1 ($l1$) and lower sheet 2 ($l2$), respectively. (b) A schematic of an adhesive-bonded lap-shear specimen near the crack tips showing the positions of the two main crack tips with the applied load per unit width, F/b.

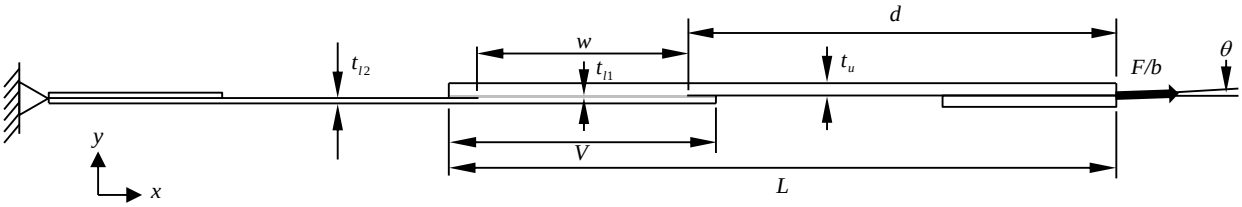

(a)

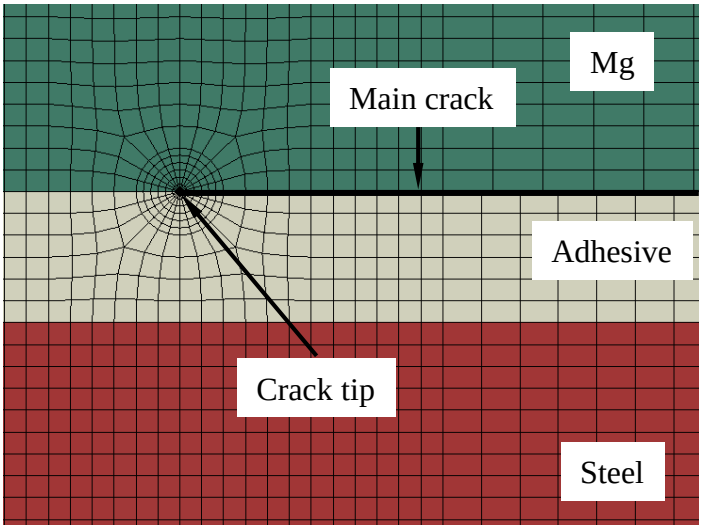

(b)

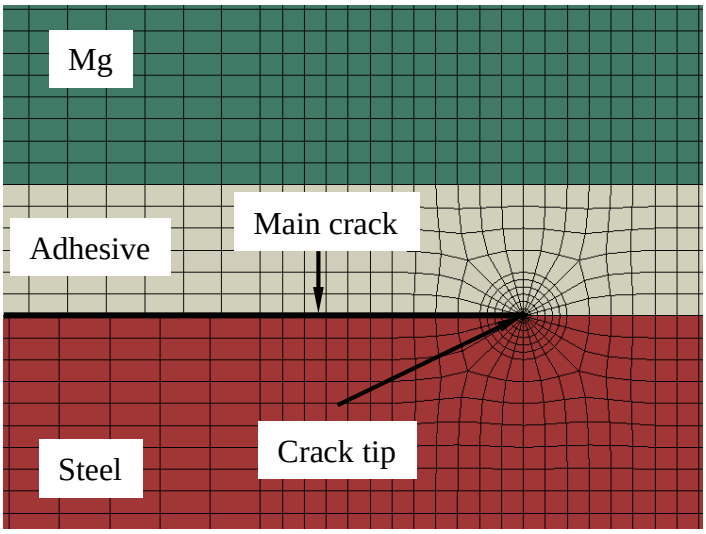

(c)

Figure 5.3. (a) A schematic of a two-dimensional adhesive-bonded lap-shear specimen with the boundary and loading conditions. Close-up views of the finite element meshes near (b) the right crack tip and (c) the left crack tip.

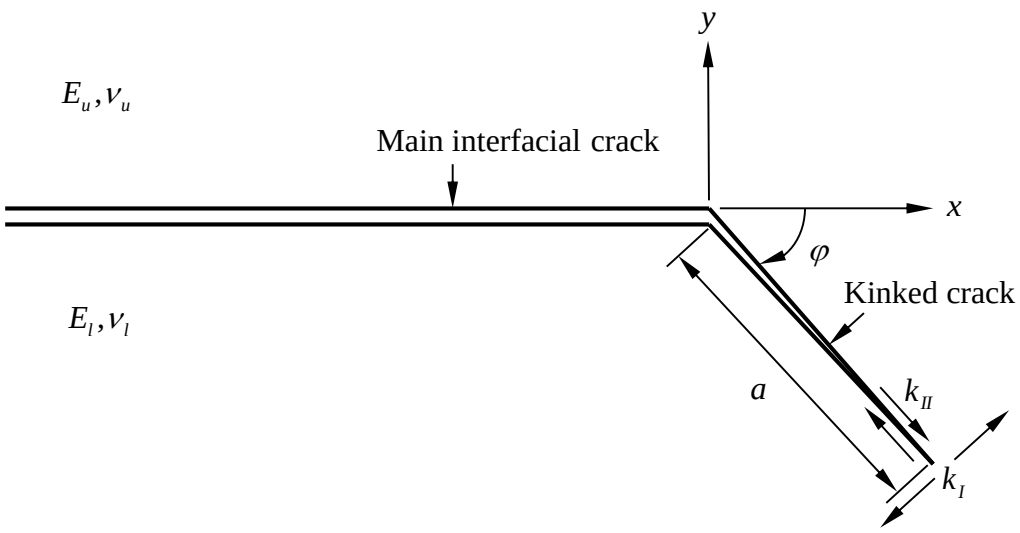

Figure 5.4. A schematic of a main crack and a kinked crack with the kink length a and the kink angle φ.

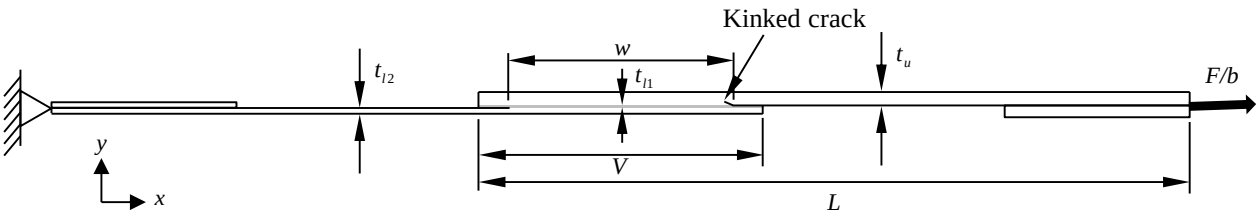

(a)

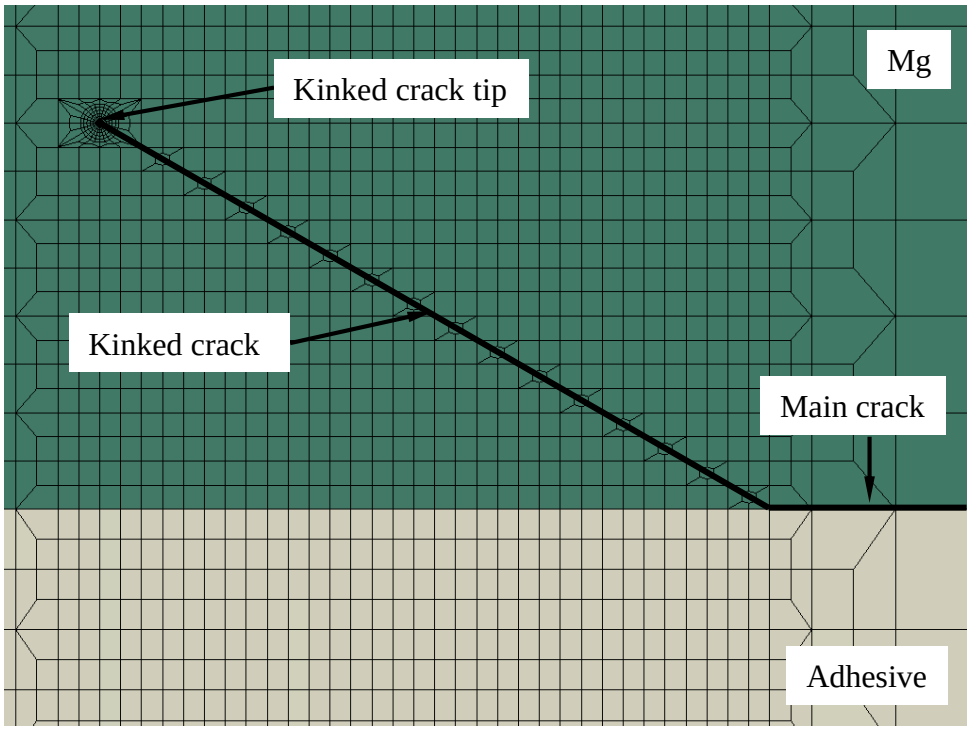

(b)

Figure 5.5. (a) A schematic of a two-dimensional finite elemental model of an adhesive-bonded lap-shear specimen with a kinked crack with the boundary and loading conditions. (b) A close-up view of the finite element mesh near the right crack tip showing the preformed crack and the kinked crack.

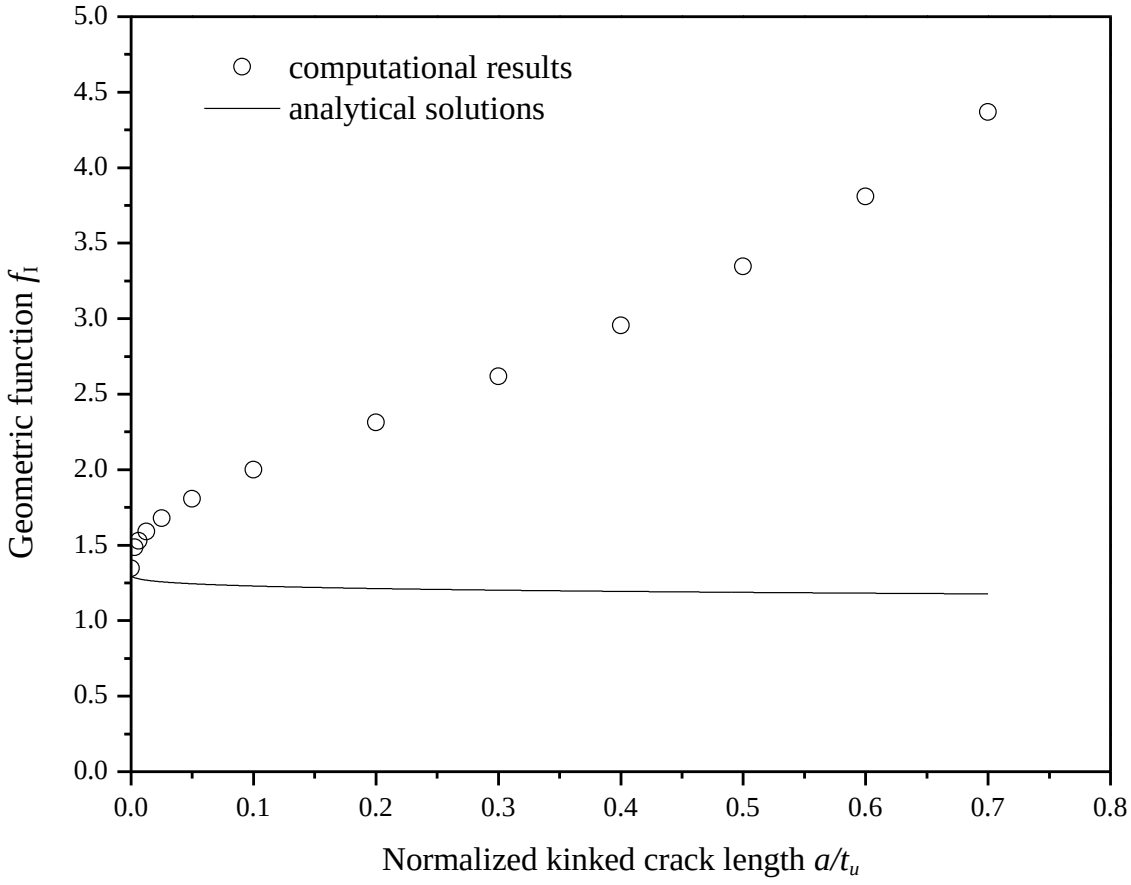
computational results
analytical solutions
Geometric function f_I
Normalized kinked crack length a/t_u
5.0
4.5
4.0
3.5
3.0
2.5
2.0
1.5
1.0
0.5
0.0
0.0
0.1
0.2
0.3
0.4
0.5
0.6
0.7
0.8

(a)

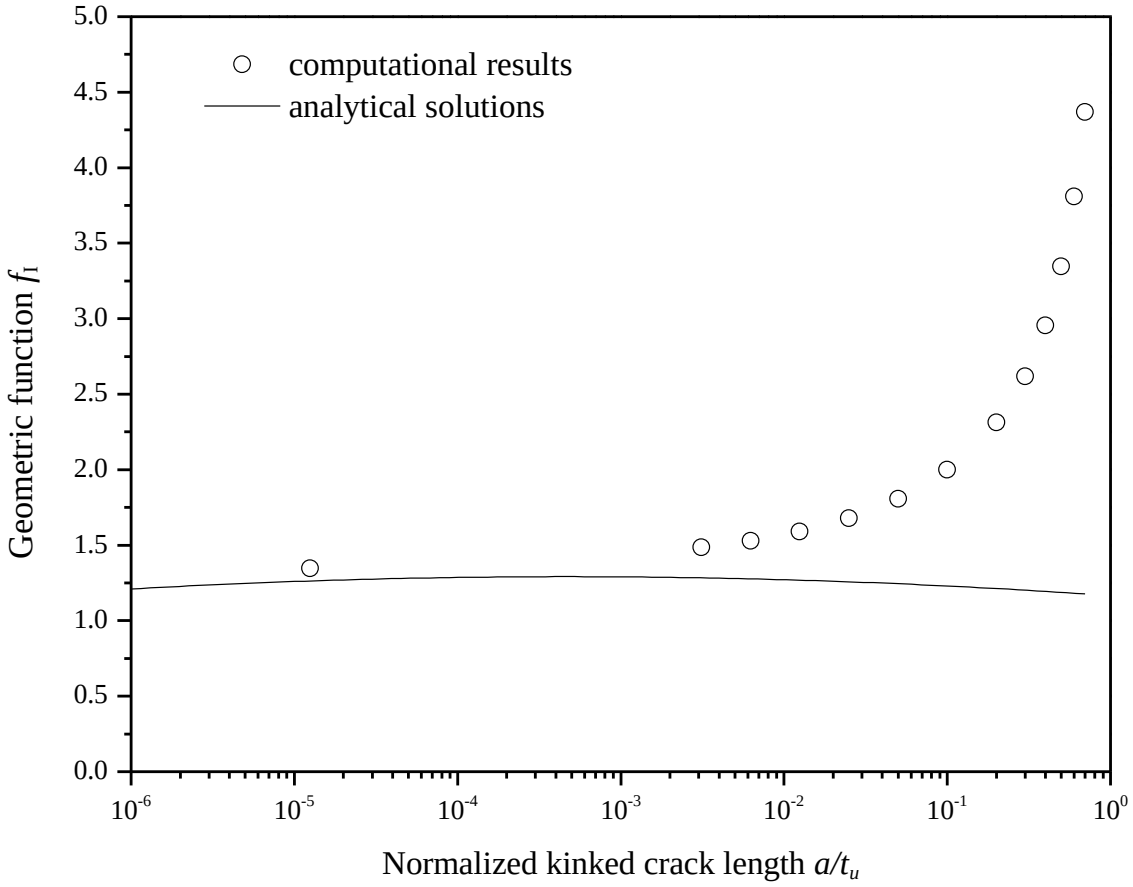
computational results
analytical solutions
Geometric function f_I
Normalized kinked crack length a/t_u
5.0
4.5
4.0
3.5
3.0
2.5
2.0
1.5
1.0
0.5
0.0
10^{-6}
10^{-5}
10^{-4}
10^{-3}
10^{-2}
10^{-1}
10^{0}

(b)

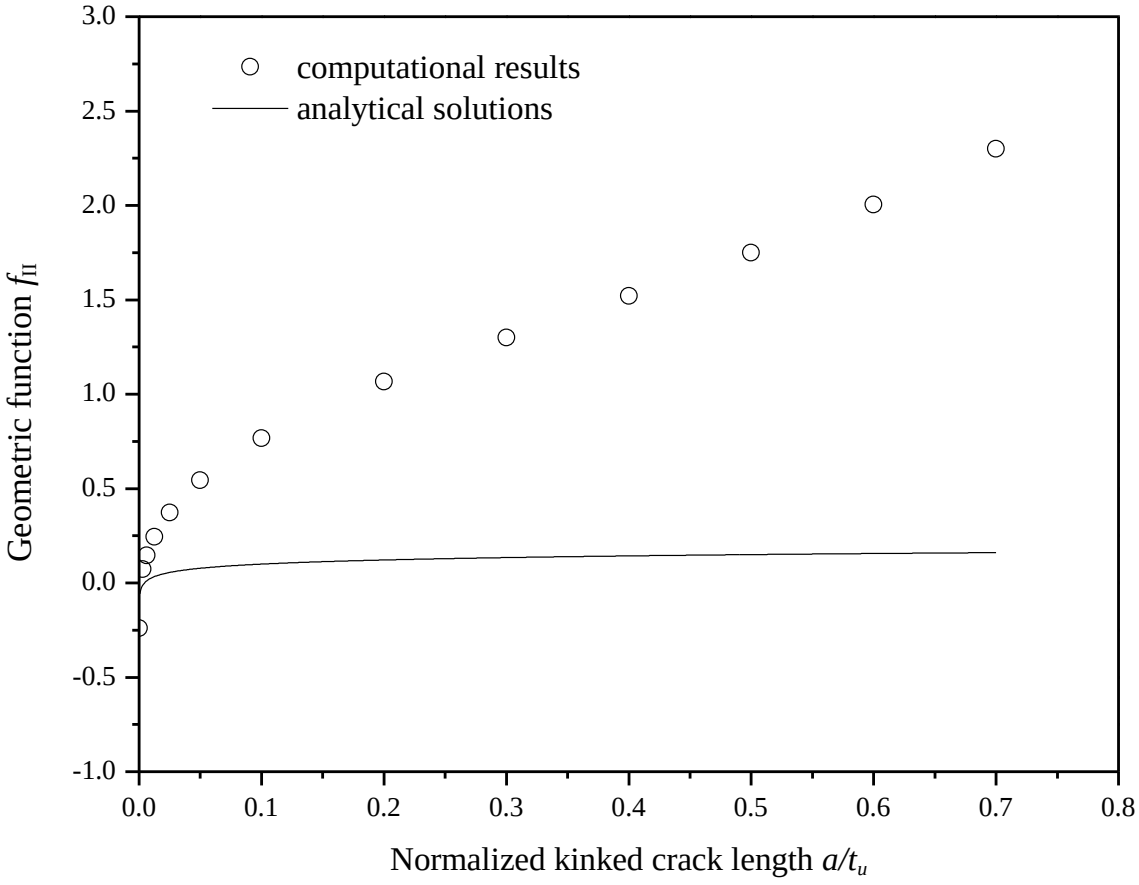
computational results
analytical solutions
Geometric function f_{II}
Normalized kinked crack length a/t_u
3.0
2.5
2.0
1.5
1.0
0.5
0.0
-0.5
-1.0
0.0
0.1
0.2
0.3
0.4
0.5
0.6
0.7
0.8

(c)

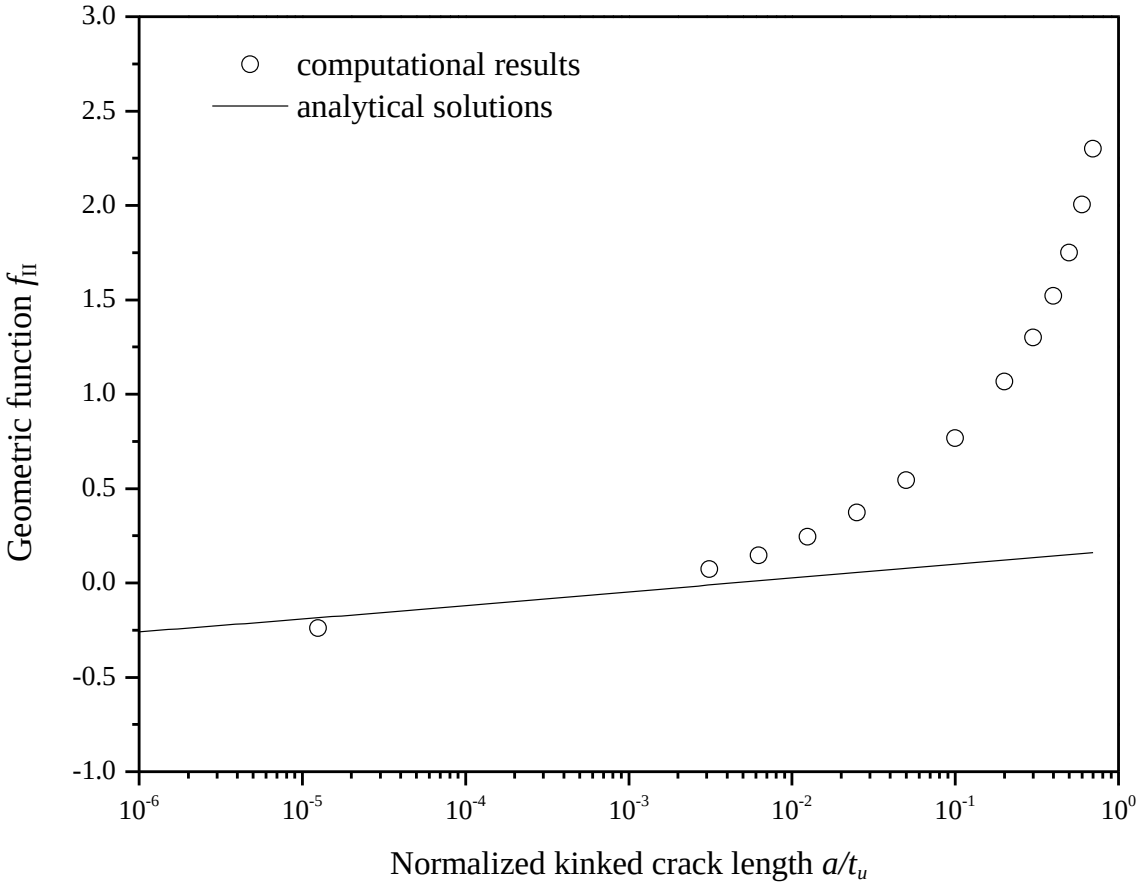
computational results
analytical solutions
Geometric function f_{II}
Normalized kinked crack length a/t_u
3.0
2.5
2.0
1.5
1.0
0.5
0.0
-0.5
-1.0
10^{-6}
10^{-5}
10^{-4}
10^{-3}
10^{-2}
10^{-1}
10^{0}

(d)

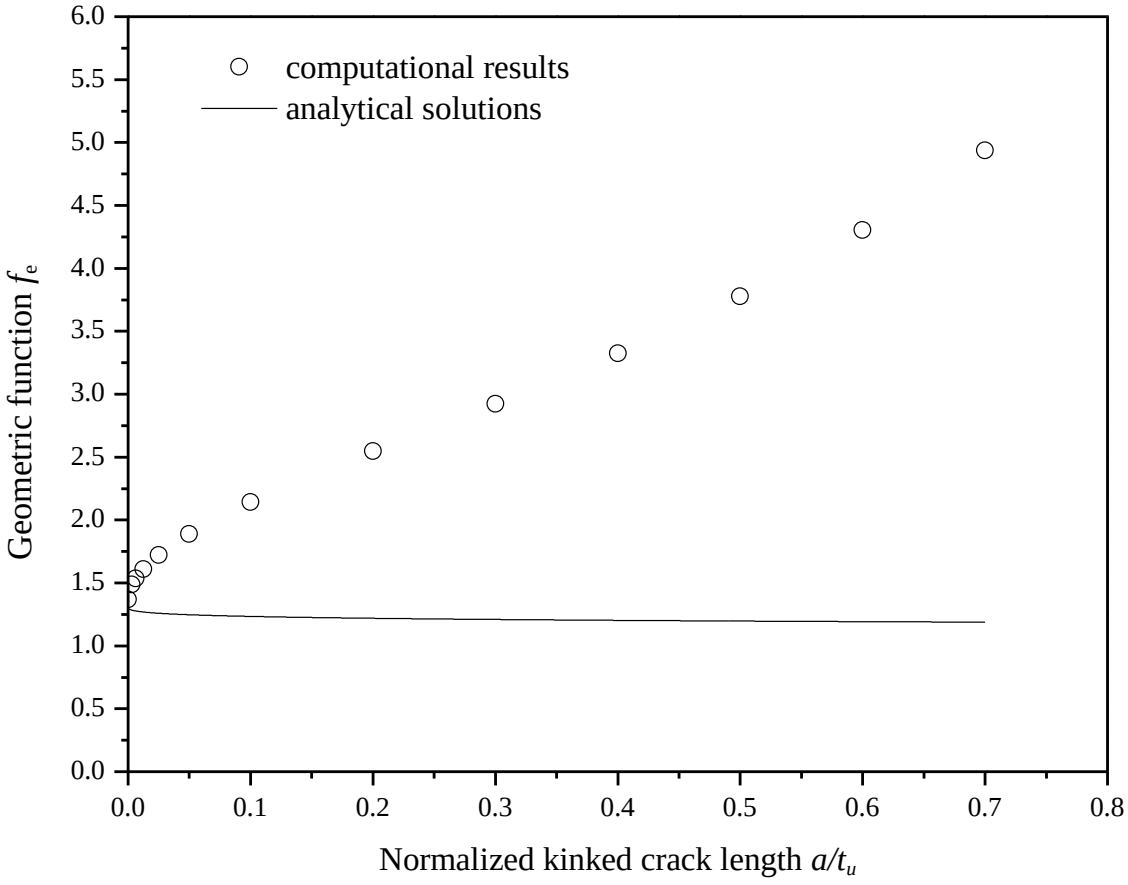
computational results
analytical solutions
Geometric function f_e
Normalized kinked crack length a/t_u
6.0
5.5
5.0
4.5
4.0
3.5
3.0
2.5
2.0
1.5
1.0
0.5
0.0
0.0
0.1
0.2
0.3
0.4
0.5
0.6
0.7
0.8

(e)

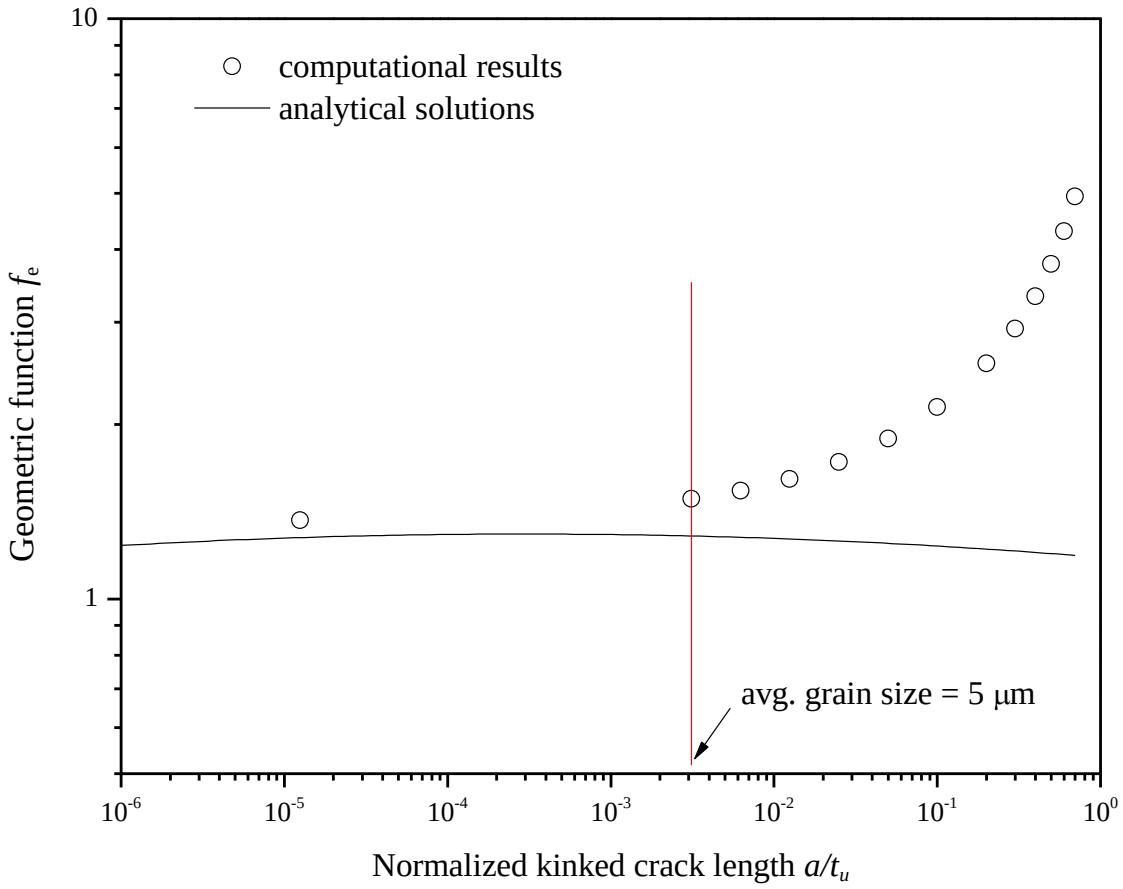

(f)

Figure 5.6. The computational results and analytical solutions for (a) f_I in the linear scale, (b) f_I in the semi-log scale, (c) f_{II} in the linear scale, (d) f_{II} in the semi-log scale, (e) f_e in the linear scale, and (f) f_e in the log-log scale as a function of the normalized kink length a/t_u for $\varphi = 30°$ for the adhesive-bonded lap-shear specimen.

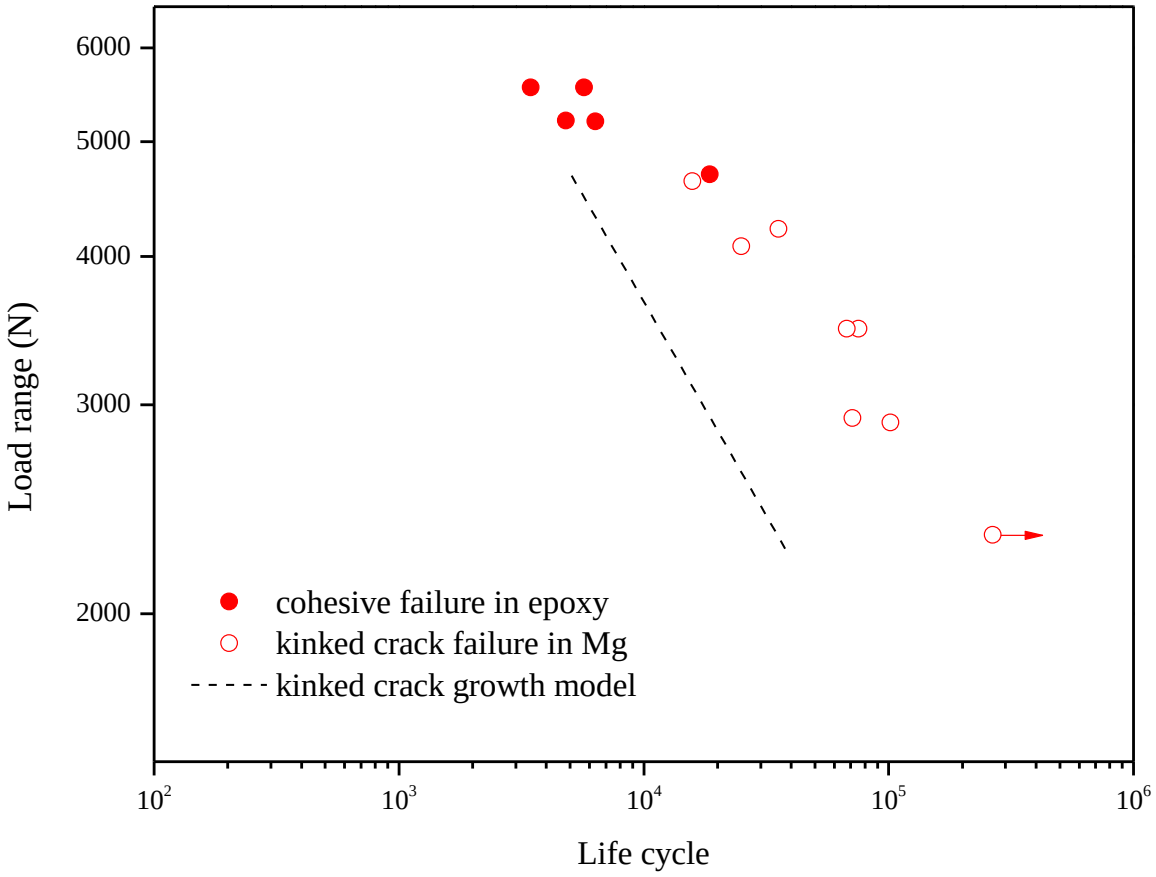

Figure 5.7. Experimental results of the fatigue tests at the load ratio R of 0.1 and fatigue life estimations for the adhesive-bonded lap-shear specimens.

Acknowledgements

This research was sponsored by the U.S. Department of Energy, Assistant Secretary for Energy Efficiency and Renewable Energy, Office of Vehicle Technologies, as part of the Lightweight Materials Program. Helpful discussion with Drs. Tsung-Yu Pan, Michael Santella and Zhili Feng of Oakridge National Laboratory and Dr. Teresa Franklin of General Motors are greatly appreciated.

References

[1] T. Franklin, "Fatigue Behavior and Life Estimation for Dissimilar Ultrasonic Welds in Lap-Shear Specimens of Magnesium and Galvanized Steel Sheets," Ph.D. thesis, Department of Mechanical Engineering, University of Michigan, Ann Arbor, Michigan, 2013.

[2] B. Cotterell and J. R. Rice, "Slightly Curved or Kinked Cracks," International Journal of Fracture, vol. 16, pp. 155-69, 1980.

[3] M.-Y. He and J. W. Hutchinson, "Kinking of a Crack out of an Interface," Journal of Applied Mechanics, vol. 56, pp. 270-8, 1989.

[4] S. Zhang, "Stress Intensities Derived from Stresses around a Spot Weld," International Journal of Fracture, vol. 99, pp. 239-257, 1999.

[5] J. R. Rice, "A Path Independent Integral and the Approximate Analysis of Strain Concentration by Notches and Cracks " Journal of Applied Mechanics, vol. 35, pp. 379-386, 1968.

[6] D. A. Wang, P. C. Lin, and J. Pan, "Geometric Functions of Stress Intensity Factor Solutions for Spot Welds in Lap-Shear Specimens," International Journal of Solids and Structures, vol. 42, pp. 6299-6318, 2005.

[7] D. A. Wang, S. H. Lin, and J. Pan, "Stress Intensity Factors for Spot Welds and Associated Kinked Cracks in Cup Specimens," International Journal of Fatigue, vol. 27, pp. 581-598, 2005.

[8] P. C. Lin and J. Pan, "Closed-Form Structural Stress and Stress Intensity Factor Solutions for Spot Welds in Commonly Used Specimens," Engineering Fracture Mechanics, vol. 75, pp. 5187-5206, 2008.

[9] J. R. Rice and G. C. Sih, "Plane Problems of Cracks in Dissimilar Media," Journal of Applied Mechanics, vol. 32, pp. 418-23, 1965.

[10] J. R. Rice, "Elastic Fracture Mechanics Concepts for Interfacial Cracks," Journal of Applied Mechanics, vol. 55, pp. 98-103, 1988.

[11] ABAQUS V6.12 User Manual, SIMULIA, 2012.

[12] M.-Y. He and J. W. Hutchinson, "Kinking of a Crack out of an Interface: Tabulated Solution Coefficients," Harvard University Report MECH-113A, 1988.

[13] M. Santella, T. Franklin, J. Pan, T.-Y. Pan, and E. Brown, "Ultrasonic Spot Welding of AZ31B to Galvanized Mild Steel," SAE International Journal of Materials and Manufacturing, vol. 3, pp. 652-657, 2010.

[14] H. Somekawa and T. Mukai, "Fracture Toughness in a Rolled AZ31 Magnesium Alloy," Journal of Alloys and Compounds, vol. 417, pp. 209-213, 2006.

[15] D. Broek, Elementary Engineering Fracture Mechanics, 4th ed. Dordrecht ; Boston : Hingham, Mass., Martinus Nijhoff, 1986.

[16] S. Ishihara, A. J. McEvily, M. Sato, K. Taniguchi, and T. Goshima, "The Effect of Load Ratio on Fatigue Life and Crack Propagation Behavior of an Extruded Magnesium Alloy," International Journal of Fatigue, vol. 31, pp. 1788-1794, 2009.

[17] Y. Uematsu, K. Tokaji, M. Kamakura, K. Uchida, H. Shibata, and N. Bekku, "Effect of Extrusion Conditions on Grain Refinement and Fatigue Behaviour in Magnesium Alloys," Materials Science and Engineering: A, vol. 434, pp. 131-140, 2006.

[18] S. Zheng, Q. Yu, and Y. Jiang, "An Experimental Study of Fatigue Crack Propagation in Extruded AZ31B Magnesium Alloy," International Journal of Fatigue, vol. 47, pp. 174-183, 2013.

[19] S. Ishihara, S. Taneguchi, H. Shibata, T. Goshima, and A. Saiki, "Anisotropy of the Fatigue Behavior of Extruded and Rolled Magnesium Alloys," International Journal of Fatigue, vol. 50, pp. 94-100, 2013.

[20] K. Tokaji, M. Nakajima, and Y. Uematsu, "Fatigue Crack Propagation and Fracture Mechanisms of Wrought Magnesium Alloys in Different Environments," International Journal of Fatigue, vol. 31, pp. 1137-1143, 2009.

Chapter 6
Graphical Stress Intensity Factor Solutions for Welds between Two Dissimilar Sheets with Different Thicknesses under Plane Strain Conditions

6.1. Introduction

Incorporating lightweight materials into the steel vehicle structure requires joining of these dissimilar materials. Therefore, fracture and fatigue analyses of dissimilar welds between steel, aluminum and magnesium sheets are of interest. For lithium-ion battery packs in electric and hybrid vehicles, the electrodes of these batteries are made of aluminum and copper. Joining the aluminum and copper tabs in battery packs is also needed. Therefore, fracture and fatigue analyses of dissimilar welds between aluminum and copper sheets are also of interest.

In many cases, analyses of continuous dissimilar welds can be treated as two-dimensional plane strain problems. Franklin [1] machined the lap-shear specimens of ultrasonic spot welds of dissimilar magnesium and steel sheets into a dog-bone shaped profile. Figures 6.1(a) and 6.1(b) show the lap-shear specimens with ultrasonic spot welds of magnesium and steel sheets before and after being machined into a dog-bone shape, respectively. Figure 4.6(a) shows an optical micrograph of the cross section near the ultrasonic spot weld in the lap-shear specimen of magnesium and steel sheets. Two-dimensional plane strain analyses can be used to model the fatigue and fracture behavior of the dissimilar welds in this kind of dog-bone lap-shear specimens [1]. Two dimensional plane strain analysis were also conducted to analyze similar laser welds in dog-bone shaped lap-shear specimens in Sripichai et al. [2]. The structural stress and stress intensity factor and J integral solutions for similar and dissimilar welds in lap-shear

specimens are quite important for fracture and fatigue analyses since lap-shear specimens are commonly used to test the fracture and fatigue of the welds. Based on the work of Zhang [3], Tran and Pan [4] recently presented analytical stress intensity factor and J integral solutions for dissimilar spot welds in lap-shear specimens of different materials and thicknesses in the normalized forms. The solutions are presented in the graphical form and they are quite conveniently used as references for fracture and fatigue analyses.

In this chapter, the analytical stress intensity factor solutions for welds in lap-shear specimens for two dissimilar sheets based on the beam bending theory are first reviewed. The analytical solutions are then presented in the normalized forms. Next, two-dimensional finite element analyses were selectively conducted to validate the analytical solutions based on the beam bending theory. The interfacial crack parameters, the stress intensity factor solutions, and the J integral solutions for welds in lap-shear specimens of different combinations of steel, aluminum, and magnesium, and the combination of aluminum and copper sheets of different thickness ratios are then presented for convenient fracture and fatigue analyses. The transition thickness ratios for critical crack locations for different combinations of dissimilar materials are then determined from the analytical solutions. The transition weld widths for applicable ranges of the weld widths for the analytical solutions based on the beam bending theory are also presented. Finally, fracture and fatigue behaviors of dissimilar ultrasonic magnesium/steel, dissimilar laser aluminum/copper, and similar laser steel welds in lap-shear specimens are examined and demonstrate the usefulness of the graphical stress intensity factor solutions presented.

6.2. Analytical stress intensity factor solutions based on the beam bending theory

Figure 6.2 shows a schematic of a lap-shear specimen. The applied force per unit width, F/b, is shown as the bold arrows. Here, b represents the specimen width. For the lap-shear specimen considered here, the weld width w is much larger than the upper and lower sheet thicknesses so that the beam bending theory is applicable. The upper and lower sheets are assumed to be isotropic linear elastic materials with the Young's modulus E_u, shear modulus G_u, and Poisson's ratio ν_u for the upper sheet material, and the Young's modulus E_l, shear modulus G_l, and Poisson's ratio ν_l for the lower sheet material. The upper and lower sheets have the nominal thicknesses t_u and t_l, respectively. The thickness and modulus ratios δ and η are defined, respectively, as

$$\delta = t_u / t_l \tag{1}$$

and

$$\eta = E'_u / E'_l \tag{2}$$

where

$$E'_u = E_u / (1-\nu_u^2) \tag{3}$$

and

$$E'_l = E_l / (1-\nu_l^2) \tag{4}$$

Figure 6.3 shows a two-dimensional model of two infinite strips made of dissimilar materials with different thicknesses and connection under plane strain conditions. The strip model can be used to represent the left or right portion of the specimen provided that the weld width w is large compared to the thicknesses of the upper and lower sheets. The normal

structural stresses σ_x^u and σ_x^l for the strip model with respect to the Cartesian coordinate system are schematically shown in Figure 6.3.

Figure 6.4 shows a schematic of the strip model near the crack tip. The normal stresses σ_{ui}, σ_{uo}, σ_{li}, σ_{lo}, σ_{ui}^*, σ_{uo}^*, σ_{li}^* and σ_{lo}^* represent the normal structural stresses at the inner (*i*) and outer (*o*) surfaces of the upper (*u*) and lower (*l*) strips, respectively. Note also that the normal structural stresses σ_{ui}^*, σ_{uo}^*, σ_{li}^* and σ_{lo}^* can be derived from the normal structural stresses σ_{ui}, σ_{uo}, σ_{li} and σ_{lo} based on the equilibrium equations and the continuity conditions of the strain and the strain gradient along the bond line as presented in Zhang [3] and Zuo and Hutchinson [5].

The asymptotic in-plane stress field around an interfacial crack tip is an oscillatory field that can be characterized by a complex stress intensity factor $\mathbf{K} = K_1 + iK_2$ ($i = \sqrt{-1}$) (Rice and Sih [6]). The stresses σ_y and τ_{xy} at a small distance r ahead of the interfacial crack tip are characterized by **K** as

$$\sigma_y + i\tau_{xy} = \frac{K_1 + iK_2}{\sqrt{2\pi r}}\left(\frac{r}{t}\right)^{i\varepsilon} \tag{5}$$

where K_1 and K_2 are mode 1 and mode 2 stress intensity factors of a crack at the interface of two dissimilar materials. Here, the bimaterial constant ε is defined as

$$\varepsilon = \frac{1}{2\pi}\ln\frac{\kappa_u / G_u + 1/G_l}{\kappa_l / G_l + 1/G_u} \tag{6}$$

where κ_u and κ_l are defined as

$$\kappa_u = 3 - 4\nu_u \tag{7}$$

and

$$\kappa_l = 3 - 4\nu_l \tag{8}$$

In Equation (5), t represents a characteristic length [3, 5, 7]. In this investigation, t is taken as the smaller value of the upper sheet thickness t_u as in Suo and Hutchinson [5] and Zhang [3]. It should be noted that when the two materials are identical, $\varepsilon = 0$. In this case, K_1 and K_2 in Equation (5) for the interfacial crack become the conventional stress intensity factors K_I and K_{II}, respectively.

Based on the J integral solution for the strip model and the analytical solutions for interfacial cracks in Suo and Hutchinson [5], Zhang [3] derived the stress intensity factor solutions K_1 and K_2 (as defined in Equation (5)) for welds joining sheets of different materials and thicknesses in terms of the structural stresses σ_{ui}, σ_{uo}, σ_{li} and σ_{lo} as

$$\begin{aligned} K_1 = {} & \frac{\cosh(\pi\varepsilon)\sqrt{t_u}}{2\sqrt{3(1+\eta)(1+4\eta\delta+6\eta\delta^2+3\eta\delta^3)(1+\tan^2\omega)}} \times \\ & \left\{ \left[\frac{(1+4\eta\delta+9\eta\delta^2+6\eta\delta^3)\tan\omega}{\sqrt{1+2\eta\delta(2+3\delta+2\delta^2)+\eta^2\delta^4}} - \sqrt{3} \right] \sigma_{ui} \right. \\ & - \left[\frac{(1+4\eta\delta+3\eta\delta^2)\tan\omega}{\sqrt{1+2\eta\delta(2+3\delta+2\delta^2)+\eta^2\delta^4}} + \sqrt{3} \right] \sigma_{uo} \\ & + \eta \left[\frac{\delta(1-2\eta\delta-3\eta\delta^2)\tan\omega}{\sqrt{1+2\eta\delta(2+3\delta+2\delta^2)+\eta^2\delta^4}} + \sqrt{3}(2+\delta) \right] \sigma_{li} \\ & \left. - \eta\delta \left[\frac{(1+4\eta\delta+3\eta\delta^2)\tan\omega}{\sqrt{1+2\eta\delta(2+3\delta+2\delta^2)+\eta^2\delta^4}} + \sqrt{3} \right] \sigma_{lo} \right\} \end{aligned} \tag{9}$$

and

$$K_2 = \frac{\cosh(\pi\varepsilon)\sqrt{t_u}}{2\sqrt{3(1+\eta)(1+4\eta\delta+6\eta\delta^2+3\eta\delta^3)(1+\tan^2\omega)}} \times$$
$$\left\{\left[\frac{1+4\eta\delta+9\eta\delta^2+6\eta\delta^3}{\sqrt{1+2\eta\delta(2+3\delta+2\delta^2)+\eta^2\delta^4}}+\sqrt{3}\tan\omega\right]\sigma_{ui}\right.$$
$$-\left[\frac{1+4\eta\delta+3\eta\delta^2}{\sqrt{1+2\eta\delta(2+3\delta+2\delta^2)+\eta^2\delta^4}}-\sqrt{3}\tan\omega\right]\sigma_{uo} \qquad (10)$$
$$+\eta\left[\frac{\delta(1-2\eta\delta-3\eta\delta^2)}{\sqrt{1+2\eta\delta(2+3\delta+2\delta^2)+\eta^2\delta^4}}-\sqrt{3}(2+\delta)\tan\omega\right]\sigma_{li}$$
$$\left.-\eta\delta\left[\frac{1+4\eta\delta+3\eta\delta^2}{\sqrt{1+2\eta\delta(2+3\delta+2\delta^2)+\eta^2\delta^4}}-\sqrt{3}\tan\omega\right]\sigma_{uo}\right\}$$

Note that the expressions shown in Equations (9) and (10) are for welds joining sheets with $\delta \le 1$. For welds joining sheets with $\delta > 1$, one should rotate the strip model by an angle of 180^o to represent the same physical system but with $\delta < 1$. The values of the angular quantity ω in Equations (9) and (10) can be found in Suo and Hutchinson [5] and Zhang [3].

The normal structural stresses for the left and right cracks in a lap-shear specimen under plane strain conditions can be obtained using a simple beam bending theory. For the left crack, the normal structural stresses are

$$\sigma_{ui} = 0 \qquad (11)$$

$$\sigma_{uo} = 0 \qquad (12)$$

$$\sigma_{li} = 4\frac{F}{bt_l} \qquad (13)$$

$$\sigma_{lo} = -2\frac{F}{bt_l} \qquad (14)$$

For the right crack, the normal structural stresses are

$$\sigma_{ui} = 4\frac{F}{bt_u} \tag{15}$$

$$\sigma_{uo} = -2\frac{F}{bt_u} \tag{16}$$

$$\sigma_{li} = 0 \tag{17}$$

$$\sigma_{lo} = 0 \tag{18}$$

The normal structural stresses in Equations (11) to (18) can then be substituted into Equations (9) and (10) to calculate K_1 and K_2 for both cracks in a lap-shear specimen of different materials and thicknesses. It should be noted for the right crack, the signs for the stress intensity factor K_2 solutions are changed to be consistent with those of the left crack.

Under plane strain conditions, for an interfacial crack between two dissimilar linear elastic materials, the J integral is related to the stress intensity factors K_1, K_2 and K_3 as [6]

$$J = \frac{K_1^2 + K_2^2}{\cosh^2(\pi\varepsilon)E^*} + \frac{K_3^2}{2G^*} \tag{19}$$

where E^* and G^* are

$$\frac{1}{E^*} = \frac{1}{2}\left(\frac{1}{E'_u} + \frac{1}{E'_l}\right) \tag{20}$$

and

$$\frac{1}{G^*} = \frac{1}{2}\left(\frac{1}{G_u} + \frac{1}{G_l}\right) \tag{21}$$

Here, K_3 is the mode 3 stress intensity factor. Since $K_3 = 0$ at the left and right cracks in a lap-shear specimen under plane strain conditions, Equation (19) can be reduced to

$$J = \frac{K_1^2 + K_2^2}{\cosh^2(\pi\varepsilon)E^*} \tag{22}$$

For welds joining sheets of identical materials ($\varepsilon = 0, \eta = 1$), Equation (22) becomes

$$J = \frac{K_I^2 + K_{II}^2}{E'} \tag{23}$$

and Equations (9) and (10) become

$$K_I = \frac{\sqrt{t_u}}{2\sqrt{2(1+\delta)(1+3\delta+3\delta^2)(1+\tan^2\omega)}} \times$$
$$\left\{\left[\frac{1+3\delta+6\delta^2}{\sqrt{3}(1+\delta)}\tan\omega - 1\right]\sigma_{ui} - \left[\frac{1+3\delta}{\sqrt{3}(1+\delta)}\tan\omega + 1\right]\sigma_{uo}\right. \tag{24}$$
$$\left. + \left[\frac{\delta(1-3\delta)}{\sqrt{3}(1+\delta)}\tan\omega + 2 + \delta\right]\sigma_{li} - \delta\left[\frac{1+3\delta}{\sqrt{3}(1+\delta)}\tan\omega + 1\right]\sigma_{lo}\right\}$$

$$K_{II} = \frac{\sqrt{t_u}}{2\sqrt{2(1+\delta)(1+3\delta+3\delta^2)(1+\tan^2\omega)}} \times$$
$$\left\{\left[\frac{1+3\delta+6\delta^2}{\sqrt{3}(1+\delta)} + \tan\omega\right]\sigma_{ui} - \left[\frac{1+3\delta}{\sqrt{3}(1+\delta)} - \tan\omega\right]\sigma_{uo}\right. \tag{25}$$
$$\left. + \left[\frac{\delta(1-3\delta)}{\sqrt{3}(1+\delta)} - (2+\delta)\tan\omega\right]\sigma_{li} - \delta\left[\frac{1+3\delta}{\sqrt{3}(1+\delta)} - \tan\omega\right]\sigma_{lo}\right\}$$

6.3. Normalized analytical solutions based on the beam bending theory

The stress intensity factor solutions for dissimilar welds based on the beam bending theory can be written in the normalized forms as

$$K_1 = k_1(\delta, \eta)\frac{F}{b\sqrt{t_u}} \tag{26}$$

and

$$K_2 = k_2(\delta, \eta)\frac{F}{b\sqrt{t_u}} \tag{27}$$

where k_1 and k_2 are the dimensionless geometric functions for a given set of δ and η. For welds joining sheets of identical materials ($\varepsilon = 0$ and $\eta = 1$), Equations (26) and (27) become

$$K_I = k_I(\delta)\frac{F}{b\sqrt{t_u}} \tag{28}$$

and

$$K_{II} = k_{II}(\delta)\frac{F}{b\sqrt{t_u}} \tag{29}$$

where k_I and k_{II} are the dimensionless geometric functions for a given δ.

The in-plane effective stress intensity factor K_e ($= \sqrt{K_1^2 + K_2^2}$) and J integral solutions can be written in the normalized forms as

$$K_e = k_e(\delta,\eta)\frac{F}{b\sqrt{t_u}} \tag{30}$$

and

$$J = j(\delta,\eta)\frac{1}{E'_u}\left(\frac{F}{b\sqrt{t_u}}\right)^2 \tag{31}$$

where k_e and j are the dimensionless geometric functions for a given set of δ and η. k_e and j can be expressed by k_1 and k_2 as

$$k_e = \sqrt{k_1^2 + k_2^2} \tag{32}$$

and

$$j = \frac{(1+\eta)\left(k_1^2 + k_2^2\right)}{2\cosh^2(\pi\varepsilon)} \tag{33}$$

For welds joining sheets of identical materials ($\varepsilon = 0$ and $\eta = 1$), Equations (30) and (31) become

$$K_e = k_e(\delta)\frac{F}{b\sqrt{t_u}} \tag{34}$$

and

$$J = j(\delta)\frac{1}{E'}\left(\frac{F}{b\sqrt{t_u}}\right)^2 \tag{35}$$

where

$$k_e = \sqrt{k_I^2 + k_{II}^2} \tag{36}$$

and

$$j = k_I^2 + k_{II}^2 \tag{37}$$

6.4. Computational model

In order to validate the analytical stress intensity factor solutions, two-dimensional finite element analyses for welds in lap-shear specimens of selected different material combinations and thickness ratios were conducted under plane strain conditions. In the finite element analyses, the materials are assumed to be linear elastic isotropic materials. The commercial finite element program ABAQUS [8] is employed to perform the computations. Second-order quarter point crack-tip elements with collapsed nodes are used to model the $1/\sqrt{r}$ singularity near the crack tip. Here, r represents the radial distance to the crack tip. The stress intensity factor and J integral solutions are directly computed by ABAQUS. The computational stress intensity factor solutions are obtained based on the interaction integral method for cracks under mixed-mode loading conditions (Shih and Asaro [9]).

It should be noted that K_1^A and K_2^A of the complex stress intensity factor $\mathbf{K}^A$ ($= K_1^A + iK_2^A$) obtained directly from ABAQUS are defined such that the stresses σ_y and τ_{xy} at a small distance r ahead of an interfacial crack tip are characterized by $\mathbf{K}^A$ as

$$\sigma_y + i\tau_{xy} = \frac{K_1^A + iK_2^A}{\sqrt{2\pi r}} r^{i\varepsilon} \tag{38}$$

The K_1 and K_2 solutions as defined in Equation (5) are related to the K_1^A and K_2^A solutions as defined in Equation (38) as

$$K_1 = K_1^A \cos(\varepsilon \ln t) - K_2^A \sin(\varepsilon \ln t) \tag{39}$$

and

$$K_2 = K_1^A \sin(\varepsilon \ln t) + K_2^A \cos(\varepsilon \ln t) \tag{40}$$

In this investigation, the computational K_1 and K_2 solutions for welds joining two sheets of dissimilar materials are obtained from Equations (39) and (40) with the K_1^A and K_2^A solutions computed by ABAQUS.

The schematic of the finite element model is shown in Figure 6.2. For the finite element analyses, the length L (= 100 mm), the overlap length V (= 40 mm), the specimen width b (= 30 mm) and the weld width w (= 9 mm) are based on the lap-shear specimens used in Franklin [1]. The upper sheet thickness t_u is 0.8 mm for different thickness ratios. In this investigation, 10 thickness ratios, 0.1, 0.2, 0.3, 0.4, 0.5, 0.6, 0.7, 0.8, 0.9, and 1.0, were modeled. Four commonly used metallic materials, steel, aluminum, magnesium and copper sheets, denoted as Fe, Al, Mg, and Cu, are considered for the analytical stress intensity factor solutions and their elastic constants are listed in Table 6.1. Two combinations of steel, aluminum, and magnesium are selectively considered for the finite element analyses to validate the analytical stress intensity

factor solutions. The interfacial crack parameters ε, η, ω, and the Dundur's parameters need to be calculated first to obtain the stress intensity factor solutions listed in Equations (9) and (10). The Dundur's parameters α and β are defined as

$$\alpha = \frac{(\kappa_l + 1)G_u - (\kappa_u + 1)G_l}{(\kappa_l + 1)G_u + (\kappa_u + 1)G_l} \tag{41}$$

$$\beta = \frac{(\kappa_l - 1)G_u - (\kappa_u - 1)G_l}{(\kappa_l + 1)G_u + (\kappa_u + 1)G_l} \tag{42}$$

The interfacial crack parameters for the 8 material combinations are listed in Table 6.2. Note that in Table 6.2, for example, Al/Fe is denoted for a weld joining upper aluminum and lower steel sheets. For the weld joining sheets of similar materials, the material property of steel was selected for the finite element model.

Figures 6.5(a) and 6.5(b) show a two-dimensional finite element mesh and a close-up view of the mesh near the weld, respectively, of a lap-shear specimen with a weld joining two sheets of the identical thickness. The boundary conditions are also schematically shown in Figure 6.5(a). Two crack tips, marked as A and B, are also shown in Figure 6.5(b). It should be noted that the results presented in the following were obtained from the same applied lap-shear loads.

6.5. Analytical solutions and computational results

Figures 6.6(a) and 6.6(b) show the dimensionless geometric functions k_I, k_{II}, k_e and j as functions of the thickness ratio δ for the left and right cracks of a weld joining sheets of identical materials based on the analytical solutions in Equations (24), (25) and (35), presented as various types of lines and the corresponding finite element analyses, presented as symbols. The results of the selected finite element analyses are reasonably in agreement with those of the

analytical solutions as shown in Figures 6.6(a) and 6.6(b). Figures 6.7 to 6.14 show the dimensionless geometric functions k_1, k_2, k_e and j as functions of the thickness ratio δ for the left and right cracks of Al/Fe, Fe/Al, Al/Mg, Mg/Al, Fe/Mg, Mg/Fe, Al/Cu and Cu/Al welds based on the analytical solutions in Equations (9), (10) and (31), presented as various types of lines, and the corresponding finite element analyses, presented as symbols.

In the finite element analyses, the ratio of the weld width to the upper sheet thickness is selected to be as large as 11.25. When the ratio of the weld width to the upper sheet thickness becomes smaller than 2, the use of the analytical solutions based on the beam bending theory should be careful as indicated in Sripichai et al. [2] for welds in lap-shear specimens of identical materials. As shown in Figures 6.7 to 6.14, the thickness ratio δ can have significant effects on the stress intensity factor solutions and their mode mixities. Also, the stress intensity factor solutions and the mode mixities are different for the left and right cracks. The analytical solutions were verified by the corresponding finite element analyses using ABAQUS for the Al/Fe and Fe/Mg welds for different thickness ratios δ, as shown in Figures 6.7 and 6.11, respectively. The results from the analytical solutions and finite element analyses in these figures agree well with each other.

It is noted that the k_1 and k_2 obtained from the finite element analyses are slightly different from the ones obtained from the analytical solutions at small thickness ratios δ in Figures 6.6, 6.7 and 6.11. The difference could attribute to two factors. First, the ratio of k_1 and k_2 is solely and strongly dependent on the angular quantity ω in Equations (9) and (10). However, the values of ω for all the material combinations are interpolated linearly from the values listed in the tables in Suo and Hutchinson [5]. It is also found that a few degree

adjustment of ω (1^{o} to 2^{o}) can make k_1 and k_2 almost perfectly match the ones obtained from the finite element analyses (< 0.5% difference). This indicates that the interpolated values of ω are just estimated values, which could introduce error in calculating analytical k_1 and k_2. The other possible reason which causes the difference of k_1 and k_2 between the ones obtained from the finite element analyses and the analytical solutions might be that the values of ω reported in Suo and Hutchinson [5] are for the large ratios of the weld width to the thickness where the beam bending theory is applicable. As shown in Figure 6.6, small difference was found in the weld joining sheets of identical materials for small thickness ratios which correspond to the small ratios of the weld width to the lower sheet thickness in the corresponding finite element analyses. However, the analytical stress intensity factor solutions are still in reasonable agreement with the results of the finite element analyses.

Based on the results presented in Figures 6.7 to 6.14, crack initiation in lap-shear specimens can be predicted. For example, for the Al/Fe welds considered here, crack initiation and growth, either growing along the interface or kinking out of the interface, can occur at the right crack tip for all thickness ratios since the geometric functions k_1 and k_2 or the stress intensity factor solutions for the right crack are much larger than those of the left crack as shown in Figures 6.7(a) and 6.7(b). The location of the crack initiation and growth from the right crack tip, the left crack tip, or both, depends on the material combination, the thickness ratio, and the fracture and fatigue properties of the weld along the interface and/or the upper and lower sheet materials.

6.6. Transition thickness ratio

For the lap-shear specimen with the stronger material (higher Young's modulus) being thicker than the weaker material (lower Young's modulus), the effective stress intensity factor is always higher at the crack tip on the loading side of the weaker material. For example, the right cracks in Mg/Al, Al/Fe, Mg/Fe and Al/Cu all have higher values of k_e, as shown in Figures 6.7, 6.8, 6.9 and 6.13, respectively. Therefore, the crack growth will take place at the right crack tip, if the stress intensity factor is the dominant driving force for fracture and fatigue. However, for the lap-shear specimen with weaker material (lower Young's modulus) being thicker than the stronger material (higher Young's modulus), the effective stress intensity factor will be higher at the crack tip on the loading side of the stronger material if the thickness ratio is higher than the transition thickness ratio, δ_T. The values of the transition thickness ratios for Al/Mg, Fe/Al, Fe/Mg and Cu/Al are listed in Table 6.3. The transition thickness ratio has significant implication for weld design since it could be a major parameter to indicate the potential failure location of the welds joining dissimilar materials.

6.7. Analytical solution for connection between two dissimilar half planes

When the weld width w becomes small compared to the upper or lower sheet thicknesses t_u and t_l, the stress intensity factors solutions for cracks in lap-shear specimen of two dissimilar materials should approach to that presented in Erdogan [10] for two half planes with a connection under remote shear loading conditions. Figure 6.15 shows a schematic of two dissimilar half planes with a weld width w under remote shear and normal loads. The remote shear forces per unit width, F/b, are applied along the x axis at $x=+\infty$ and $x=-\infty$ of the upper and lower planes, respectively. The remote normal forces per unit width, N/b, are

applied along the y axis at $y=+\infty$ and $y=-\infty$ of the upper and lower planes, respectively. Under these loading conditions, the stresses σ_y and τ_{xy} at a small distance r ahead of the interfacial crack tip are characterized by the stress intensity factor solutions, K_1^E and K_2^E, as

$$\sigma_y + i\tau_{xy} = \frac{K_1^E + iK_2^E}{\sqrt{2\pi r}}\left(\frac{r}{w}\right)^{i\varepsilon} \tag{43}$$

The stress intensity factor K_1^E and K_2^E solutions developed by Erdogan's [10] are rewritten in the forms that are consistent with the form in Equation (43) as

$$K_1^E = \frac{\sqrt{2}}{\sqrt{\pi w}}\frac{N}{b}\cosh(\pi\varepsilon) \tag{44}$$

and

$$K_2^E = \frac{\sqrt{2}}{\sqrt{\pi w}}\frac{F}{b}\cosh(\pi\varepsilon) \tag{45}$$

As shown in Figure 6.2 and Figure 6.15, when $N=0$ for lap-shear loading considered here, $K_1^E = 0$. Equation (43) can be rewritten again to be consistent with the form in Equation (5) as

$$\sigma_y + i\tau_{xy} = \frac{K_1^E + iK_2^E}{\sqrt{2\pi r}}\left(\frac{t}{w}\right)^{i\varepsilon}\left(\frac{r}{t}\right)^{i\varepsilon} = \left\{\cos\left[\varepsilon\ln\left(\frac{t}{w}\right)\right] + i\sin\left[\varepsilon\ln\left(\frac{t}{w}\right)\right]\right\}\frac{iK_2^E}{\sqrt{2\pi r}}\left(\frac{r}{t}\right)^{i\varepsilon} \tag{46}$$

Substituting Equation (45) into Equation (46) and comparing with Equation (5), the stress intensity factor solutions can be expressed in Equation (5) as

$$K_1 = -\sin\left[\varepsilon\ln\left(\frac{t}{w}\right)\right]\left[\frac{\sqrt{2}}{\sqrt{\pi w}}\frac{F}{b}\cosh(\pi\varepsilon)\right] \tag{47}$$

and

$$K_2 = \cos\left[\varepsilon\ln\left(\frac{t}{w}\right)\right]\left[\frac{\sqrt{2}}{\sqrt{\pi w}}\frac{F}{b}\cosh(\pi\varepsilon)\right] \tag{48}$$

The amplitude of the complex stress intensity factor **K** can be written as

$$K_1^2 + K_2^2 = \frac{2}{\pi w}\frac{F^2}{b^2}\cosh^2(\pi\varepsilon) \tag{49}$$

6.8. Transition weld width

As investigated in Sripichai et al. [2] and Franklin [1], when the weld width w/t_u becomes small, the analytical stress intensity factor solutions in Equations (9) and (10) for the lap-shear specimens are not applicable anymore. Sripichai et al. [2] defined the transition weld width such that when the weld width is larger than the transition weld width, the stress intensity factor solutions based on the beam bending theory can be used, whereas, when the weld width is smaller than the transition weld width, the stress intensity factor solutions based on the small connection of two half planes can be used for approximations. Sripichai et al. [2] developed more accurate stress intensity factor solutions for the range of weld widths near the transition crack length for the lap-shear specimen of equal thickness based on finite element analyses. However, it is quite tedious to develop a set of accurate stress intensity factor solution near the transition weld width for all possible combinations of dissimilar materials. Here, the normalized transition weld widths w/t_u for several combinations of dissimilar welds in lap-shear specimens can be obtained to determine the lower bound for the normalized weld width that the stress intensity factor solutions based on the beam bending theory presented in this study can be applicable.

Since the stress intensity factor solutions for interfacial cracks are in the complex form, the magnitude of the stress intensity factors are used to define the transition weld width. Substitute Equations (28) and (29) into Equation (49) gives

$$\left(k_1^2 + k_2^2\right)\frac{F^2}{b^2 t} = k_e^2\frac{F^2}{b^2 t} = \frac{2}{\pi w}\frac{F^2}{b^2}\cosh^2(\pi\varepsilon) \tag{50}$$

The normalized transition weld width can be derived as

$$\frac{w}{t} = \frac{2}{\pi}\cosh^2(\pi\varepsilon)\frac{1}{k_e^2} \tag{51}$$

The normalized transition weld widths w/t_u for different material combinations are listed in Table 6.4 for $\delta = 1.0$. Note that the characteristic length t is taken as the smaller value of the upper sheet thicknesses. Since the right crack tips always have higher effective stress intensity factors in the lap-shear specimens with the softer material (lower Young's modulus) being the thinner sheet, only the right cracks in Mg/Al, Al/Fe, Mg/Fe and Al/Cu are considered here. As listed in Table 6.4, the values of the normalized transition weld width w/t_u are quite small in the range of 0.2 to 0.4 for $\delta = 1.0$. Figure 6.16 shows the values of the normalized transition weld widths w/t_u for the right crack tip of the Mg/Al, Al/Fe, Mg/Fe and Al/Cu welds as functions of the thickness ratio δ. As shown in the figure, the values of the normalized transition weld width w/t_u decrease slightly as δ decreases. However, the values of the normalized transition weld widths w/t_u are still quite small. The result indicates that the applicable weld width ranges of the stress intensity factor solutions (Equations (9) and (10)) for dissimilar welds based on the beam bending theory are more than that for similar welds.

6.9. Discussions

Examples are given here to demonstrate the usefulness of the normalized stress intensity factor solutions presented in this study. The first example is an ultrasonic spot welded lap-shear specimen of magnesium and steel sheets of equal thickness ($\delta = 1.0$). Figure 6.17 shows an optical micrograph of the cross section of a failed ultrasonic spot welded lap-shear specimen of magnesium and steel sheets of equal thickness under cyclic loading conditions (Franklin [1]). It

can be seen that the left crack grows into the magnesium sheet while the right crack stays intact. The normalized effective stress intensity factor of the left crack of 1.76 is higher than that of the right crack of 0.73 based on the analytical stress intensity factor solutions shown in Figures 6.11(a) and 6.11(b) for $\delta = 1.0$. The normalized effective stress intensity factor solutions based on the finite element analyses are 1.82 for the left crack and 0.72 for the right crack with consideration of indentation for the lower magnesium sheet also show consistent results.

The second example is also the lap-shear specimen of magnesium and steel sheets mentioned in the first example with a different thickness ratio of $\delta = 0.5$. Figure 6.18 shows an optical micrograph of the cross section of a failed ultrasonic spot welded lap-shear specimen of magnesium and steel sheets under cyclic loading conditions. It can be seen that the left crack grows into the magnesium sheet while the right crack stays intact. The normalized effective stress intensity factor of the left crack of 1.24 is higher than that of the right crack of 0.79 based on the analytical stress intensity factor solutions shown in Figures 6.11(a) and 6.11(b) for $\delta = 0.5$. The normalized effective stress intensity factor solutions based on the finite element analyses are 1.21 for the left crack and 0.80 for the right crack with consideration of the indentation on the lower magnesium sheet also show consistent results.

Lai et al. [11] machined laser welded lap-shear specimens of dissimilar aluminum and copper sheets into a dog-bone shaped profile. Figure 6.19(a) shows a lap-shear specimen of aluminum and copper sheets with two parallel laser welds after being machined into a dog-bone shape. Figures 6.19(b) and 6.19(c) show optical micrographs of the cross sections near two failed laser welds in the lap-shear specimen of aluminum and copper sheets under cyclic loading conditions. As shown in the figures, the fracture occurs from cracks growing from the right and left cracks. For the thickness ratio $\delta = 0.5$, the normalized transition weld width w/t_u is 0.28 as

shown in Figure 6.16. The stress intensity factor solutions for both cracks of the laser weld based on the beam bending theory should be applicable. Using the two parallel laser welds to increase the effective weld width to lower the stress intensity factors at both cracks is not necessary. Also, the stress intensity factor solutions presented in Figure 6.13 can be used. The normalized effective stress intensity factor of the right crack of 1.5 is higher than that of the left crack of 0.74 based on the analytical stress intensity factor solutions shown in Figure 6.13 for $\delta = 0.5$. However, crack growth occurred for both cracks. The experimental observations indicate that crack growth also depends on the mode mixities of the stress intensity factors, the fatigue strength of interfacial cracks, and the fatigue strength of the upper and lower sheet materials.

Figures 6.20(a) and 6.20(b) show a laser-welded lap-shear specimen of high strength low alloy steel sheets and an optical micrograph of the etched cross section of a partially failed laser weld in a lap-shear specimen of high strength low alloy steel sheets under cyclic loading conditions, respectively. It can be seen that the right crack grows longer than the left crack. The original thickness ratio δ of the lap-shear specimen is 1.0. However the weld bead on the bottom sheet decreases the effective thickness ratio such that $\delta < 1.0$. As shown in Figures 6.6(a) and 6.6(b), the normalized effective stress intensity factor for the right crack is always higher than that of the left crack for $\delta < 1.0$. The normalized effective stress intensity factor solutions calculated from the finite element analyses are 1.29 for the right crack and 1.14 for the left crack reported by Asim et al. [12], which are consistent with the results shown in Figures 6.6(a) and 6.6(b).

6.10. Conclusions

In this chapter, the analytical stress intensity factor and J integral solutions for welds in lap-shear specimens for two dissimilar sheets based on the beam bending theory are presented in the normalized forms and validated by two-dimensional finite element analyses. The interfacial crack parameters, the stress intensity factor solutions, and the J integral solutions for welds in lap-shear specimens of different combinations of steel, aluminum, and magnesium, and the combination of aluminum and copper sheets of different thickness ratios are then presented for convenient fracture and fatigue analyses. The transition thickness ratios for critical crack locations for different combinations of dissimilar materials are then determined from the analytical solutions. The transition weld widths for applicable ranges of the weld widths for the analytical solutions based on the beam bending theory are also presented. Finally, fracture and fatigue behaviors of dissimilar ultrasonic magnesium/steel, dissimilar laser aluminum/copper, and similar laser steel welds in lap-shear specimens are examined and demonstrate the usefulness of the graphical stress intensity factor solutions presented in this chapter.

Table 6.1. The elastic constants for steel, aluminum, magnesium and copper sheets.

	E (GPa)	v	G (GPa)
Fe	207	0.30	79.6
Al	69.0	0.33	25.9
Mg	45.0	0.35	16.7
Cu	110	0.34	41.0

Table 6.2. The values of interfacial crack parameters for dissimilar welds.

	α	β	ε	η	ω (δ=0.1)	ω (δ=0.5)	ω (δ=1.0)
Al/Fe	-0.492	-0.117	0.037	0.340	52.8	51.9	51.2
Fe/Al	0.492	0.117	-0.037	2.938	54.0	49.8	47.9
Al/Mg	0.203	0.038	-0.012	1.510	54.2	49.9	49.0
Mg/Al	-0.203	-0.038	0.012	0.662	53.7	50.1	49.4
Fe/Mg	0.632	0.136	-0.043	4.436	55.8	50.9	48.5
Mg/Fe	-0.632	-0.136	0.043	0.225	53.0	52.2	51.3
Al/Cu	-0.233	-0.063	0.020	0.623	54.0	51.0	50.3
Cu/Al	0.233	0.063	-0.020	1.606	53.1	49.2	48.1

Table 6.3. Transition thickness ratios δ_T for different material combinations.

	δ_T
Fe/Mg	0.23
Fe/Al	0.34
Al/Mg	0.66
Cu/Al	0.62
Similar material	0.78

Table 6.4. Normalized Transition weld widths w/t_u for different material combinations when $\delta = 1.0$.

	w/t_u
Mg/Fe	0.209
Al/Fe	0.231
Mg/Al	0.295
Al/Cu	0.287
similar material	0.364

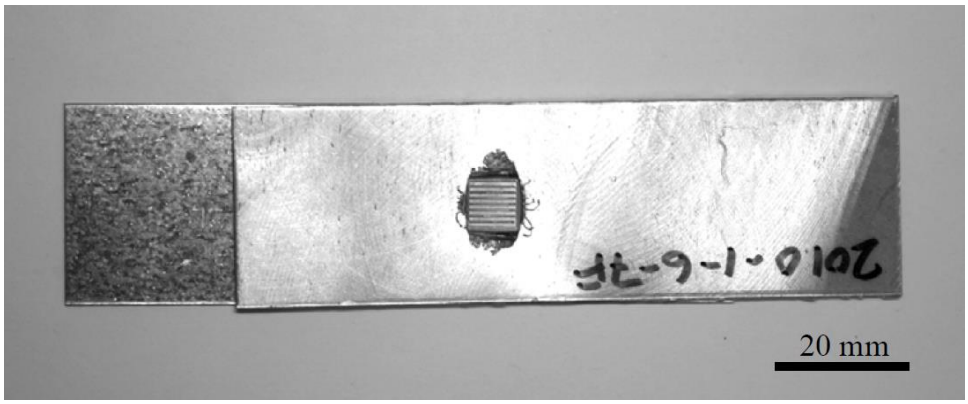

(a)

(b)

Figure 6.1. An ultrasonic spot welded lap-shear specimen of magnesium and steel sheets (a) before being machined and (b) after being machined into a dog-bone shape [1].

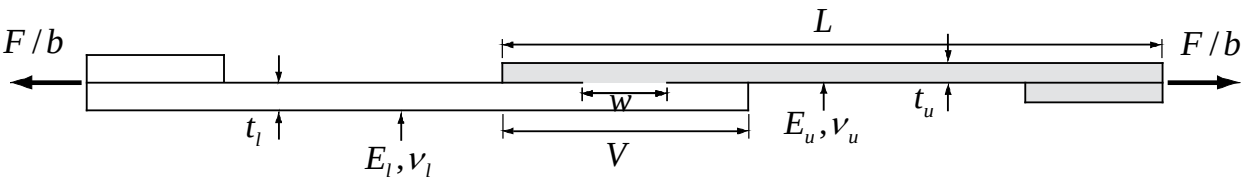

Figure 6.2. A schematic of a lap-shear specimen. The applied force per unit width, F/b, is shown as the bold arrows.

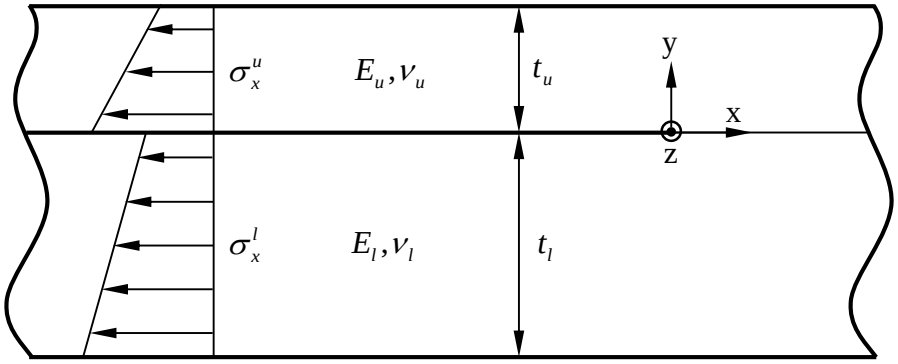

Figure 6.3. A two-dimensional model of two infinite strips made of dissimilar materials with different thicknesses and connection under plane strain conditions.

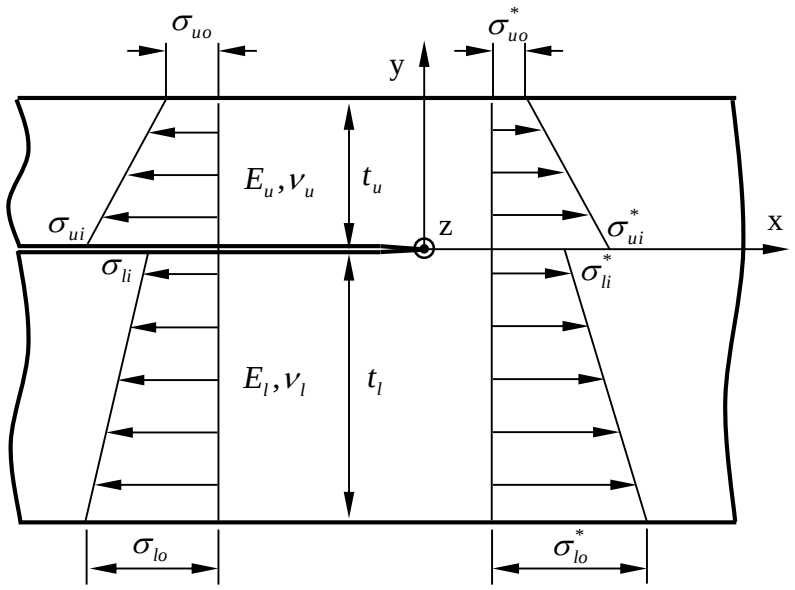

Figure 6.4. A schematic showing the strip model near the crack tip. The normal stresses σ_{ui}, σ_{uo}, σ_{li}, σ_{lo}, σ^*_{ui}, σ^*_{uo}, σ^*_{li} and σ^*_{lo} represent the normal structural stresses at the inner (i) and outer (o) surfaces of the upper (u) and lower (l) strips, respectively.

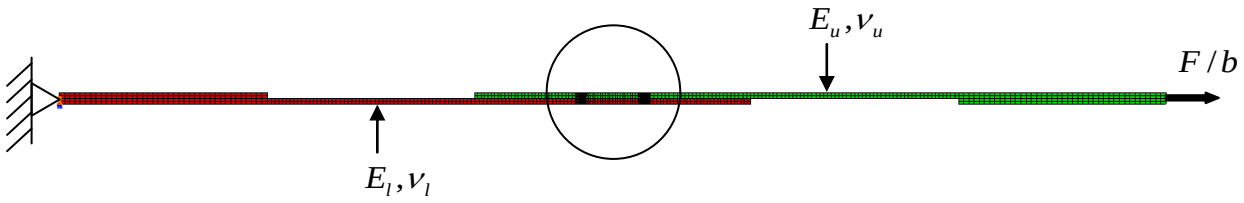

(a)

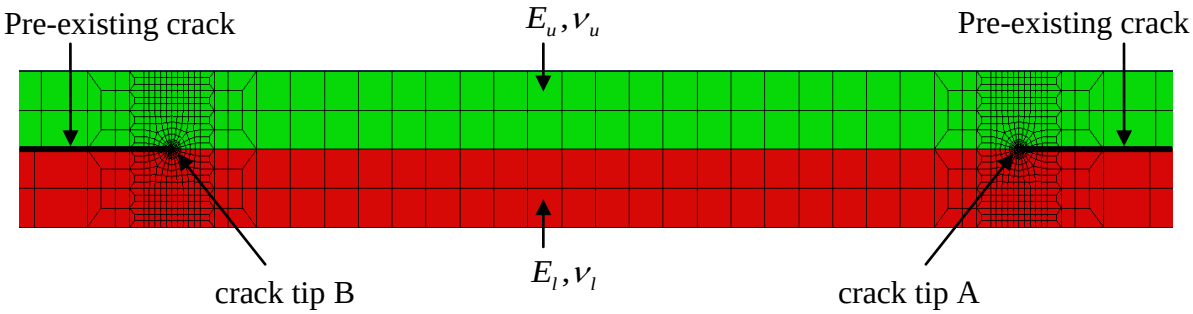

(b)

Figure 6.5. (a) A two-dimensional finite element mesh for a lap-shear specimen with a weld joining two sheets of different materials with the same thickness $t_u = t_l =$ 0.8 mm, (b) a close-up view of the mesh near the weld.

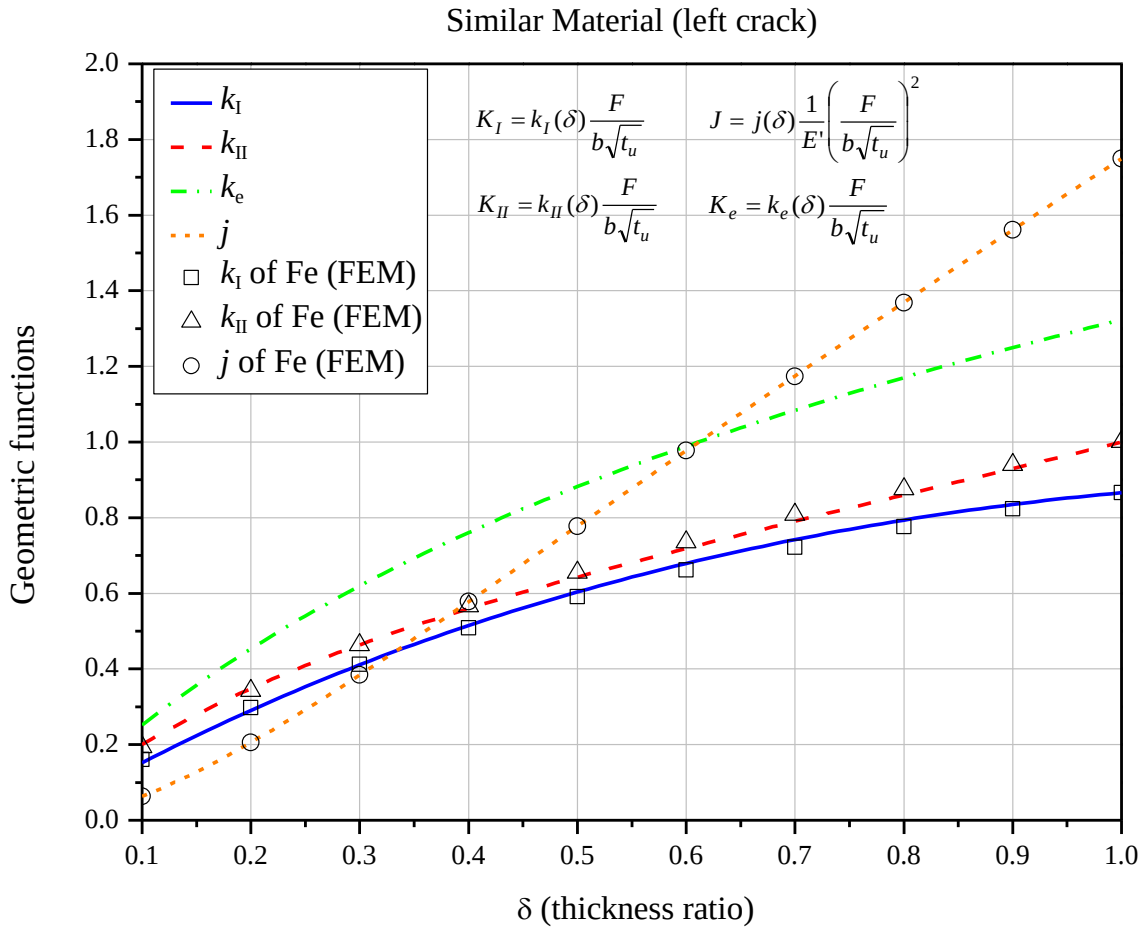
Similar Material (left crack)
Geometric functions
δ (thickness ratio)
k_I
k_{II}
k_e
j
k_I of Fe (FEM)
k_{II} of Fe (FEM)
j of Fe (FEM)
$K_I = k_I(\delta)\frac{F}{b\sqrt{t_u}}$
$J = j(\delta)\frac{1}{E'}\left(\frac{F}{b\sqrt{t_u}}\right)^2$
$K_{II} = k_{II}(\delta)\frac{F}{b\sqrt{t_u}}$
$K_e = k_e(\delta)\frac{F}{b\sqrt{t_u}}$
0.0
0.2
0.4
0.6
0.8
1.0
1.2
1.4
1.6
1.8
2.0
0.1
0.2
0.3
0.4
0.5
0.6
0.7
0.8
0.9
1.0

(a)

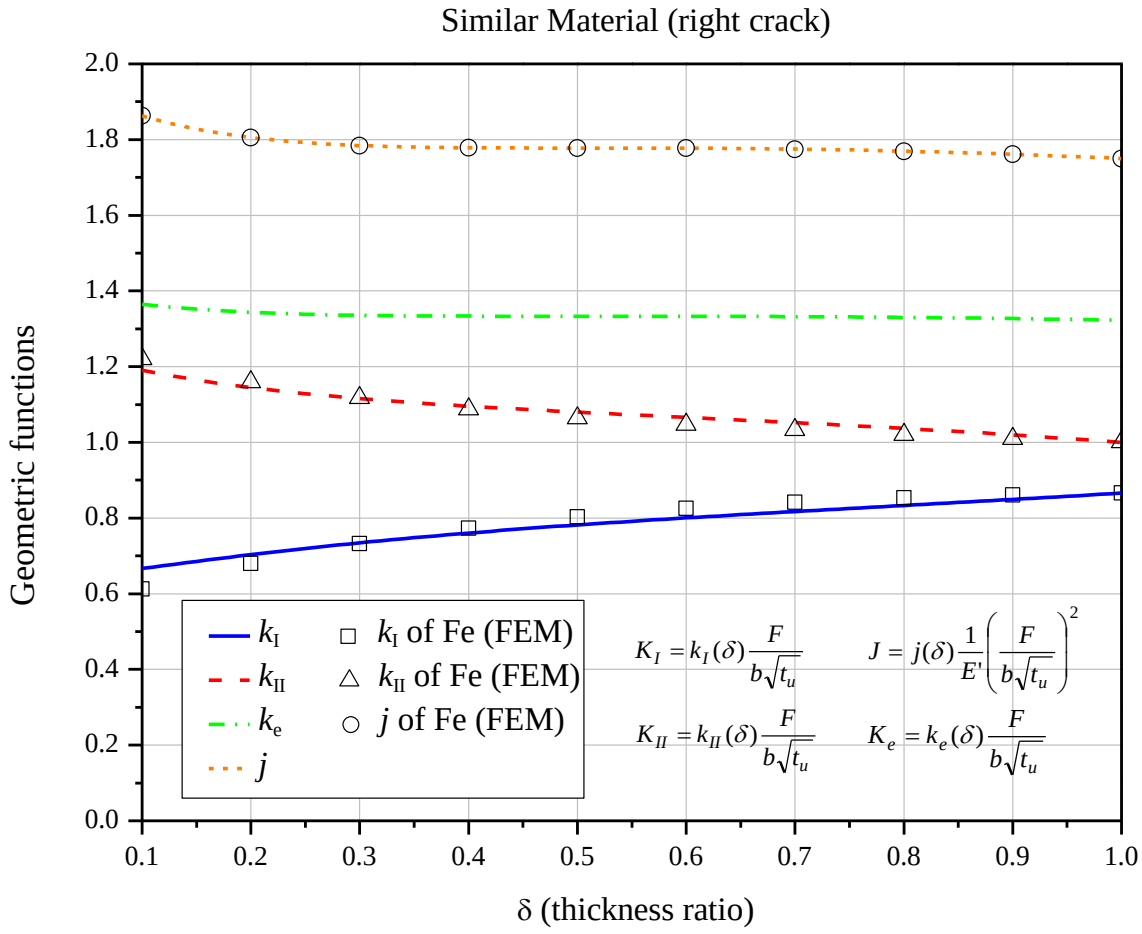

(b)

Figure 6.6. The dimensionless geometric functions k_I, k_{II}, k_e and j as functions of the thickness ratio δ for (a) the left and (b) the right cracks of a weld joining sheets of identical materials based on the analytical solutions and the corresponding finite element analyses using steel .

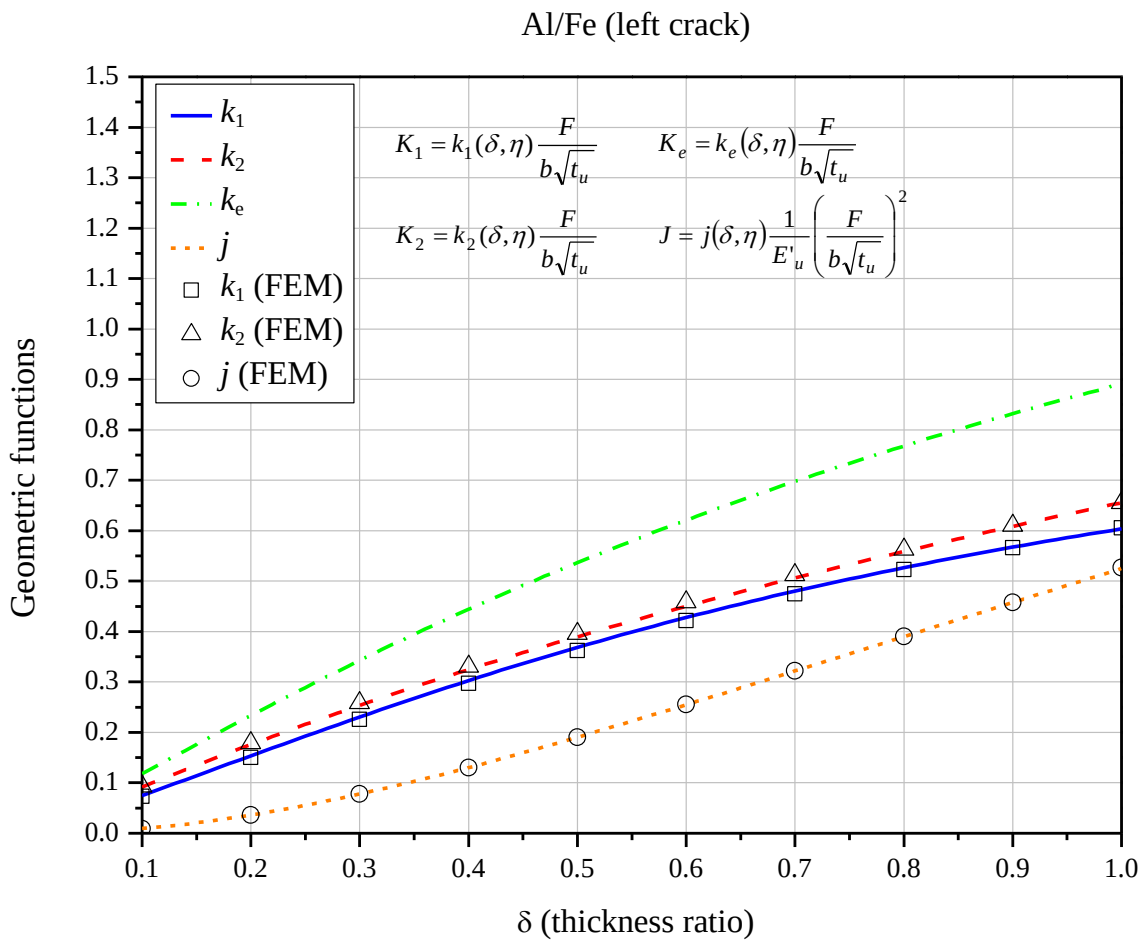
Al/Fe (left crack)
Geometric functions
δ (thickness ratio)
k1
k2
ke
j
k1 (FEM)
k2 (FEM)
j (FEM)
K1 = k1(δ,η) F/(b√tu)
Ke = ke(δ,η) F/(b√tu)
K2 = k2(δ,η) F/(b√tu)
J = j(δ,η) 1/E'u (F/(b√tu))2
0.0
0.1
0.2
0.3
0.4
0.5
0.6
0.7
0.8
0.9
1.0
1.1
1.2
1.3
1.4
1.5

(a)

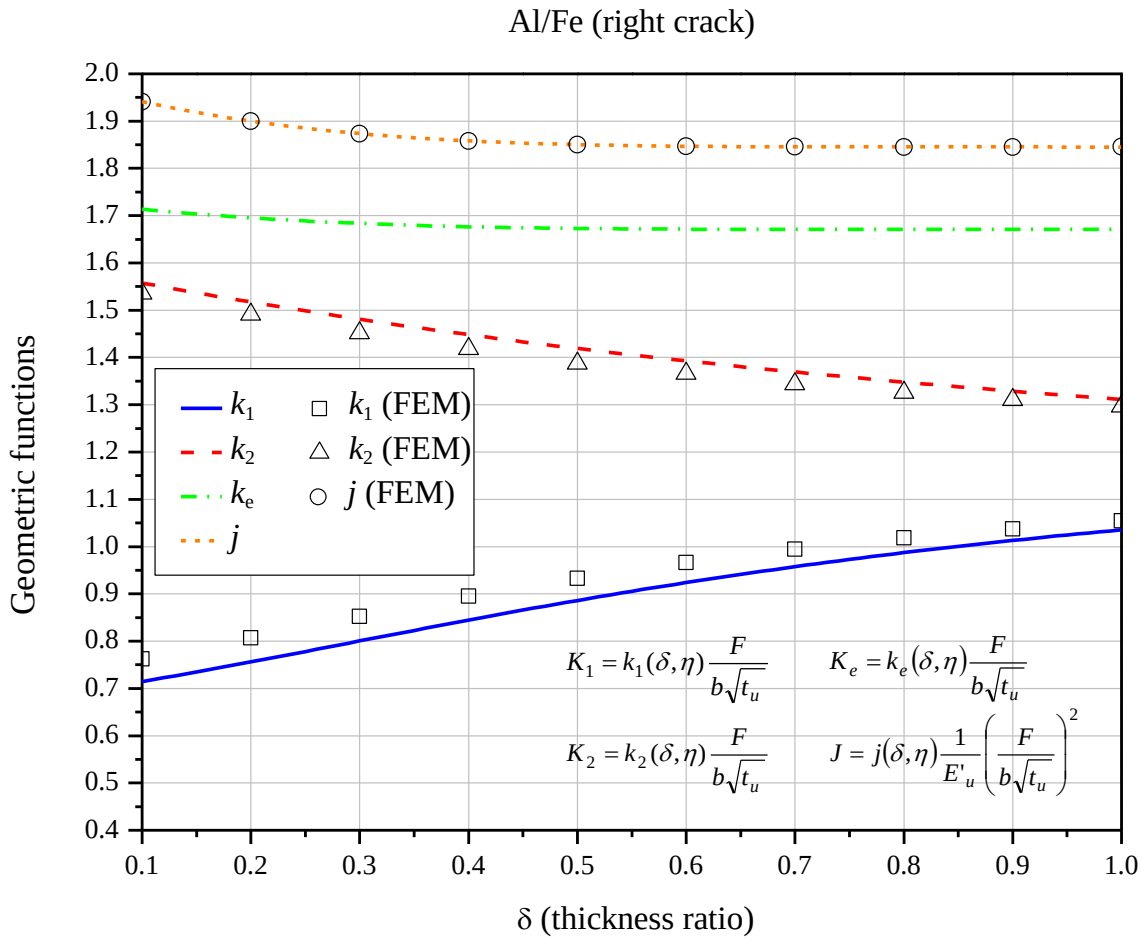

(b)

Figure 6.7. The dimensionless geometric functions k_1, k_2, k_e and j as functions of the thickness ratio δ for (a) the left and (b) the right cracks of an Al/Fe weld based on the analytical solutions and the corresponding finite element analyses.

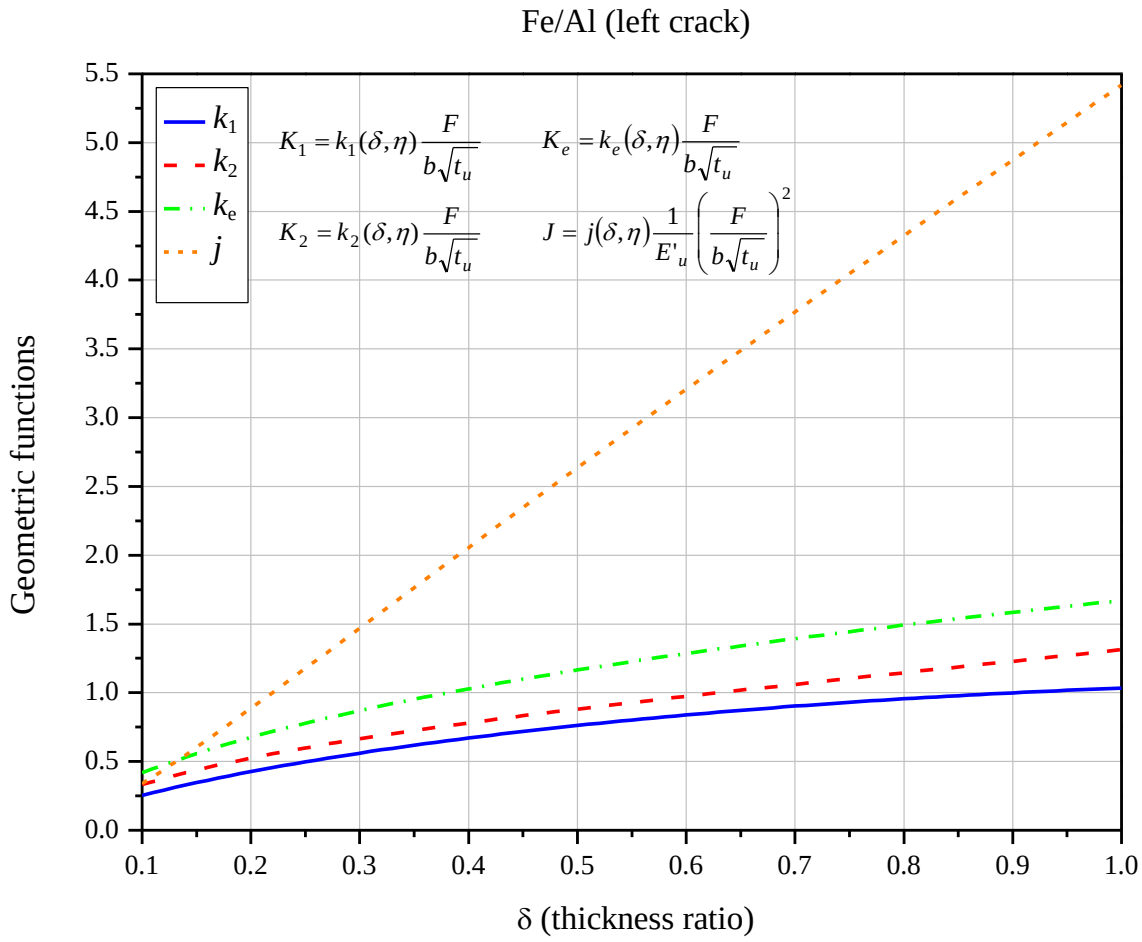
Fe/Al (left crack)
Geometric functions
δ (thickness ratio)
k1
k2
ke
j
K1 = k1(δ,η) F/(b√tu)
K2 = k2(δ,η) F/(b√tu)
Ke = ke(δ,η) F/(b√tu)
J = j(δ,η) 1/E'u (F/(b√tu))^2
0.0
0.5
1.0
1.5
2.0
2.5
3.0
3.5
4.0
4.5
5.0
5.5
0.1
0.2
0.3
0.4
0.5
0.6
0.7
0.8
0.9
1.0

(a)

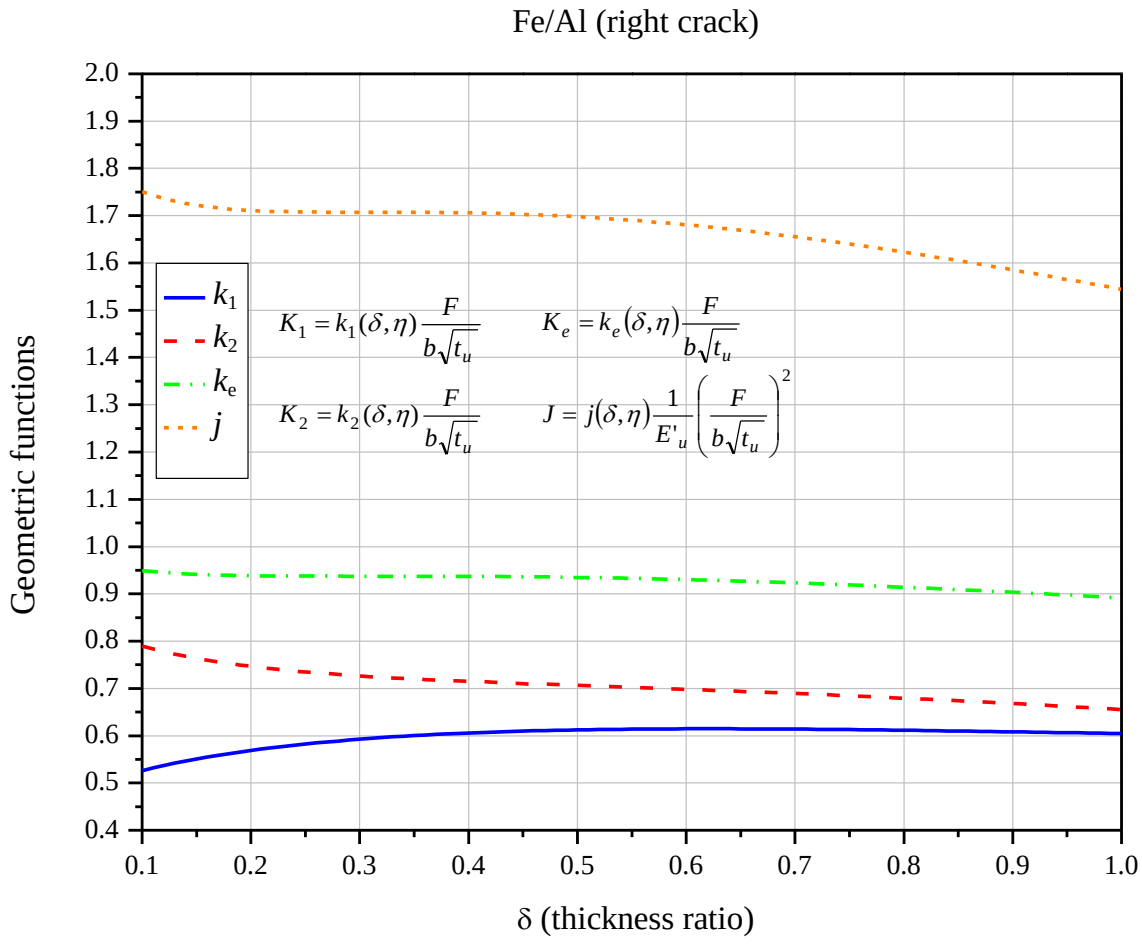

(b)

Figure 6.8. The dimensionless geometric functions k_1, k_2, k_e and j as functions of the thickness ratio δ for (a) the left and (b) the right cracks of an Fe/Al weld based on the analytical solutions.

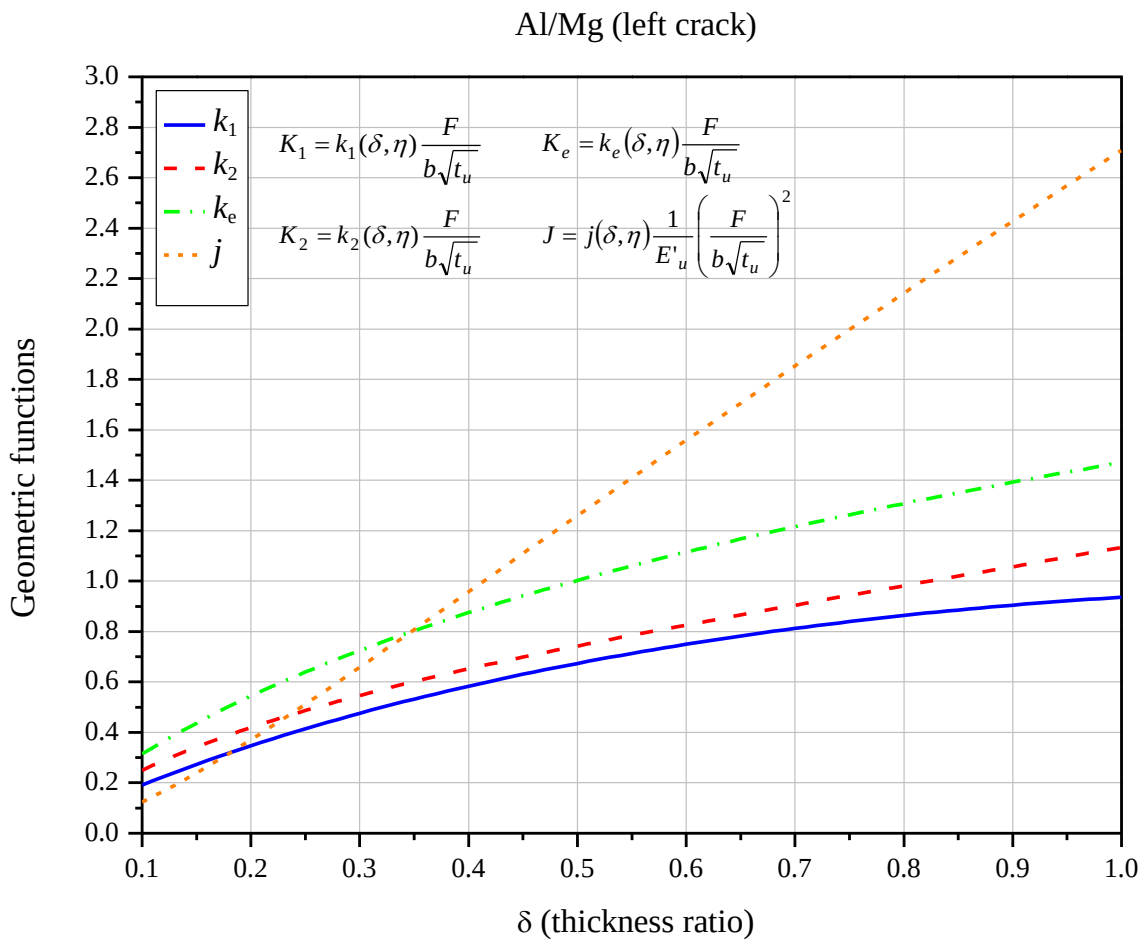
Al/Mg (left crack)
Geometric functions
δ (thickness ratio)
k1
k2
ke
j
K1 = k1(δ,η) F/(b√tu)
Ke = ke(δ,η) F/(b√tu)
K2 = k2(δ,η) F/(b√tu)
J = j(δ,η) 1/E'u (F/(b√tu))^2
3.0
2.8
2.6
2.4
2.2
2.0
1.8
1.6
1.4
1.2
1.0
0.8
0.6
0.4
0.2
0.0
0.1
0.2
0.3
0.4
0.5
0.6
0.7
0.8
0.9
1.0

(a)

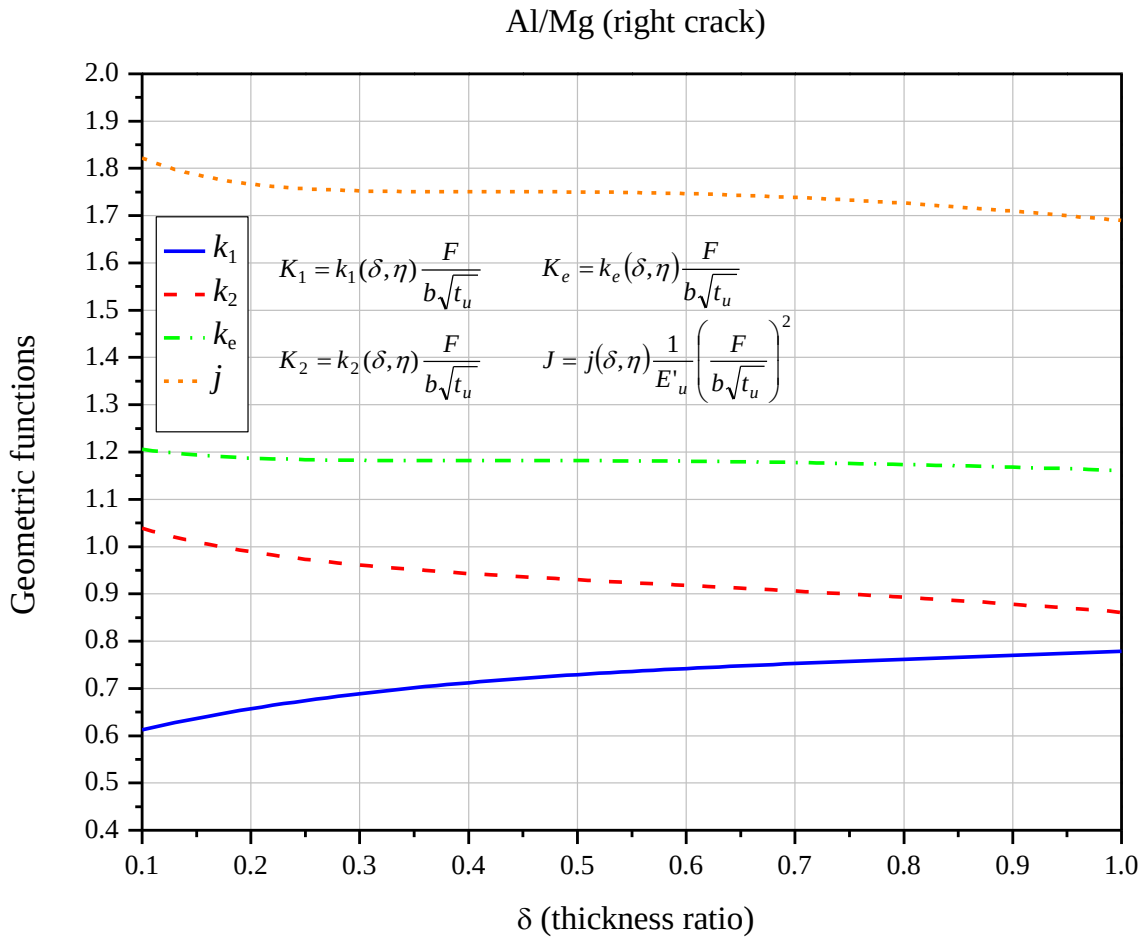

(b)

Figure 6.9. The dimensionless geometric functions k_1, k_2, k_e and j as functions of the thickness ratio δ for (a) the left and (b) the right cracks of an Al/Mg weld based on the analytical solutions.

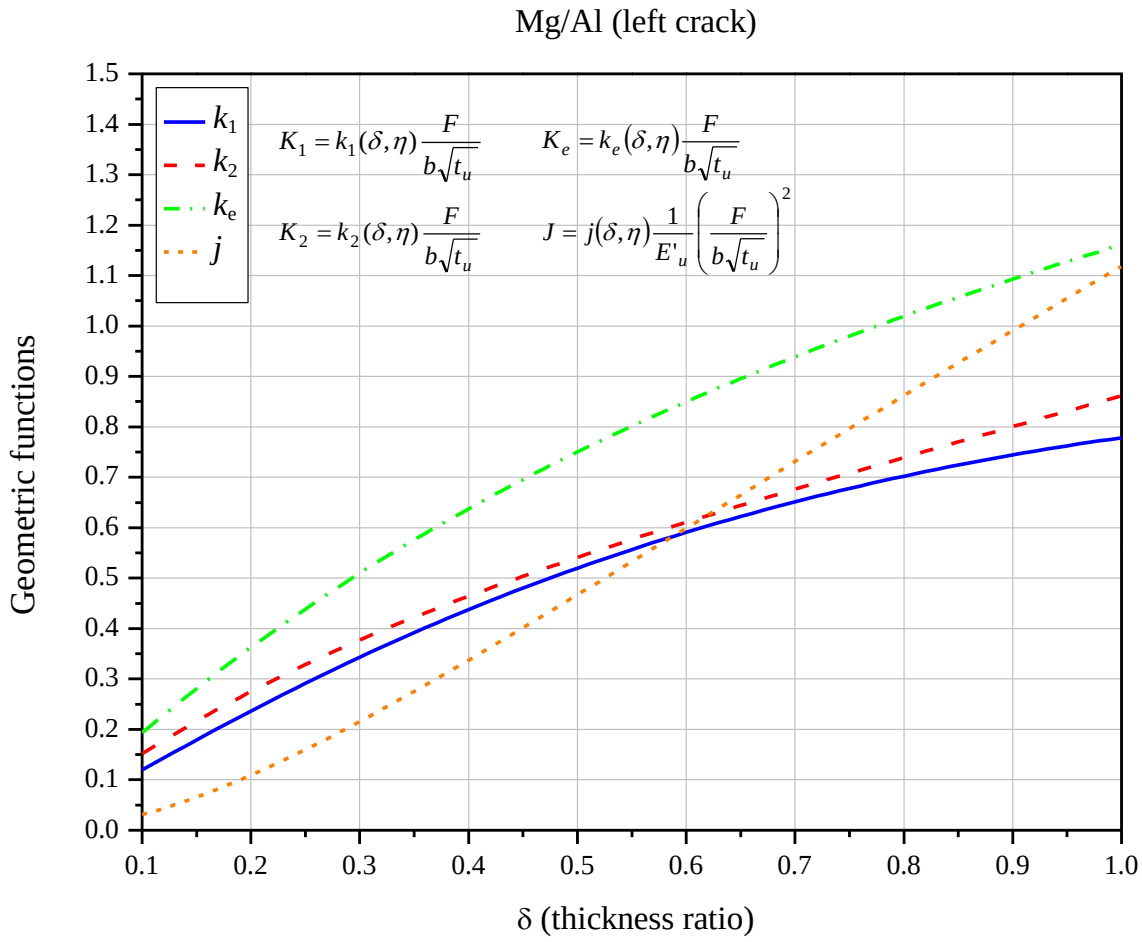
Mg/Al (left crack)
Geometric functions
δ (thickness ratio)
k1
k2
ke
j
K1 = k1(δ,η) F/(b√tu)
K2 = k2(δ,η) F/(b√tu)
Ke = ke(δ,η) F/(b√tu)
J = j(δ,η) 1/E'u (F/(b√tu))^2
0.0
0.1
0.2
0.3
0.4
0.5
0.6
0.7
0.8
0.9
1.0
1.1
1.2
1.3
1.4
1.5
0.1
0.2
0.3
0.4
0.5
0.6
0.7
0.8
0.9
1.0

(a)

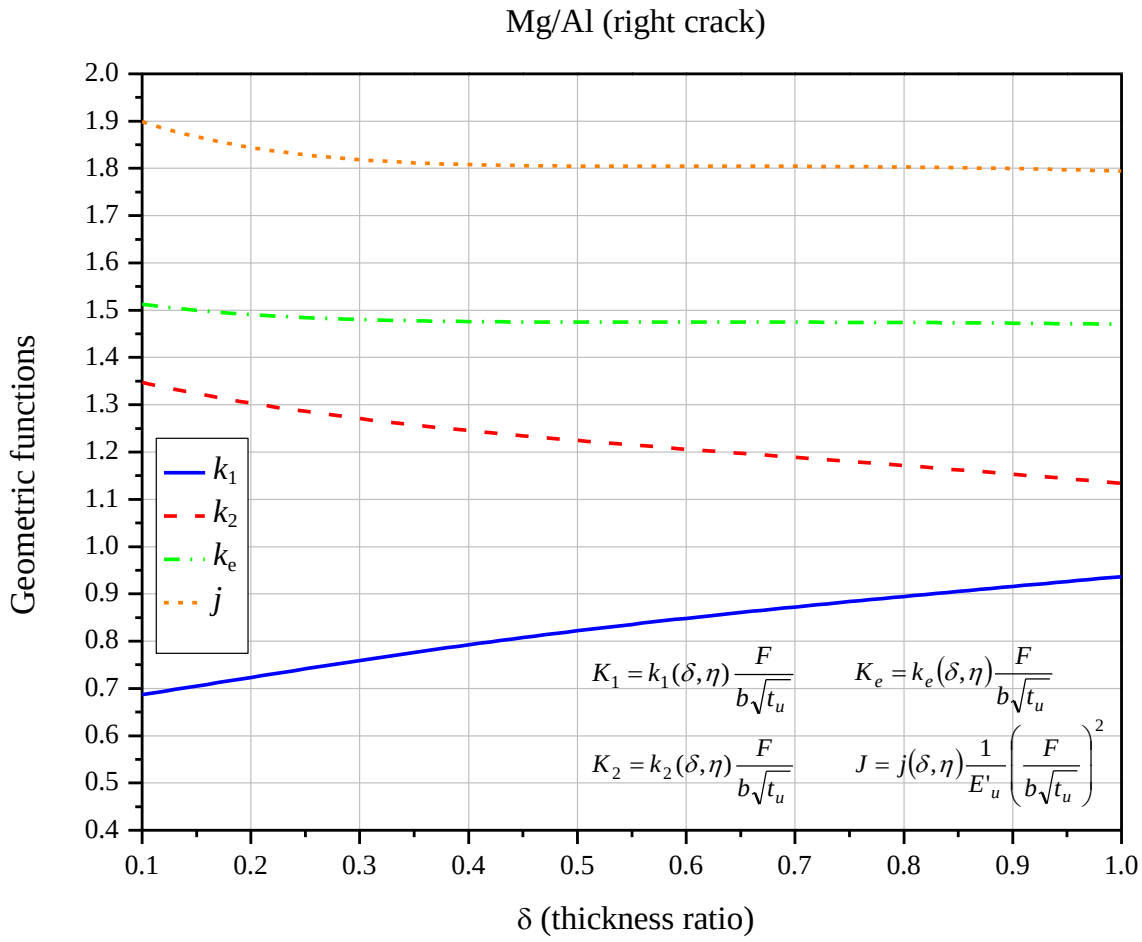

(b)

Figure 6.10. The dimensionless geometric functions k_1, k_2, k_e and j as functions of the thickness ratio δ for (a) the left and (b) the right cracks of a Mg/Al weld based on the analytical solutions.

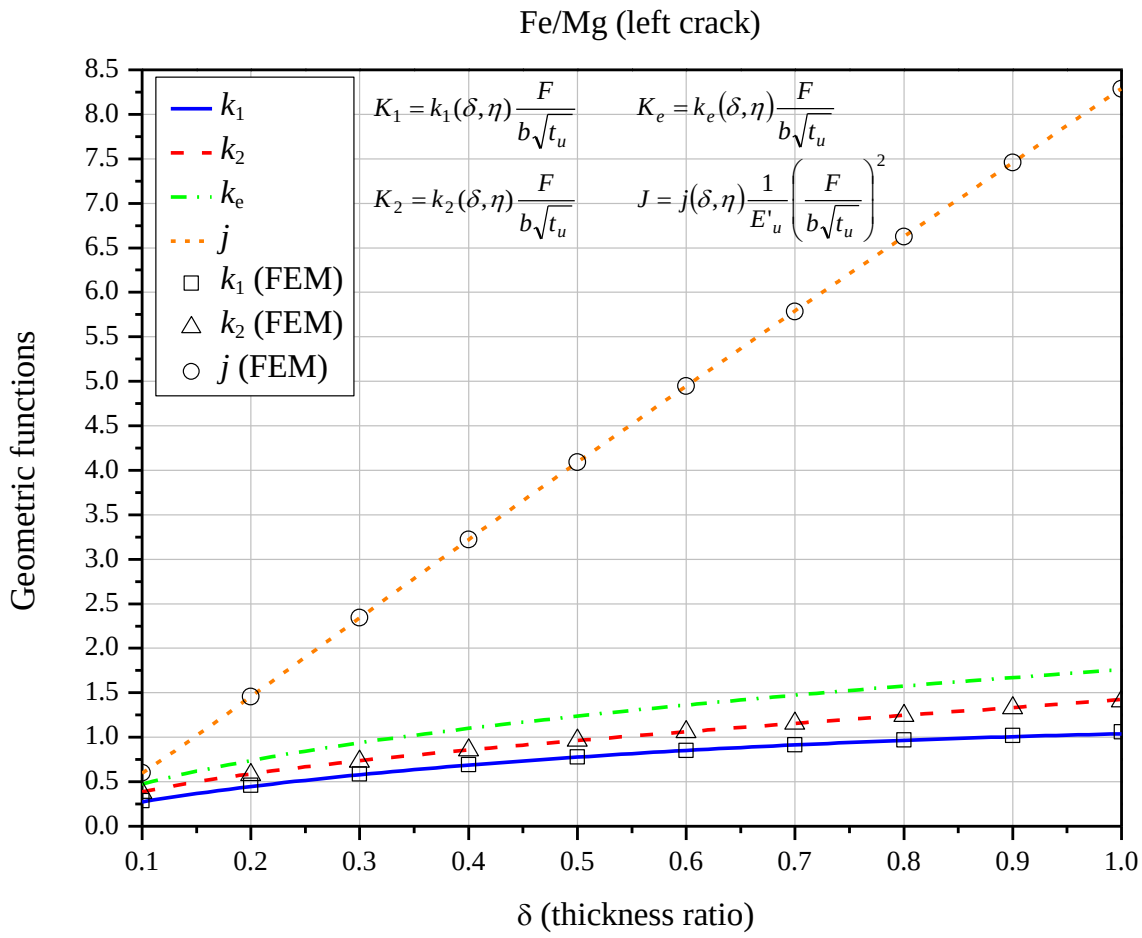
Fe/Mg (left crack)
Geometric functions
δ (thickness ratio)
k1
k2
ke
j
k1 (FEM)
k2 (FEM)
j (FEM)
K1 = k1(δ,η) F/(b√tu)
Ke = ke(δ,η) F/(b√tu)
K2 = k2(δ,η) F/(b√tu)
J = j(δ,η) 1/E'u (F/(b√tu))2
0.0
0.5
1.0
1.5
2.0
2.5
3.0
3.5
4.0
4.5
5.0
5.5
6.0
6.5
7.0
7.5
8.0
8.5
0.1
0.2
0.3
0.4
0.5
0.6
0.7
0.8
0.9
1.0

(a)

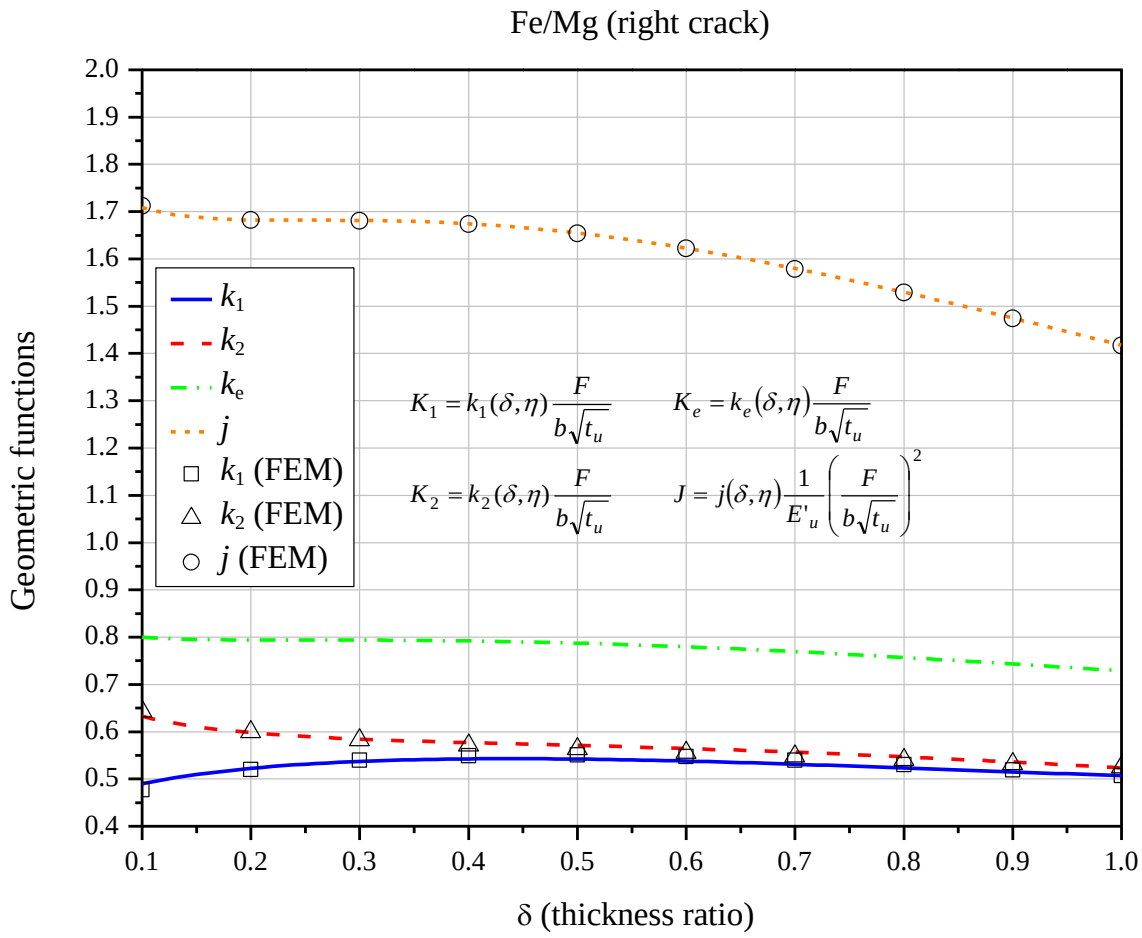

(b)

Figure 6.11. The dimensionless geometric functions k_1, k_2, k_e and j as functions of the thickness ratio δ for (a) the left and (b) the right cracks of an Fe/Mg weld based on the analytical solutions and the corresponding finite element analyses.

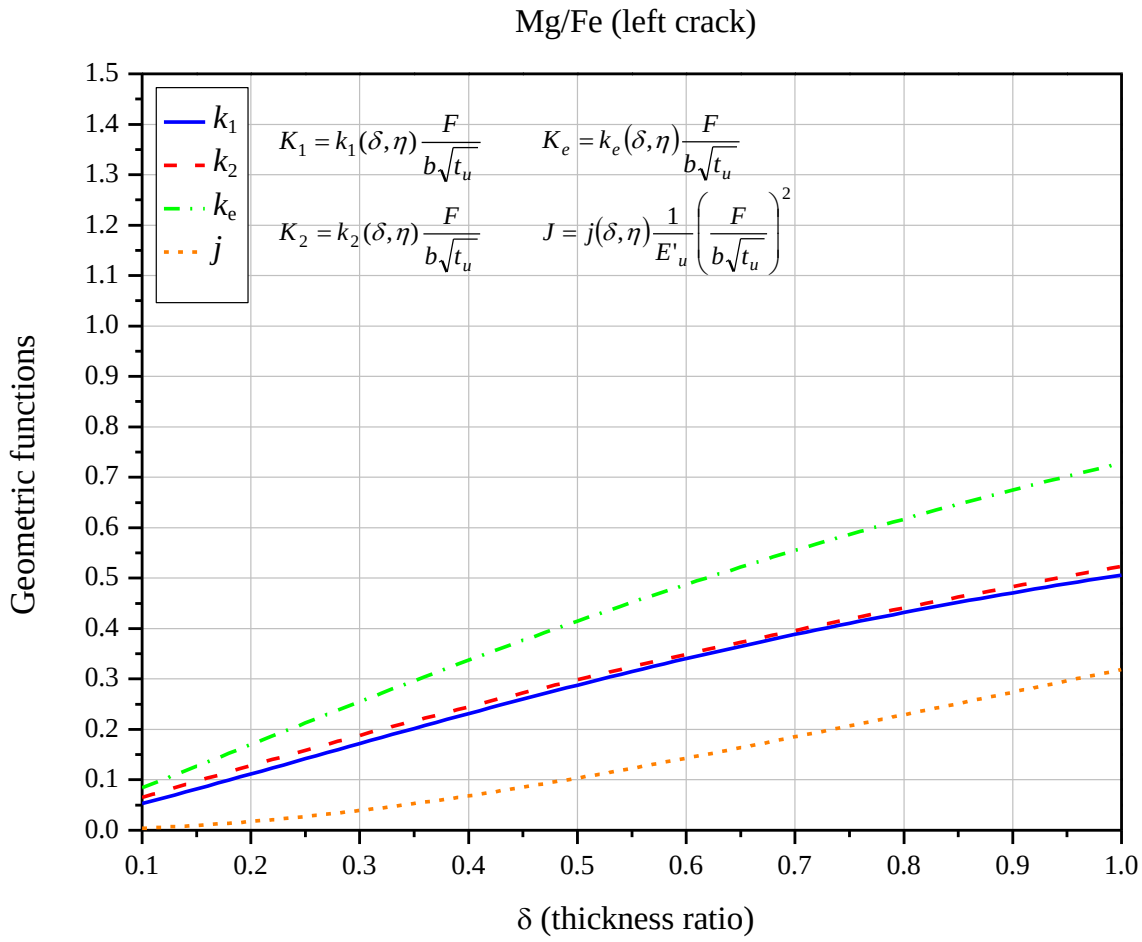
Mg/Fe (left crack)
Geometric functions
δ (thickness ratio)
k1
k2
ke
j
K1 = k1(δ,η) F/(b√tu)
Ke = ke(δ,η) F/(b√tu)
K2 = k2(δ,η) F/(b√tu)
J = j(δ,η) 1/E'u (F/(b√tu))^2
0.0
0.1
0.2
0.3
0.4
0.5
0.6
0.7
0.8
0.9
1.0
1.1
1.2
1.3
1.4
1.5
0.1
0.2
0.3
0.4
0.5
0.6
0.7
0.8
0.9
1.0

(a)

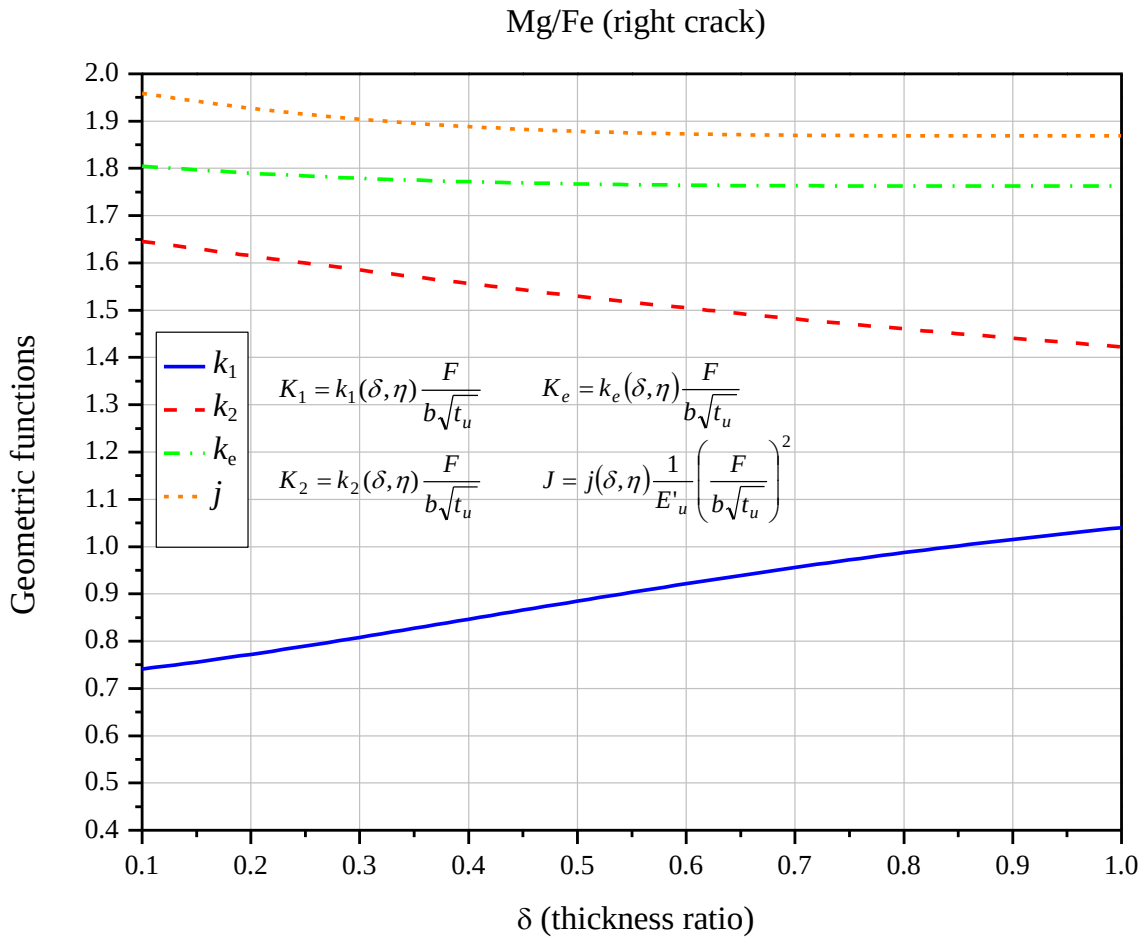

(b)

Figure 6.12. The dimensionless geometric functions k_1, k_2, k_e and j as functions of the thickness ratio δ for (a) the left and (b) the right cracks of a Mg/Fe weld based on the analytical solutions.

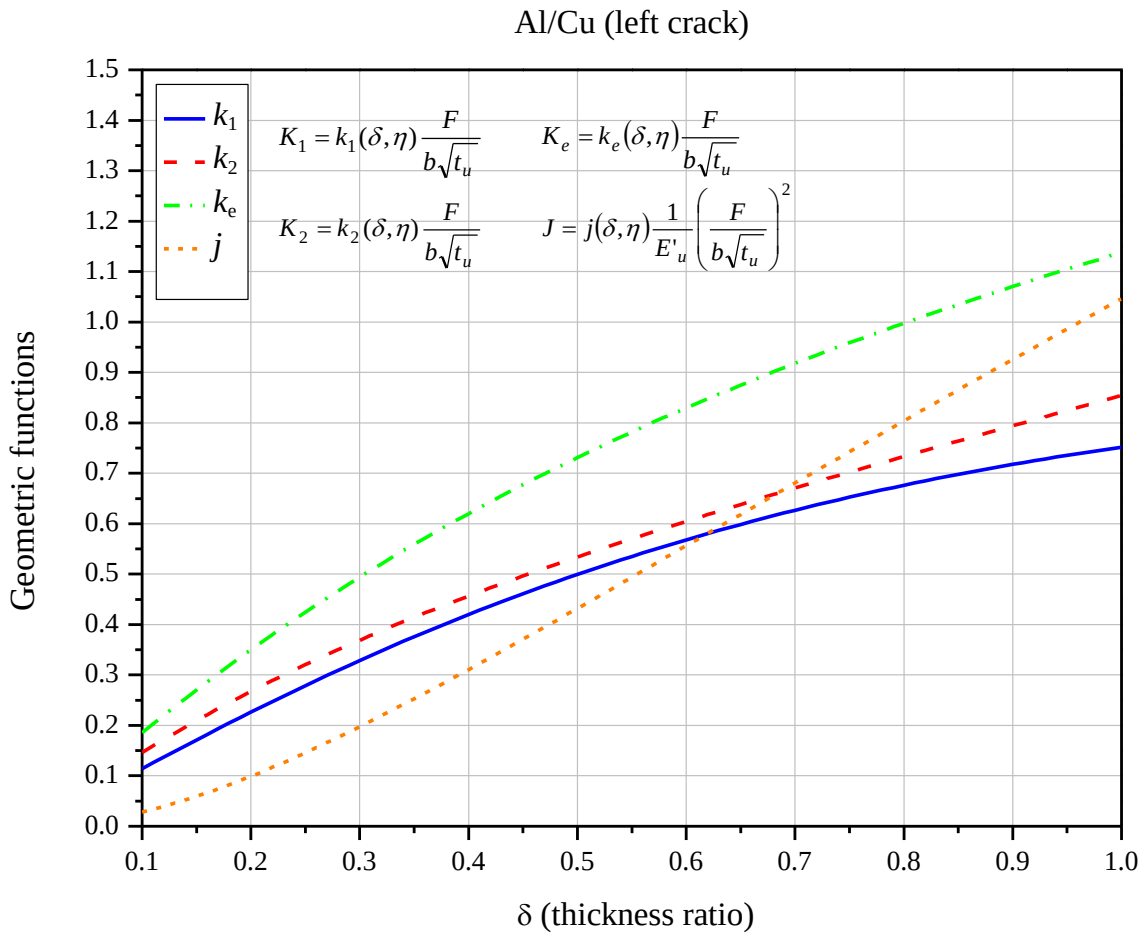
Al/Cu (left crack)
Geometric functions
δ (thickness ratio)
k1
k2
ke
j
K1 = k1(δ,η) F/(b√tu)
Ke = ke(δ,η) F/(b√tu)
K2 = k2(δ,η) F/(b√tu)
J = j(δ,η) 1/E'u (F/(b√tu))^2
1.5
1.4
1.3
1.2
1.1
1.0
0.9
0.8
0.7
0.6
0.5
0.4
0.3
0.2
0.1
0.0
0.1
0.2
0.3
0.4
0.5
0.6
0.7
0.8
0.9
1.0

(a)

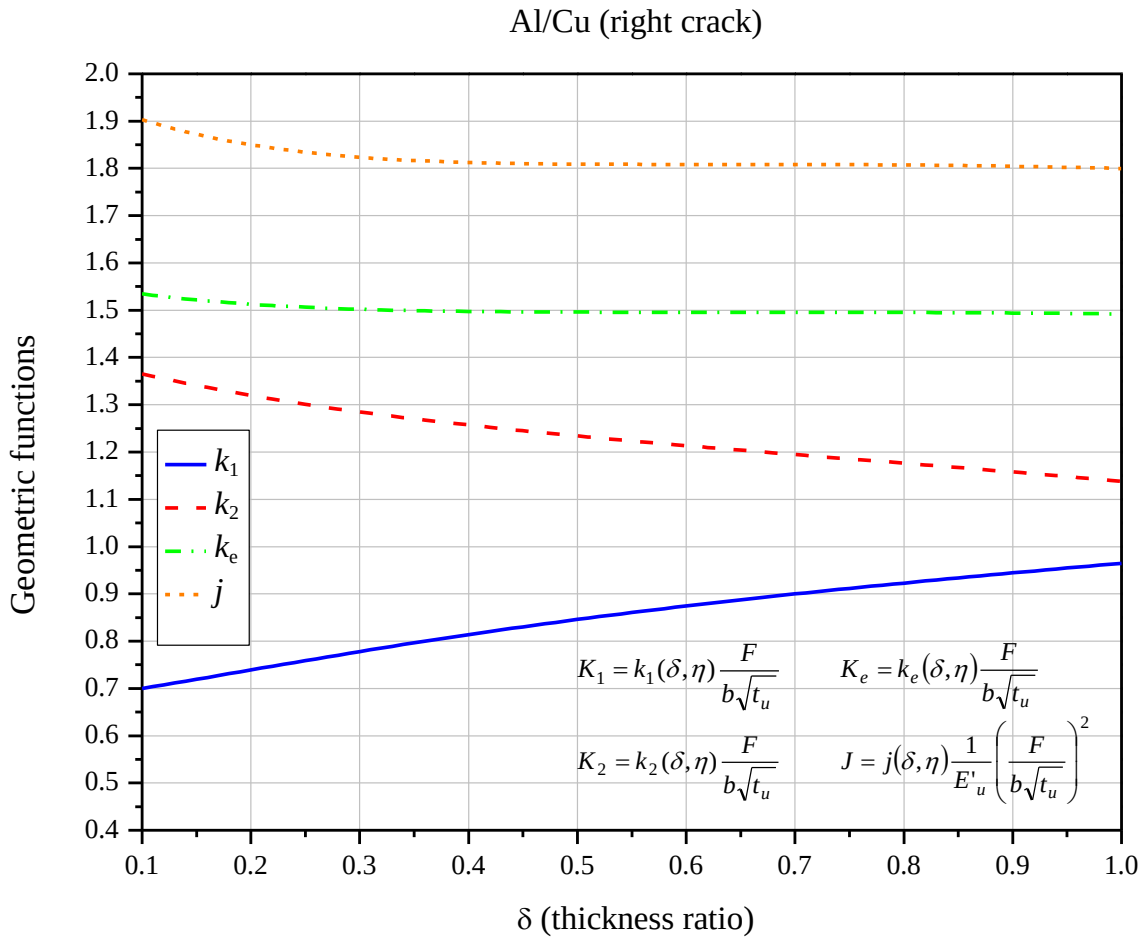

(b)

Figure 6.13. The dimensionless geometric functions k_1, k_2, k_e and j as functions of the thickness ratio δ for (a) the left and (b) the right cracks of an Al/Cu weld based on the analytical solutions.

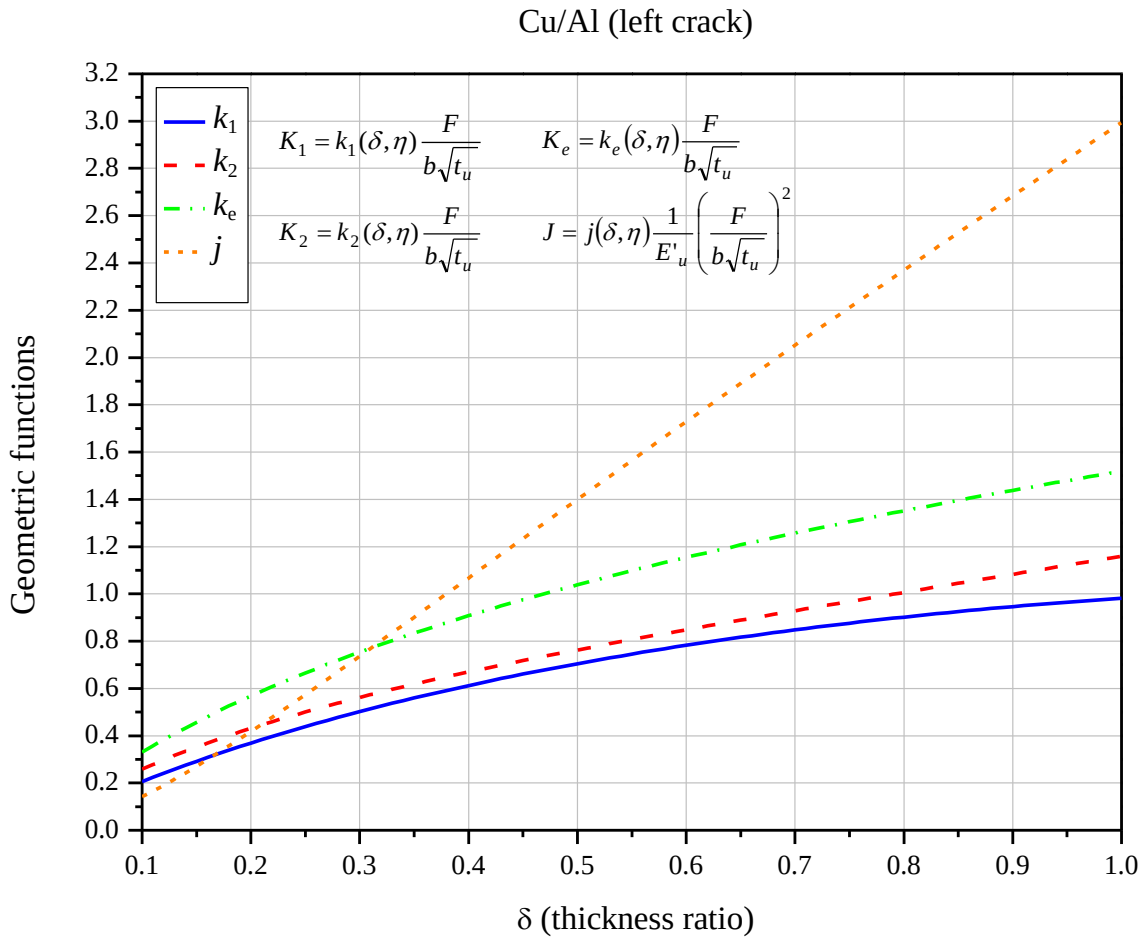
Cu/Al (left crack)
Geometric functions
δ (thickness ratio)
k1
k2
ke
j
K1 = k1(δ,η) F/(b√tu)
Ke = ke(δ,η) F/(b√tu)
K2 = k2(δ,η) F/(b√tu)
J = j(δ,η) 1/E'u (F/(b√tu))^2
3.2
3.0
2.8
2.6
2.4
2.2
2.0
1.8
1.6
1.4
1.2
1.0
0.8
0.6
0.4
0.2
0.0
0.1
0.2
0.3
0.4
0.5
0.6
0.7
0.8
0.9
1.0

(a)

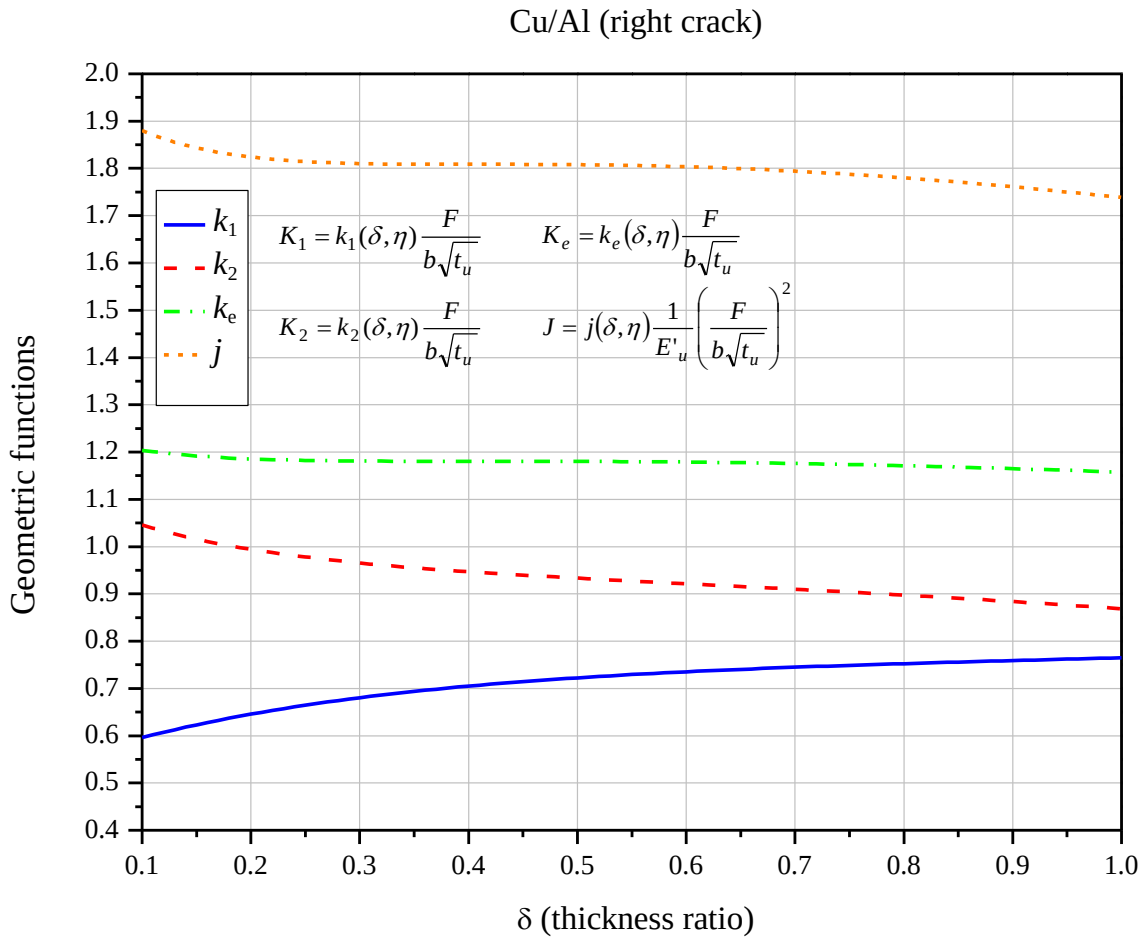

(b)

Figure 6.14. The dimensionless geometric functions k_1, k_2, k_e and j as functions of the thickness ratio δ for (a) the left and (b) the right cracks of a Cu/Al weld based on the analytical solutions.

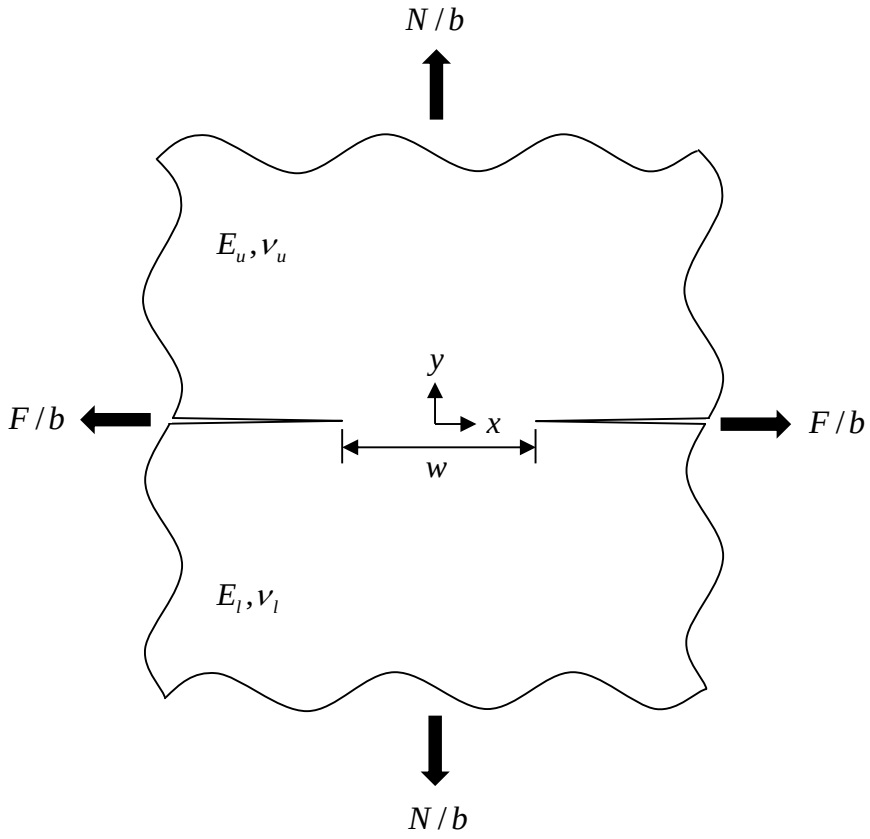

Figure 6.15. A schematic diagram of two half planes of dissimilar materials with connection of the length w. The Cartesian $x-y$ coordinate system is shown. The shear forces per unit width, F/b, are applied along the x axis at $x=+\infty$ and $-\infty$ of the upper solid and lower solid, respectively. The normal forces per unit width, N/b, are applied along the y axis at $y=+\infty$ and $-\infty$ of the upper plane and lower plane, respectively.

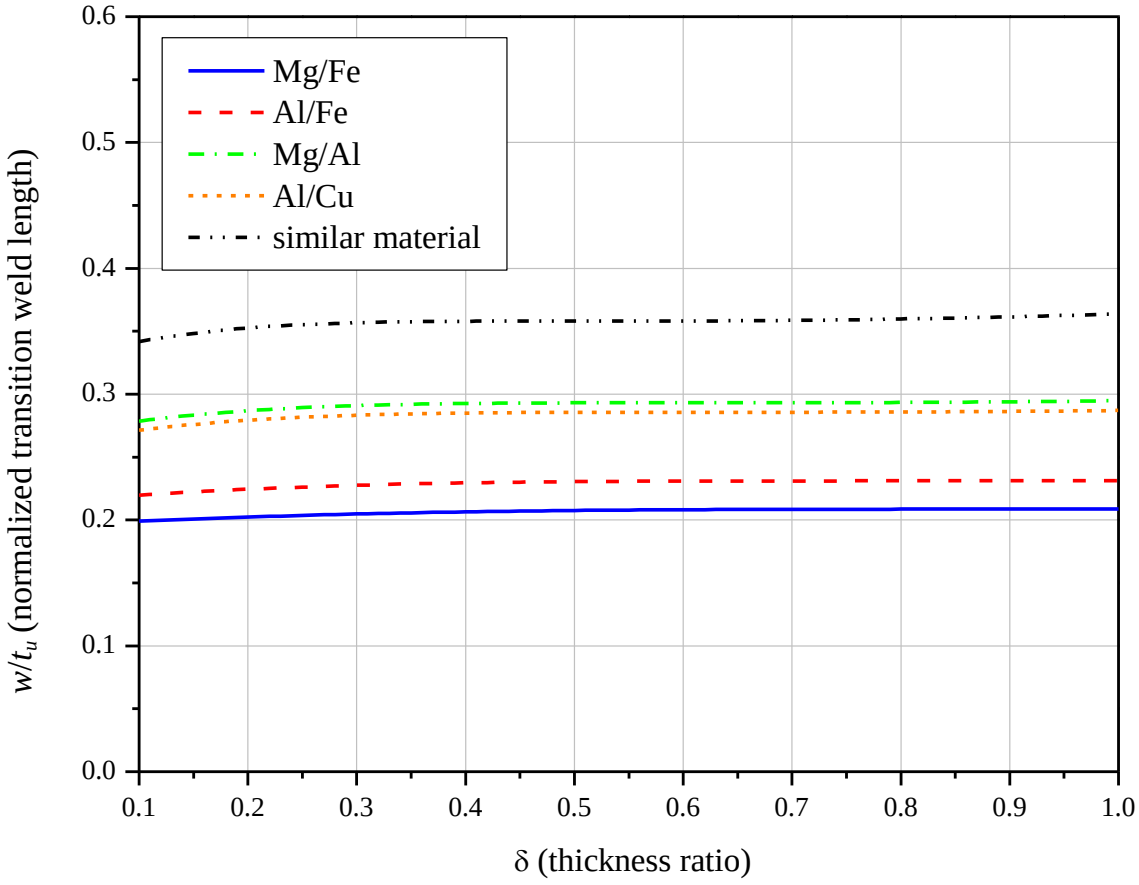

Figure 6.16. Normalized transition weld width as a function of δ for welds joining dissimilar and similar materials.

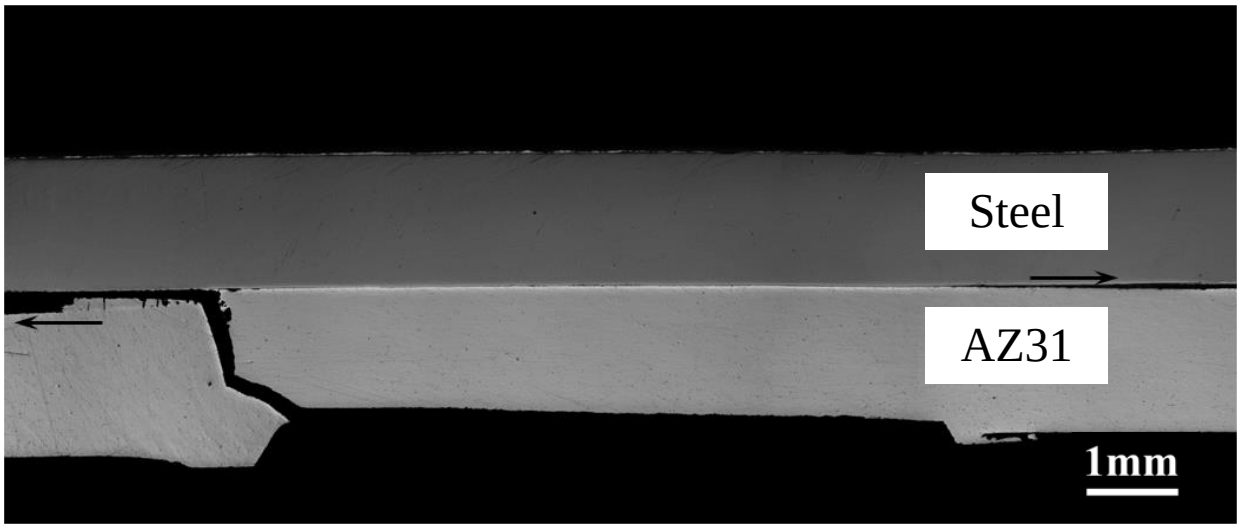

Figure 6.17. An optical micrograph of the cross section of a failed ultrasonic spot welded lap-shear specimen of magnesium and steel sheets under cyclic loading conditions [1]. The thickness ratio $\delta = 1.0$.

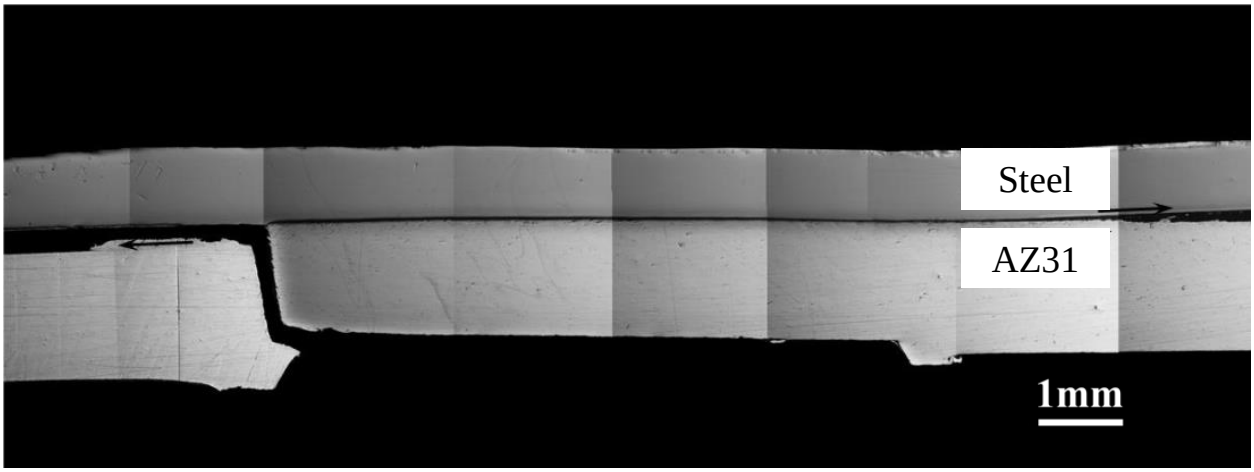

Figure 6.18. An optical micrograph of the cross section of a failed ultrasonic spot welded lap-shear specimen of magnesium and steel sheets under cyclic loading conditions [1]. The thickness ratio $\delta = 0.5$.

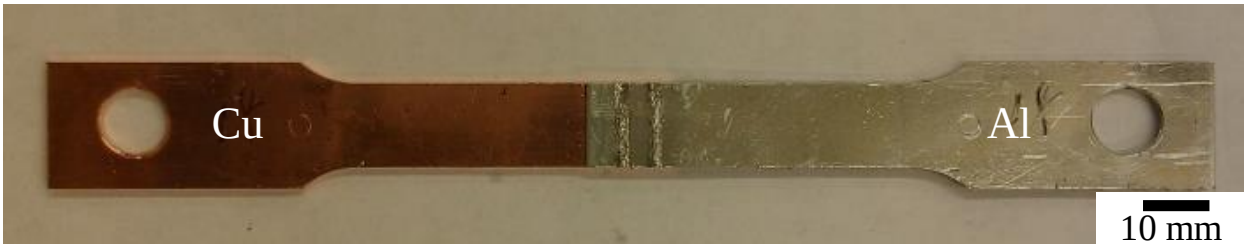

(a)

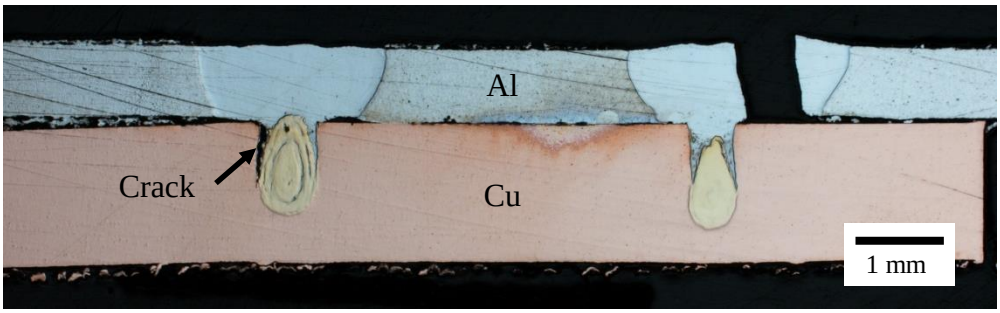

(b)

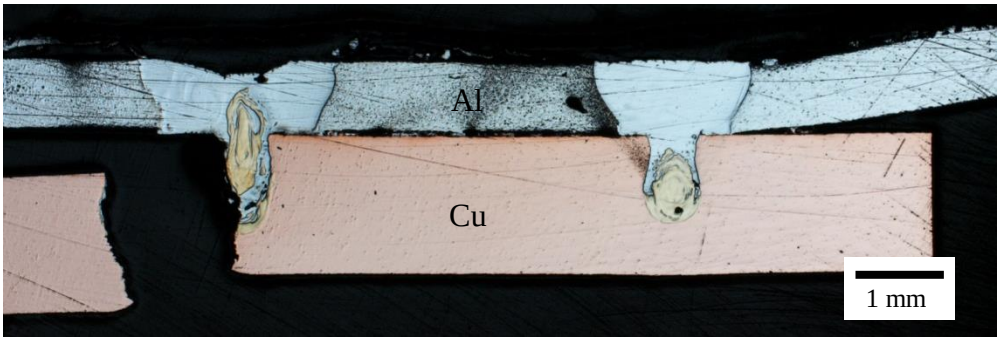

(c)

Figure 6.19. (a) A laser welded lap-shear specimen of copper and aluminum sheets which has been machined into a dog-bone shape. Optical micrographs of the cross sections of failed laser welded lap-shear specimens of copper and aluminum sheets under (b) low-cycle and (c) high-cyclic loading conditions, respectively [11]. The thickness ratio $\delta = 0.5$.

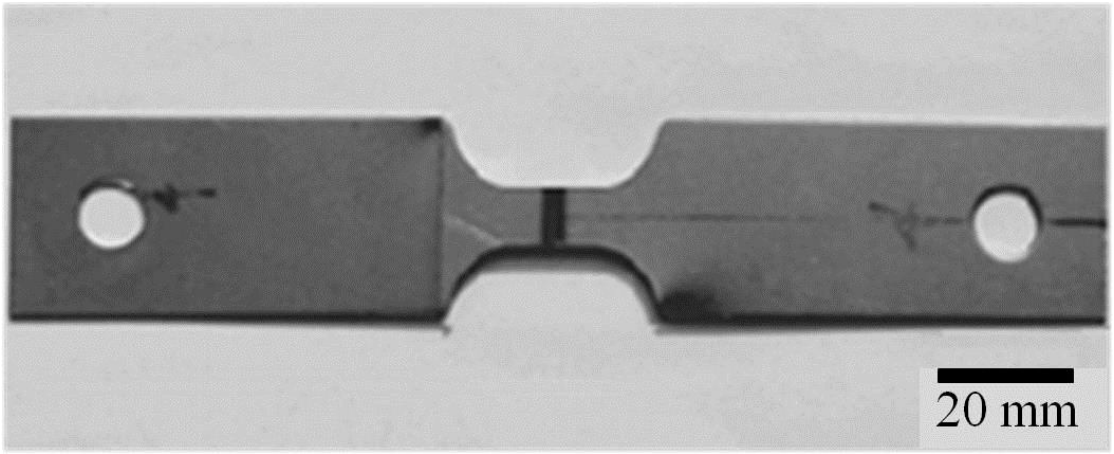

(a)

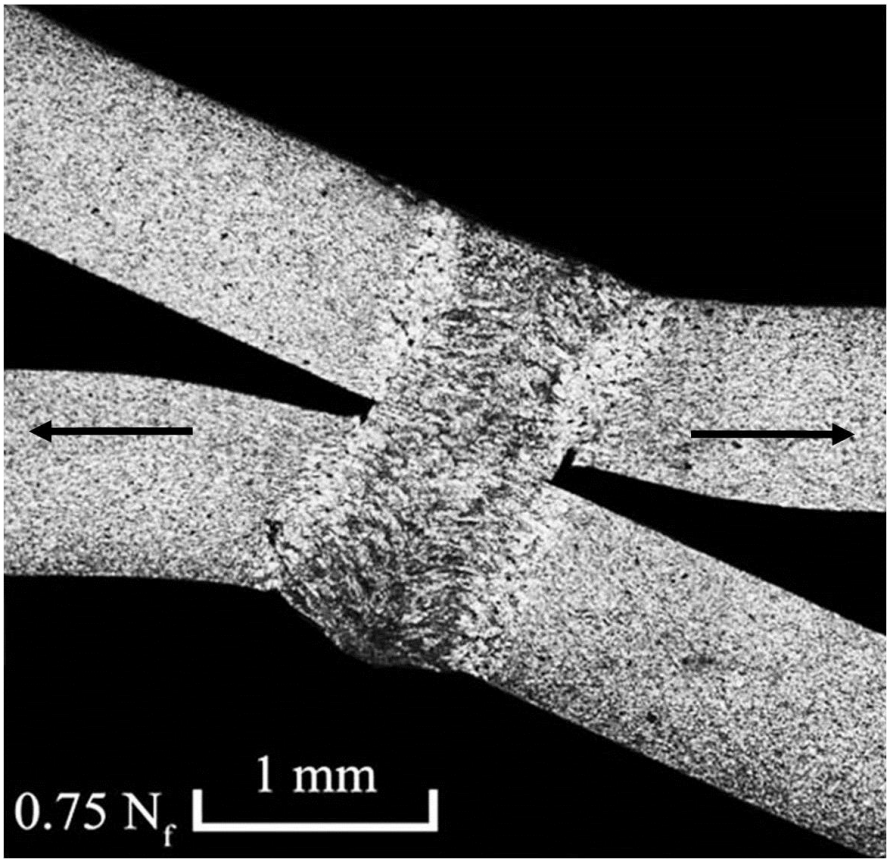

(b)

Figure 6.20. (a) A laser welded lap-shear specimen of high strength low alloy steels sheets which has been machined into a dog-bone shape. (b) An optical micrograph of the etched cross section of a partially failed laser welded lap-shear specimen of high strength low alloy steel sheets under cyclic loading conditions [12].

Acknowledgments

Partial support by the U.S. Department of Energy, Assistant Secretary for Energy Efficiency and Renewable Energy, Office of Vehicle Technologies, as part of the Lightweight Materials Program is greatly appreciated.

References

[1] T. Franklin, "Fatigue Behavior and Life Estimation for Dissimilar Ultrasonic Welds in Lap-Shear Specimens of Magnesium and Galvanized Steel Sheets," Ph.D. thesis, Department of Mechanical Engineering, University of Michigan, Ann Arbor, Michigan, 2013.

[2] K. Sripichai, K. Asim, and J. Pan, "Stress Intensity Factor Solutions for Estimation of Fatigue Lives of Laser Welds in Lap-Shear Specimens," Engineering Fracture Mechanics, vol. 78, pp. 1424-1440, 2011.

[3] S. Zhang, "Stress Intensities Derived from Stresses around a Spot Weld," International Journal of Fracture, vol. 99, pp. 239-257, 1999.

[4] V.-X. Tran and J. Pan, "Analytical Stress Intensity Factor Solutions for Resistance and Friction Stir Spot Welds in Lap-Shear Specimens of Different Materials and Thicknesses," Engineering Fracture Mechanics, vol. 77, pp. 2611-2639, 2010.

[5] Z. Suo and J. W. Hutchinson, "Interface Crack between Two Elastic Layers," International Journal of Fracture, vol. 43, pp. 1-18, 1990.

[6] J. R. Rice and G. C. Sih, "Plane Problems of Cracks in Dissimilar Media," Journal of Applied Mechanics, vol. 32, pp. 418-23, 1965.

[7] J. R. Rice, "Elastic Fracture Mechanics Concepts for Interfacial Cracks," Journal of Applied Mechanics, vol. 55, pp. 98-103, 1988.

[8] ABAQUS V6.12 User Manual, SIMULIA, 2012.

[9] C. F. Shih and R. J. Asaro, "Elastic-Plastic Analysis of Cracks on Bimaterial Interfaces: Part I-Small Scale Yielding," Journal of Applied Mechanics, Transactions ASME, vol. 55, pp. 299-316, 1988.

[10] F. Erdogan, "Stress Distribution in a Nonhomogeneous Elastic Plane with Cracks," Journal of Applied Mechanics, vol. 30, pp. 232-236, 1963.

[11] W.-J. Lai, S.-J. Sung, J. Pan, Y. Guo, and X. Su, "Failure Mode and Fatigue Behavior of Dissimilar Laser Welds in Lap-Shear Specimens of Aluminum and Copper Sheets," SAE Technical Paper No. 2014-01-1986, Society of Automotive Engineers, Warrendale, PA, 2014.

[12] K. Asim, K. Sripichai, and J. Pan, "Fatigue Failure of Laser Welds in Lap-Shear Specimens of High Strength Low Alloy (HSLA) Steels under Cyclic Loading Conditions," SAE International Journal of Materials and Manufacturing, vol. 4, pp. 571-580, 2011.

Chapter 7
Conclusion

In Chapter 2, the quasi-static in-plane constrained compression test results indicate that the load carrying behavior of cell RVE specimens is characterized by the buckling of cells with a wavelength on the order of the thickness of the cells, kink and shear band formation, and the final densification of the cell components. The different nominal compressive stress-strain curves in the in-plane and out-of-plane directions suggest that the cells can be modeled as anisotropic foams or cellular materials. This is important information for development of macro homogenized anisotropic material models for crashworthiness analyses. The initial elastic buckling mode of the cell RVE specimen under in-plane constrained compression can be correlated to the elastic buckling solution of a beam with lateral constraints. The development of the higher order buckling modes of the component sheets and the critical stresses observed in experiments are in agreement with the results of the analytical buckling solutions and the corresponding finite element analyses. The elastic buckling analyses also justify the length selection of the cell RVE specimens. An idealized kinematics model is developed to explain the kink and shear band formation in the cell RVE specimens under in-plane constrained compression. The nominal strains in the regions inside and outside of the shear band can be estimated by the idealized model and the results give some insight on the physical deformation process observed in experiments.

In Chapter 3, the quasi-static tensile test results of the module components indicate that the active materials on the cathode and anode sheets have nearly no load carrying capacity. In the quasi-static in-plane constrained compression tests of the module RVE specimens, the nominal stress-strain curves show stress drops due to buckling and then final densification. The stress drops of the curves were correlated to the deformation patterns. It is noted that no significant size effect was observed for the module RVE specimens of different heights under in-plane constrained compression tests when the strain is below 30%. Above the strain of 30%, the nominal stress of the double-height specimens increases faster as the strain increases. The different nominal compressive stress-strain curves of module RVE specimens under in-plane and out-of-plane compression suggest that the lithium-ion battery modules can be modeled as anisotropic foams or cellular materials. This is important information for development of macro homogenized anisotropic material models for crashworthiness analyses. The calculated buckling stress agrees well with the experimental results based on the buckling analyses. Finally, the results of a constrained punch indentation test on a small-scale module specimen indicate that the tested specimen shows the similar buckling mode as observed for the module RVE specimens under in-plane constrained compression tests. The experimental results for the small-scale module specimen can be used to benchmark and validate new macro homogenized material models.

In Chapter 4, the test results indicate that the ultrasonic spot weld appears not to provide extra strength to the weld-bonded lap-shear specimen under quasi-static and cyclic loading conditions. The quasi-static and fatigue strengths of adhesive-bonded and weld-bonded lap-shear specimens appear to be the same. For the ultrasonic spot welded lap-shear specimens, the optical micrographs indicate that failure mode changes from the partial nugget pullout mode

under quasi-static and low-cycle loading conditions to the kinked crack failure under high-cycle loading conditions. For the adhesive-bonded lap-shear specimens, the optical micrographs indicate that failure mode changes from the near interface cohesive failure under quasi-static and low-cycle loading conditions to the kinked crack growth mode under high-cycle loading conditions. For the weld-bonded lap-shear specimens, the optical micrographs indicate that failure mode changes from the near interface cohesive failure through the adhesive and interfacial failure through the spot weld under quasi-static and low-cycle loading conditions to the kinked crack failure under high-cycle loading conditions.

In Chapter 5, the stress intensity factor solutions for adhesive-bonded lap-shear specimens of magnesium and steel sheets with and without kinked cracks are investigated first. The analytical global J integral and effective stress intensity factor solutions for main cracks in lap-shear specimens of three dissimilar sheets under plane strain conditions are developed based on beam bending theory. Next, the global stress intensity factor solutions for the main cracks in the lap-shear specimens are validated by the corresponding finite element analyses. The computational local stress intensity factor solutions for kinked cracks appear to approach to the analytical solutions as the kink length decreases to a very small kink length and the kinked crack is under dominant mode I loading conditions. The experimentally observed kink angle in general agrees with the analytical solution. The computational results also indicate that the local stress intensity factor solutions at a small kink length of microstructural significance may be used as the initial stress intensity factor solutions for zero kink length for fatigue life estimations when the computational results are not available. Finally, the general trend of fatigue life estimations agrees with that of the experimental results, but the fatigue life estimations are lower than the experimental results.

In Chapter 6, the analytical stress intensity factor and J integral solutions for welds in lap-shear specimens for two dissimilar sheets based on beam bending theory are presented in the normalized forms and validated by two-dimensional finite element analyses. The interfacial crack parameters, the stress intensity factor solutions, and the J integral solutions for welds in lap-shear specimens of different combinations of steel, aluminum, and magnesium, and the combination of aluminum and copper sheets of different thickness ratios are then presented for convenient fracture and fatigue analyses. The transition thickness ratios for critical crack locations for different combinations of dissimilar materials are then determined from the analytical solutions. The transition weld widths for applicable ranges of the weld widths for the analytical solutions based on the beam bending theory are also presented. Finally, fracture and fatigue behaviors of dissimilar ultrasonic magnesium/steel, dissimilar laser aluminum/copper, and similar laser steel welds in lap-shear specimens are examined and demonstrate the usefulness of the graphical stress intensity factor solutions.